EXOCYTOSIS AND ENDOCYTOSIS OF SYNAPTIC VESICLES IS REGULATED BY CALCIUM

Marc Andrew Meadows

A DISSERTATION

Thesis submitted to the Neuroscience Graduate Program at the Vollum Institute

Oregon Health and Science University

School of Medicine

In Partial Fulfillment of the Requirements for the Degree of Doctor of Philosophy

January 2022

Advisor, Henrique von Gersdorff, Ph.D.

Member & Chair, Catherine Morgans, Ph.D.

Member, Stephen M. Smith, M.B., B.S., Ph.D.

Member, Benjamin Sivyer, Ph.D.

Member, Anusha Mishra, Ph.D.

Member, Stefan Hallermann, M.D.

I. Certificate of Approval

In-Progress: Certificate of Approval

Row 1

Date Submitted	01/25/22 1:13 PM
Date Submitted (2-Week Notification)	
Date Modified	01/31/22 9:43 AM
Modified By	gookinl@ohsu.edu
Date Completed	01/31/22
Graduate Studies Review	
Program/Student Notification	Jessica Parks
UID	U00064913
Student's First Name	Marc
Student's Last Name	Meadows
OHSU Email	Meadowsm@ohsu.edu
Program	Neuroscience
Degree	PhD
Dissertation/Thesis Title	EXOCYTOSIS AND ENDOCYTOSIS OF SYNAPTIC VESICLES IS REGULATED BY CALCIUM
Date of Exam	01/05/21
Chair's First & Last Name	Catherine Morgans
Chair's Email	Morgansc@ohsu.edu
Mentor's First & Last Name	Henrique von Gersdorff
Mentor's Email	vongersd@ohsu.edu
Member A: First & Last Name	Stephen M. Smith

Member A: Email	smisteph@ohsu.edu
Additional Members	3 Additional Members
Member B: First & Last Name	Benjamin Sivyer
Member B: Email	sivyer@ohsu.edu
Member C: First & Last Name	Anusha Mishra
Member C: Email	mishraa@ohsu.edu
Member D: First & Last Name	Stefan Hallermann
Member D: Email	stefan_jens.hallermann@uni-leipzig.de
Committee Chair's Approval	Approved
Committee Mentor's Approval	Approved
Member A Approval	Approved
Member B Approval	Approved
Member C Approval	Approved
Member D Approval	Approved

Comments

stefan_jens.hallermann@uni-leipzig.de | January 29, 2022 5:42 AM

Congratulations again!

II. Table of Contents

III. Common Abbreviations

AC	amacrine cell
AII-AC	AII amacrine cell
ATP	adenosine triphosphate
BAPTA	1,2-bis(o-aminophenoxy)ethane-N,N,N′,N′-tetraacetic acid
BC	bipolar cell
cAMP	cyclic adenosine monophosphate
CBC	cone bipolar cell
CICR	calcium induced calcium release
C_m	capacitance
cone	cone photoreceptor
Cx36	connexin 36
EGTA	ethylene glycol-bis(β-aminoethyl ether)-N,N,N′,N′-tetraacetic acid
EPAC	exchange protein directly activated by cAMP
ER	endoplasmic reticulum
fF	femptofarad
GC	ganglion cell
GCL	ganglion cell layer
GPCR	g-protein coupled receptor
GTP	guanosine triphosphate
I_{Ca}	calcium current
iGluR	ionotropic glutamate receptor
I_m	membrane current
INL	inner nuclear layer
IPL	inner plexiform layer
mGluR	metabotropic glutamate receptor
mIPSC	miniature inhibitory current
mV	millivolt
OFF	OFF pathway
ON	ON pathway
ONL	outer nuclear layer
OPL	outer plexiform layer
pC	picocoulomb
PKA	protein kinase A
P_r	Probability of release
RBC	rod bipolar cell
RF	retrieval fraction
R_m	membrane resistance
rod	rod photoreceptor
RRP	Readily releasable pool
R_s	series resistance
sIPSC	spontaneous inhibitory current
SOCE	store operated calcium entry
τ	exponential time constant
TRPM	transient receptor potential cation channel subfamily M
VGCC	voltage gated calcium channel
VGSC	voltage gated sodium channel
V_m	membrane voltage

IV. Dedication

This work is dedicated to all the family, friends, and colleagues who helped me bear the burdens of graduate school. I'd like to share my appreciation for my mentor, Henrique, who has and continues to believe in my aptitude as a scientist. Additionally, I want to thank past and present members of the von Gersdorff lab who make our workspace a generous and joyful environment. This has been the best work environment that I've ever had. Special thanks to Andre Dagostin who always takes time from his busy schedule to help me with my coding problems. Secondly, the members of my thesis committee Catherine Morgans, Benjamin Sivyer, Stephen Smith, and Anusha Mishra for their encouragement and excitement for my work. Thirdly, I would like to acknowledge my co-bargaining members of the graduate researchers united Sam Papadakis, Danielle Mathieson, and Rich Posert who have radically changed my perspectives and hope for the world. My fellow bargaining team members along with the many founding members have improved lives of graduate researchers at OHSU, and give me hope for better future.

Finally, I want to dedicate this work to my family members. My mother, brothers, wife and all their families continue to give me the love and care I needed to finish a doctoral thesis in the middle of a global health crisis. Dave and Sharon gave me a lot of support and always enlisted me in their adventures. Lisa Meadows has remained my loving wife, partner and best friend throughout all the hardships that come along with finishing graduate school. She makes me laugh, she makes me better. This work is ultimately dedicated to Mi-suk (미숙) Cooper and Bill Silva who my families unexpectedly lost during my time as a graduate student. My mother in-law and stepfather were a big part of my life and gave me the means and confidence to pursue a doctoral degree. Losing them has been like losing a part of myself, but their memory gives me reason to work hard, be loving, and help others at the times when I doubt myself.

난 그냥 사람, 사람 사람
I'm just a human, human, human
넌 나의 모든 모서릴 잠식
You erode all my edges
나를 사랑, 사랑, 사랑으로 만들어 만들어
and make me a love, love, love

--김남준

V. Abstract

Neurons communicate with each other either through electrical synapses formed by gap junctions, or by the synaptic release of neurotransmitters. Release of neurotransmitter into the synaptic cleft is occurs when loaded synaptic vesicles fuse to the plasma membrane (exocytosis). Neurons have a compensatory process that retrieves fused vesicle membrane from the active zone (endocytosis), maintaining membrane homeostasis. Presynaptic capacitance (C_m) measurements can directly test exo- and endocytosis mechanisms with microsecond temporal resolution without interference from saturation or desensitization of postsynaptic receptors. The biggest limitation of C_m measurements is that they require high frequency stimulation, which has limited this technique to cells with simple morphology or patchable large terminals. Developments in this field indicate that neurons and synaptic terminals with more complicated morphology can be studied using this technique. The focus of this study is on a retinal interneuron, the AII amacrine cell (AII-AC), that is the only inhibitory interneuron to be studied using C_m measurements to date. AII-ACs are at the center of rod-mediated scotopic (night) and cone-mediated photopic (day) vision pathways. Rod bipolar cells (RBCs) and ON-cone bipolar cells (ON-CBCs) provide excitatory input to the AII-AC that is converted into glycine release to OFF-pathways (crossover inhibition). Unlike other retinal amacrine cells, the AII-ACs release glycine from dendritic lobules close to the soma and electronically accessible with C_m measurements. Preceding work found that AII-ACs have two vesicle pools, and they are adapted for sustained release. The work in this thesis found mechanisms for potentiation and endocytosis in AII-ACs. Chapter 1 of this thesis introduces retinal circuits and background information about C_m measurements in cells with complex morphology. Chapter 2 will discuss our published findings on cAMP-dependent potentiation where we uncovered mechanisms involve EPAC2 and Ca^{2+} stores and show an increase in crossover inhibition to OFF-CBCs. Chapter 3 will present a study on endocytosis. We found that dynamin, and clathrin are necessary for endocytosis in AII-ACs. We also found that endocytosis is loosely nanodomain coupled to L-type Ca^{2+} channels that we speculate are clustered near a readily retrievable pool in peri-active zones. Chapter 4 covers experiments developing Ca^{2+} imaging using the genetically encoded Ca^{2+} indicator, GCaMP6f, which we used to show that EPAC2 triggers Ca^{2+} induced Ca^{2+} release. We also show that dopamine reduces glycine release by modulating the AII-AC spike properties.

Chapter 1: Introduction

Section 1.1: Preface

Photons are first created during the energetic fusion reactions deep in the core of stars. It can take up to 40,000 years before a photon reaches the surface of our sun after being absorbed and emitted by densely packed atoms. Our sun emits trillions of photons per second, and after only 8 minutes they reach earth, travelling at 300,000 km/s (i.e., the constant speed of light in a vacuum). The high energy and low entropy of the sun's photons powers life on earth (Kirk A, 2015). Most eukaryotic life exhibits phototaxic behaviors— photosynthetic plants and algae use cues from photons to alter their orientation and blooming patterns (Jékely, 2009). As a unique example of phototaxic behaviors, we will briefly discuss the symbiotic interactions between the golden jellyfish and algae (dinoflagellates) of the marine lakes of Palau. The golden jellyfish have non-image-forming vision and exhibit diel migration patterns through water's vertical axis, which provides the algae living in their tissue access to nutrient rich lake-bottom. While the golden jellyfish provide protection and transportation, they receive nutrients from the photosynthetic algae. The jellyfish have adapted horizontal migration patterns throughout the day and a rotating swimming behavior to evenly bathe their symbiotic algae with photons from the sun's rays (Dawson and Hamner, 2003; Dawson, 2005). More complex animal behaviors emerged with the development of eyes, evolving from the dense clustering of photoreceptors, which provided animals with image forming vision (Randel and Jékely, 2016). Early vertebrate camera-style eyes developed 500 mya (millions of years ago), with a primordial retina— the sensory neural tissue at the back of the eye— containing only photoreceptors and output neurons. Over 100 mya, the retina acquired a three layered cellular structure and more processing power through the evolution of bipolar cells, amacrine cells, and duplex (rod + cone) visual pathways (Lamb et al., 2007). Forty years after Einstein first suggested that light interacts with matter as both a wave and a shower of particles, photons, early behavioral experiments determined that only 100 photons aimed at the cornea with a spot diameter covering 100 – 1000 rod photoreceptors was detectible by the human retina. Decades of experiments in different mammals have shown that a few photons are required to generate a detectable signal and the cellular processes of the rod

photoreceptors (rods) allow for reliable single-photon responses (reviewed in Field and Sampath, 2017). Even more remarkable is the dynamic range of the retina that emerged with duplex visual pathways. At scotopic (nighttime) conditions, light intensity ranges from 10^{-4} to 10^{-2} candela/cm^2 are likened to a moonless night. When photons are at a premium during scotopic conditions, anti-correlated responses from highly sensitive rods produce monochromatic visual responses. Photopic (daytime) are when light conditions extend beyond 10^2 candela/cm^2 (Kelber et al., 2017). Under a clear sky, roughly 10^{17} photons irradiate a 1 cm^2 sun-facing area every second (Kirk A, 2015), so it is wise not to stare directly at the sun. When photons are over-abundant in photopic conditions, cone photoreceptors are active and their correlated responses produce color vision (Kelber et al., 2017; Roy and Field, 2019). Cones also produce a faster and more transient response than rods to rapidly changing visual stimuli, making them better detectors of moving objects. Rods are thought to have evolved from more ancient cone photoreceptors, as mammals adapted to a nocturnal terrestrial environment that was apparently safer from dinosaur predators. Rods then led to a specialized retinal circuitry of bipolar and amacrine cells to process dim-light signals. In each instance, visual cues begin when a single photon hits a protein called opsin that transforms the energy from a single photon into a biochemical signal. The visual cues animals receive ultimately shape their behaviors, from non-image forming invertebrates to raptors with highly evolved eyes. Photons can cue an animal to move away from a looming predator, to swoop down to grab an unsuspecting meal, or to contemplate one's own smallness while gazing at the cosmos.

Section 1.2: Retina structure and pathways

1.2.1 Nuclear and synaptic layers of the retina

The retina is the sensory neuronal tissue on the back of the eye that transduces light into biochemical and electrical signals that are interpretable by the brain. Over millions of years, the retina has evolved from its primordial structure consisting only of photoreceptors and output neurons into a powerful microprocessor of light information. The vertebrate retina has three cellular layers separated by two synaptic layers (Fig. 1.1). The three cellular layers are called: the

Figure[1.1]

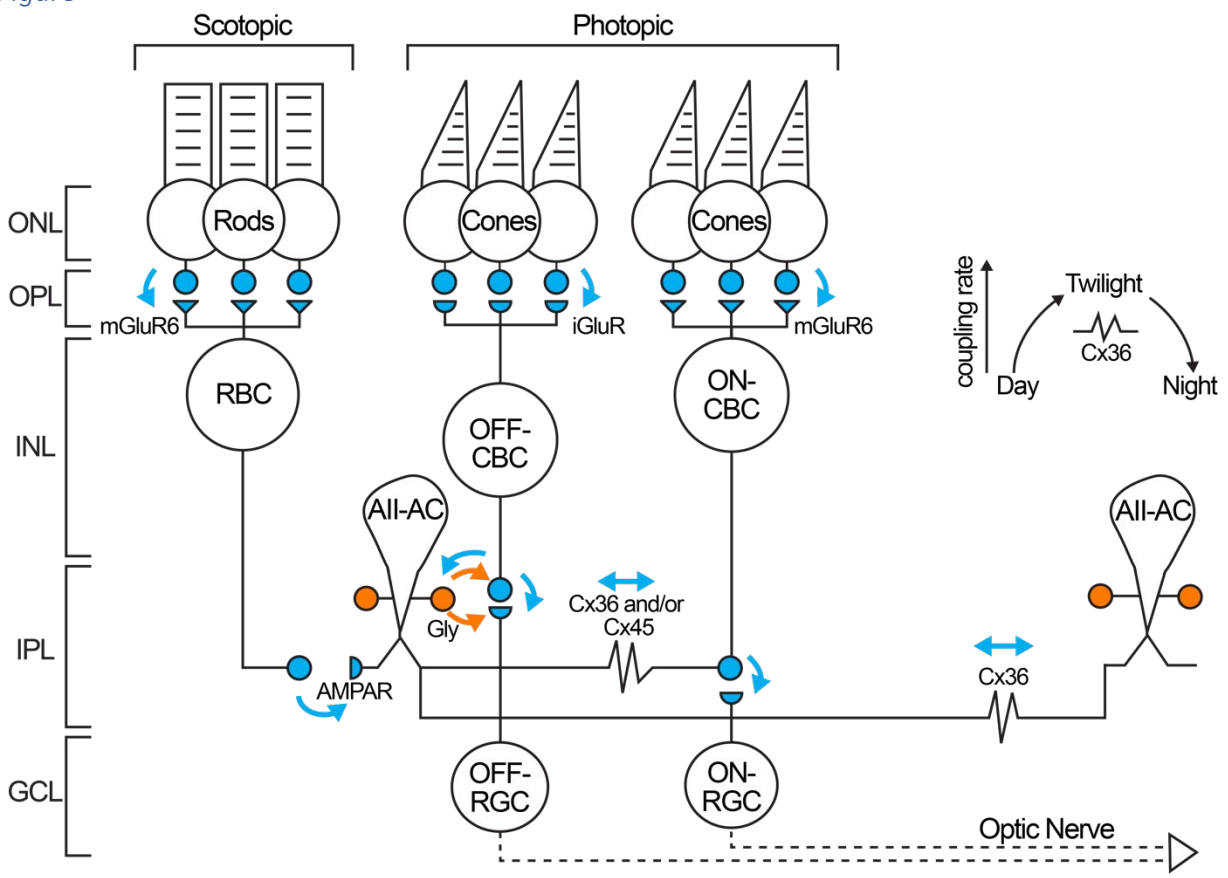

[1.1] Schematic of retinal circuits involved in crossover inhibition pathways.

Shown are the layers of the retina (see text for description). ONL contains rod and cone photoreceptors that detect light during scotopic (night) and photopic (day) conditions, respectively. INL contains RBCs, OFF-CBCs, and ON-CBCs. Synaptic transfer of light signals between photoreceptors and BCs occurs in the outer plexiform layer (OPL). Photoreceptors continuously release glutamate (blue circles) in the absence of light. RBCs and ON-CBCs have sign inverting synapses containing mGluR6 (blue triangles) mediating the inhibition of TRPM1 channels. TRPM1s open and depolarizes RBC and ON-CBCs when light responses cause a relief in glutamate signaling. OFF-CBCs have AMPA/Kainate receptors (iGluRs; blue semicircles), and depolarize in the absence of a light signal. AII-AC cell bodies are located at the bottom of the inner nuclear layer, and have bistratified dendrites projecting into the OFF- and ON- sublamina of the IPL. The distal AII-AC dendrites receive excitatory glutamatergic inputs from RBCs and electrical synapses through gap junctions with ON-CBCs and other AII-ACs. RBC signals are relayed by AII-ACs to the ON-CBC terminals through gap junctions. Crossover inhibition refers to the transformation of excitatory signals into glycinergic inhibition (orange circles) provided to OFF-CBCs and OFF-GCs. Also shown is homocellular gap junction coupling between AII-ACs in adjacent receptive fields. Coupling state is regulated by transitions from scotopic to photopic conditions, with the highest network coupling in twilight (mesopic) ambient light conditions.

outer nuclear layer (ONL), inner nuclear layer (INL), and ganglion cell layer (GCL). Photoreceptors are located in the ONL and responsible for phototransduction (see section 1.2.2). Rods and cones are also coupled via gap junctions to each other (not shown). Bipolar cells in the INL relay signals to output neurons called ganglion cells (GCs) which are located in the GCL. Horizontal cells (not shown) and amacrine cells located in the INL perform lateral processing of visual signals (see section 1.2.4).

1.2.2 Phototransduction

The retina is oriented such that the photoreceptors in the ONL are located at the most posterior region of the retina, closest to the back of the eye. Light must pass through the entire retina before reaching the photoreceptor outer segments where it is converted into bioelectrical signals by photoreceptors. How are photons transformed into electric signals? The outer segments contain specialized g-protein coupled receptors (GPCRs) called opsins. Like all GPCRs, they have seven transmembrane domains, but unique to opsins is a binding pocket that contains a covalently bound retinaldehyde. The retinaldehyde, or retinal, is derived from vitamin A and is bound in the 11-cis conformation. The energy from a photon is absorbed by the retinal causing the photoisomerization of the molecule from 11-cis to all-trans isoform. This causes a conformational change in the opsin initiating a phototransduction cascade; the light dependent reduction of cyclic-GMP (cGMP) concentrations leads to hyperpolarization of the photoreceptor, which has cGMP-gated cation channels in the outer segments (Arshavsky et al., 2002). Therefore, photoreceptors continuously release glutamate in the absence of light, and a light response translates into a hyperpolarization that causes a relief of glutamate release to BCs, which depolarizes ON-type BCs and hyperpolarizes OFF-type BCs.

1.2.3 Parallel pathways for transmission of light signals through the retina

The retina operates under a wide dynamic range of light intensity by splitting visual signals into multiple adaptable visual pathways (Demb and Singer, 2012; Hartveit and Veruki, 2012; Roy and Field 2019). Photoreceptors are divided into rods and cones. There is a 10-fold difference in response latency times between rods and cones, 500 ms vs 50 ms for the same light flash (Schnapf and Copenhagen; 1982). Rods are adapted for super-sensitive single photon detection

and recover slowly, thereby making them suitable for scotopic vision. Cones need more photons for activation, but can recover more quickly allowing them to operate in a wider range of ambient light levels (mesopic to photopic).

Bipolar cells (BCs) are located in the INL with dendrites that stratify in the OPL, and receive glutamate signals from photoreceptors. There are at least 15 types of bipolar cells including the rod bipolar cell (RBC), 6 OFF-type cone bipolar cells (OFF-CBCs), and 8 ON-type cone bipolar cells (ON-CBCs), which are classified by their photoreceptor inputs and genetic markers (Shekar et al., 2016). RBCs are the designated BC for transmitting signals from rods, while ON- and OFF-CBCs receive inputs from mainly from cones. Both RBCs and ON-CBCs have type 6 metabotropic glutamate receptors (mGluR6) in their dendritic tips that inhibit TRPM1 channels. Light signals relieve inhibition of TRPM1, thus depolarizing the ON-type BCs (Morgans et al., 2009, 2010). OFF-CBCs express ionotropic glutamate receptors (iGluR), and depolarize in the absence of light when cones are continually releasing glutamate. There is evidence that OFF-CBCs express AMPA and/or kainate receptors (DeVries, 2000; Puller et al., 2013, Borghuis et al., 2014). ON- and OFF-CBCs project axon terminals that contact ganglion cell (GC) dendrites at specific layers of the IPL. The GCs cell bodies are located in the GCL, but their dendrites stratify in the IPL. The schematic (Fig. 1.1) only shows GCs with dendrites stratifying in ON or OFF sublamina of the IPL. Not depicted, however, are bistratified ON-OFF GCs (Sanes et al., 2015). GCs are the output neurons of the retina; their axons form the optic nerve. Analog light signals are therefore processed through parallel pathways that are encoded into patterns of all-or-nothing (digital) action potential spikes.

1.2.4 Inhibitory pre-processing of visual signals

Lateral networks of horizontal cells (not shown) and amacrine cells perform intermediary pre-processing of visual signals. Horizontal cell dendrites stratify in the IPL providing feedback to photoreceptors and feedforward inhibition to BCs (Thoreson et al., 2004; Yang et al., 1991). We only show a single type of amacrine cell, the AII amacrine cell (AII-AC; Fig. 1.1); however, there are approximately 60 distinct types of ACs that are generally divided into narrow-field glycinergic and wide-field GABAergic cells (Yan et al., 2020). The AII-AC is a glycinergic amacrine cell located at the INL/IPL border with bistratified dendrites that project within the IPL. Shown in Figure 1.1,

the RBC does not have a designated GC, but releases glutamate to AMPA receptors at the AII-AC's distal dendrites. The AII-AC relays signals from the rod pathway to ON-CBC through electrical synapses (Veruki et al., 2002b; Wässle, 2004; Graydon et al., 2018). The AII-AC is also involved in crossover inhibition, where excitatory light responses from RBCs and ON-CBCs are converted into glycinergic inhibition of OFF-CBCs and OFF-GCs.

1.2.5 Gap junction networks

Gap junctions are widespread throughout the retina. For instance, rods form electrical synapses with cones through gap junctions in their pedicles, as an alternate signaling pathway for scotopic vision. AII-ACs also form vast homocellular (same cell type) gap junction networks, in addition to coupling with ON-CBCs. Connexin 36 is expressed in AII-ACs and mediates homocellular coupling, as shown with ultrastructure, tracer dye, and electrophysiological experiments (Kolb and Famiglietti 1974, Hampson et al., 1992; Strettoi et al., 1992, Veruki and Hartveit, 2002a). The AII-AC network is heavily regulated across transitions from scotopic to photopic light conditions (illustrated in Fig. 1.1). Light adapted changes to the AII-AC network result in reduced tracer dye spread in scotopic and photopic conditions, and maximal spread in mesopic (twilight) conditions (Bloomfield and Völgyi, 2009). The pattern of tracer dye mobility when plotted against ambient light intensity forms an upside-down U-shape or arching pattern associated with the open state of gap junctions (illustrated in Fig. 1.1). The arching pattern in the spread of tracer dye is in part due to rising dopamine levels and a cAMP signaling cascade that dephosphorylates gap junctions (Hampson et al., 1992; Kothmann et al., 2009; Mills and Massey, 1995; Urschel et al., 2006). Blocking coupling between AII-ACs with meclofenamic acid (MFA) during paired recordings leads to increases in their input resistance, providing key physiological relevance to the role of gap junctions in AII-AC signaling (Veruki et al., 2010). The gap junctions between ON-BCs and AII-ACs are functional bidirectional electrical synapses (Veruki and Hartveit, 2002b, 2009; Graydon et al., 2018). ON-CBCs express both connexin 36 and 45, although is not known which type or both are responsible for coupling with AII-ACs (Han and Massey, 2005; Lin et al., 2005; Dedek et al., 2006). The connections between ON-CBCs and AII-ACs serve as a primary connection pathway for rod vision and cone mediated crossover inhibition. Adaptation of the homocellular network allows the AII-AC to function under a wide dynamic range of background light intensity (scotopic,

mesopic, and photopic): 1) Scotopic: Uncoupling preserves single-photon rod responses during dim-light conditions. 2) Mesopic: Coupling summates low-intensity signals during medium-light conditions. 3) Photopic: Uncoupling preserves spatial resolution of cone responses by providing crossover inhibition to a limited narrow receptive field (Hartveit and Veruki, 2012; Roy and Field 2019).

Section 1.3: Capacitance measurements in AII-ACs

1.3.1 Time-resolved capacitance measurements

Figure[1.2]

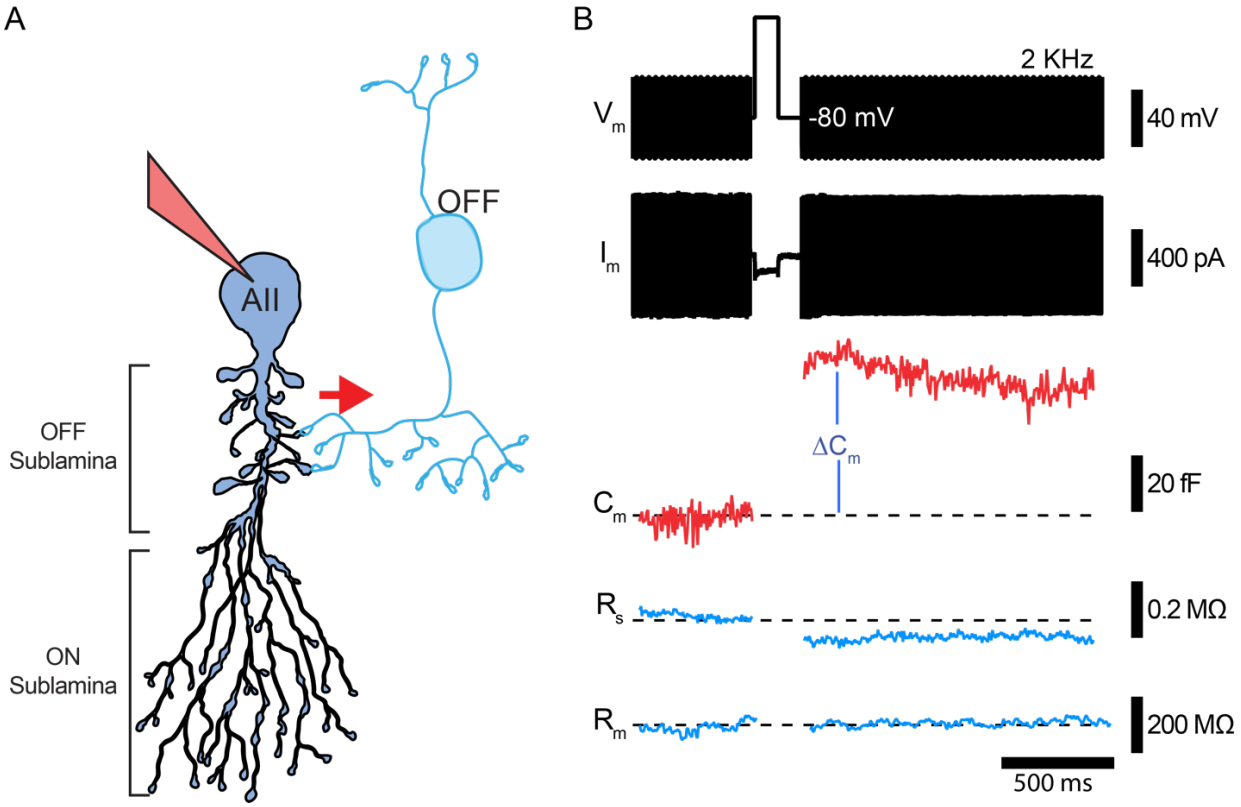

[1.2]AII-ACs are multi compartment cells suitable for C_m measurements.

A, Schematic inhibitory glycine release (red arrow) to the OFF-CBC from proximal dendritic lobules of the AII-AC. Labeled are the OFF and ON sublamina of the IPL. The release sites of the AII-AC are depicted near the soma, conveniently located near the recording patch-pipette (red scalene triangle). ***B,*** Whole-cell voltage-clamp recording from a mouse AII-AC showing the voltage stimulus (V_m; black) consisting of a sinusoidal wave (2 kHz; 30 mV peak-to-peak) super imposed on a -80 mV holding potential that are separated by a 100 ms depolarizing step pulse to -10 mV. Below is the current response (I_m; black) and the Ca^{2+} current (I_{Ca}). Passive membrane properties can be calculated from I_m: the capacitance (C_m; red), series resistance (R_s; blue) and membrane resistance (R_m; blue). Notice the correlated increase in the C_m jump response (ΔC_m) and inverse change in R_m.

Capacitance (C_m) measurements designed for high temporal resolution can provide an important tool for studying vesicle fusion (exocytosis) and membrane retrieval (endocytosis) in living cells (Neher and Marty, 1982). These measurements are sensitive enough to measure small changes in the membrane surface area during exo- and endocytosis of single vesicles (Lindau and Neher 1988). We use the "sine + DC" method in this thesis to measure the three passive properties of the cell (C_m, R_m, and R_s). In this method, the direct current (DC) is measured and then sinusoidal voltage stimulus (V_m) is used to generate and alternating membrane current response (I_m). Real time calculations are made of C_m by separating real and imaginary components of the admittance based measurement (Chen and Gillis, 2000). The passive properties of the cell are separable because the sinusoidal current response (I_m) is not in phase with the voltage stimulus. The phase of I_m is determined by resistance and capacitance components, which are respectively in phase and 90° orthogonal to the voltage stimulus (see Gillis, 2000). An example whole-cell voltage-clamp recording from a mouse AII-ACs (Fig. 1.2) shows how I_m is obtained by giving a sinusoidal V_m. The lock-in emulator software of Patchmaster (HEKA) together with the circuitry of the EPC10 is used to calculate the passive membrane properties of cells in real-time.

1.3.2 Capacitance measurement in complex neurons

A simple equivalence circuit with one capacitor can model an isopotential (spherical) cell like a chromaffin cell. The changes in C_m should correspond to net surface area changes and should not correlate with changes in R_m or R_s, assuming that $R_m >> R_s$. However, modeling synapses with complex morphology like CA1 mossy fiber synapse required a three-compartment model Hallermann et al., 2003). This is relevant for our work because the AII-AC was traditionally considered a small isopotential cell. C_m measurements from AII-ACs, however, suggest they have at least two distinct compartments (Balakrishnan et al., 2015). One important conclusion from Hallermann's multicompartmental electrical model was that a correlative decrease in R_s indicates that the C_m change is occurring relatively close to the recording site. Together, these findings support that for AII-ACs a local compartment contains the soma and proximal dendritic lobules in the OFF sublamina, while a distal compartment corresponds to dendrites in the ON sublamina, which constitute a secondary compartment (Fig. 1.2). Somatic whole-cell patch recordings of RBCs can reveal C_m measurements of terminals up to 45 µm away when the sinewave frequency

is reduced to 100-300 Hz. However, this also introduced significant noise in C_m measurements when compared to high frequency sinewave stimulation (Oltedal and Hartveit, 2010). Recently, a thorough analysis of C_m recordings in AII-ACs has been based on a detailed morphological model (Hartveit et al., 2019). This work validates the use of C_m measurements in AII-ACs; however, the study cautions that high frequency sine waves could underestimate release from lobules by 10-20%, while low frequency stimulation with high amplitude risks activating L-type Ca^{2+} channels. We found that reducing the sine frequency in mouse recordings resulted in larger baseline C_m measurements, but did not change the ΔC_m response (Balakrishnan et al., 2015), indicating that we were measuring more cell surface area (i.e. distal dendrites) where glycine release presumably does not occur. This was also true for mature rat AII-ACs (see Chapter 3; Fig. S3.2). This is one advantageous feature of the AII-AC, which has synaptic release sites close to the soma, unlike wide-field and other narrow-field amacrine cells. We identify AII-ACs using differential interference contrast (DIC) optics that uses a prism to split polarized light, that travels through parts of the tissue with different wavelengths, and gives contrast to our transparent retina slices once these light paths are recombined. Amacrine cell bodies are located at the bottom of the INL, and AII-ACs are distinguishable using DIC because they have a thick root dendrite. We fill the cells with fluorescent dye during recording to confirm their morphology. We occasionally patch AII-ACs with severed distal dendrites that still exhibit ΔC_m responses (Fig. 1.3A), indicating that release is from the lobules close to the soma. We also have recordings from other amacrine cell types, including wide-field and narrow-field without lobules. Recordings from amacrine cells that were not AII-ACs did not produce a ΔC_m responses (Fig. 1.3 B,C). We presume C_m measurements with a high frequency sine wave are not suitable for amacrine cells other that AII-ACs, although reducing the sine frequency could theoretically work for small narrow-field cells.

Figure[1.3]

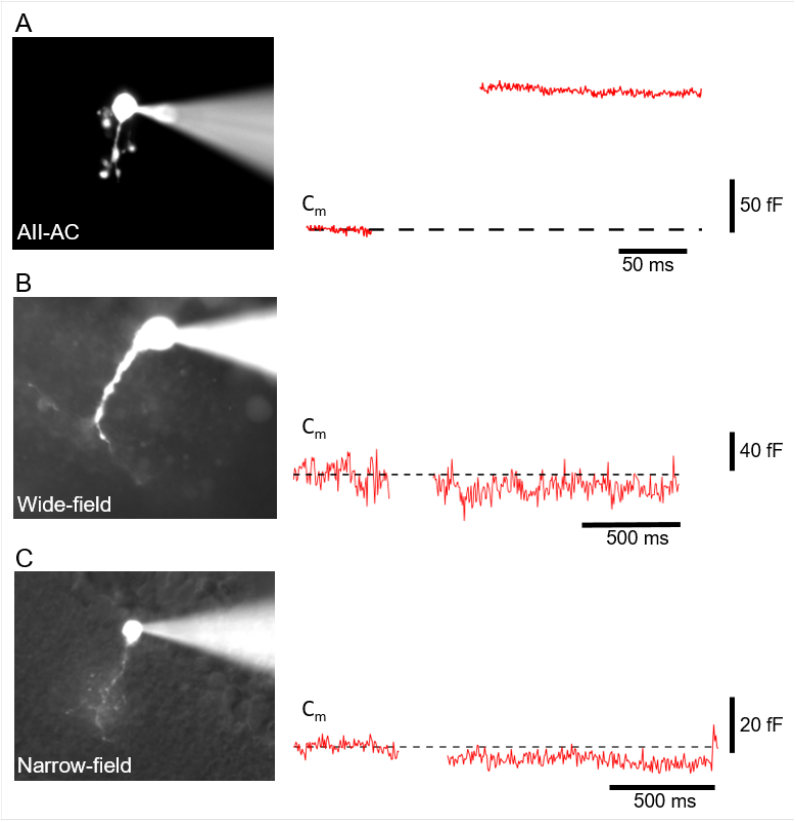

[1.3] **ΔCm responses occur in lobules near the AII-AC soma.** Whole-cell C_m recordings performed in different amacrine cells using a Cs-based internal solution containing Alexa 488 dye. Epifluorescence images of an AII-AC with severed distal dendrites (***A***), wide- (***B***), and narrow-field amacrine cells (***C***). C_m traces shown for each cell (right). Notice how the AII-AC traces have ΔC_m responses even without their distal dendrites. The Wide- and narrow-field cells with no proximal lobules have no ΔC_m responses.

1.3.3 AII-AC dendritic release correlates with lobular surface area

We predicted that AII-ACs with larger surface area and presumably more lobular appendages would produce larger ΔC_m responses. We found that plotting ΔC_m responses from mouse AII-ACs versus their C_m baseline values produced a positive correlation (Fig. 1.4A, B), which suggests that AII-ACs with more lobules and/or with larger proximal dendritic lobules produce more overall exocytosis and glycine release. Rat AII-ACs soma and OFF sublamina dendrites have a combined surface area of ~577 μm^2, estimated from morphological reconstructions (Zandt et al., 2018), which converts to 5.77 pF using a specific membrane capacitance of 10 $fF/\mu m^2$. This is just slightly larger than our average baseline C_m measurements (4.375 pF) in mouse AII-ACs.

Figure[1.4]

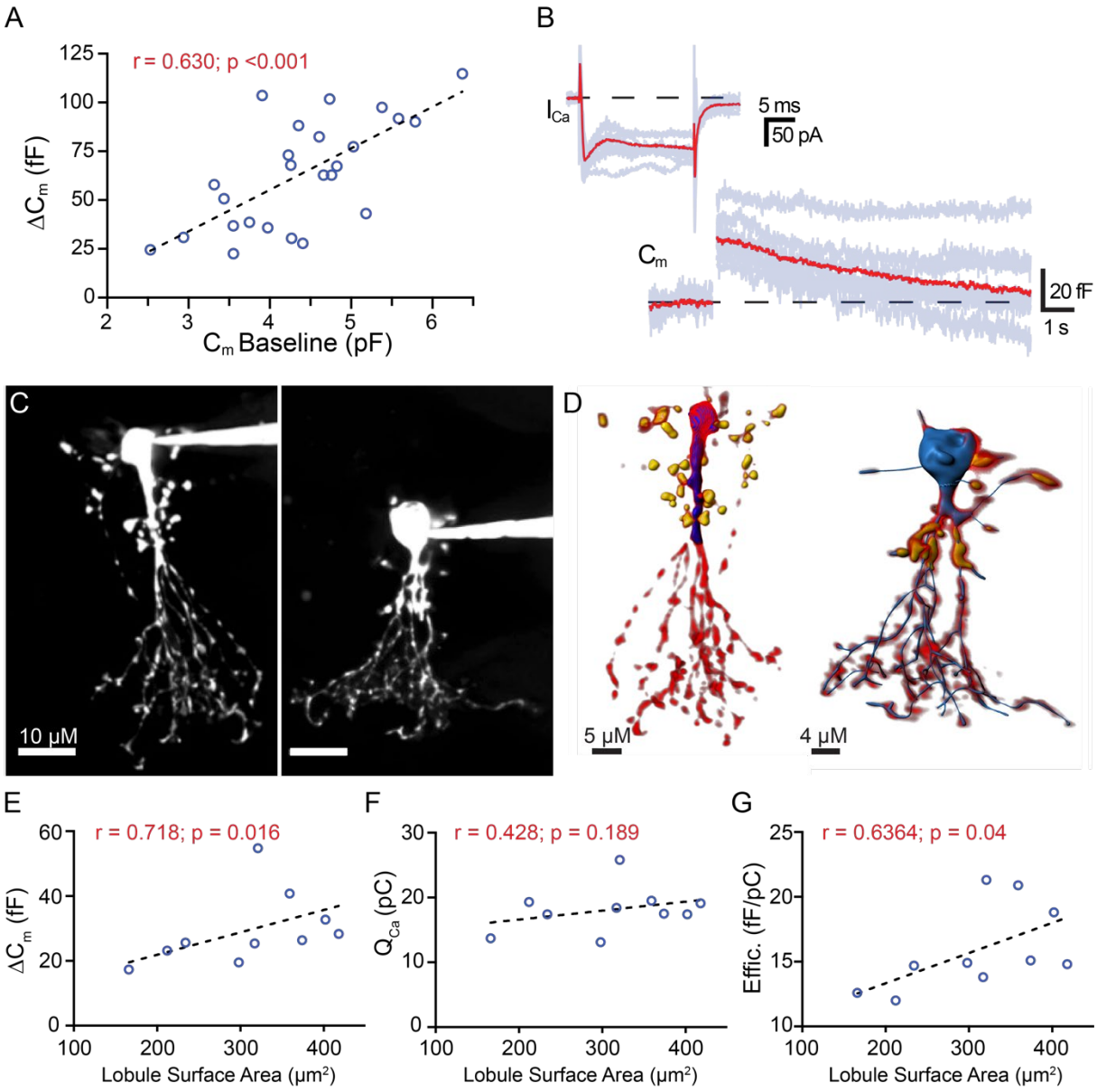

[1.4] AII-AC ΔC_m responses correlate to proximal dendritic surface area.

A, ΔC_m responses to a 100 ms depolarizing pulse plotted against baseline C_m responses for AII-ACs from p30-35 mice (n = 25). Dashed line depicts linear regression fit showing positive correlation (r = 0.630; p <0.001; Spearman). ***B,*** Whole-cell traces of C_m and I_{Ca} responses recordings in AII-ACs from 5 week old Sprague-Dawley rats. Shown are traces from individual AII-ACs (grey; n = 10), and a grand average trace (red). ***C,*** Micrographs of rat AII-ACs filled with Alexa 488. Shown are epifluorescence max intensity projections (z = 0.5 µm) after CMLE iterative deconvolution (Huygens Essential; Scientific Volume Imaging, Hilversum, the Netherlands). ***D,*** Representative 3D volume fills (Imaris) of soma and OFF-sublamina dendrites (blue) with lobules (yellow), and fluorescence intensity overlay (red). Same cells as in panel ***C***. ***E-G,*** Summary plots of electrophysiological data against lobule surface area acquired from 3D reconstructions for 10 AII-ACs. Shown are plots for ΔC_m (***E***; r = 0.718;

p =0.016), Q_{ca} (***F***; r = 0.428; p = 0.189), and exocytosis efficiency (***G***; r = 0.6364; p = 0.04). Open circles represent individual AII-ACs. Notice how the increase in ΔC_m correlates with the lobule surface area, indicating that these cells may have more synaptic active zones. Dashed lines indicate linear fits. Statistical significance was determined using the Spearman correlation test. Results from ***B-C*** were generated by Marc Meadows with supervision and guidance of Drs. Margaret Veruki, and Espen Hartveit (University of Bergen, Norway).

We paired C_m measurements with morphometric imaging data to test if ΔC_m responses correlate with lobular surface area (Fig. 1.4 B - G). Our estimates of the OFF sublamina surface area (564 ± 37.8 μm^2) was slightly smaller than expected from baseline C_m estimates (6.23 ± 0.30 pF). We also found a positive correlation between the ΔC_m jump size and lobule surface area (Fig. 1.4 E), Ca^{2+} current charge (Q_{Ca}), and exocytosis efficiency (ΔC_m / Q_{Ca}).

1.3.4 Scope of synaptic measurements in the retina

C_m measurements were pioneered in the retina using goldfish bipolar cell synaptic terminals (von Gersdorff and Matthews, 1994) and photoreceptors salamander photoreceptors (Rieke and Schwartz, 1994). This technique has been used extensively to study exocytosis and endocytosis mechanisms in rods, cones, and RBCs (and mixed-BC in goldfish retina). These cells have specialized ribbon synapses with non-inactivating L-type Ca^{2+} channels for tonic exocytosis. Photoreceptors are able to provide continuous and graded glutamate release (Jackman et al., 2009), while BCs can provide either fast phasic or slow graded glutamate release (von Gersdorff et al., 1998; Singer and Diamond, 2006).

We chose the AII-AC to be the centerpiece of this thesis for their importance to visual processing, as they are downstream to both photoreceptor and RBCs. Currently, AII-ACs are the first example of an inhibitory synapse to be studied using C_m measurements and can provide both phasic and graded levels of glycine release despite having conventional synapses (Balakrishnan et al., 2015). The AII-ACs also have L-type Ca^{2+} channels (Habermann et al., 2008). Moreover, they also have two large readily releasable pools of vesicles, as do goldfish bipolar cells. A growing number of studies are finding that some conventional active zone synapses can be suited for sustained exocytosis (although they lack synaptic ribbons) and may share some molecular mechanisms for vesicle trafficking with ribbon synapses (Hallermann and Silver, 2013).

Section 1.4: Acknowledgments

This work was supported by National Institutes of Health Grants EY014043 and DC12938 to H.v.G.; and Casey Eye Institute P30 Grant EY010572. This work was union-made and upheld fair labor practices approved by AFSCME Local 402 OHSUGRU. Special thanks to my laboratory members Andre Dagostin, Benjamin Zemel, and Paulo Strazza. I am truly grateful for my thesis committee members Catherine Morgans, Stephen Smith, Benjamin Sivyer, Anusha Mishra, and Stefan Hallermann for their guidance and support. Special thanks to Margaret Veruki and Espen Hartveit for hosting me in Bergen and collaborating on the morphology work. I can only try to emulate the excitement and methodical approach that Veruki and Hartveit have. Thanks to Joseph Leffler and Paulo Strazza for their edits and comments.

Section 1.5: References

Arshavsky VY, Lamb TD, Pugh EN Jr (2002) G proteins and phototransduction. Annu Rev Physiol 64:153-87.

Bloomfield SA, Völgyi B (2009) The diverse functional roles and regulation of neuronal gap junctions in the retina. Nat Rev Neurosci 10(7):495-506.

Borghuis BG, Looger LL, Tomita S, Demb JB (2014) Kainate receptors mediate signaling in both transient and sustained OFF bipolar cell pathways in mouse retina. J Neurosci 34(18):6128-39.

Cembrowski MS, Logan SM, Tian M, Jia L, Li W, Kath WL, Riecke H, Singer JH (2012) The mechanisms of repetitive spike generation in an axonless retinal interneuron. Cell Rep 1(2):155-66.

Chen P, Gillis KD. The noise of membrane capacitance measurements in the whole-cell recording configuration. Biophys J. 2000 Oct;79(4):2162-70.

Dawson MN, Hamner WM (2003) Geographic variation and behavioral evolution in marine plankton: the case of Mastigias (Scyphozoa, Rhizostomeae). Marine Biology 143, 1161–1174 (2003).

Dawson MN (2005). Five new subspecies of Mastigias (Scyphozoa: Rhizostomeae: Mastigiidae) from marine lakes, Palau, Micronesia. Journal of the Marine Biological Association of the United Kingdom, 85(3), 679-694.

DeVries SH (2000) Bipolar cells use kainate and AMPA receptors to filter visual information into separate channels. Neuron 28(3):847-56.

Dedek K, Schultz K, Pieper M, Dirks P, Maxeiner S, Willecke K, Weiler R, Janssen-Bienhold U (2006) Localization of heterotypic gap junctions composed of connexin45 and connexin36 in the rod pathway of the mouse retina. Eur J Neurosci 24(6):1675-86.

Demb JB, Singer JH (2012) Intrinsic properties and functional circuitry of the AII amacrine cell. Vis Neurosci 29:51-60.

Field GD, Sampath AP (2017) Behavioural and physiological limits to vision in mammals. Philos Trans R Soc Lond B Biol Sci 372(1717):20160072.

Field GD, Sampath AP, Rieke F (2005) Retinal processing near absolute threshold: from behavior to mechanism. Annu Rev Physiol 67:491-514.

Fournel R, Hartveit E, Veruki ML (2021) Differential Contribution of Gap Junctions to the Membrane Properties of ON- and OFF-Bipolar Cells of the Rat Retina. Cell Mol Neurobiol 41(2):229-245.

Gillis KD (2000) Admittance-based measurement of membrane capacitance using the EPC-9 patch-clamp amplifier. Pflugers Arch 439:655-664.

Graydon CW, Lieberman EE, Rho N, Briggman KL, Singer JH, Diamond JS (2018) Synaptic transfer between rod and cone pathways mediated by AII amacrine cells in the mouse retina. Curr Biol 28(17):2739-2751.e3.

Habermann CJ, O'Brien BJ, Wässle H, Protti DA (2003) AII amacrine cells express L-type calcium channels at their output synapses. J. Neurosci 23(17):6904-13.

Hallermann S, Pawlu C, Jonas P, Heckmann M (2003) A large pool of releasable vesicles in a cortical glutamatergic synapse. Proc Natl Acad Sci USA 100(15):8975-80.

Hallermann S, Silver RA (2013) Sustaining rapid vesicular release at active zones: potential roles for vesicle tethering. Trends Neurosci 36(3):185-94.

Hampson EC, Vaney DI, Weiler R (1992) Dopaminergic modulation of gap junction permeability between amacrine cells in mammalian retina. J Neurosci 12:4911-4922.

Han Y, Massey SC (2005). Electrical synapses in retinal ON cone bipolar cells: subtype-specific expression of connexins. Proc Natl Acad Sci U S A 102(37):13313-8.

Hartveit E, Veruki ML (2012) Electrical synapses between AII amacrine cells in the retina: Function and modulation. Brain Res 1487:160-72.

Hartveit E, Veruki ML, Zandt BJ (2019) Capacitance measurement of dendritic exocytosis in an electrically coupled inhibitory retinal interneuron: an experimental and computational study. Physiol Rep. 7(15):e14186.

Jékely G (2009) Evolution of phototaxis. Philos Trans R Soc Lond B Biol Sci 364(1531):2795-808.

Kelber A, Yovanovich C, Olsson P (2017) Thresholds and noise limitations of colour vision in dim light. Philos Trans R Soc Lond B Biol Sci 372(1717):20160065.

Kirk A (2015) From Nuclear Fusion to Sunlight. In: Solar Photovoltaic Cells (Kirk A, ed), pp 9-22. Academic Press.

Kolb H, Famiglietti EV (1974) Rod and cone pathways in the inner plexiform layer of cat retina. Science 186:47–49.

Kothmann WW, Massey SC, O'Brien J (2009) Dopamine-stimulated dephosphorylation of connexin 36 mediates AII amacrine cell uncoupling. J Neurosci 29:14903-14911.

Lamb TD, Collin SP, Pugh EN Jr (2007) Evolution of the vertebrate eye: opsins, photoreceptors, retina and eye cup. Nat Rev Neurosci. 8(12):960-76.

Lin, B., Jacobs, T.C. & Masland, R.H. (2005) Different functional types of bipolar cells use different gap-junctional proteins. J. Neurosci 25(28):6696-701.

Liu JH, Singh JB, Veruki ML, Hartveit E (2021) Morphological properties of the axon initial segment-like process of AII amacrine cells in the rat retina. J Comp Neurol 529(16):3593-3620.

Mennerick S, Zenisek D, Matthews G (1997) Static and dynamic membrane properties of large-terminal bipolar cells from goldfish retina: experimental test of a compartment model. J Neurophysiol 78(1):51-62.

Mills SL, Massey SC (1995) Differential properties of two gap junctional pathways made by AII amacrine cells. Nature 377(6551):734-7.

Morgans CW, Brown RL, Duvoisin, RM (2010) TRPM1: the endpoint of the mGluR6 signal transduction cascade in retinal ON-bipolar cells. Bioessays 32(7) 609-614.

Morgans C W, Zhang J, Jeffrey BG, Nelson S M, Burke NS, Duvoisin RM, Brown RL (2009) TRPM1 is required for the depolarizing light response in retinal ON- bipolar cells. Proc Natl Acad Sci USA 106(45), 19174–19178.

Oltedal L, Hartveit E (2010) Transient release kinetics of rod bipolar cells revealed by capacitance measurement of exocytosis from axon terminals in rat retinal slices. J Physiol 588(Pt 9):1469-87.

Randel N, Jékely G (2016) Phototaxis and the origin of visual eyes. Philos Trans R Soc Lond B Biol Sci 371(1685):20150042.

Rieke F, Schwartz EA (1994) A cGMP-gated current can control exocytosis at cone synapses. Neuron 13(4):863-73.

Roy S, Field GD (2019) Dopaminergic modulation of retinal processing from starlight to sunlight. J Pharmacol Sci 140(1):86-93.

Puller C, Ivanova E, Euler T, Haverkamp S, Schubert T (2013) OFF bipolar cells express distinct types of dendritic glutamate receptors in the mouse retina. Neuroscience 243:136-48.

Sanes JR, Masland RH (2015) The types of retinal ganglion cells: current status and implications for neuronal classification. Annu Rev Neurosci. 38:221-46.

Schnapf JL, Copenhagen DR (1982) Differences in the kinetics of rod and cone synaptic transmission. Nature 296(5860):862-4.

Shekhar K, Lapan SW, Whitney IE, Tran NM, Macosko EZ, Kowalczyk M, Adiconis X, Levin JZ, Nemesh J, Goldman M, McCarroll SA, Cepko CL, Regev A, Sanes JR (2016) Comprehensive Classification of Retinal Bipolar Neurons by Single-Cell Transcriptomics. Cell 166(5):1308-1323.e30.

Singer JH, Diamond JS (2006) Vesicle depletion and synaptic depression at a mammalian ribbon synapse J Neurophysiol 95:31913198.

Thoreson WB, Bryson EJ (2004) Chloride equilibrium potential in salamander cones. BMC Neurosci 5:53.

Thoreson WB, Babai N, Bartoletti TM (2008) Feedback from horizontal cells to rod photoreceptors in vertebrate retina. J Neurosci 28(22):5691-5.

Urschel S, Hoher T, Schubert T, Alev C, Sohl G, Worsdorfer P, Asahara T, Dermietzel R, Weiler R, Willecke K (2006) Protein kinase A-mediated phosphorylation of connexin36 in mouse retina results in decreased gap junctional communication between AII amacrine cells. J Biol Chem 281:33163-33171.

Veruki ML, Hartveit E (2002a) AII (rod) amacrine cells form a network of electrically coupled interneurons in the mammalian retina. Neuron 33:935–946.

Veruki ML, Hartveit E (2002b) Electrical synapses mediate signal transmission in the rod pathway of the mammalian retina. J Neurosci 22:10558–10566.

Veruki ML, Hartveit E (2009) Meclofenamic acid blocks electrical synapses of retinal AII amacrine and ON-cone bipolar cells. J Neurophysiol 101:2339–2347.

von Gersdorff H, Matthews G (1994) Dynamics of synaptic vesicle fusion and membrane retrieval in synaptic terminals. Nature 367(6465):735-9.

von Gersdorff H, Sakaba T, Berglund K, Tachibana M (1998) Submillisecond kinetics of glutamate release from a sensory synapse. Neuron 21:11771188.Wässle, H. (2004). Parallel processing in the mammalian retina. Nat Rev Neurosci 5, 747-757.

Wässle H, Boycott BB (1991) Functional architecture of the mammalian retina. Physiol Rev 71(2):447-80.

Yan W, Laboulaye MA, Tran NM, Whitney IE, Benhar I, and Sanes JR (2020) Mouse Retinal Cell Atlas: Molecular Identification of over Sixty Amacrine Cell Types. J. Neurosci. 40(27), 5177–5195.

Yang XL, Wu SM (1991) Feedforward lateral inhibition in retinal bipolar cells: input-output relation of the horizontal cell-depolarizing bipolar cell synapse. Proc Natl Acad Sci USA 88(8):3310-3.

Zandt BJ, Veruki ML, Hartveit E (2018) Electrotonic signal processing in AII amacrine cells: compartmental models and passive membrane properties for a gap junction-coupled retinal neuron. Brain Struct Funct. 2018 Sep;223(7):3383-3410.

Chapter 2: Glycine Release Is Potentiated by cAMP via EPAC2 and Ca^{2+} Stores in a Retinal Interneuron

Marc A. Meadows,[1*] Veeramuthu Balakrishnan,[1*] Xiaohan Wang[1] and Henrique von Gersdorff[1,2,3]

[1]The Vollum Institute, Oregon Health & Science University, Portland, Oregon 97239

[2]Casey Eye Institute, Department of Ophthalmology, Oregon Health & Science University, Portland, Oregon 97239

[3]Department of Chemical Physiology and Biochemistry, Oregon Health & Science University, Portland, Oregon 97239

*M.A.M. and V.B. contributed equally to this work as co-first authors.

Published in Journal of Neuroscience. 2020 Nov. 17; 41(46):9503-9520.

Doi: 10.1523/JNEUROSCI.0670-21.2021

Section 2.1: Summary

Neuromodulation via the intracellular second messenger cAMP is ubiquitous at presynaptic nerve terminals. This modulation of synaptic transmission allows exocytosis to adapt to stimulus levels and reliably encode information. The AII amacrine cell (AII-AC) is a central hub for signal processing in the mammalian retina. The main apical dendrite of the AII-AC is connected to several lobular appendages that release glycine onto OFF cone bipolar cells and ganglion cells. However, the influence of cAMP on glycine release is not well understood. Using membrane capacitance measurements from mouse AII-ACs to directly measure exocytosis, we observe that intracellular dialysis of 1 mM cAMP enhances exocytosis without affecting the L-type Ca^{2+} current. Responses to depolarizing pulses of various durations show that the size of the readily releasable pool of vesicles nearly doubles with cAMP, while paired-pulse depression experiments

suggest that release probability does not change. Specific agonists and antagonists for exchange protein activated by cAMP 2 (EPAC2) revealed that the cAMP-induced enhancement of exocytosis requires EPAC2 activation. Furthermore, intact Ca^{2+} stores were also necessary for the cAMP potentiation of exocytosis. Postsynaptic recordings from OFF cone bipolar cells showed that increasing cAMP with forskolin potentiated the frequency of glycinergic spontaneous IPSCs. We propose that cAMP elevations in the AII-AC lead to a robust enhancement of glycine release through an EPAC2 and Ca^{2+} store signaling pathway. Our results thus contribute to a better understanding of how AII-AC crossover inhibitory circuits adapt to changes in ambient luminance.

Section 2.2: Introduction

Light signals are transduced by photoreceptors into graded glutamate release onto bipolar cell (BC) dendrites and then by BC terminals via glutamate release onto retinal ganglion cell (RGC) dendrites in the inner plexiform layer (IPL). Amacrine cells (ACs) form inhibitory synapses in the IPL with BC terminals, with other ACs and with RGC dendrites (Strettoi et al., 1992; Wässle, 2004). AII ACs (AII-ACs) are the most abundant glycinergic narrow-field AC in the mammalian retina and are found even in the primate fovea (Vaney et al., 1991; Wässle et al., 2009; Strettoi et al., 2018). Their dendritic arbors are bistratified in the IPL and perform two compartment specific functions that are crucial for night (scotopic) and daytime (photopic) vision. First, glutamate from rod BC terminals activates AMPARs on AII-AC distal dendrites, and these excitatory signals are relayed to neighboring AII-ACs and ON-cone BCs (ON-CBCs) through gap junctions (Demb and Singer, 2012). Second, signals from ON rod BCs or ON-CBCs crossover to inhibit OFF-cone BCs (OFF-CBCs) and OFF-RGCs via the AII-AC proximal dendritic lobular appendages. These lobular terminals express L-type $Ca_v1.3$ Ca^{2+} channels at active zones for exocytosis and contain a large pool of synaptic vesicles loaded with glycine (Habermann et al., 2003; Marc et al., 2014). This crossover inhibition from ON to OFF channels enhances the signal-to-noise ratio of retinal circuits (Liang and Freed, 2012).

The dynamic range of the rod and cone photoreceptors operates from 1 to >100,000 photons, yet little is known about how crossover inhibition adapts to such a wide range of light intensities. The adaptation of retinal circuits to changes in ambient light is dependent on neuromodulators

(Roy and Field, 2019). Light-evoked uncoupling of AII-ACs networks, for example, relies on the elevation of retinal dopamine (Hampson et al., 1992), which in turn induces cAMP-dependent dephosphorylation of connexin 36 (Cx36) hemichannels (Kothmann et al., 2009). This decreases gap-junction conductances between AII-ACs, which relies on cAMP binding and activating protein kinase A (PKA) in the distal dendritic arbors (Kothmann et al., 2009; Field and Sampath, 2017). Although dopaminergic ACs form *en passant* synapses onto AII-ACs (Voigt and Wässle, 1987), it is still unclear how changes in dopamine and cAMP levels affect crossover inhibition via glycine release.

Changes in the concentration of cAMP can induce changes in presynaptic release probability (P_r) or the size of the readily releasable pool (RRP) of vesicles at different CNS synapses (Vaden et al., 2019). This can be mediated by activating PKA or the effector protein directly activated by cAMP (EPAC) at excitatory and inhibitory synapses (Katsurabayashi et al., 2001; Sakaba and Neher, 2001; Kaneko and Takahashi, 2004; Fernandes et al., 2015). The proximity of the AII-AC lobules to the cell soma makes these release sites electronically accessible for time-resolved membrane capacitance (C_m) recordings (Balakrishnan et al., 2015; Hartveit et al., 2019). The AII-AC contains a large RRP of vesicles, which may account for this interneuron's ability to provide both phasic and graded modes of synaptic transmission (Graydon et al., 2018). This versatility in neurotransmitter release may allow AII-ACs to reliably encode different temporal frequencies.

Here we used C_m measurements of exocytosis from AII-ACs and recordings of spontaneous IPSCs (sIPSCs) from OFF-CBCs to provide direct evidence that cAMP can enhance inhibitory synaptic transmission. We find that this cAMP-induced potentiation of exocytosis is not PKA-dependent. Instead, this potentiation depends on EPAC2 activation and intact internal Ca^{2+} stores. Importantly, cAMP elevation did not change significantly the total charge influx of the L-type Ca^{2+} current, which triggers exocytosis and is localized to the lobular appendages of the AII-ACs (Habermann et al., 2003; Balakrishnan et al., 2015). We propose that EPAC2 activation promotes Ca^{2+} release from Ca^{2+} stores that enhances glycine release onto OFF-CBC synaptic terminals. Changes of cAMP levels in AII-ACs thus constitute an important signaling pathway that modulates glycine release in the mammalian retina.

Section 2.3: Results

2.3.1 Plastic changes in glycine release by the AII-AC

2.3.1a Dialysis of cAMP potentiates exocytosis in AII-ACs

We performed whole-cell voltage-clamp experiments by patching AII-AC somas with a Cs-based internal pipette solution containing 1 mM cAMP (Fig. 2.1A). AII-ACs were targeted by the characteristic location of their somas near the border between the INL and IPL. Dye-filled cells were examined after each recording to morphologically confirm their identity as AII-ACs (Fig. 2.1B). A 100 ms depolarizing pulse from −80 to −10 mV elicits a noninactivating L-type Ca^{2+} current (I_{Ca}; Fig. 2.1C,D, insets), which was isolated after offline leak subtraction (see Materials & Methods). After whole-cell break-in, depolarizing pulses were given at <1 min and shortly after >4 min of whole-cell dialysis with the internal solution. The I_{Ca} responses observed in control (without cAMP; Fig. 2.1C) were similar to I_{Ca} recordings performed with 1 mM cAMP (Fig. 2.1D). The I_{Ca} current was integrated over the entire pulse duration to measure the Ca^{2+} charge transfer (Q_{Ca}). As shown in Figure 2.1E, Q_{Ca} did not change significantly between 1 and 4 min of dialysis with the control solution (1 min: 10.4 ± 1.15 pC; and 4 min: 10.8 ± 0.95 pC; n = 22; p = 0.552; Wilcoxon). The I_{Ca} thus remained stable and did not rundown or runup during whole-cell recordings. As shown in Figure 2.1F, 1 mM cAMP did not affect the Q_{Ca} (1 min: 9.16 ± 1.06 pC; and 4 min: 9.05 ± 1.02 pC; n = 22; p = 0.924; Wilcoxon), which indicates that cAMP has no significant effect on the L-type Ca^{2+} currents of AII-ACs.

Time-resolved C_m measurements can correlate strongly with synaptic vesicle exocytosis and neurotransmitter release at different nerve terminals (Grabner and Zenisek, 2013; Ritzau-Jost et al., 2014). We next measured ΔC_m before and after the dialysis with control internal solution. Similar to our previous report (Balakrishnan et al., 2015), we did not observe a significant rundown or change in ΔC_m when using our control internal solution within a time window of ∼10 min after break-in (Fig. 2.1C,E; 1 min: 62.6 ± 6.32 fF; and 4 min: 60.7 ± 5.54 fF; n = 22; p = 0.6333; Wilcoxon). However, when the pipette solution contained 1 mM cAMP, we observed significantly larger ΔC_m jumps after 4 min of whole-cell dialysis (Fig. 2.1D,F; 1 min: 48.56 ± 4.48 fF; and 4 min: 66.9 ± 7.41 fF; n = 22; p = 0.0006; Wilcoxon), although Q_{Ca} remained the same (Fig. 2.1F).

Figure[2.1]

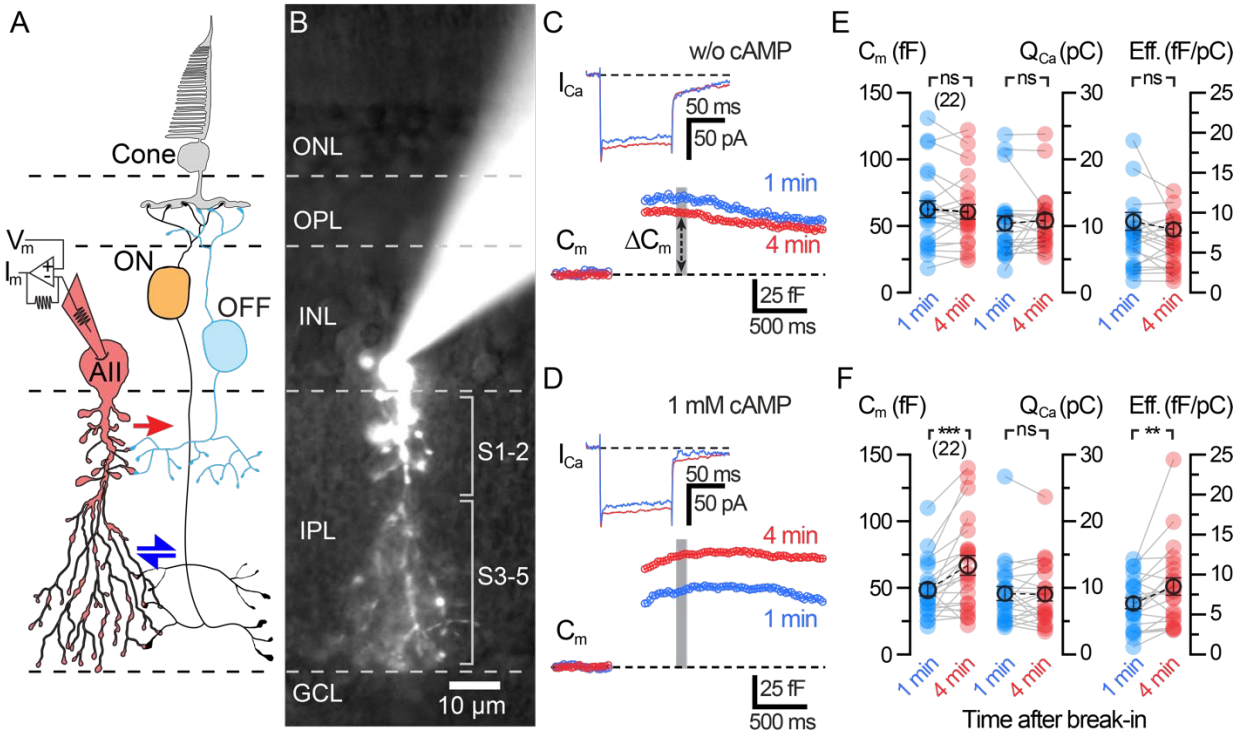

[2.1] Dialysis with cAMP (1 mM) potentiates evoked exocytosis in AII-ACs.

A, Schematic of the crossover inhibitory circuit and the AII-AC. Signals from cone photoreceptors are split into ON- and OFF-type BCs and mixed by AII-ACs. Excitation from gap junction (blue arrows) coupled ON-BCs is converted by the AII-AC into synaptic release of inhibitory glycine to OFF-BCs (red arrow). ***B***, Epifluorescence micrograph of an AII-AC filled with an internal solution containing Alexa 488 (20 µM) after whole-cell patch-clamp recording. Labeled on image are lines indicating layers and sublayers of the retina. ***C***, ***D***, Average traces of C_m and I_{Ca} responses to a 100 ms depolarizing pulse (from −80 to −10 mV) within 1 min (blue) and 4 min (red) after break-in. Gray bar represents the region where C_m values were averaged. ***C***, Recordings from AII-ACs using a control internal solution (no cAMP). ***D***, Recordings from AII-ACs using an internal solution containing 1 mM cAMP. ***E***, ***F***, Summary plots for ΔC_m, the I_{Ca} integrated charge transfer (Q_{Ca}), and exocytosis efficiency ($\Delta C_m/Q_{Ca}$) showing pairwise comparisons between each time after break-in. Solid circles represent data from individual AII-ACs. Open circles with error bars represent mean ± SEM. ***E***, Summary plots for control dataset. There is no change in ΔC_m, Q_{Ca}, or $\Delta C_m/Q_{Ca}$ after 4 min of recording. Statistical significance for ΔC_m was tested using a paired t test, while Q_{Ca} and efficiency were tested using a Wilcoxon t test. ***F***, Summary plots for 1 mM cAMP dataset. ΔC_m and exocytosis efficiency increase significantly at 4 min with no change in Q_{Ca}. Statistical significance for the 1 mM cAMP datasets was determined using Wilcoxon t tests: ns, $p > 0.05$; **$p < 0.01$; ***$p < 0.001$. Data collected by Marc Meadows and Veeramuthu Balakrishnan.

This suggests that a cAMP-dependent potentiation of exocytosis is present in AII-ACs, and this enhancement of vesicle fusion occurs without augmenting L-type Ca^{2+} currents. The efficiency of

exocytosis (ratio of ΔC_m divided by Q_{Ca}) did not change in controls (1 min: 7.13 ± 0.89 fF/pC; and 4 min: 6.32 ± 0.65 fF/pC; n = 22; p = 0.3248; Wilcoxon). However, we observed an increase in exocytosis efficiency with 1 mM cAMP (1 min: 6.40 ± 0.68 fF/pC; and 4 min: 8.50 ± 1.08 fF/pC; n = 22; p = 0.0059; Wilcoxon).

The passive parameters of R_s (1 min: 28.4 ± 2.87 MΩ; and 4 min: 24.8 ± 2.45 MΩ; n = 22; MΩ; p = 0.002) and R_m (1 min: 956 ± 300 MΩ; and 4 min: 603 ± 127 MΩ; n = 22; p = 0.0738; Wilcoxon) were also recorded in control experiments. These values were similar to those from cells dialyzed with 1 mM cAMP for both R_s (1 min: 25.4 ± 2.54 MΩ; and 4 min: 27.5 ± 3.62 MΩ; n = 22; p = 0.5879) and R_m (1 min: 1040 ± 247 MΩ; and 4 min: 742 ± 118 MΩ; n = 22; p = 0.0684; Wilcoxon). As long as $R_m \gg R_s$, the ΔC_m measurements should be a good estimate of exocytosis (Gillis, 2000).

2.3.1b Tracking the diffusion of small molecules within AII-ACs

The AII-AC has been classically modeled as a compact isopotential cell despite its complex morphology (Vardi and Smith, 1996). However, recent electrotonic and morphologic modeling suggests that electrical compartments can filter the spread of voltage between distal and proximal regions of the AII-AC in rat retina (Zandt et al., 2018). Furthermore, the dendritic compartments and the narrow tubes linking lobules with dendrites can act as diffusion barriers, which may complicate our study of cAMP modulation on synaptic vesicle exocytosis.

We thus tracked the fluorescent dye Alexa-488 as it diffused from the pipette solution and mixed with the AII-AC cytosol. Alexa-488 does not permeate across membranes but will dialyze into cells after whole-cell break-in. The perfusion rate of small mobile molecules depends on the molecular weight of the molecule, the cell volume, and the pipette R_s (Neher and Almers, 1986; Oliva et al., 1988). In addition, tortuosity (geometry of the pathway), viscosity of the cytosol, binding or degradation of the molecule, and the diffusion coefficient all influence diffusion rates. We thus measured the dialysis of Alexa-488 after making whole-cell patches of AII-ACs (R_s: 28.7 ± 4.59 MΩ; n = 5). Shown in Figure 2.2A are representative images from a time-lapse video of a single AII-AC being filled with Alexa-488 dye. Time-lapse imaging captured the dialysis time course after whole-cell break-in (Fig. 2.2Ai,Aii). Proximal dendritic compartments began filling within 1 min of dialysis, and the AII-AC was fully dialyzed with Alexa dye after 3 min. Time-series

images were acquired at multiple focal plans to capture the branched distal compartments (Fig. 2.2Aii,Aiii). Similar observations were obtained in 5 AII-ACs; however, we were unable to capture distal and fine arbors in 2 of 5 cells.

Specific ROIs were selected for measuring fluorescence intensity: the soma, lobular varicosities, dendritic branches, and distal dendritic arbors (Fig. 2.2B). Lobular appendages have diverse structures, so multiple lobules were selected from each cell to accommodate for variations in size and distance from the soma's central axis (Zandt et al., 2018). Changes in absolute fluorescence were observed immediately after the moment of break-in (t = 0 min) within the soma and plateaued within 3 min at distal compartments. Because of the wide range in fluorescence intensity among different ROIs (i.e., F_{max} in the soma was 10-fold higher compared with lobules), traces were normalized for comparing diffusion rates (Fig. 2.2C). By comparing normalized fluorescence intensity traces, we were able to better estimate the time course of diffusion of Alexa dye through complex structures of the AII-AC dendrites (Fig. 2.2C, left). Mean traces from each ROI plotted in 3D were pseudocolored (Fig. 2.2D) to show the time necessary to reach a steady fluorescence (red), illustrating that simple structures (soma and apical dendrite) reach a steady state faster than distal compartments (lobules and distal arboreal dendrites) where thinner and more complex dendritic branching may act as a diffusion barrier. Individual fluorescent traces were fit with a single exponential function to estimate diffusion time constants. This diffusion time constant was a linear function of the whole-cell R_s with positive slope (data not shown; Pearson's test; r = 0.9021; p = 0.036; n = 5) in agreement with previous studies (Neher and Almers, 1986; Oliva et al., 1988). Plotting the time constant τ values (Fig. 2.2E) shows that diffusion times in proximal compartments (soma and apical dendrite) saturate within seconds after break-in (τ_{soma} = 0.47 ± 0.06 min; τ_{apical} = 0.49 ± 0.06 min). Slower τ values were seen for lobules and dendritic branch structures (τ_{lobule}: 0.85 ± 0.10 min; τ_{branch} = 0.84 ± 0.11 min), although this trend was not significant. However, distal arboreal dendrites required significantly more time to reach the same level of fluorescence as the soma (τdistal = 1.34 ± 0.35 min; $p < 0.03$; n = 3), suggesting that the thin processes act as a diffusion barrier. After 3 min, even the distal arboreal dendrites were fully saturated with dye and reached a steady state.

Figure 2.2

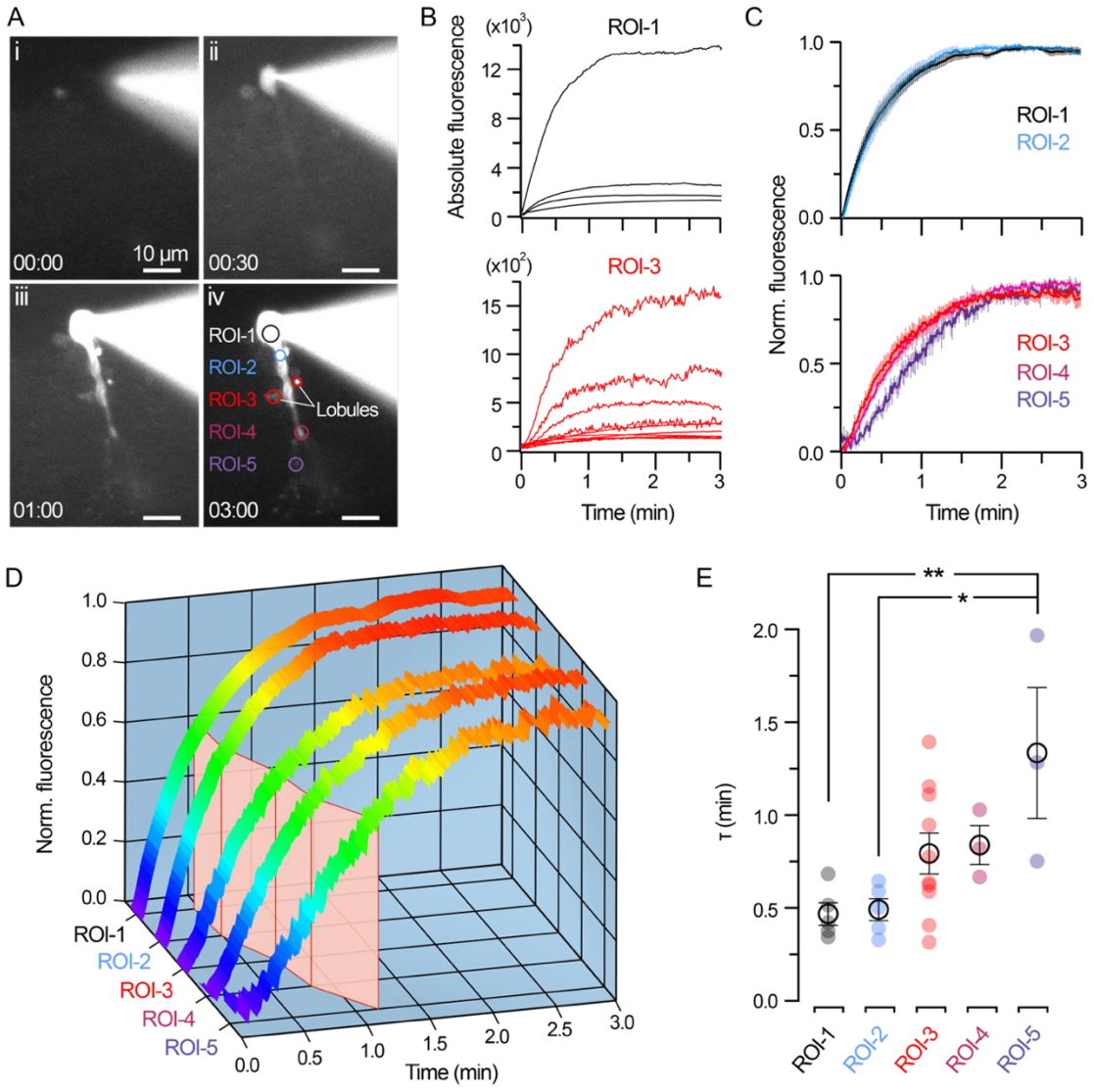

[2.2]Dialysis time course of AII-ACs after whole-cell break-in.

A, Sequence of micrographs showing epifluorescence images of an AII-AC during whole-cell dialysis with an internal solution containing 20 µM Alexa-488. Image stacks were acquired (see Material and Methods) before break- in (***Ai***) and during whole-cell dialysis (***Aii–Aiv***). ROIs indicate morphologic features of the AII-ACs (1: soma; 2: root dendrite; 3: lobular varicosities; 4: dendrite branch; and 5: distal arboreal dendrite). Time displayed as mm:ss. Scale bar, 10 µm. ***B***, Example traces of absolute fluorescence intensity from individual AII-AC somas (top) and multiple lobules (bottom). ***C***, Traces of normalized fluorescence plotted as mean ± SEM. Top, Datasets from the soma (ROI-1; n = 5), and root dendrite (ROI-2; n = 5). Bottom, Datasets from the lobules (ROI-3; n = 10), dendrite branch (ROI-4; n = 3), and distal arboreal dendrite (ROI-5; n = 3). ***D***, 3D histogram showing normalized fluorescence intensity profiles (same as in ***C***). Traces are colored (violet to red) to indicate normalized fluorescence intensity. The mean time constant τ from an exponential fit (red plane) show the slower time course in distal processes of AII-ACs. ***E***, Plots of τ values obtained from exponential fits to raw fluorescence intensity traces. Closed circles represent data from individual ROIs. Open circles and error bars represent mean ± SEM. Statistical significance was determined using a one-way ANOVA and Tukey's test: *$p < 0.05$; **$p < 0.01$.

Similar observations were made for five distinct AII-ACs. The dialysis of Alexa-488 was complete within <3 min for all five AII-ACs. Given that the molecular weight of Alexa-488 (547.85 g/mol) is larger than cAMP (329.2 g/mol), these results suggest that the concentration of cAMP in the lobular appendages may also reach a steady-state level within <3 min after whole-cell break-in.

2.3.1c cAMP increases the initial and secondary vesicle pool size

The size of the RRP of synaptic vesicles can be determined by giving depolarizing pulses of increasing durations to evoke ΔC_m jumps until a plateau level is reached. This protocol revealed two kinetically distinct pools of vesicles in AII-ACs (Balakrishnan et al., 2015). We measured C_m responses to a range of depolarizing pulse durations from 1 to 500 ms. The pulses were spaced 15-30 s apart, and results were quantified at 4 min after break-in across several AII-ACs using either control or 1 mM cAMP internal solutions. We estimated the effects of cAMP on the RRP size by plotting ΔC_m as a function of the depolarizing pulse duration for each dataset (Fig. 2.3). Examples of I_{Ca} response to short (1-10 ms) and long pulses (100 ms) illustrate the similar peak amplitudes, total charge, and inactivation kinetics of the L-type Ca^{2+} currents from AII-ACs recorded with control and 1 mM cAMP internal solutions (Fig. 2.3A). The initial RRP was estimated using short pulses ranging from 1 to 100 ms in duration performed 4 min after break-in (Fig. 2.3B). The initial RRP size was determined by averaging responses from 40 to 100 ms for each dataset, which was significantly larger with 1 mM cAMP (control: 37.3 ± 1.85 fF; and cAMP: 63.4 ± 3.75 fF; $p < 0.0001$, Student's t test). Time constants from fitting with a single exponential function from 1 to 60 ms were similar (control: τ = 3.28 ms; and cAMP: τ = 4.82 ms), as well as the initial rate of exocytosis (control: 11.4 fF/ms; and cAMP: 13.2 fF/ms). These results suggest cAMP is enhancing the size of the initial RRP of vesicles without altering the initial kinetics of exocytosis. Longer depolarizing pulse durations (from 200 to 500 ms) revealed that ΔC_m continued to rise for both the control and cAMP datasets (Fig. 2.3B).

Figure[2.3]

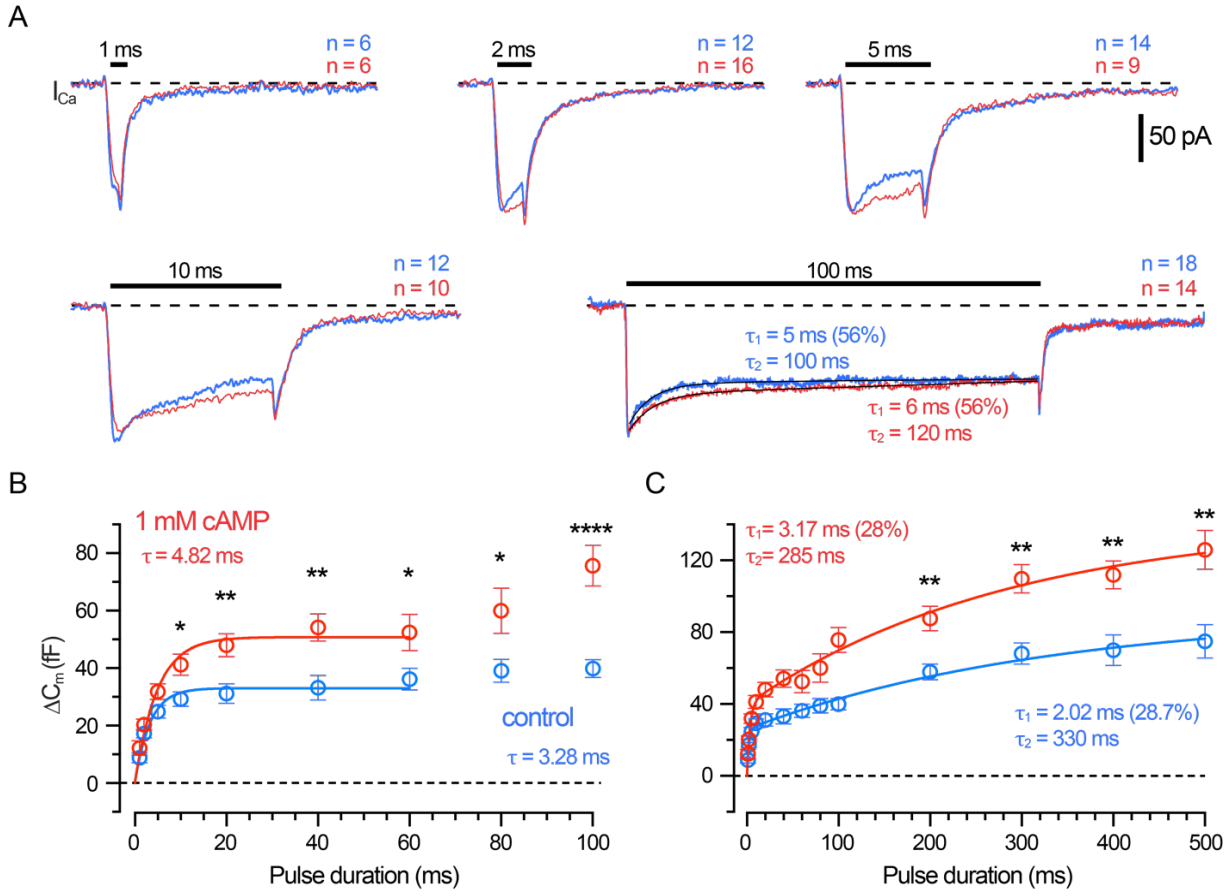

[2.3] Vesicle pool size increases with 1 mM cAMP in the patch pipette.

A, Average I_{Ca} for different depolarizing pulse durations stepping from −80 to −10 mV recorded from AII-ACs using a control (blue) and 1 mM cAMP containing (red) internal solutions. Average I_{Ca} responses are shown for 1, 2, 5, 10, and 100 ms; the number cells (n) are labeled on each graph. All recordings were performed between 4 and 7 min after break-in and were spaced 15-30 s apart. The vertical scale bar is the same for all traces. Black lines on the 100 ms I_{Ca} show double exponential fits. The decay time constants had a fast (τ_1; control: 5 ms, and cAMP: 6 ms) component, which was 56% of the total decay; and a slow component (τ_2; control: 100 ms, and cAMP: 120 ms). ***B***, Plot of ΔC_m responses versus pulse durations ranging from 1 to 100 ms. The ΔC_m saturates for pulse durations of ~20-60 ms for controls (blue) and for 1 mM cAMP dataset (red). Solid lines indicate an exponential fit for control (R^2 = 0.28) and 1 mM cAMP (R^2 = 0.48) datasets. Time constants are labeled on the graph (control: τ = 3.28 ms; and cAMP: τ = 4.82 ms). The size of the RRP can be estimated from the saturating C_m responses for 40-60 ms pulses. ***C***, Plot of ΔC_m responses versus pulse durations ranging from 1 to 500 ms for control (blue) and 1 mM cAMP (red) datasets. Solid lines are double exponential fits to each dataset. The curve fitting improved for the control (R^2 = 0.57) and cAMP (R^2 = 0.65) datasets. Time constants are shown on the graph: control: τ_1 = 2.02 ms (28.0%); τ_2 = 330 ms, and 1 mM cAMP: τ_1 = 3.17 ms (28.7%); τ_2 = 285 ms. The double-exponential fit suggests that a secondary vesicle pool, with slower release kinetics, can be evoked for longer pulses. This secondary pool was also larger with 1 mM cAMP in the patch pipette. Open circles with error bars represent mean ± SEM. Statistical significance determined using unpaired parametric t tests: *p < 0.05; **p < 0.01; ****p < 0.0001. Results are summarized in Table 1. Data collected by Marc Meadows and Veeramuthu Balakrishnan.

The entire dataset was well fit by a double exponential function. Both control and cAMP datasets have a fast initial RRP with similar time constants (τ_1; control: 2.02 ms; and cAMP: 3.16 ms), which accounted for 28% of the total pool size. The remaining secondary pool had a much slower kinetics (control: τ_2 = 330 ms; and cAMP: τ_2 = 285 ms). The kinetics of the overall RRP were thus not affected by cAMP. However, the overall RRP size was significantly larger with cAMP, which nearly doubled the size of the overall RRP (estimated using ΔC_m averaged from 200 to 500 ms for control: 67.5 ± 3.65 fF; and cAMP: 108 ± 4.46 fF; $p < 0.0001$). Results and statistical tests are summarized in Table 1.

Table 1. Vesicle exocytosis is enhanced by 1 mM cAMP[a]

Duration	ΔC_m Mean ± SEM	n	t-test	Duration	ΔC_m Mean ± SEM	n	t-test
1ms	control: 8.79 ± 1.76	6	p = 0.2948; ns	80 ms	control: 39.1 ± 4.01	12	p = 0.0168; *
	cAMP:12.2 ± 2.57	6			cAMP: 60.0 ± 7.91	8	
2 ms	18.3 ± 1.80	9	p = 0.2011; ns	100 ms	39.9 ± 3.11	21	p = <0.0001; ****
	23.7 ± 2.61	20			75.6 ± 7.05	22	
5 ms	24.8 ± 2.27	14	p = 0.0689; ns	200 ms	57.9 ± 4.36	12	p = 0.0039; **
	31.9 ± 2.72	19			87.6 ± 6.82	20	
10 ms	29.2 ± 2.56	12	p = 0.0184; *	300 ms	68.2 ± 5.97	11	p = 0.001; **
	41.2 ± 3.65	16			110 ± 7.87	19	
20 ms	31.1 ± 3.42	18	p = 0.003; **	400 ms	70.0 ± 8.48	6	p = 0.005; **
	48.0 ± 4.03	16			112 ± 7.72	14	
40 ms	33.2 ± 4.25	14	p = 0.0031; **	500 ms	76.8 ± 10.1	10	p = 0.0057; **
	54.2 ± 4.80	13			126 ± 10.9	17	
60 ms	36.2 ± 3.80	16	p = 0.0263; *				
	52.4 ± 6.26	11					

[a]Summary results for Figure 2.3B,C.

Displayed are ΔC_m responses to depolarizing pulse durations from 1 to 500 ms. Recordings were performed between 4 and 7 min after whole-cell break-in with control internal pipette solutions or with 1 mM cAMP containing internal solutions in separate groups of AII-ACs. Pulses were given in random order across different cells. ΔC_m values are listed as mean ± SEM for control and 1 mM cAMP datasets. The number of AII-AC recordings (n) and results from a Student's t test are listed. NS ($p > 0.05$); *$p < 0.05$; **$p < 0.001$; ****$p < 0.0001$.

2.3.1d Effects of 1 mM cAMP on paired-pulse depression

Like retinal ribbon synapses (Rabl et al., 2006; Cho and von Gersdorff, 2012), the synapses of ACs can exhibit strong paired pulse depression that takes several seconds to fully recover (Li et al., 2007; Vickers et al., 2012). To study short-term depression and test the effects of 1 mM cAMP on P_r and RRP size, we performed double-pulse ΔC_m recordings. Paired-pulse depression was tested by measuring ΔC_m responses for two depolarizing pulses (20 ms; from −80 to −10 mV) interleaved

between sinewaves (2 kHz) and with an interpulse duration of 500 ms. This produced marked paired-pulse ΔC_m depression (Fig. 2.4). Recordings were performed in AII-ACs within 1 min after whole-cell break-in and just after 4 min of break-in using a control internal solution (Fig. 2.4A) and an internal solution containing 1 mM cAMP (Fig. 2.4B). The ΔC_m responses to the first pulse (ΔC_1) for control experiments did not change after 4 min (1 min: 38.4 ± 4.26 fF; and 4 min: 38.1 ± 5.53 fF; n = 8; p = 0.8998, paired t test). The ΔC_1 did increased significantly with 1 mM cAMP (Fig. 2.4C; 1 min: 36.6 ± 4.05 fF; and 4 min: 54.7 ± 6.35 fF; n = 11; p = 0.0017, paired t test). The Q_{Ca} values after 4 min were significantly reduced for both control (1 min: 1.92 ± 0.19 pC; and 4 min: 1.59 ± 0.23 pC; n = 8; p = 0.0369, paired t test) and 1 mM cAMP (1 min: 1.84 ± 0.21; and 4 min: 1.56 ± 0.19; n = 11; p = 0.0387, paired t test). However, the values of Q_{Ca} at 1 min for control and cAMP, and at 4 min for control and cAMP, were not significantly different. In both conditions, the ΔC_m to the second pulse (ΔC_2) was smaller than the first pulse (ΔC_1), whereas I_{Ca} responses to both pulses were the same (Fig. 2.4A,B). The paired pulse ratio (PPR; $\Delta C_2/\Delta C_1$; Fig. 2.4D) did not change for control (1 min: 0.39 ± 0.06; and 4 min: 0.39 ± 0.03; n = 8; p = 0.9434, paired t test). The PPR for experiments with 1 mM cAMP exhibited a slight increase, but this was not significant (1 min: 0.37 ± 0.05; and 4 min: 0.47 ± 0.03; n = 11; p = 0.0841, paired t test). Paired-pulse depression cannot be explained by changes in I_{Ca} charge because Q_{ratio} (Q_2/Q_1) was ≅ 1.0 (Fig. 2.4D) and did not change significantly for control (1 min: 1.04 ± 0.06; and 4 min: 1.058 ± 0.05; n = 8; p = 0.8742, paired t test) or with cAMP (1 min: 1.02 ± 0.05; and 4 min: 1.08 ± 0.05; n = 11; p = 0.3613, paired t test). Estimates for the maximum overall pool size (B_{max}; Fig. 2.4E) were calculated by using the following formula:

$$B_{max} = \frac{\Delta C_1 + \Delta C_2}{1 - (\Delta C_2/\Delta C_1)^2}$$

This formula assumes that the same fraction of the pool is released with each pulse (Gillis et al., 1996; M. Chen and von Gersdorff, 2019). If there is a larger fraction of release during the second pulse (e.g., because of residual Ca^{2+} from the first pulse) or significant vesicle recruitment during the second pulse, then B_{max} will overestimate the actual initial pool size. Therefore, the actual

Figure[2.4]

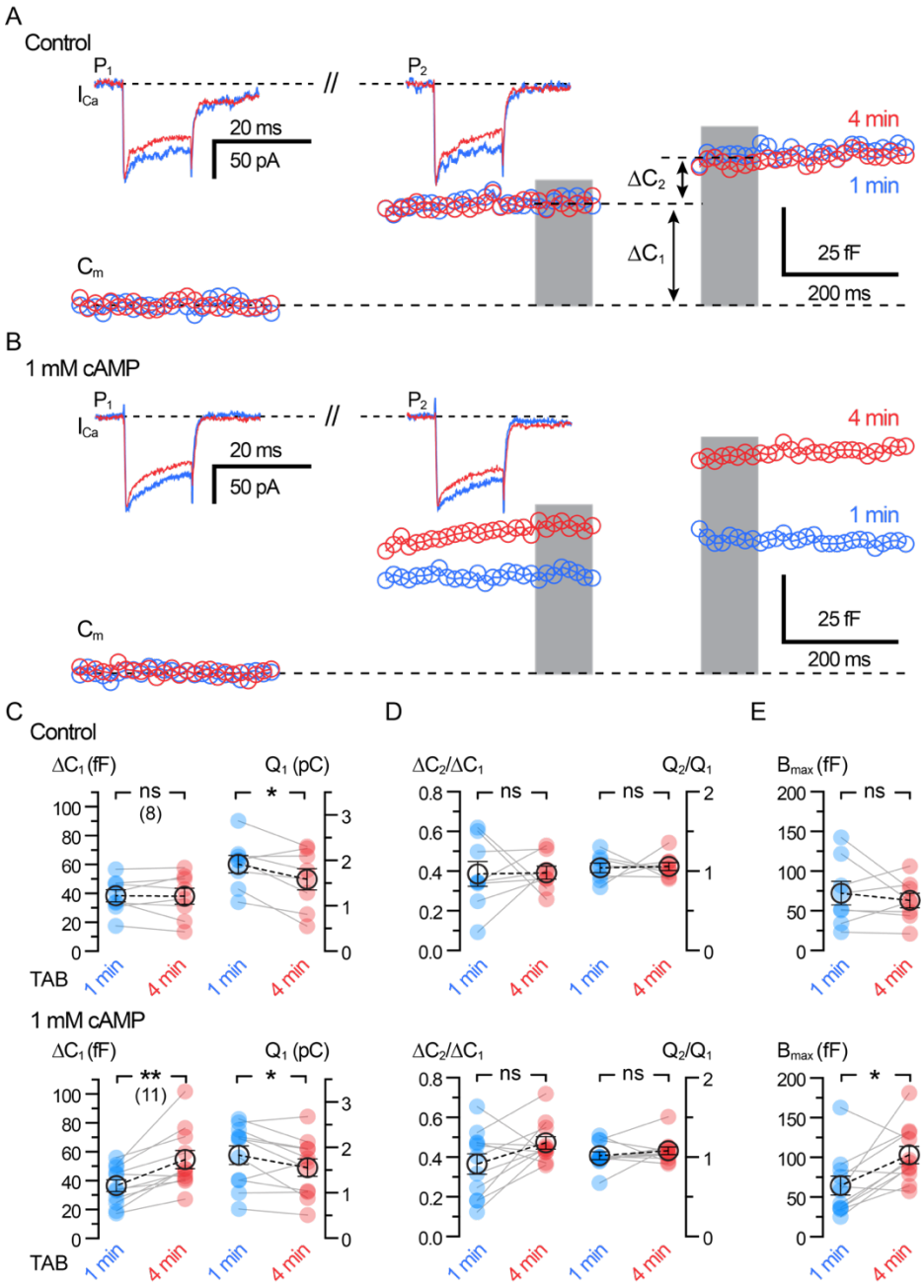

[2.4] Short-term plasticity: Effects of 1 mM cAMP on paired-pulse depression.

Whole-cell voltage-clamp recordings of C_m and I_{Ca} from AII-ACs are shown for two consecutive depolarizing pulses (20 ms duration) separated by 500 ms. Recordings of C_m jumps show paired-pulse synaptic depression. Shown are C_m and I_{Ca} traces performed within 1 min (blue) and at 4 min (red) after whole-cell break-in. Labeled on the graph is the pulse number (P_1 and P_2) corresponding to each C_m jump (ΔC_1 and ΔC_2). Gray bar represents the region where C_m values were averaged. ***A***, Average C_m and I_{Ca} traces for recordings performed using a control internal solution (with no cAMP). The ΔC_2 is depressed with no change in the I_{Ca}. ΔC_1 and ΔC_2 did not change after 4 min of recording. ***B***, Average C_m and I_{Ca} recordings performed with an internal solution containing 1 mM cAMP. Notice

how ΔC_1 increases after 4 min for the 1 mM cAMP dataset. ***C-E***, Summary plots showing pairwise comparisons for recordings made within 1 min (blue) and after 4 min (red) of break-in. Displayed are datasets for recordings with control (top) and 1 mM cAMP (bottom) internal solutions. Closed circles represent data from individual AII-AC. Open circles with error bars represent mean ± SEM. ***C***, Summary plots of ΔC_1 and I_{Ca} charge (Q_1) for each dataset. With 1 mM cAMP, the ΔC_1 increases after 4 min, while the Q_1 decreases. ***D***, Summary plots of the paired-pulse C_m jump ratio ($\Delta C_2/\Delta C_1$) and Q ratio (Q_2/Q_1). The Q ratio is near 1, indicating that the I_{Ca} charge for each pulse is unchanged. The paired-pulse $\Delta C_2/\Delta C_1$ and Q ratio after 4 min also do not change significantly. ***E***, Summary plot for estimates of B_{max} (maximum vesicle pool size). B_{max} increases after 4 min with 1 mM cAMP. Statistical significance determined using a paired t test: ns, $p > 0.05$; *$p < 0.05$; **$p < 0.01$.

pool size lies between ΔC_1 and B_{max}. There was no change in B_{max} after 4 min for controls (1 min: 72.2 ± 14.8 fF; and 4 min: 63.05 ± 9.28 fF; n = 8; p = 0.4809, paired t test), but a significant increase for experiments with 1 mM cAMP (1 min: 64.5 ± 11.9 fF; and 4 min: 103 ± 10.9 fF; n = 11; p = 0.0143, paired t test). The PPR we measured varied from 0.4 to 0.5, which suggests a high P_r, reflecting the strength of our depolarizing pulse from −80 to −10 mV. We found that PPR did not change significantly with 1 mM cAMP; however, B_{max} did increase significantly. This further supports our findings in Figure 2.3, suggesting that 1 mM cAMP increases the RRP size, without changing the release kinetics or the initial P_r.

2.3.2 cAMP enhances the exocytosis of AII-ACs from Cx36$^{-/-}$ mice

Electrical synapses are formed between AII-ACs through Cx36 gap junctions located at the distal arboreal dendrites, forming a vast AII-ACs coupled network (Hartveit and Veruki, 2012; Marc et al., 2014). We considered the possibility that cAMP may introduce artifacts by altering the coupling state between AII-ACs, which could change the input resistance (Vardi and Smith, 1996; Urschel et al., 2006; Veruki et al., 2010). We thus performed ΔC_m recordings using standard solutions and with cAMP in the transgenic Cx36 global knock out (*Cx36*$^{-/-}$) mouse (Hormuzdi et al., 2001; Christie, et al., 2005; Balakrishnan et al., 2015). This addresses the issue of whether cAMP-dependent modulation of gap junctions may influence an increase in the ΔC_m jump size. Recordings from *Cx36*$^{-/-}$ AII-ACs produced normal I_{Ca} currents before 1 min and 4 min after break-in (Fig. 2.5A, inset). We observed no changes in Q_{Ca} resulting from 100 ms pulses (1 min: 11.2 ± 1.54 pC; and 4 min: 12.0 ± 1.45 pC; n = 5; p = 0.5356, paired t test). ΔC_m recordings were also performed before and after 1 mM cAMP dialysis (Fig. 2.5B). After 4 min of dialysis with cAMP,

ΔC_m increased significantly (1 min: 33.8 ± 5.83 fF; and 4 min: 60.4 ± 7.84 fF; n = 5; p = 0.0004, paired t test).

Figure[2.5]

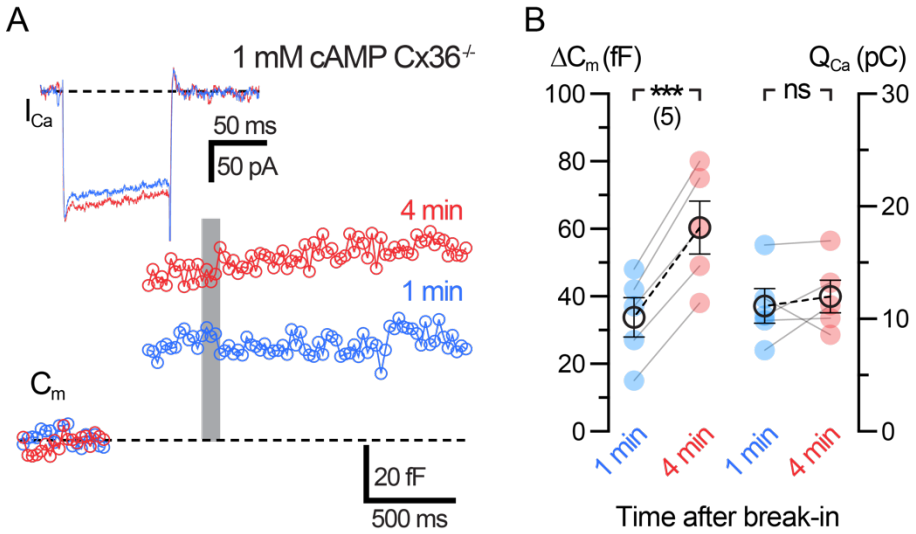

[2.5] Effects of cAMP on exocytosis are independent of AII-AC gap junction coupling. Whole-cell voltage-clamp recordings in AII-ACs from *Cx36*$^{-/-}$ mice performed using an internal solution containing 1 mM cAMP. ***A***, Average C_m and I_{Ca} responses to a 100 ms depolarizing pulse. Recordings were performed before 1 min (blue) and at 4 min (red) after break-in. C_m jumps are larger after 4 min, with no changes in I_{Ca} traces. Gray bar represents the region where C_m values were averaged. ***B***, Summary plots for ΔC_m and Q_{Ca} showing pairwise comparisons between the time after break-in for each recording. Closed circles represent data from individual AII-ACs. Open circles with error bars represent mean ± SEM. ΔC_m significantly increase after 4 min without any corresponding changes in Q_{Ca}. Statistical significance determined using a paired t test: ns, $p > 0.05$; ***$p < 0.001$. Data collected by Veeramuthu Balakrishnan.

These results are very similar to the WT mice and rule out the possibility that cAMP modulation of gap junctions are augmenting ΔC_m jumps. We conclude that cAMP is enhancing vesicle fusion independently of gap junctions. Dialysis of 1 mM cAMP did not change R_s (1 min: 41.1 ± 9.69 MΩ; and 4 min: 45.0 ± 20.3 MΩ; n = 5; p = 0.8125, Wilcoxon) or R_m (1 min: 2100 ± 945 MΩ; and 4 min: 1203 ± 253.5 MΩ; n = 5; p = 0.0625, Wilcoxon). Compared with AII-ACs from WT C57 mice, 1 mM cAMP experiments with *Cx36*$^{-/-}$ did have significantly higher R_s (p = 0.035, Mann–Whitney) and R_m (p = 0.003, Mann–Whitney). We observed a higher average R_m in mutant *Cx36*$^{-/-}$ mice (2100 ± 945 MΩ at 1 min) than in WT C57 (1040 ± 247 MΩ at 1 min), as expected from the lack of gap junction coupling between AII-ACs in the *Cx36*$^{-/-}$ mouse retina.

2.3.3 Forskolin enhances the exocytosis from AII-ACs

2.3.3a Forskolin potentiates presynaptic C_m responses in AII-ACs

We have shown that vesicle exocytosis is enhanced by directly applying 1 mM cAMP through the patch pipette. Forskolin is a membrane-permeable activator of adenylyl cyclase that can enhance synaptic transmission by increasing endogenous levels of cAMP (C. Chen and Regehr, 1997; Tzounopoulos et al., 1998; Kamiya et al., 2002; Kaneko and Takahashi, 2004; Choi et al., 2009; Alasbahi and Melzig, 2012). We thus preincubated retinal slices with 25 µM forskolin for 30 min before whole-cell recordings. Forskolin was also continuously perfused during recording,

Figure[2.6]

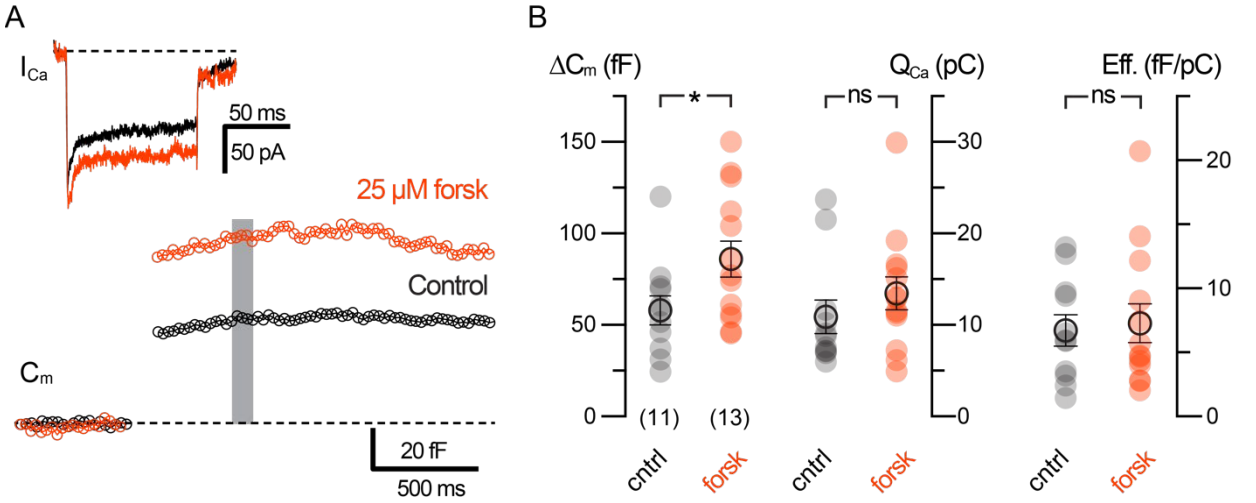

[2.6]Upregulation of adenylyl cyclase potentiates exocytosis. Whole-cell voltage-clamp recordings were performed in retinal slices that were preincubated for 10 min with Ames (control; black) or containing in addition 10 µM forskolin (orange), a potent activator of adenylyl cyclase. ***A***, The C_m and I_{Ca} recordings were performed 4 min after break-in. AII-ACs treated with forskolin produced on average larger ΔC_m jumps than controls. Gray bar represents the region where C_m values were averaged. ***B***, Summary plots for ΔC_m (left), Q_{Ca} (middle), and exocytosis efficiency ($\Delta C_m/Q_{Ca}$; right) showing comparisons between AII-ACs for control and 10 µM forskolin datasets. Closed circles represent data from individual AII-ACs. Open circles with error bars represent mean ± SEM. ΔC_m was significantly increased when 10 µM forskolin was present in the external solution, whereas Q_{Ca} did not change significantly. Statistical significance was determined using an unpaired Student's t test: ns, $p > 0.05$; *$p < 0.05$. Data collected by Marc Meadows and Veeramuthu Balakrishnan.

whereas in separate control experiments cells within retinal slices were perfused with control Ames medium without forskolin (Fig. 2.6A). Figure 2.6B shows that, in AII-ACs treated with 25 µM forskolin, the ΔC_m jumps evoked by 100 ms pulses were nearly twofold larger than in controls

(control: 58.6 ± 7.95 fF, n = 11; and forskolin: 86.9 ± 9.92 fF, n = 13; p = 0.0408, Mann–Whitney). The Q_{Ca} in cells with forskolin application was slightly larger than controls, although this was not significant (control: 10.9 ± 1.82 pC, n = 11; and forskolin: 13.5 ± 1.80 pC, n = 13; p = 0.2066, Mann–Whitney). Our results indicate that increases the ΔC_m is independent of changes in the L-type Ca^{2+} channel current. Recorded R_s values (control: 24.4 ± 3.79 MΩ, n = 11; and forskolin: 21.9 ± 3.46 MΩ, n = 13; p = 0.6234; t test) and R_m (control: 509 ± 180 MΩ, n = 11; and forskolin: 237 ± 48.1 MΩ, n = 13; p = 0.1297; t test) did not change significantly.

2.3.3b Forskolin increases glycinergic inhibition to OFF-CBCs

OFF-CBC terminals receive glycinergic inhibition from AII-ACs (Wässle et al., 2009). We used whole-cell voltage-clamp recordings from OFF-CBCs to record glycinergic sIPSCs as a measure of spontaneous glycine release from AII-ACs, which are the most abundant AC in the mammalian retina (Fig. 2.7A). ON- and OFF-type BCs can be targeted by their soma position in the INL using infrared DIC optics and distinguished by their morphology when filled with fluorescent dyes (Fig. 2.7B). Figure 2.7B shows examples of ON-CBCs and OFF-CBCs. ON-CBC axon terminates in the ON-sublamina of the IPL (Fig. 2.7Bi), whereas OFF-CBCs terminate near the AII-AC lobules in the OFF-sublamina (Fig. 2.7Bii). Whole-cell voltage-clamp recordings from rat and/or mouse OFF-CBCs resulted in large inward sIPSCs when held at −70 mV. Subtypes of primate OFF-CBCs exhibit similar glycinergic sIPSCs (McLaughlin et al., 2021). Rat retina OFF-CBCs were used because they are larger and easier to identify and patch clamp. These sIPSCs were all sensitive to 2 µM strychnine, which blocked sIPSCs in 6 of 6 recordings in rat retina (Fig. 2.7C).

We next tested the effects of bath application of 25 µM forskolin during sIPSCs recordings. Figure 2.7D shows example traces from an OFF-CBC recording that illustrates sIPSCs before drug treatment (controls; top trace) and the subsequent increase in frequency occurring after 25 µM forskolin application (bottom trace). We quantified sIPSCs using custom mini analysis procedures (see Materials and Methods) for rat OFF-BCs (n = 7) and sIPSCs recorded in retinal slices from transgenic *Syt2*-EGFP mice (n = 3). Analysis from mouse and rat OFF-CBCs were grouped together (n = 10). Events measured 30 s before drug application (control; 4347 events) were compared with the last 60 s of recording during forskolin application (12,452 events). Figure 2.7E shows

cumulative probability distributions of the interevent intervals between sIPSC events. The cumulative histogram shows that the interevent interval after the application of 25 µM forskolin significantly shifts to the left ($p < 0.0001$; Kolmogorov–Smirnov test). The shift to shorter interevent intervals can be better visualized in plots on a log time-scale (Fig. 2.7F). The absolute frequency was measured before and after 25 µM forskolin treatment for each OFF-CBC (Fig. 2.7G). The application of forskolin significantly increased the sIPSC frequency (pretreatment: 3.42 ± 0.96 Hz; and forskolin: 4.88 ± 1.12 Hz; $p = 0.002$, paired t test). These results indicate that forskolin is producing presynaptic changes that increase the frequency of spontaneous glycine release. We also examined whether forskolin changes sIPSC amplitudes. Figure 2.7H shows the grand average waveform for all sIPSCs recorded before and after drug application. A distribution histogram comparing sIPSC amplitudes (Fig. 2.7I) suggests that sIPSC amplitude is not affected by forskolin. The centers of log-Gaussian fits (DF = 58) did not shift after forskolin treatment (control: 23.6 pA; $R^2 = 0.99$, and forskolin: 24.6 pA; $R^2 = 0.97$). Median sIPSC amplitudes from individual cells (Fig. 2.7J) also did not change significantly after forskolin treatment (control: 36.4 ± 6.44 pA; and forskolin: 41.8 ± 10.4 pA; $p = 0.43$; Wilcoxon). This suggests that forskolin does not cause changes to postsynaptic glycine receptors in OFF-CBCs or the quantal content of sIPSCs. However, the average sIPSC traces took slightly longer to decay after forskolin application. We speculate that higher release rates may produce excess glycine in the synaptic cleft, thereby increasing the open probability of glycine receptors, and perhaps causing significantly longer decay time constants (control: $\tau = 1.82 \pm 0.43$ ms; and forskolin: $\tau = 2.05 \pm 0.42$ ms; $p = 0.03$; Wilcoxon).

These results suggest that the forskolin is activating adenylyl cyclase and thus producing cAMP-induced changes that enhance the presynaptic release of glycine. We next determined the onset of potentiation by continuously recording sIPSCs during 25 µM forskolin application. OFF-CBCs were targeted in *Syt2*-EGFP mice that we backcrossed onto a C57 background (Fig. 2.7K). Figure 2.7L shows a diary plot of sIPSC frequency (15 s bins) across the duration of recording in a single OFF-CBC. The basal sIPSC frequency remained stable during the first 5 min of recording before forskolin reached the batch chamber. We observed an increase in frequency by 4 min of 25 µM forskolin treatment. Diary plots of average sIPSC frequency (15 s bins) are shown in Figure 2.7M.

Figure[2.7]

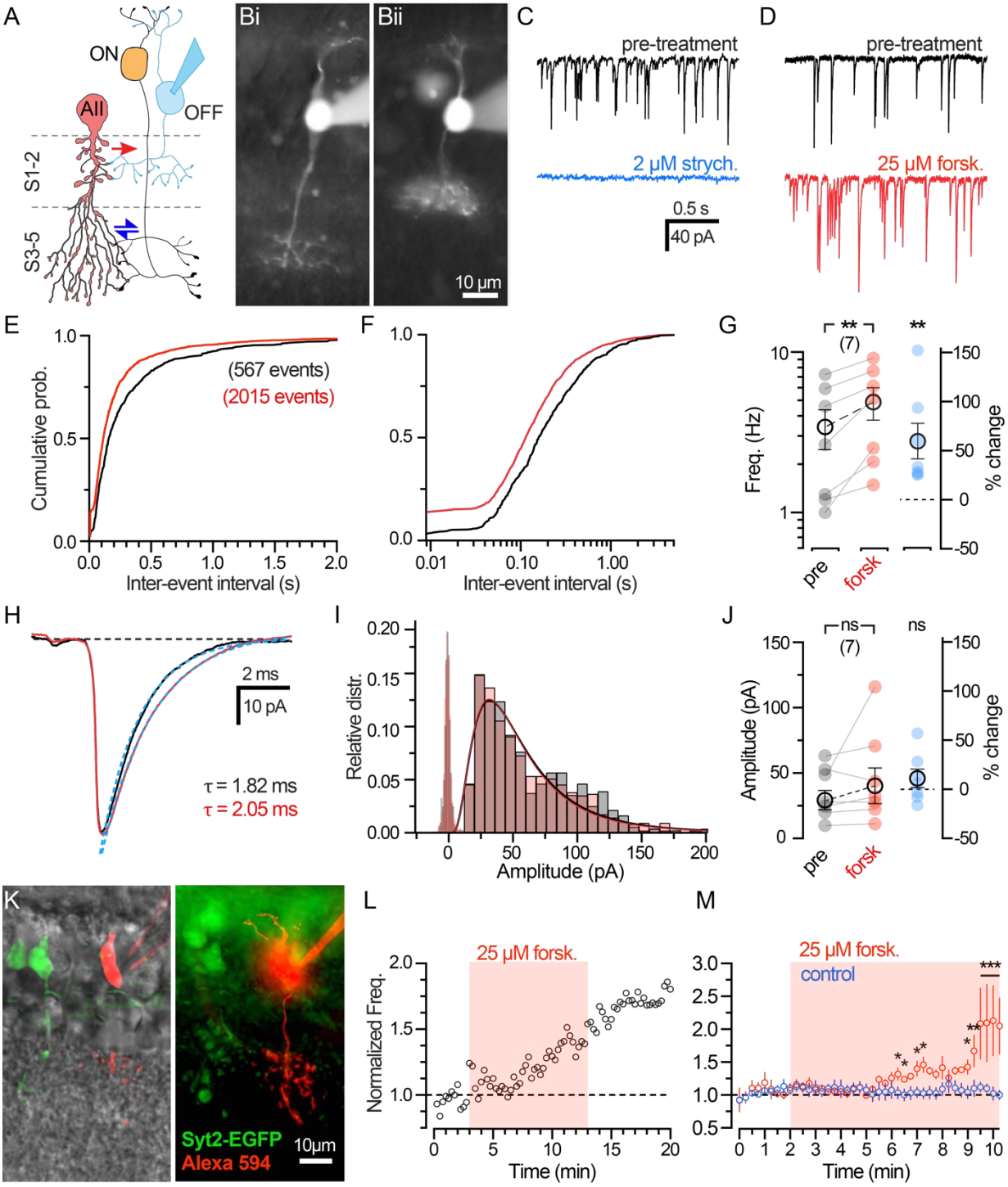

[2.7] Upregulation of adenylyl cyclase leads to an increase in the frequency of spontaneous glycine release. ***A***, Diagram of the crossover inhibition circuit showing that OFF-BCs receive glycinergic inhibition from AII-ACs. Whole-cell voltage-clamp experiments were performed in OFF-BCs, held at −70 mV, using a high chloride internal. ***B***, Micrograph of epifluorescence images of CBCs in rat retinal slices after whole-cell recording with an internal

solution containing 20 µM Alexa-488 dye. BC subtypes identified by their axon stratification in the ON (***Bi***) or OFF (***Bii***) sublamina of the IPL. OFF-CBCs were also targeted in transgenic *Syt2*-EGFP mice (***K***) and pooled with recordings from rats. ***C***, Example OFF-BC recordings of glycinergic sIPSCs performed in Ames medium with synaptic blockers (see Materials and Methods). Recordings were made before (pretreatment; black) and after application of 2 µM strychnine (blue). sIPSCs are completely abolished with 2 µM strychnine. ***D***, Example traces show sIPSCs before (pretreatment; black) and during 25 µM forskolin wash (red), which caused an increase in glycinergic sIPSCs. ***E***, Histogram represents normalized cumulative distribution of interevent interval times between sIPSCs. Labeled on graph is the number of events detected (pretreatment: 567 events; and after 25 µM forskolin treatment: 2015 events; n = 7 cells). The application of forskolin shifted the distribution to left. ***F***, Histogram represents the cumulative distribution (***E***) plotted on a log axis to illustrate the increase in events with small interevent interval. ***G***, Plot of the sIPSC frequency showing the sIPSC rate recorded from OFF-BCs before (black) and during 25 µM forskolin wash (red). There is significantly larger sIPSC frequency with 25 µM forskolin. Also shown as percent change (right; blue). Statistical significance was determined using a Wilcoxon paired t test. ***H***, Grand average traces of the sIPSC waveform before (black) and during 25 µM forskolin wash (red). Solid line indicates an exponential fit to the decay phase (blue dashed lines) with time constants labeled on the graph (pretreatment: 1.82 ms; and 25 µM forskolin: 2.05 ms). ***I***, Histogram represents the relative frequency distribution of sIPSC amplitudes before (black) and during 25 µM forskolin wash (red). Binned values were fitted with a log-Gaussian function showing no changes in amplitude. Noise analysis (open bars) did not overlap with sIPSC amplitudes. ***J***, Plot of the median sIPSC amplitudes from individual OFF-BCs before (black) and during 25 µM forskolin wash (red). Amplitudes did not change significantly after forskolin application, also shown as percent change (right; blue). Statistical significance was determined using a Wilcoxon paired t test. ***K***, Micrograph of an epifluorescence image of OFF-BCs from a *Syt2*-EGFP mouse with a DIC overlay. Type 2 Off-BCs expresses GFP (green) and targeted for whole-cell recording with an internal containing 20 Alexa-594 (red). Maximum projection (z = 0.5 µm). ***L***, Example diary plot of normalized sIPSC frequency (30 s bins; open circles) in a mouse OFF-BC during 25 µM forskolin treatment (red shading). ***M***, Diary plot of mean values during 25 µM forskolin treatment (red circles; n = 6), and in control conditions (blue: n = 5). Open circles with error bars represent mean ± SEM. Statistical significance was determined using a two-way ANOVA and Sidak test for multiple comparisons: ns, $p > 0.05$; *$p < 0.05$; **$p < 0.01$; ***$p < 0.001$. Data collected by Marc Meadows and Xiaohan Wang.

Bath application of 25 µM forskolin was given to OFF-BCs from mouse (n = 3) and rat (n = 3). Separate control experiments were performed in OFF-CBCS that did not receive drug application (n = 5). By 6.5 to 7.0 min after forskolin application, the frequency of IPSCs was significantly higher than control ($p < 0.001$; except at 6.75 min, $p = 0.003$), and by 7.25 min the frequency doubled ($p < 0.0001$; degrees of freedom = 91; two-way ANOVA and Sidak test).

2.3.4 Second messenger pathway involving EPAC potentiates AII-ACs

2.3.4a cAMP potentiates exocytosis by an EPAC-dependent and PKA-independent mechanism

PKA is a kinase activated by cAMP and implicated in the uncoupling of AII-AII AC electrical synapses by mediating the dephosphorylation of Cx36 gap junctions (Urschel et al., 2006; Kothmann et al., 2009). We then tested whether PKA enhances glycinergic release at the AII-AC to OFF-BC synapse using an internal solution containing 1 mM cAMP and 2 µM H89 (Fig. 2.1A1-A2), a competitive antagonist, highly specific for PKA (Hidaka et al., 1991). Example traces for experiments with 2 µM H89 (Fig. 2.8A1) illustrate that the antagonist did not suppress cAMP-induced potentiation in AII-ACs. Potentiation was consistently observed across several AII-ACs, resulting in a significant increase ΔC_m even with 2 µM H89 (1 min: 60.2 ± 7.35 fF; and 4 min: 76.3 ± 8.17 fF; n = 9; p = 0.002, paired t test). There were no changes in L-type Q_{Ca} (1 min: 8.02 ± 0.91 pC; and 4 min: 7.95 ± 1.19 pC; n = 9; p = 0.874, paired t test; Fig. 2.8A2). Building on our finding that 1 mM cAMP enhances exocytosis in AII-ACs (Fig. 2.1), the result from this experiment suggests that cAMP-induced potentiation requires a PKA-independent pathway. Furthermore, we observed no changes in R_s values with 2 µM H89 (1 min: 20.7 ± 1.01 MΩ; and 4 min: 22.8 ± 2.17 MΩ; n = 9; p = 0.6523, Wilcoxon), and R_m (1 min: 529 ± 269 MΩ; and 4 min: 471 ± 332 MΩ; n = 9; p = 0.097, Wilcoxon). We next tested the potential role of EPAC2 at this synapse by adding 1 µM HJC0350, a specific inhibitor of EPAC2 (H. Chen et al., 2013), to our internal solution containing 1 mM cAMP. Figure 2.8B1 shows representative I_{Ca} and C_m traces as AII-ACs were dialyzed with the internal solution. ΔC_m did not increase after 4 min with 1 µM HJC0350 even with cAMP in the patch pipette (1 min: 57.0 ± 9.17 fF; and 4 min: 59.6 ± 8.69 fF; n = 10; p = 0.59, paired t test; Fig. 2.8B2). These results suggest that cAMP-induced potentiation of exocytosis relies on an EPAC2-dependent mechanism. Furthermore, there were no significant changes in Q_{Ca} (1 min: 9.05 ± 0.77 pC; and 4 min: 9.71 ± 0.71 pC; n = 10; p = 0.112, paired t test). The mean R_s from recordings with 2 µM HJC0350 was as follows: 1 min: 25.4 ± 2.39 MΩ; and at 4 min: 24.2 ± 1.26 MΩ (n = 11; p = 0.5771; Wilcoxon); and mean R_m was as follows: 1 min: 1880 ± 1220 MΩ; and at 4 min: 759.8 ± 211 MΩ (n = 10; p = 0.3223, Wilcoxon).

Figure[2.8]

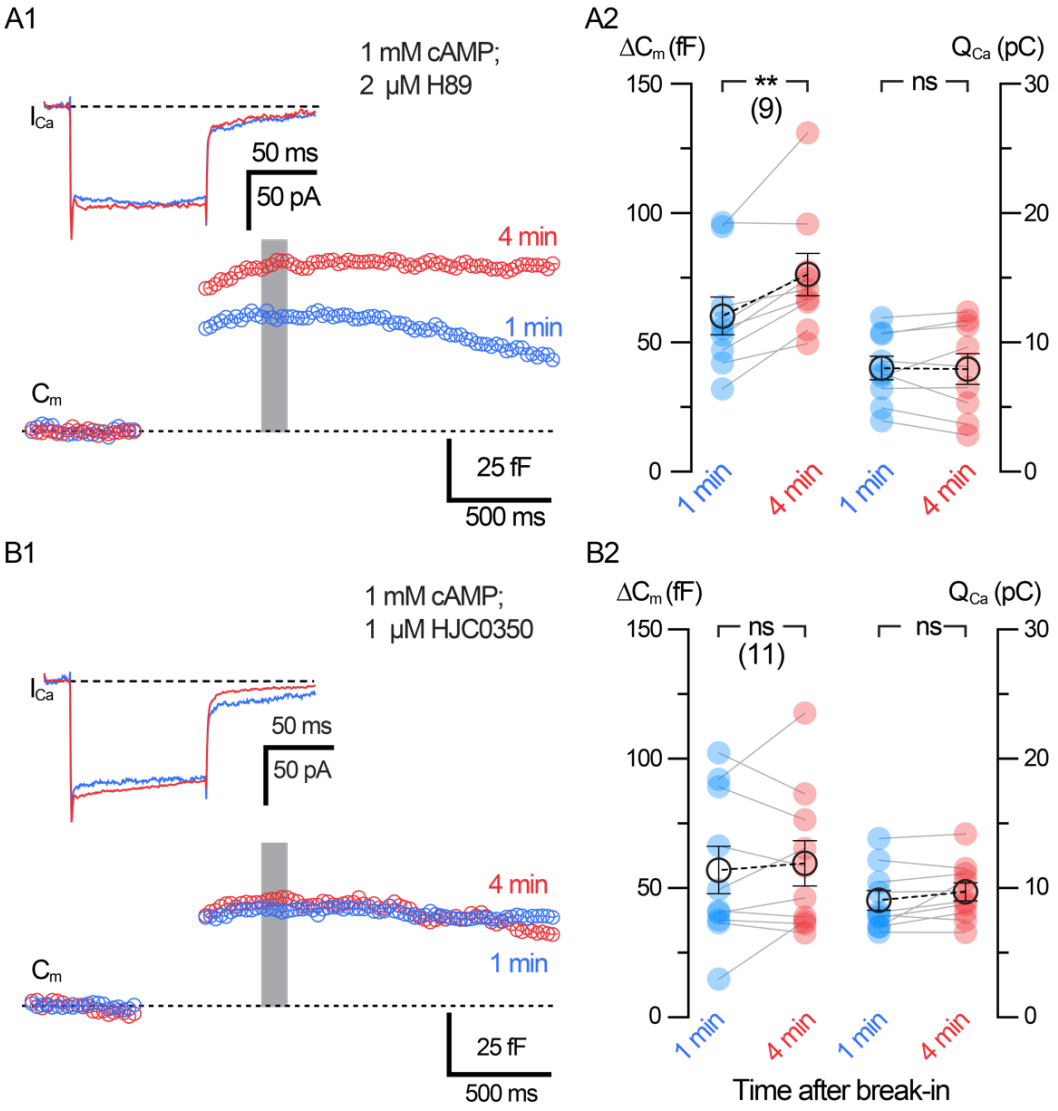

[2.8] The mechanism for cAMP-induced potentiation is EPAC2-dependent. Whole-cell voltage-clamp recordings were performed in AII-ACs using an internal solution containing 1 mM cAMP. Internal solutions also contained either 2 µM H89 (PKA inhibitor) or 1 µM HJC0350 (EPAC2 inhibitor). ***A1***, ***B1***, Average C_m and I_{Ca} responses to a 100 ms depolarizing pulse. Shown are recordings made before 1 min (blue) and 4 min (red) after break-in. Gray bar represents the region where C_m values were averaged. ***A1***, C_m and I_{Ca} responses from AII-ACs recorded with 2 µM H89. ***B1***, C_m and I_{Ca} responses from AII-ACs recorded with 1 µM HJC0350. ***A2***, ***B2***, Summary plots of ΔC_m and Q_{Ca} showing pairwise comparisons for each time after break-in. Closed circles represent data from individual AII-ACs. Open circles with error bars represent mean ± SEM. ***A2***, Summary plots for the 2 µM H89 dataset. ΔC_m increases after 4 min with no changes to Q_{Ca}, suggesting that 1 mM cAMP does not require PKA activation for cAMP-induced potentiation. ***B2***, Summary plots for the 1 µM HJC0350 dataset. ΔC_m does not increase after 4 min, suggesting that cAMP-induced potentiation is EPAC2-dependent. Statistical significance was determined using a paired t test: ns, $p > 0.05$; **$p < 0.001$.

2.3.4b Direct activation of EPAC potentiates exocytosis

EPAC2-mediated potentiation of exocytosis is widespread at synapses and secretory cells (Sakaba and Neher, 2001; Kamiya et al., 2002; Zhong and Zucker, 2005; Komai et al., 2014; Fernandes et al., 2015). We further tested for a role of EPAC mechanisms at AII-ACs with the specific EPAC activator 8-pCPT. This EPAC specific analog of cAMP has a threefold higher binding affinity than cAMP (Enserink et al., 2002) with no preference for EPAC isoforms; therefore, we substituted cAMP with 10 µM 8-pCPT in our internal solution. Figure 2.9A shows the detailed morphology of

Figure[2.9]

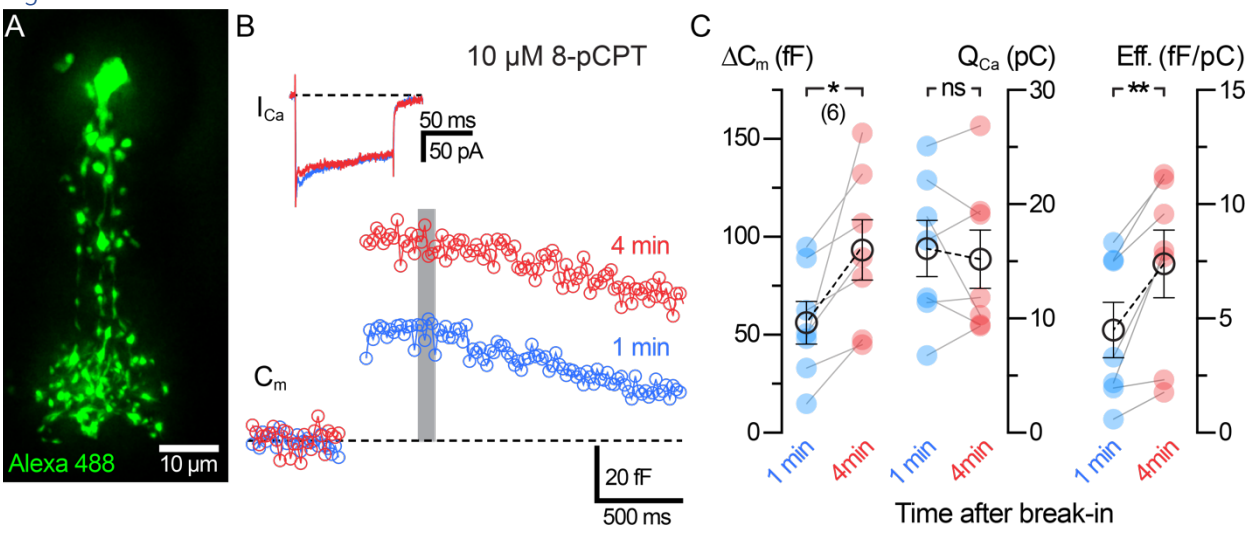

[2.9] Direct activation of EPAC potentiates the exocytosis of AII-ACs. Whole-cell voltage-clamp recordings were performed in AII-ACs before 1 min and after 4 min after break-in using an internal solution containing 10 µM 8-pCPT (EPAC specific activator). ***A***, Epifluorescence maximum intensity projection (z = 0.5 µm) of an AII-AC filled with Alexa-488 (20 µM), processed using iterative deconvolution. ***B***, Example C_m and I_{Ca} traces for responses to a 100 ms depolarizing pulse performed within 1 min (blue) and at 4 min (red) after break-in. Gray bar represents the region where C_m values were averaged. ***C***, Summary plots for ΔC_m and Q_{Ca} showing pairwise comparisons between each time after break-in. Closed circles represent data from individual AII-ACs. Open circles with error bars represent mean ± SEM. ΔC_m increases after 4 min with no change in Q_{Ca}, thus significantly increasing synaptic efficiency. Statistical significance was determined using a paired t test: ns, $p > 0.05$; *$p < 0.05$; **$p < 0.001$. Data collected by Marc Meadows and Veeramuthu Balakrishnan.

an AII-AC dialyzed with Alexa-488 after iterative image deconvolution. Figure 2.9B shows representative C_m and I_{Ca} traces recorded with 10 µM 8-pCPT in the patch pipette. Using 8-pCPT, we again did not see a significant change in Q_{Ca} (1 min: 16.1 ± 2.46 pC; and 4 min: 15.2 ± 2.54 pC; n = 7; p = 0.565, paired t test). However, dialysis with 8-pCPT increased the ΔC_m jumps

significantly after 4 min from break-in (Fig. 2.9C; 1 min: 56.2 ± 10.9 fF; and 4 min: 93.3 ± 15.35 fF; n = 7; p = 0.021, paired t test). The efficiency of exocytosis also increased with 8-pCPT (1 min: 4.49 ± 1.21 fF/pC; and 4 min: 7.39 ± 1.48 fF/pC; n = 7; p = 0.0066, paired t test). Our concentration of 8-pCPT (10 µM) was 100-fold lower than what we used for cAMP (1 mM). Nevertheless, ΔC_m jumps increased almost twofold with 8-pCPT. This supports our findings in Figure 2.8 that cAMP increases exocytosis via an EPAC2 pathway based on the isoform specificity of HJC0350. The mean R_s was (1 min: 29.7 ± 5.7 MΩ; and 4 min: 32.7 ± 7.4 MΩ; n = 6; p = 0.2697, paired t test) and mean R_m was (1 min: 487.6 ± 121.4 MΩ; and 4 min: 348.7 ± 100.4 MΩ; n = 7; p = 0.042, paired t test).

2.3.5 Inhibition of CICR stores reduces cAMP-induced potentiation

Ca^{2+} induced Ca^{2+} release (CICR) is a major regulator of exocytosis at synapses (Padamsey et al., 2019). ACs use sarcoplasmic-endoplasmic reticulum (SERCA) Ca^{2+} pumps to regulate internal Ca^{2+} levels (Krizaj, 2005). EPAC2 has been shown to enhance CICR from the ER in a cAMP-dependent manner by modulating Ca^{2+} release from ryanodine and inositol 1,4,5-trisphosphate (IP3) receptors (Holz et al., 2006). CICR can trigger exocytosis at AC synapses (Warrier et al., 2005) and ribbon-type synapses of photoreceptors and hair cells (Babai et al., 2010; Castellano-Munoz et al., 2016). By contrast, short-term plasticity at several CNS synapses is not affected by CICR (Carter et al., 2002). EPAC2 is involved in CICR during β-cell insulin secretion (Rorsman et al., 2012; Stožer et al., 2021). However, EPAC2-dependent exocytosis enhancement and EPAC2-dependent CICR have not been observed previously in the retina. We used 2-APB (50 µM) as a competitive IP3 receptor antagonist and store-operated Ca^{2+} entry channel antagonist, which should deplete ER Ca^{2+} stores (Bootman et al., 2002; Majewski and Kuznicki, 2015). Importantly, 2-APB (50 µM) has been shown to significantly reduce CICR from depolarized GABAergic AC dendrites (Warrier et al., 2005). We incubated retina slices with 50 µM 2-APB for 10-15 min and then whole-cell voltage-clamped the AII-AC with an internal solution containing 1 mM cAMP while 50 µM 2-APB was continuously perfused (Fig. 2.10A1). ΔC_m responses from AII-ACs pretreated with 2-APB slightly increased after 4 min, but this was not statistically significant (1 min: 44.1 ± 5.67 fF; and 4 min: 59.8 ± 12.3 fF; n = 10; p = 0.1197, paired t test; Fig. 2.10A2).

Figure[2.10]

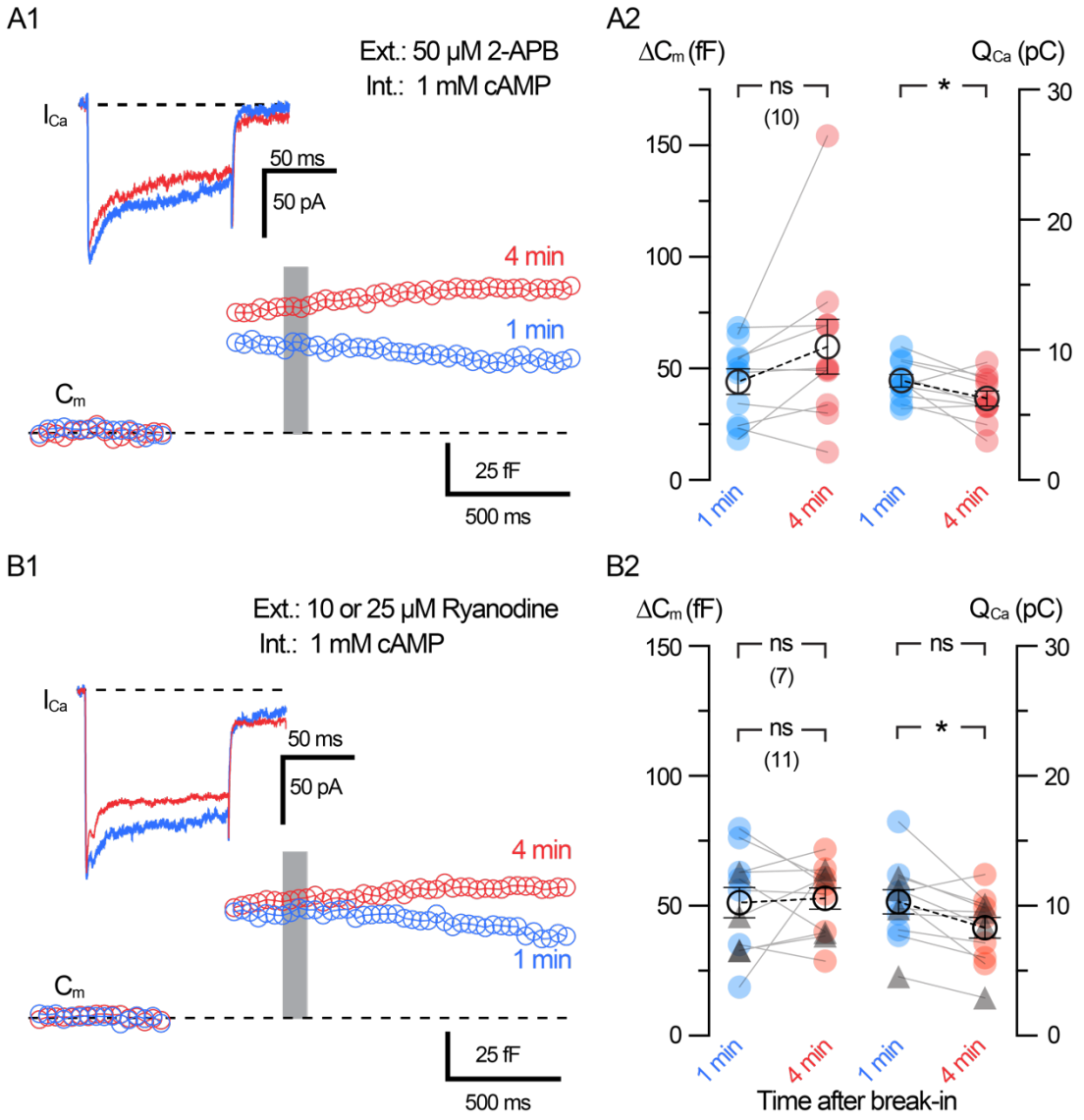

[2.10] Inhibition of Ca^{2+} release from Ca^{2+} stores reduces cAMP-induced potentiation.

Whole-cell voltage-clamp recordings were performed in AII-ACs using an internal solution containing 1 mM cAMP. The AII-ACs were preincubated for 10 min with 50 µM 2-APB (blocker of IP3 receptors and store-operated Ca^{2+} entry channels) or ryanodine (10 or 25 µM) in the external bath solution before whole-cell break-in. These drugs were then perfused continuously during the recordings. ***A1***, ***B1***, Average C_m and I_{Ca} responses from AII-ACs performed within 1 min (blue) and at 4 min (red) after break-in using an internal solution containing 1 mM cAMP. Gray bar represents the region where C_m values were averaged. ***A1***, Average C_m and I_{Ca} responses for AII-ACs preincubated with 50 µM 2-APB. ***B1***, Average C_m and I_{Ca} responses for AII-ACs preincubated with 10 or 25 µM ryanodine, which depletes and partially blocks Ca^{2+} stores. ***A2***, ***B2***, Summary plots for ΔC_m and Q_{Ca} for AII-ACs showing pairwise comparisons between each time after break-in. Closed circles represent data from individual cells. Open circles with error bars represent mean ± SEM. ***A2,*** Summary plots for the 50 µM 2-APB dataset. ***B2***,

Summary plots for the 10 or 25 µM ryanodine dataset. Triangles represent cells with 25 µM ryanodine (n = 4). Labeled on the graphs are statistical summaries for 10 µM ryanodine dataset (top; n = 7) and dataset including 25 µM ryanodine (bottom; n = 11). ΔC_m does not increase after 4 min with 1 mM cAMP in the internal solution, while Q_{Ca} decreases only for the whole combined dataset (n = 11). Statistical significance was determined using a paired t test: ns, $p > 0.05$; *$p < 0.05$.

The Q_{Ca} slightly decreased after 4 min with the 2-APB pretreatment (1 min: 7.63 ± 0.487 pC; and 4 min: 6.27 ± 0.57 pC; n = 10; p = 0.0306, paired t test). To study CICR from ryanodine receptors (RyRs), we incubated retina slices with 10 µM ryanodine for 10-15 min before whole-cell voltage-clamp recordings with 1 mM cAMP in the internal solution (Fig. 2.10B1). Ryanodine at 10 µM can lock RyR in a low conductance state and thus cause a slow and tonic leak of Ca^{2+} from ER stores, thereby depleting them (Ehrlich et al., 1994; Kang et al., 2005; Ster et al., 2007). Slow Ca^{2+} release from ER stores triggered by 10 µM ryanodine can produce non-ribbon Ca^{2+}-dependent exocytosis in rod photoreceptors (M. Chen et al., 2014). Therefore, we also used a higher concentration (25 µM) to block Ca^{2+} release from RyR, as shown by Warrier et al. (2005) using caffeine to induce Ca^{2+} release from stores in AC dendrites (see also Sosa et al., 2002; Vigh and Lasater, 2003; Vigh et al., 2005; Chávez et al., 2010). Resulting ΔC_m responses with a 1 mM cAMP internal did not potentiate 4 min after break-in when pretreated with 10 or 25 µM ryanodine (1 min: 51.3 ± 5.91 fF; and 4 min: 52.8 ± 4.15 fF; n = 11; p = 0.7863, paired t test; Fig. 2.10B2). Q_{Ca} did not significantly decrease when 10 µM ryanodine was used (n = 7), although Q_{Ca} did decrease significantly when we combined the datasets for 10 and 25 µM ryanodine (1 min: 10.3 ± 0.92 pC; and 4 min: 8.32 ± 0.81 pC; n = 11; p = 0.0104, paired t test). The reduction in Q_{Ca} when Ca^{2+} stores were emptied may be because of Ca^{2+}-dependent inactivation of the L-type Ca^{2+} current (von Gersdorff and Matthews, 1996). These results suggest that intact ER stores loaded with Ca^{2+} and thus capable of CICR are necessary for the cAMP-induced potentiation of exocytosis.

Section 2.4: Discussion

This study used presynaptic capacitance measurements and postsynaptic recordings of sIPSCs to uncover mechanisms of cAMP-induced potentiation of glycine release from AII-ACs. We propose that cAMP plays dual roles in AII-ACs through two distinct morphologic compartments and signaling pathways. First, a PKA-dependent pathway uncouples electrical synapses at the distal

tips of dendrites in layers S3-5 of the IPL (Kothmann et al., 2009). Second, an EPAC2-dependent signaling pathway potentiates the exocytosis of synaptic vesicle fusion, enhancing crossover inhibition to OFF-CBCs at the lobular appendages in layers S1-2 of the IPL (Fig. 2.7A).

2.4.1 Elevation of cAMP concentration increases RRP size at AII-ACs

The lobular appendages of the AII-AC contain a large pool of glycine loaded vesicles in their cytoplasm and multiple extensive active zones with several docked vesicles (Strettoi et al., 1992; Marc et al., 2014). Here we show that both the initial RRP with a high release rate and the secondary RRP with slower rate were potentiated in size nearly twofold by intracellular 1 mM cAMP (Fig. 2.3). In the calyx of Held, nerve terminal cAMP changes the Ca^{2+} sensitivity of synaptotagmin, potentiating only the initial fast releasing pool of vesicles (Yao and Sakaba, 2010). Our results also contrast with results from hippocampal mossy fiber boutons, where cAMP only increases the initial release rate without changing the overall RRP size (Midorikawa and Sakaba, 2017).

Recent computer modeling of the AII-AC morphology in adult Sprague Dawley rats suggests that the thin dendrites may filter global C_m measurements when high-frequency sine waves are used (Zandt et al., 2018). Our measurements of total RRP size using a 2 kHz sinusoidal wave may therefore underestimate the total RRP of the AII-AC by 10%-20% (Hartveit et al., 2019). However, we have shown previously that reducing the sinusoidal frequency does not change the ΔC_m jump size in our juvenile C57 mouse (postnatal days 16-28) AII-ACs, which we presume are more electrotonically compact (Balakrishnan et al., 2015), suggesting that the lobules are not electrotonically distant from the soma in mouse AII-ACs.

2.4.2 EPAC2 and Ca^{2+} store signaling pathways for exocytosis potentiation

The molecular pathways for cAMP-dependent potentiation differ across synapses (Seino and Shibasaki, 2005). PKA is a classic substrate for cAMP that promotes potentiation in hippocampal (Trudeau et al., 1996; Castillo et al., 1997) and cerebellar synapses (C. Chen and Regehr, 1997). PKA can enhance Ca^{2+} entry by directly phosphorylating L-type Ca^{2+} channels (Nanou and Catterall, 2018). However, enhancement of the Ca^{2+} current cannot explain cAMP-induced

potentiation of exocytosis in AII-ACs because Ca^{2+} current peak amplitudes, charge, and inactivation kinetics did not change (Figs. 1, 3A, 5–9). Indeed, we observed a slight but significant reduction of Q_{Ca} in some instances (Figs. 4 and 10). PKA-dependent increases in RRP can occur without changes in P_r via a shift in release mode from univesicular to coordinated multivesicular release (Vaden et al., 2019). However, our results show that cAMP potentiation of exocytosis in AII-ACs is mediated by EPAC2 (Figs. 8 and 9).

Presynaptic EPAC-dependent potentiation appears to be an evolutionary ancient modulatory pathway that has also been observed at the crayfish neuromuscular junction (Zhong and Zucker, 2005), as well as at spinal cord glycinergic interneurons (Katsurabayashi et al., 2001; Choi et al., 2009). Recently, an increase in RRP via EPAC2 has been shown at hippocampal mossy fiber synapses (Fernandes et al., 2015) and parallel fiber synapses to Purkinje cells (Martín et al., 2020). Hippocampal synapses may have a fast and slow mode of potentiation regulated by EPAC and PKA, respectively (Gekel and Neher, 2008). In pancreatic β cells, both PKA and EPAC2 potentiate Ca^{2+}-dependent exocytosis, modulating the release of insulin large dense-core vesicles and small GABA vesicles (Eliasson et al., 2003; Hatakeyama et al., 2007; Henquin and Nenquin, 2014). Our findings show that cAMP enhancement of exocytosis is PKA-independent in AII-ACs. We confirmed this by (1) showing that H-89 does not block potentiation, (2) directly activating EPAC using the 8-pCPT analog, which has a 100-fold higher binding preference for EPACs over PKA (Enserink et al., 2002), and (3) directly blocking potentiation with a specific EPAC2 antagonist (HJC0350; 130-fold higher binding efficiency than cAMP) (H. Chen et al., 2013). We note that 8-pCPT may partially activate PKA (only 5%-7% at 50 µM) (Christensen et al., 2003). Direct activation of HCN channels by cAMP can also cause presynaptic potentiation (Zhong et al., 2004); however, I_h currents have not been reported in AII-ACs (Firl et al., 2015) and our experiments were performed in voltage-clamp. In summary, our results suggest that cAMP potentiation of exocytosis is solely driven by EPAC2 by increasing in RRP and without changing P_r as shown in PPR experiments (Fig. 2.4).

What are potential EPAC2-dependent molecular mechanisms that directly “superprime” the initial RRP and contribute to nearly doubling its size? Key proteins involved in vesicle priming are

RIM, RBP, Rab3, and Munc13, and they are necessary for cAMP potentiation (Lonart et al., 1998; Castillo et al., 2002; Yang and Calakos, 2011). RIM proteins anchor Munc13 and Rab3 at active zones, and EPAC2 also binds to the scaffold proteins piccolo and RIM1/2 (Ozaki et al., 2000; Kashima et al., 2001; Schoch et al., 2002). RIM1/2 can also bind to the α-subunit of L-type Ca^{2+} channels via RBP to modulate exocytosis (Hibino et al., 2002; Grabner et al., 2015; Krinner et al., 2017) or directly to the β-subunit of $Ca_V1.3$ to modulate Ca^{2+} current inactivation (Gandini et al., 2011). These are all potential downstream targets of EPAC2 and need further characterization.

Additionally, we also found that inhibiting CICR from internal Ca^{2+} stores reduced cAMP-induced potentiation (Fig. 2.10). Our results with H89 (Fig. 2.8) suggest that PKA does not alter CICR. EPAC2 can increase CICR by acting on RyR and IP3 receptors (Holz et al., 2006). EPAC2 mediates RyR phosphorylation via CaMKII in cardiac myocytes (Pereira et al., 2013). Cerebellar neurons also exhibit EPAC2-dependent modulation of CICR through Rap and p38 MAPK activation (Ster et al., 2007). Spontaneous release can also be regulated by CICR (M. Chen et al., 2014; Williams and Smith, 2018; Chanaday et al., 2021), which may explain the increase in sIPSCs seen in Figure 2.7. In summary, our results suggest that the cAMP-induced potentiation of exocytosis in AII-ACs requires both EPAC2 and CICR from intact Ca^{2+} stores; however, more work is necessary to determine in detail how EPAC2 and Ca^{2+} stores interact to promote exocytosis.

2.4.3 Neuromodulators can increase cAMP levels

The second messenger cAMP plays multiple roles in visual processing by tuning retinal circuits during development and sharpening local receptive fields (Stellwagen et al., 1999; Dunn et al., 2009). Fluorescent imaging of cAMP levels has shown that forskolin and several neuromodulators can increase cAMP levels in CNS nerve terminals (Vincent et al., 2008; Muntean et al., 2018). Among neuromodulators, dopamine, in particular, is responsible for long-lasting changes in retinal circuitry (Roy and Field, 2019). Dopamine also promotes the release of the antioxidant ascorbate from retinal neurons via EPAC2 (Encarnação et al., 2018); where D1 and EPAC activation increased ascorbate release from cultured retinal neurons. This study also found expression of EPAC2 from their cultured neurons and Müller glia. Dopamine and forskolin can potentiate exocytosis from BCs (Heidelberger and Matthews, 1994), and modulate AII-AC

networks by closing gap junctions (Hampson et al., 1992). Dopaminergic ACs form *en passant* synapses around the root dendrite of AII-ACs (Voigt and Wässle, 1987), and there is evidence that AII-ACs exhibit D1-like receptor activity (Witkovsky et al., 2007). However, antibody localization of D1-like receptors in AII-ACs still remains uncertain (Veruki and Wässle, 1996). Interestingly, D1-like receptor activation reduces glycinergic inhibition to OFF-BCs and changes the spike output of ganglion cells during photopic conditions (Jensen, 1989; Mazade et al., 2019; Mazade and Eggers, 2020). It is possible that D1-like activity can increase cAMP in AII-ACs while reducing inhibition through global changes in retinal networks. Further studies are clearly needed to better understand the complex effects of light-evoked neuromodulator release on the local cAMP levels of AII-ACs.

2.4.4 Chemical compartmentalization, adenylyl cyclases, and microdomains of cAMP

The AII-AC is a bistratified neuron with well-separated cellular compartments (Figs. 1B and 9A). Indeed, changes in Ca^{2+} levels within a particular lobular appendage do not spread to nearby lobules or dendrites (Balakrishnan et al., 2015; Kim and von Gersdorff, 2016). Likewise, physiological changes in cAMP levels at different lobules or in the distal dendritic arbors may all occur locally and independently of each other.

Our recordings of sIPSCs from the OFF-CBCs show a significant increase in the frequency of sIPSC after forskolin application (Fig. 2.7). This continuous and robust release of glycine is presumably potentiated by elevations of cAMP via stimulation of adenylyl cyclases by forskolin. Changes in cAMP levels may also be regulated by Ca^{2+}-dependent adenylyl cyclases near L-type Ca^{2+} channels (Halls and Cooper, 2011). Local clustering of adenylyl cyclases may elevate cAMP to the higher levels needed to activate EPAC2 and translocate it to docked vesicles (Alenkvist et al., 2017), whereas cytoplasmic phosphodiesterases may confine high cAMP levels to local microdomains near the plasma membrane (Rich et al., 2001; Kuhn and Nadler, 2020). The lobular appendage geometry (small bubble-like structures, densely packed with vesicles and mitochondria, and connected by thin and short tubes to the apical dendrite) seems ideally suited to form diffusional

barriers that restrict Ca^{2+} and cAMP microdomains near the membrane where synaptic vesicles are docked.

In conclusion, our findings show that elevations of cAMP in the AII-ACs can increase both phasic and tonic inhibition to OFF-CBC terminals and OFF ganglion cells (Balakrishnan et al., 2015; Graydon et al., 2018). We propose that these changes in glycine release may help to reduce synaptic noise contamination between the OFF and ON pathways of the retina. This may help to sharpen contrast gain at different ambient light levels (Freed and Liang, 2014).

Section 2.5: Materials & Methods

Rodents and retinal slices

Procedures were approved by the Institutional Animal Care and Use Committee of Oregon Health & Science University, and were in accordance with National Institutes of Health guidelines. C57BL/6 background mice and Sprague Dawley rats of either sex (postnatal day 25-35) were used in the experiments. Animals were anesthetized with isoflurane (Novaplus) and then after death, the eyes were removed and dissected to extract the retina in carbogenated Ames medium (US Biologicals) at room temperature. Experiments were also performed using connexin-36 knockout mice (*Cx36*$^{-/-}$; generated as described by Hormuzdi et al., 2001), and transgenic synaptotagmin2-EGFP mice (*Syt2*-EGFP; MMRRC).

Retinas were embedded in low melting temperature agarose (σ Type VIIA, 3% in Ames medium), and 250 µm slices were prepared using a vibratome (Leica Microsystems, VT1200S) in carbogenated low-Na^+ sucrose-based cutting solution containing the following (in mm): 2.5 KCL, 35 NaHCO3, 1.25 NaH2PO4, 0.5 CaCl2, 6 MgCl2, 10 glucose, 3 Na-pyruvate, 210 sucrose, and 20 HEPES and buffered to pH 7.4 with NaOH. Retinal slices were stored at room temperature in carbogenated Ames solution before being transferred to the recording chamber. Ames solution (containing 1.15 mM free Ca^{2+}) (Ames and Nesbett, 1981) was continuously perfused over the retinal slices during recordings and heated to near physiological temperature (32°C-34°C) for all experiments.

Live cell imaging

Retina slices were viewed with differential interference contrast (DIC) microscopy using a water immersion objective lens (60×, Olympus) on a fixed stage, upright microscope (BX51WI, Olympus). Experiments were also performed with a 40× objective on an Axio Examiner microscope (Carl Zeiss). AII-ACs and OFF-CBCs were identified by the soma shape and position in the inner nuclear layer (INL). Epifluorescence images were taken to determine the cell morphology perfused with Alexa-488 or -594 dye (20 µM; Invitrogen) after whole-cell recordings. Images were captured with a QIClick CCD camera (Q-Imaging). Z stacks and time-series image acquisition was performed using an Orca Flash 4.0LT CMOS camera (Hamamatsu Photonics) controlled with CellSens deconvolution image software (Olympus). Image stacks were also generated using a piezo collar (Pi) on the objective and used to capture both AII-AC and OFF-CBC morphology using epifluorescence and DIC image channels (z = 0.5 µm optical slices; ranging from 50 to 95 slices varying from cell to cell).

Tracking whole-cell dialysis of Alexa-488 was done with a time-lapse (10 Hz) video at a single focal plane for 30 s. This was immediately followed by a time-lapse video at 5 Hz using a piezo collar (Pi) on the objective to cycle through 5 focal planes. After these videos were captured and the cell was fully dialyzed, we performed a z-stack image of the entire cell.

Patch clamp electrophysiology

Single-cell voltage-clamp recordings were performed using a double EPC-9 or EPC-10 patch-clamp amplifier and either Pulse or Patchmaster software (HEKA Elektronik). Thick-walled borosilicate glass pipettes (8-10 MΩ; 1B150F-4, World Precision Instruments) were pulled using a Narishige puller-PP830 (Tokyo) and coated with dental wax (Cavex) or Parafilm to reduce stray capacitance and electrical noise. Data were acquired at 10 or 20 kHz sampling rate and filtered with 2 kHz low-pass filter.

Presynaptic recordings of Ca^{2+} currents and C_m measurements

Whole-cell voltage-clamp recordings of C_m and Ca^{2+} currents (I_{Ca}) were performed in mouse AII-ACs. Recordings were performed in photopic conditions. Ames external solution was supplemented with (in µM) as follows: 10 NBQX or 10 CNQX, 50 DL-AP5, 2 strychnine, 3 SR95531, 5 bicuculline, and 1 TTX. These drugs blocked AMPA, NMDA, glycine, and GABA receptors, as well

as Na^+ channels during C_m and I_{Ca} recordings. Pipettes were back-filled with a filtered internal solution designed to isolate Ca^{2+} currents by blocking K^+ currents (in mM) as follows: 40 CsCl, 60 Cs-gluconate, 10 tetraethyl ammonium chloride, 28 HEPES, 3 adenosine 5'-triphosphate magnesium salt (ATP-Mg), 1 guanosine 5'-triphosphate disodium salt (GTP-Na2), and 2 EGTA; osmolarity was adjusted to 270 mOsm using glucose, and pH to 7.3 with CsOH. Ultrapure salts for internal and external solutions were purchased from Sigma-Aldrich.

Time-resolved C_m measurements were made using the "sine+DC" method (Gillis, 2000; Kushmerick and von Gersdorff, 2003; Balakrishnan et al., 2015; Hartveit et al., 2019). A pair of sinusoidal waves (2 kHz; 30 mV peak-to-peak) superimposed on membrane holding potential (−80 mV) were given before and after a square depolarizing pulse from −80 to −10 mV for maximum activation of L-type Ca^{2+} current (Balakrishnan et al., 2015), which triggered Ca^{2+}-dependent vesicle fusion (exocytosis). Leak voltage-clamp pulses (to −66 mV) were used to calculate leak-subtracted L-type Ca^{2+} currents and were resolved using offline P/5 leak subtraction. In addition, I_{Ca} were sometimes isolated by subtraction of the leak current after application of 1 µM isradipine. Experiments were not corrected for liquid junction potential, which was measured (−6 mV) post hoc using methods described by Neher (1992). Of the total of 79 AII-AC recordings, the average series resistance (R_S) for AII-ACs was 29.04 ± 14.8 MΩ and the membrane resistance (R_m) was 1025 ± 193 MΩ.

Online calculations of passive membrane properties (C_m, R_s, R_m) were done by the HEKA software. Traces were imported to IgorPro software (Wavemetrics) for offline analysis. Net exocytosis was determined by the change in the C_m response after a depolarizing pulse: $\Delta C_m = C_m$ (after pulse) – C_m (baseline). This was performed by subtracting averaged C_m data points after the depolarizing pulse from baseline C_m (indicated by gray bars on figures with C_m). ΔC_m response was measured from 300 to 500 ms after the depolarizing pulse, allowing time for all evoked conductances to decay back to baseline.

Postsynaptic recordings from OFF-CBCs

Whole-cell voltage-clamp recordings of sIPSCs from OFF-CBCs in retina slices from rat and *Syt2*-EGFP mice: recordings were performed in an external ACSF solution containing the following (in

mm): 125 NaCl, 2.5 KCl, 25 NaHCO3, 1.25 NaH2PO4, 2.5 CaCl2, 1 MgCl2, 10 glucose, pH 7.4, and using a Cs-based internal solution containing the following (in mm): 50 CsCl, 60 Cs-gluconate, 10 HEPES, 6 EGTA, 4 ATP-Mg, 0.4 GTP-Na2, 0.1 CaCl2, and 1 MgCl2; osmolarity was adjusted to 270 mOsm using glucose, and pH to 7.3 with CsOH. Glycinergic sIPSCs from OFF-CBCs were isolated using the following drugs in the external bath solution (in µm): 10 CNQX, 25 D-AP5, 5 bicuculline, and 3 SR95531. Similar experiments were also performed on OFF-CBCs in slices from *Syt2*-EGFP mice continuously perfused with Ames medium. The datasets for sIPSCs from rat and mouse OFF-CBCs were similar in amplitude and kinetics and were grouped together. A total of five OFF-CBC recordings from *Syt2*-EGFP mice were used in this study, the mean R_s was 21.3 ± 3.952 MΩ, and holding current was −95.4 ± 36.24 pA.

Glycinergic sIPSCs were analyzed using custom procedures in IgorPro software using a sliding scale template method for detecting and isolating events (Clements and Bekkers, 1997). Analysis was performed using a detection threshold of −10 and −15 pA, with no change in event detection. The medians of events for each cell were used for statistical comparisons before and after treatment. Plots of frequency and cumulative distribution were generated by grouping all events for each dataset, which were generated and fitted using Prism software (GraphPad). Using Prism software (GraphPad), we made log-Gaussian fits to frequency distribution histograms of sIPSC events using the following function:

$$P(x) = \left(\frac{A}{(x)}\right) * e^{-0.5\left(\frac{ln(\frac{x}{\mu})}{ln(\sigma)}\right)^2}$$

Where µ is the geometric mean and σ is the geometric standard deviation. A is a constant related to the distribution area (P_{area}) and amplitude (P_{max}) as defined by the following equations:

$$P_{area} = A * ln(\sigma) * \sqrt{2\pi}$$

$$P_{max} = \frac{A * e^{0.5ln(\sigma)^2}}{\mu}$$

Drugs and toxins

Stock concentrations of drugs and salts were prepared using purified water (Millipore). The synaptic blockers NBQX, CNQX, SR95531, and DL-AP5 and bicuculline were obtained from Tocris Bioscience. TTX and strychnine were obtained from Sigma. Internal solutions contained HJC0350, H89, and 8-pCPT-2-O-Me-cAMP (8-pCPT) when indicated (Tocris Biosciences). Forskolin, 2-APB, and ryanodine were bath-applied in the external solution when indicated (Tocris Biosciences). HJC0350, H89, and forskolin were first dissolved in DMSO (final DMSO concentration of 0.01%, v/v). Internal solutions were prepared and stored [1.25×] for no longer than 3 months and diluted [1×] before use with purified water (Milli-Q; Millipore) or freshly prepared 25 mM stock cAMP sodium salt (Sigma). Pipette filling syringes containing internal solutions were kept on ice to avoid thermal degradation of cAMP, GTP, and ATP-Mg.

Experimental design and statistical analysis

Datasets for all experiments were tested for normal distribution using a Shapiro–Wilk test. For most experiments, pairwise comparisons were made between recordings taken within 1 min (30 s to 1 min) and at 4 min after break-in using a two-tailed paired t test or Wilcoxon test, respectively, for datasets with normal and non-normal distribution with an α level of 0.05. For comparisons of independent groups, we performed either a Student's t test or Mann–Whitney test, respectively, for normal and non-normal distribution. For comparisons between multiple groups, we indicate where we use one-way and two-way ANOVA tests followed by post hoc tests. All statistical tests were performed in Prism 9 software (GraphPad). Grouped data are written as mean ± SEM. Statistical significance is noted by asterisks, while not significant ($p > 0.05$) is either labeled or not indicated.

Section 2.6: Acknowledgements

This work was supported by National Institutes of Health Grants EY014043 and DC12938 to H.v.G.; and Casey Eye Institute P30 Grant EY010572. This work was union-made and upheld fair labor practices approved by AFSCME Local 402 OHSUGRU. We thank Gary Westbrook for providing the *Cx36*$^{-/-}$ mice; Holger Taschenberger for providing mini-IPSC software analysis procedures. Special thanks to my laboratory members Andre Dagostin, Benjamin Zemel, and

Paulo Strazza. I am truly grateful for my thesis committee members Catherine Morgans, Stephen Smith, Benjamin Sivyer, Anusha Mishra, and Stefan Hallermann for their guidance and support. Thanks to Espen Hartveit, and Margaret Veruki for perspectives and numerous discussions.

Section 2.7: References

Alasbahi RH, Melzig MF (2012) Forskolin and derivatives as tools for studying the role of cAMP. Pharmazie 67:5-13.

Alenkvist I, Gandasi NR, Barg S, Tengholm A (2017) Recruitment of EPAC2 to insulin granule docking sites regulates priming for exocytosis. Diabetes 66:2610-2622.

Ames A, Nesbett, F (1981) *In Vitro* retina as an experimental model of the central nervous system. J Neurochem 37:867-877.

Babai N, Morgans CW, Thoreson WB (2010) Calcium-induced calcium release contributes to synaptic release from mouse rod photoreceptors. Neurosci 165:1447-1456.

Balakrishnan V, Puthussery T, Kim MH, Taylor WR, von Gersdorff H (2015) Synaptic vesicle exocytosis at the dendritic lobules of an inhibitory interneuron in the mammalian retina. Neuron 87:563-575.

Bootman MD, Collins TJ, Mackenzie L, Roderick HL, Berridge MJ, Peppiatt C_m (2002) 2 aminoethoxydiphenyl borate (2-APB) is a reliable blocker of store-operated Ca^{2+} entry but an inconsistent inhibitor of InsP3-induced Ca^{2+} release. FASEB J 16:1145-50.

Carter AG, Vogt KE, Foster KA, Regehr WG (2002) Assessing the role of calcium-induced calcium release in short-term presynaptic plasticity at excitatory central synapses. J Neurosci 22:21-28.

Castellano-Munoz M, Schnee ME, Ricci AJ (2016) Calcium-induced calcium release supports recruitment of synaptic vesicles in auditory hair cells. J Neurophysiol 115:226-239.

Castillo PE, Schoch S, Schmitz F, Sudhof TC, Malenka RC (2002) RIM1alpha is required for presynaptic long-term potentiation. Nature 415:327-330.

Castillo PE, Janz R, Sudhof TC, Tzounopoulos T, Malenka RC, Nicoll RA (1997) Rab3A is essential for mossy fibre long-term potentiation in the hippocampus. Nature 388:590-593.

Chanaday NL, Nosyreva E, Shin OH, Zhang H, Aklan I, Atasoy D, Bezprozvanny I, Kavalali ET (2021) Presynaptic store-operated Ca^{2+} entry drives excitatory spontaneous neurotransmission and augments endoplasmic reticulum stress. Neuron 109(8):1314-1332.e5.

Chen C, Regehr WG (1997) The mechanism of cAMP-mediated enhancement at a cerebellar synapse. J Neurosci 17:8687-8694.

Chen H, Tsalkova T, Chepurny OG, Mei FC, Holz GG, Cheng X, Zhou J (2013) Identification and characterization of small molecules as potent and specific EPAC2 antagonists. J Med Chem 56:952-962.

Chen M, Krizaj D, Thoreson WB (2014) Intracellular calcium stores drive slow non-ribbon vesicle release from rod photoreceptors. Front Cell Neurosci 8:20.

Chen M, von Gersdorff H (2019) How to build a fast and highly sensitive sound detector that remains robust to temperature shifts. J Neurosci 39:7260-7276.

Cho S, von Gersdorff H (2012) Ca^{2+} influx and neurotransmitter release at ribbon synapses. Cell Calcium 52:208-216.

Choi IS, Nakamura M, Cho JH, Park HM, Kim SJ, Kim J, Lee JJ, Choi BJ, Jang IS (2009) Cyclic AMP-mediated long-term facilitation of glycinergic transmission in developing spinal dorsal horn neurons. J Neurochem 110:1695-1706.

Christensen AE, Selheim F, de Rooij J, Dremier S, Schwede F, Dao KK, Martinez A, Maenhaut C, Bos JL, Genieser HG, Døskeland SO (2003) cAMP analog mapping of Epac1 and cAMP kinase: Discriminating analogs demonstrate that Epac and cAMP kinase act synergistically to promote PC-12 cell neurite extension. J Biol Chem 278:35394-402.

Christie JM, Bark C, Hormuzdi SG, Helbig I, Monyer H, Westbrook GL (2005) Connexin36 mediates spike synchrony in olfactory bulb glomeruli. Neuron 46:761-72.

Clements JD, Bekkers JM (1997) Detection of spontaneous synaptic events with an optimally scaled template. Biophys J 73(1):220-229.

Demb JB, Singer JH (2012) Intrinsic properties and functional circuitry of the AII amacrine cell. Vis Neurosci 29:51-60.

Dunn TA, Storm DR, Feller MB (2009) Calcium-dependent increases in protein kinase-A activity in mouse retinal ganglion cells are mediated by multiple adenylate cyclases. PLoS ONE 4(11): e7877.

Ehrlich BE, Kaftan E, Bezprozvannaya S, Bezprozvanny I (1994) The pharmacology of intracellular Ca^{2+}-release channels. Trends Pharmacol Sci 15:145-149.

Eliasson L, Ma X, Renström E, Barg S, Berggren PO, Galvanovskis J, Gromada J, Jing X, Lundquist I, Salehi A, Sewing S, Rorsman P (2003) SUR1 regulates PKA-independent cAMP-induced granule priming in mouse pancreatic B-cells. J Gen Physiol 121:181-197.

Encarnação TG, Portugal CC, Nogueira CE, Santiago FN, Socodato R, Paes-de-Carvalho R (2018) Dopamine promotes ascorbate release from retinal neurons: Role of D1 receptors and the exchange protein directly activated by cAMP type 2 (EPAC2). Mol Neurobiol 55:7858–7871.

Enserink JM, Christensen AE, de Rooij J, van Triest M, Schwede F, Genieser HG, Døskeland SO, Blank JL, Bos JL (2002) A novel Epac-specific cAMP analogue demonstrates independent regulation of Rap1 and ERK. Nat Cell Biol 4(11):901-906.

Fernandes HB, Riordan S, Nomura T, Remmers CL, Kraniotis S, Marshall JJ, Kukreja L, Vassar R, Contractor A (2015) Epac2 mediates cAMP-dependent potentiation of neurotransmission in the hippocampus. J Neurosci 35:6544-6553.

Field GD, Sampath AP (2017) Behavioural and physiological limits to vision in mammals. Philos Trans R Soc Lond B Biol Sci 372(1717):20160072.

Firl A, Ke JB, Zhang L, Fuerst PG, Singer JH, Feller MB (2015) Elucidating the role of AII amacrine cells in glutamatergic retinal waves. J Neurosci. 35(4):1675-86.

Freed MA, Liang Z (2014) Synaptic noise is an information bottleneck in the inner retina. J Physiol 592(4):635-51.

Gandini MA, Sandoval A, González-Ramírez R, Mori Y, de Waard M, Felix R (2011) Functional coupling of Rab3-interacting molecule 1 (RIM1) and L-type Ca^{2+} channels in insulin release. J Biol Chem 286:15757-15765.

Gekel I, Neher E (2008) Application of EPAC activator enhances neurotransmitter release at excitatory central synapses. J Neurosci 28:7991-8002.

Gillis KD (2000) Admittance-based measurement of membrane capacitance using the EPC-9 patch-clamp amplifier. Pflugers Arch 439:655-664.

Gillis KD, Mossner R, Neher E (1996) Protein kinase C enhances exocytosis from chromaffin cells by increasing the size of the readily releasable pool of secretory granules. Neuron 16(6):1209-20.

Grabner CP, Zenisek D (2013) Amperometric resolution of a prespike stammer and evoked phases of fast release from retinal bipolar cells. J Neurosci. 33:8144-8158.

Grabner CP, Gandini MA, Rehak R, Le Y, Zamponi GW, Schmitz F (2015) RIM1/2 mediated facilitation of $Ca_v1.4$ channel opening is required for Ca^{2+}-stimulated release in mouse rod photoreceptors. J Neurosci 35:13133–13147.

Graydon CW, Lieberman EE, Rho N, Briggman KL, Singer JH, Diamond JS (2018) Synaptic transfer between rod and cone pathways mediated by AII amacrine cells in the mouse retina. Curr Biol 28:2739-2751.

Habermann CJ, O'Brien BJ, Wässle H, Protti DA (2003). AII amacrine cells express L-type calcium channels at their output synapses. J. Neurosci 23(17):6904-13.

Halls ML, Cooper DMF (2011) Regulation of Ca^{2+}-signaling pathways of adenylyl cyclases. Cold Spring Harb Perspect Biol 3:a004143.

Hampson EC, Vaney DI, Weiler R (1992) Dopaminergic modulation of gap junction permeability between amacrine cells in mammalian retina. J Neurosci 12:4911-4922.

Hartveit E, Veruki ML (2012) Electrical synapses between AII amacrine cells in the retina: Function and modulation. Brain Res 1487:160-172.

Hartveit, E., M.L. Veruki, and B.J. Zandt (2019) Capacitance measurement of dendritic exocytosis in an electrically coupled inhibitory retinal interneuron: an experimental and computational study. Physiol Rep 7(15): p. e14186.

Hatakeyama H, Takahashi N, Kishimoto T, Nemoto T, Kasai H (2007) Two cAMP-dependent pathways differentially regulate exocytosis of large dense-core and small vesicles in mouse beta-cells. J Physiol. 582(3):1087-98.

Heidelberger R, Matthews G (1994) Dopamine enhances Ca^{2+} responses in synaptic terminals of retinal bipolar neurons. Neuroreport 5:729-32.

Henquin JC, Nenquin M (2014) Activators of PKA and Epac distinctly influence insulin secretion and cytosolic Ca^{2+} in female mouse islets stimulated by glucose and tolbutamide. Endocrinology 155:3274-3287.

Hibino H, Pironkova R, Onwumere O, Vologodskaia M, Hudspeth AJ, Lesage F (2002) RIM binding proteins (RBPs) couple Rab3-interacting molecules (RIMs) to voltage-gated Ca^{2+} channels. Neuron 34:411-423.

Holz GG, Kang G, Harbeck M, Roe MW, Chepurny OG (2006) Cell physiology of cAMP sensor Epac. J Physiol 577:5-15.

Hormuzdi SG, Pais I, LeBeau FE, Towers SK, Rozov A, Buhl EH, Whittington MA, Monyer H (2001) Impaired electrical signaling disrupts gamma frequency oscillations in connexin 36-deficient mice. Neuron 31:487-495.

Jensen RJ (1989) Mechanism and site of action of a dopamine D1 antagonist in the rabbit retina. Vis Neurosci. 3:573-85

Kamiya H, Umeda K, Ozawa S, Manabe T (2002) Presynaptic Ca^{2+} entry is unchanged during hippocampal mossy fiber long-term potentiation. J Neurosci 22:10524-10528.

Kaneko M, Takahashi T (2004) Presynaptic mechanism underlying cAMP-dependent synaptic potentiation. J Neurosci 24:5202-5208.

Kang G, Chepurny OG, Rindler MJ, Collis L, Chepurny Z, Li WH, Harbeck M, Roe MW, Holz GG (2005) A cAMP and Ca^{2+} coincidence detector in support of Ca^{2+}-induced Ca^{2+} release in mouse pancreatic beta cells. J Physiol 566:173-188.

Kashima Y, Miki T, Shibasaki T, Ozaki N, Miyazaki M, Yano H, Seino S (2001) Critical role of cAMP-GEFII-Rim2 complex in incretin-potentiated insulin secretion. J Biol Chem 276:46046-46053.

Katsurabayashi S, Kubota H, Wang ZM, Rhee JS, Akaike N (2001) cAMP-dependent presynaptic regulation of spontaneous glycinergic IPSCs in mechanically dissociated rat spinal cord neurons. J Neurophysiol 85:332-340.

Kim MH, von Gersdorff H (2016) Postsynaptic plasticity triggered by Ca^{2+}-permeable AMPA receptor activation in retinal amacrine cells. Neuron 89:507-520

Komai AM, Brannmark C, Musovic S, Olofsson CS (2014) PKA-independent cAMP stimulation of white adipocyte exocytosis and adipokine secretion: modulations by Ca^{2+} and ATP. J Physiol 592:5169-5186.

Kothmann WW, Massey SC, O'Brien J (2009) Dopamine-stimulated dephosphorylation of connexin 36 mediates AII amacrine cell uncoupling. J Neurosci 29:14903-14911.

Krinner S, Butola T, Jung S, Wichmann C, Moser T (2017) RIM-Binding Protein 2 promotes a large number of $Ca_v1.3$ Ca^{2+}-channels and contributes to fast synaptic vesicle replenishment at hair cell active zones. Front Cell Neurosci 11:334.

Krizaj D (2005) Serca isoform expression in the mammalian retina. Exp Eye Res 81:690-699.

Kuhn SM, Nadler A (2020) Nanoscale signaling: messages across time and space. eLife 9:e63845.

Kushmerick C, von Gersdorff H (2003) Exo-endocytosis in at mossy fiber terminals: Toward capacitance measurements in cells with arbitrary geometry. Proc Nat Acad Sci. 100:507-520.

Lagnado L, Schmitz F. Ribbon Synapses and Visual Processing in the Retina. Annu Rev Vis Sci. 2015 Nov 24;1:235-262.

Li G-L, Vigh J, von Gersdorff H (2007) Short-term depression at the reciprocal synapses between a retinal bipolar cell terminal and amacrine cells. J Neurosci 27:7377-7385.

Liang Z, Freed MA (2012) Cross inhibition from ON to OFF pathway improves the efficiency of contrast encoding in the mammalian retina. J Neurophysiol 108:2679-88.

Lonart G, Janz R, Johnson KM, Sudhof TC (1998) Mechanism of action of rab3A in mossy fiber LTP. Neuron 21:1141-1150.

Majewski L, Kuznicki J (2015) SOCE in neurons: Signaling or just refilling? Biochim Biophys Acta 1853(9).

Marc RE, Anderson JR, Jones BW, Sigulinsky CL, Lauritzen JS (2014) The AII amacrine cell connectome: a dense network hub. Front Neural Circuits 8:104.

Martín R, García-Font N, Suárez-Pinilla AS, Bartolomé-Martín D, Ferrero JJ, Luján R, Torres M, Sánchez-Prieto J (2020) β-Adrenergic receptors/EPAC signaling increases the size of the readily releasable pool of synaptic vesicles required for parallel fiber LTP. J Neurosci 40:8604-8617.

Mazade RE, Flood MD, Eggers ED (2019) Dopamine D1 receptor activation reduces local inner retinal inhibition to light-adapted levels. J Neurophysiol 121:1232-1243.

Mazade RE, Eggers ED (2020) Inhibitory components of retinal bipolar cell receptive fields are differentially modulated by dopamine D1 receptors. Vis Neurosci 12;37:E01.

McLaughlin AJ, Percival KA, Gayet-Primo J, Puthussery T (2021) Glycinergic inhibition targets specific Off cone bipolar cells in primate retina. eNeuro 8:0432.

Midorikawa M, Sakaba T (2017) Kinetics of releasable synaptic vesicles and their plastic changes at hippocampal mossy fiber synapses. Neuron 96:1033-1040 e1033.

Muntean BS, Zucca S, MacMullen CM, Dao MT, Johnston C, Iwamoto H, Blakely RD, Davis RL, Martemyanov KA (2018) Interrogating the Spatiotemporal Landscape of Neuromodulatory GPCR Signaling by Real-Time Imaging of cAMP in Intact Neurons and Circuits. Cell Rep 22(1):255-268.

Neher E, Almers W (1986) Patch pipettes used for loading small cells with fluorescent indicator dyes. Adv Exp Med Biol 211:1-5.

Neher, E (1992) Correction for liquid junction potential in patch clamp experiments. Enzymol. 207:123.

Nanou E, Catterall WA (2018) Calcium channels, synaptic plasticity, and neuropsychiatric disease. Neuron. 98(3):466-481.

Oliva C, Cohen IS, Mathias RT (1988) Calculation of time constants for intracellular diffusion in whole cell patch clamp configuration. Biophys J 54:791-799.

Oltedal L, Hartveit E. Transient release kinetics of rod bipolar cells revealed by capacitance measurement of exocytosis from axon terminals in rat retinal slices. J Physiol. 2010 May 1;588(Pt 9):1469-87.

Ozaki N, Shibasaki T, Kashima Y, Miki T, Takahashi K, Ueno H, Sunaga Y, Yano H, Matsuura Y, Iwanaga T, Takai Y, Seino S (2000) cAMP-GEFII is a direct target of cAMP in regulated exocytosis. Nat Cell Biol 2:805-811.

Pereira L, Cheng H, Lao DH, Na L, van Oort RJ, Brown JH, Wehrens XH, Chen J, Bers DM (2013) Epac2 mediates cardiac β1-adrenergic-dependent sarcoplasmic reticulum Ca2+ leak and arrhythmia. Circulation 127(8):913-22.

Rabl K, Cadetti L, Thoreson WB (2006) Paired-pulse depression at photoreceptor synapses. J Neurosci 26:2555-2563.

Regehr WG, Tank DW (1991) The maintenance of LTP at hippocampal mossy fiber synapses is independent of sustained presynaptic calcium. Neuron 7:451-459.

Rich TC, Fagan KA, Tse TE, Schaack J, Cooper DMF, Karpen JW (2001) A uniform extracellular stimulus triggers distinct cAMP signals in different compartments of a simple cell. PNAS 98: 13049–13054.

Ritzau-Jost A, Delvendahl I, Rings A, Byczkowicz N, Harada H, Shigemoto R, Hirrlinger J, Eilers J, Hallermann S (2014) Ultrafast action potentials mediate kilohertz signaling at a central synapse. Neuron 84:152-163.

Rorsman P, Braun M, Zhang Q (2012) Regulation of calcium in pancreatic α- and β-cells in health and disease. Cell Calcium 51:300-308.

Roy S, Field GD (2019) Dopaminergic modulation of retinal processing from starlight to sunlight. J Pharmacol Sci. 140(1):86-93.

Sakaba T, Neher E (2001) Preferential potentiation of fast-releasing synaptic vesicles by cAMP at the calyx of Held. Proc Natl Acad Sci U S A 98:331-336.

Schoch S, Castillo PE, Jo T, Mukherjee K, Geppert M, Wang Y, Schmitz F, Malenka RC, Sudhof TC (2002) RIM1alpha forms a protein scaffold for regulating neurotransmitter release at the active zone. Nature 415:321-326.

Seino S, Shibasaki T (2005) PKA-dependent and PKA-independent pathways for cAMP-regulated exocytosis. Physiol Rev 85:1303-1342.

Sosa R, Hoffpauir B, Rankin ML, Bruch RC, Gleason EL (2002) Metabotropic glutamate receptor 5 and calcium signaling in retinal amacrine cells. J Neurochem 81:973-983.

Stellwagen D, Shatz CJ, Feller MB (1999) Dynamics of retinal waves are controlled by cyclic AMP. Neuron 24:673-685.

Ster J, De Bock F, Guérineau NC, Janossy A, Barrère-Lemaire S, Bos JL, Bockaert J, Fagni L (2007) Exchange protein activated by cAMP (Epac) mediates cAMP activation of p38 MAPK and modulation of Ca^{2+}-dependent K^{+} channels in cerebellar neurons. Proc Natl Acad Sci 104:2519-24.

Stožer A, Paradiž Leitgeb E, Pohorec V, Dolenšek J, Križančić Bombek L, Gosak M, Skelin Klemen M. (2021) The role of cAMP in beta cell stimulus-secretion and intercellular coupling. Cells 10:1658.

Strettoi E, Raviola E, Dacheux RF (1992) Synaptic connections of the narrow-field, bistratified rod amacrine cell (AII) in the rabbit retina. J Comp Neurol 325:152-168.

Strettoi E, Masri RA, Grunert U (2018) AII amacrine cells in the primate fovea contribute to photopic vision. Scientific Reports 8:16429.

Trudeau LE, Emery DG, Haydon PG (1996) Direct modulation of the secretory machinery underlies PKA-dependent synaptic facilitation in hippocampal neurons. Neuron 17:789-797.

Tzounopoulos T, Janz R, Sudhof TC, Nicoll RA, Malenka RC (1998) A role for cAMP in long-term depression at hippocampal mossy fiber synapses. Neuron 21:837-845.

Urschel S, Hoher T, Schubert T, Alev C, Sohl G, Worsdorfer P, Asahara T, Dermietzel R, Weiler R, Willecke K (2006) Protein kinase A-mediated phosphorylation of connexin36 in mouse retina results in decreased gap junctional communication between AII amacrine cells. J Biol Chem 281:33163-33171.

Vaden JH, Banumurthy G, Gusarevich ES, Overstreet-Wadiche L, Wadiche JI (2019) The readily-releasable pool dynamically regulates multivesicular release. Elife 31;8:e47434.

Vaney DI, Gynther IC, Young HC (1991) Rod-signal interneurons in the rabbit retina: 2. AII amacrine cells. J Comp Neurol. 310:154-169.

Vardi N, Smith RG (1996) The AII amacrine network: coupling can increase correlated activity. Vision Res 36:3743-3757.

Veruki ML, Wässle H (1996) Immunohistochemical localization of dopamine D1 receptors in rat retina. Eur J Neurosci 8:2286-2297.

Veruki ML, Oltedal L, Hartveit E (2010) Electrical coupling and passive membrane properties of AII amacrine cells. J Neurophysiol 103:1456-1466.

Vickers E, Kim MH, Vigh J, von Gersdorff H (2012) Paired-pulse plasticity in the strength and latency of light-evoked lateral inhibition to retinal bipolar cell terminals. J Neurosci 32:11688-11699.

Vigh J, Lasater EM (2003) Intracellular calcium release resulting from mGluR1 receptor activation modulates GABAA currents in wide-field retinal amacrine cells: a study with caffeine. Eur J Neurosci 17:2237-2248.

Vincent P, Gervasi N, Zhang J (2008) Real-time monitoring of cyclic nucleotide signaling in neurons using genetically encoded FRET probes. Brain Cell Biol 36:3-17.

Voigt T, Wässle H (1987) Dopaminergic innervation of AII amacrine cells in mammalian retina. J Neurosci 7:4115-4128.

von Gersdorff H, Matthews G (1996) Calcium-dependent inactivation of calcium current in synaptic terminals of retinal bipolar neurons. J Neurosci 16:115-122.

Warrier A, Borges S, Dalcino D, Walters C, Wilson M (2005) Calcium from internal stores triggers GABA release from retinal amacrine cells. J Neurophysiol 94:4196-4208.

Wässle H (2004) Parallel processing in the mammalian retina. Nat Rev Neurosci 5:747-757.

Wässle H, Heinze L, Ivanova E, Majumdar S, Weiss J, Harvey RJ, Haverkamp S (2009) Glycinergic transmission in the mammalian retina. Front Mol Neurosci 2:6.

Williams CL, Smith SM (2018) Calcium dependence of spontaneous neurotransmitter release. J Neurosci Res 96(3):335-347.

Witkovsky P, Svenningsson P, Yan L, Bateup H, Silver R (2007) Cellular localization and function of DARPP-32 in the rodent retina. Eur J Neurosci 25:3233-3242.

Yang Y, Calakos N (2011) Munc13-1 is required for presynaptic long-term potentiation. J Neurosci 31:12053-12057.

Yao L, Sakaba T (2010) cAMP modulates intracellular Ca^{2+} sensitivity of fast-releasing synaptic vesicles at the calyx of Held synapse. J Neurophysiol 104:3250-3260.

Zandt BJ, Veruki ML, Hartveit E (2018) Electrotonic signal processing in AII amacrine cells: compartmental models and passive membrane properties for a gap junction-coupled retinal neuron. Brain Struct Funct 223:3383-3410.

Zhong N, Beaumont V, Zucker RS. (2004) Calcium influx through HCN channels does not contribute to cAMP-enhanced transmission. J Neurophysiol. 92(1):644-7.

Zhong N, Zucker RS (2005) cAMP acts on exchange protein activated by cAMP/cAMP-regulated guanine nucleotide exchange protein to regulate transmitter release at the crayfish neuromuscular junction. J Neurosci 25:208-214.

Chapter 3: Fast endocytosis at an inhibitory synapse is triggered by a Ca^{2+}-sensor tightly coupled to Ca^{2+} channels

Marc A. Meadows[1] and Henrique von Gersdorff[1,2,3]

[1] The Vollum Institute, Oregon Health & Science University, Portland, OR 97239, USA.

[2] Casey Eye Institute, Dep. of Ophthalmology, Oregon Health & Science University, Portland, OR 97239

[3] Dep. of Chemical Physiology and Biochemistry, Oregon Health & Science University, Portland, OR 97239

Author Contributions: M.A.M. and H.v.G. designed the studies; M.A.M performed experiments; M.A.M. and H.v.G. wrote the paper.

Manuscript in preparation for Neuron.

Section 3.1: Summary

Fast and slow endocytosis depend on stimulus strength at excitatory nerve terminals. However, the kinetics of endocytosis remains largely unknown at inhibitory synapses. Here we show membrane C_m measurements from living synaptic terminals of glycinergic amacrine cells embedded in adult rat retina. We find that fast compensatory endocytosis is triggered after short depolarizing pulses. This occurs even in the presence of strong but slow Ca^{2+} buffers (10 mM EGTA). Conversely, weaker but faster Ca^{2+} buffering with 1 mM BAPTA fully blocked fast endocytosis, while only partially reducing exocytosis. Increasing stimulus pulse duration slowed the kinetics of endocytosis, suggesting that a reduced availability of endocytotic proteins causes endocytosis to slow down, as stronger stimuli increase the exocytotic load. Endocytosis was dependent on GTP, dynamin and actin polymerization. Our findings suggest that a readily retrievable pool of plasma membrane is tightly coupled to Ca^{2+} channels, because it is EGTA-insensitive, but highly BAPTA-sensitive.

Section 3.2: Introduction

Nerve terminals release neurotransmitter at presynaptic active zones through the Ca^{2+}-dependent fusion (exocytosis) of synaptic vesicles to communicate to the postsynaptic cell. Synaptic vesicle endocytosis is a crucial component of synaptic transmission that recycles vesicle membrane after exocytosis. Endocytosis of the plasma membrane presumably helps to clear and recover the active zones for reuse after exocytosis by retrieving excess membrane and recycling synaptic proteins. It is thus a compensatory process that maintains nerve terminal surface area and perhaps helps to set an optimal membrane tension for exocytosis. Endocytosis is also thought to be critical for maintaining the readily releasable pool of synaptic vesicles after strong or continuous stimulation (Pyle et al., 2000). This may be especially critical for fast spiking inhibitory interneurons. However, little is known about the kinetics of endocytosis at inhibitory nerve terminals.

The AII amacrine cell (AII-AC), is an interneuron in the mammalian retina that releases glycine from its proximal dendritic lobular appendages. Electron microscopy (EM) studies have shown that the lobules contain large conventional active zones that provide tonic and graded levels of inhibition to OFF-cone bipolar cell terminals (Strettoi et al., 1992). The AII-AC lobules thus function as large inhibitory synaptic terminals with a large reserve pool of vesicles that can be measured using time-resolved C_m measurements of exocytosis (Balakrishnan et al., 2015; Hartveit et al., 2020; Meadows et al., 2021). The large vesicle pool allows AII-ACs to provide tonic release in response to strong stimulation for long durations. Tonic synaptic transmission was thought to be a feature at specialized ribbon synapses (von Gersdorff and Matthews, 1994; Jackman et al., 2008); although evidence shows that conventional synapses can have large vesicle pools suited for long-durations of synaptic transmission. Depletion of these pools with strong stimulation can lead to synaptic depression. Faithful neurotransmission requires replenishment of vesicles and trafficking them to active zones, although there is a diverse repertoire of molecular machinery across synapses (Hallermann and Silver, 2013). Endocytosis is an important step in vesicle recycling because it clears and reforms fully fused vesicles, which can then replenish vesicle pools (Smith et al., 2007). We propose that EM data from Strettoi et al., (1992)

provides evidence of clathrin-mediated endocytosis in AII-ACs. The underlying mechanisms of endocytosis at this synapse are however unknown.

Here we use time-resolved membrane capacitance (C_m) measurements to directly measure the kinetics of endocytosis in AII-AC inhibitory synapses. C_m measurements from excitatory CNS nerve terminals reveal that endocytosis can occur within tens of milliseconds after exocytosis and proceeds with variable kinetics depending on stimulus strength and duration. Several studies have distinguished at least two modes of endocytosis: a fast mode operates on a timescale of tens to hundreds of milliseconds (time constant of 0.3 - 2 sec) while a slow mode is tens of seconds (Smith et al., 2007; Hallermann and Silver 2013). There is evidence that the fast mode is clathrin-independent and the slow mode is clathrin-dependent (Jockusch et al 2005). Both modes of endocytosis seem to require both dynamin and actin polymerization (Delvendahl et al., 2016). Fast and slow endocytosis have been observed at retinal bipolar cell synaptic terminals, photoreceptors, and inner hair cells in response to short and long depolarizing pulses (reviewed in Moser et al., 2020). A fast (or ultrafast) mode of endocytosis has been observed at invertebrate (*C. Elegans*) nerve terminals (Watanabe et al., 2013) small hippocampal synaptic boutons (Watanabe et al., 2013b) and large mossy fiber boutons (Delvendahl et al., 2016) in response to single action potential stimulation. Our study presents data that AII-ACs have a fast mode of endocytosis that is dependent on clathrin, actin and dynamin. The endocytosis rate slows down with increased stimulus duration, as observed in bipolar cell terminals and photoreceptors (Cork and Thoreson, 2014).

The influence of Ca^{2+} on endocytosis has been debated since it was first discovered that it slows down with increased [Ca^{2+}] influx in bipolar cells (von Gersdorff and Matthews, 1994b). The effects of Ca^{2+} on endocytosis may differ across different synapses and may depend strongly on experimental conditions (e.g. temperature, pH and developmental stage). Furthermore, the exocytosis load after Ca^{2+} entry (or the amount of multivesicular release) may affect the subsequent endocytosis rate (Cork and Thoreson, 2014). The use of Ca^{2+} buffers with different binding kinetics shows that strong internal Ca^{2+} buffering slows endocytosis, yet this changes with development (Yamashita et al., 2010; reviewed in Yamashita, 2012). From our C_m measurements,

we found that fast endocytosis is robust and stable in adult AII-ACs from 3 to 12 month old rat retina, but washes out quickly during whole-cell recordings in younger AII-ACs that are 20 to 35 days old. In adult AII-ACs we find that the size of the fast exocytosis pool of synaptic vesicles is not changed in 2 or 10 mM internal EGTA, but is reduced by 30% in 1 mM BAPTA. A fast exocytosis sub-pool of docked vesicles thus lies within a few tens of nanometers from Ca^{2+} channels, where it remains insensitive to 1 mM BAPTA. After exocytosis the kinetics of endocytosis is also not changed from 2 to 10 mM EGTA. However, endocytosis is completely blocked by 1 mM BAPTA. Endocytosis thus has a Ca^{2+} sensor that triggers the fast internalization of a readily retrievable portion of the plasma membrane. This Ca^{2+} sensor for endocytosis is tightly coupled to Ca^{2+} channels, because it is insensitive to 10 mM EGTA. However, it lies further then tens of nanometers because it is blocked by 1 mM BAPTA. Synaptic vesicles at active zones for exocytosis may thus be docked within tens of nanometers from Ca^{2+} channel clusters, whereas hot spots of endocytosis on the plasma membrane may lie on average further away from Ca^{2+} channel clusters in a "peri-active zone" specialized for membrane retrieval. We thus propose that active zones of exocytosis are separated from hot spots of endocytosis by several tens of nanometers, although both exo- and endocytosis are triggered by high Ca^{2+} elevations.

Section 3.3: Results

3.3.1 The rates of endocytosis depend on pulse duration in AII-ACs

3.3.1.a RRP and vesicle release rate in AII-ACs from brown Norway adult rats

To study net changes in the surface area of living cells we performed time-resolved membrane C_m measurements (Lindau and Neher, 1998). Whole-cell voltage-clamp recordings were performed in adult rat AII-ACs using a pipette solution containing a Cs-based internal solution with our standard of 2 mM EGTA. Shown in Figure 3.1 is a schematic of the crossover inhibition network and an example of an AII-AC filled with Alexa 594 during whole-cell recording (Fig. 3.1 A,B). We used the "sine + DC'' method (Gillis et al., 2000) by giving a 2 kHz sinusoidal voltage command superimposed on a holding potential (V_h = -80mV) to measure the passive membrane properties (C_m, R_m, and R_s; Fig. 3.1C-F). We gave a depolarizing pulse (-10 mV) between two sine waves to activate L-type Ca^{2+} channels (Fig. 3.1E), seen after offline p/10 leak subtraction.

Figure[3.1]

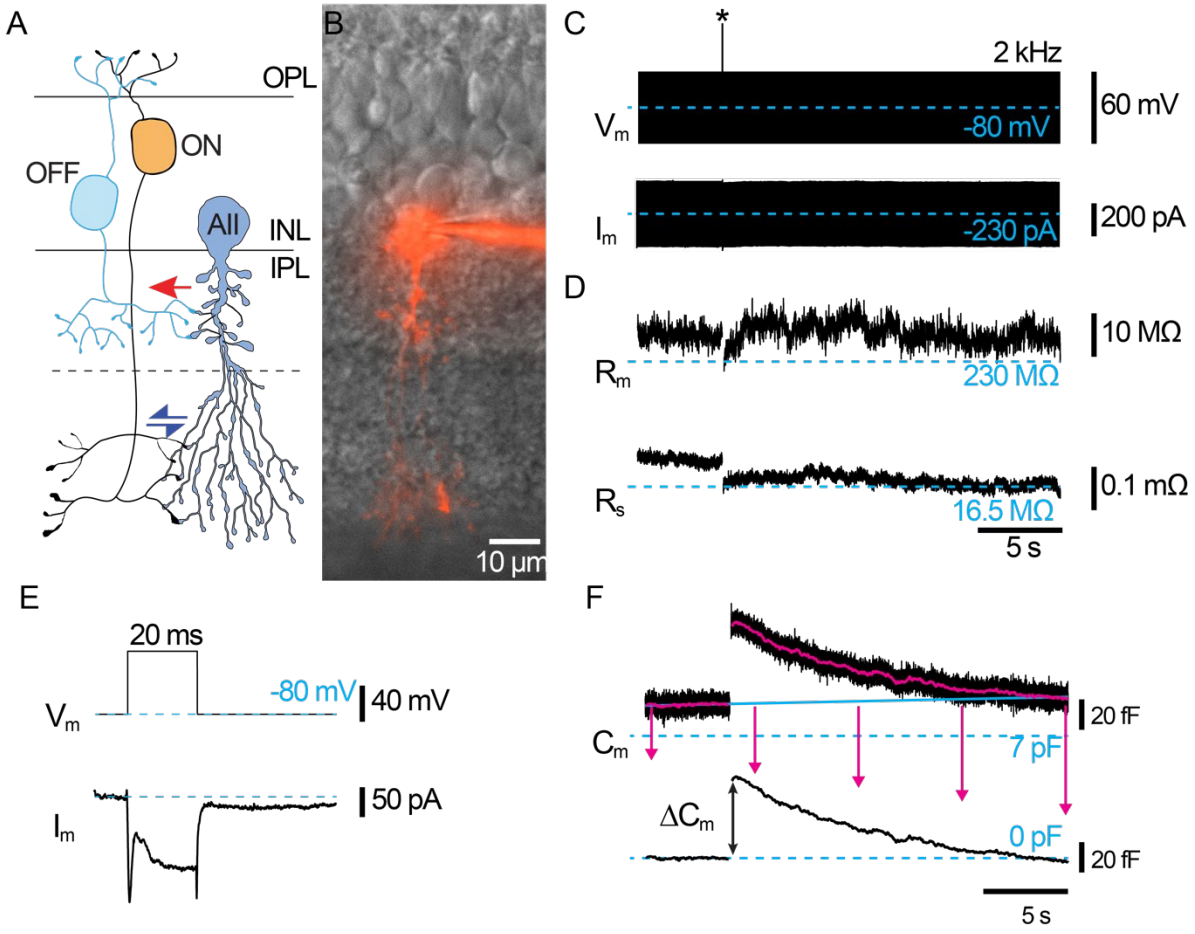

[3.1] Whole-cell C_m measurements of exo and endocytosis in AII-ACs from mature brown Norway rats.

A, Schematic of the retina crossover inhibition circuit. Shown are excitatory signals (blue arrows) passed through gap junctions between AII-ACs and ON-CBCs. AII-ACs convert excitatory signals into glycinergic inhibition (red arrow) to the OFF-CBC. Not shown are glutamatergic inputs to the AII-AC from rod BCs, which also contributes to crossover inhibition in scotopic conditions. Layers of the retina are labeled: outer plexiform layer (OPL), inner nuclear layer (INL) and inner plexiform layer (IPL). ***B,*** Micrograph showing an epifluorescence image of an AII-AC filled with Alexa 549 on a DIC overlay, taken after whole-cell patch-clamp recording. ***C,*** Example whole-cell voltage-clamp recording showing to sinusoidal voltage command (2 kHz; 30 mV peak-to-peak) superimposed on a -80 mV holding potential. Separating the two sine waves is a step depolarizing pulse indicated by and asterisk (-10 mV; 20 ms), which is shown in E with an expanded time scale. Bottom trace is the current response, also shown is an expansion of the depolarizing pulse and Ca^{2+} current response (***E***). ***D,*** Example traces of R_m and R_s. ***F,*** Example traces of C_m before (black) and after filtering (red; see materials and methods). Continuous blue line represents linear fit to the C_m baseline, used for correcting baseline drift. Bottom trace is the corrected C_m response. The change in C_m after the depolarizing pulse (ΔC_m) correlating to net vesicle exocytosis.

In the example shown in Figure 3.1, we gave a 20 ms depolarizing pulse that produced a 40 fF jump with no correlative change in the R_m. We do notice that there is an inverse change in the R_s after depolarization, which is expected of a multicompartmental model where release is close to the recording site (Hallermann et al., 2003). We often observed drift in the C_m baseline, which is possibly caused by membrane disruptions from whole-cell break-in (Hull and von Gersdorff, 2004). In addition to digitally filtering C_m responses, we corrected the baseline by subtracting a linear fit (Fig. 3.1 F).

Our previous study determined that the whole-cell dialysis of an AII-AC occur within about 3 to 4 minutes (Meadows et al., 2021); therefore, we waited until 4 min after whole-cell break-in to begin recording. We did not observe rundown of exocytosis in BN rats, unlike our recordings in C57 (Fig. S3.1), therefore were able to record and average multiple responses for each pulse duration (4 to 5 traces), for several minutes after break-in.

3.3.1b Sinusoidal frequency does not drastically affect C_m measurements of exocytosis

AII-AC active zones are located in densely packed lobules branching off a main apical dendrite. The thin necks connecting the lobules may filter the high frequency sine wave stimulation. We measured C_m responses using sinusoidal waves ranging from 300 Hz to 2000 Hz, and found no change in ΔC_m (Fig. S3.2A). We did find that that increasing the sine frequency reduced the baseline C_m (Fig. S3.2B). Increasing the sinusoidal frequency reduces the overall measured surface area, indicating that distal processes filter high frequency stimulation—also observed in other studies (Balakrishnan et al., 2015). Although our results would indicate that vesicle release is relatively close to the soma, and accurate C_m measurements can be obtained with a 2 kHz sinewave, recent models show that the thin lobule necks could lead to a 10 - 20% underestimation of the net exocytosis with high frequency recording (Hartveit et al., 2019). Furthermore, a recent study indicates that AII-ACs release glycine from their distal dendritic processes to OFF-GC somas and ON-GC dendrites (Grimes et al., 2021), which we are inadvertently excluding from our measurements.

3.3.1c Rat AII-ACs exhibit a large readily releasable vesicle pool

Figure[3.2]

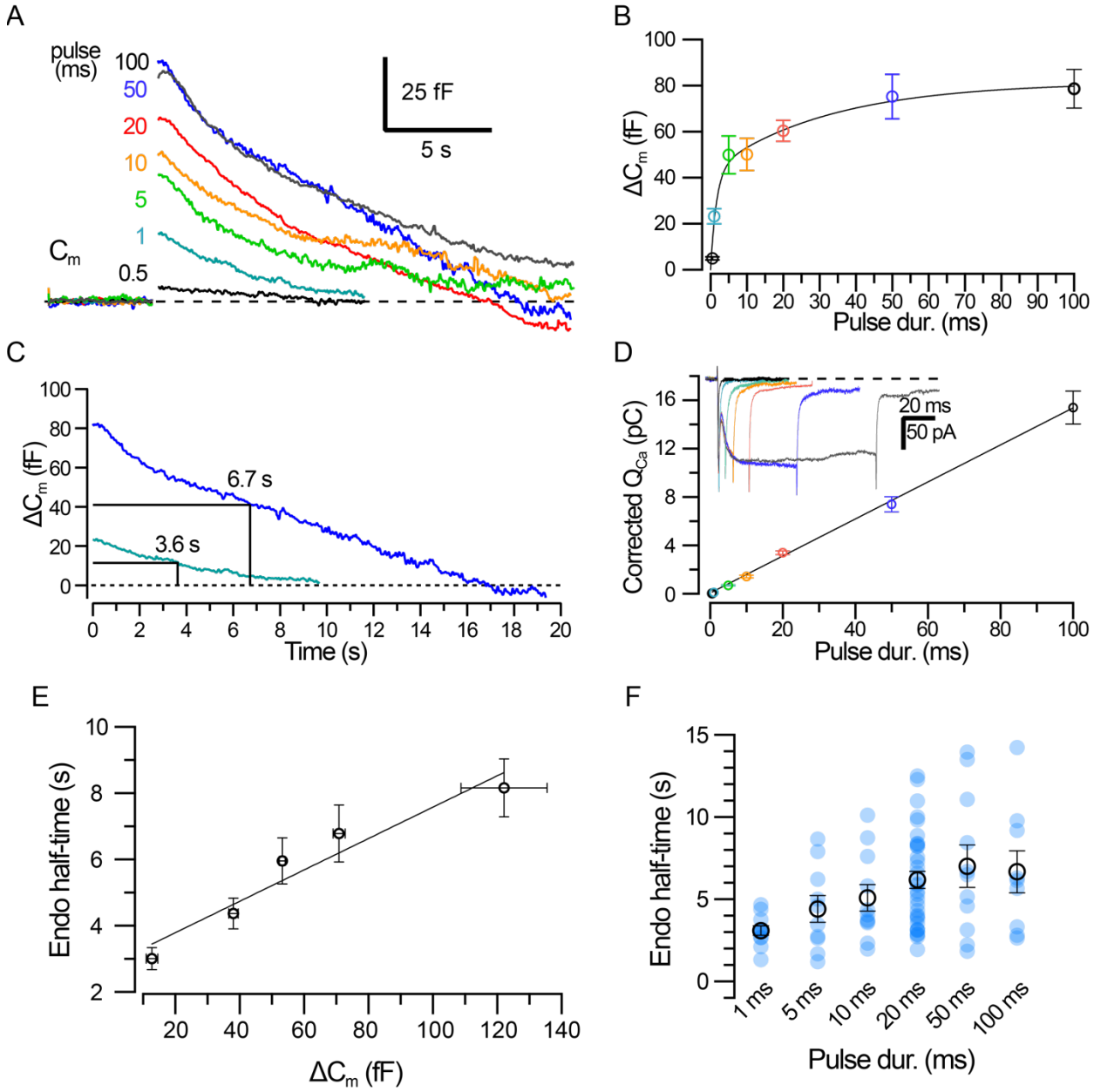

[3.2] Whole-cell C_m measurements of exo- and endocytosis in rat AII-AC inhibitory synapses.

A, Grand average C_m responses to incremental square pulse durations (labeled on graph in ms) with a 2 mM EGTA internal solution at 33 °C. ***B,*** ΔC_m plotted against pulse duration. Notice that ΔC_m initially plateaus at 10 ms, indicating a fast readily releasable pool. The solid line represents a biexponential fit (R^2 = 0.4487) with time constants of 1.62 s (τ_1; 52%) and 32.5 s (τ_2). ***C,*** Average normalized C_m responses for 1 ms and 50 ms with labeled endocytosis half-times. ***D,*** Corrected charge transfer for Ca^{2+} current (I_{Ca}; inset) plotted against pulse duration. Solid line represents a linear fit to data (R^2 = 0.8907; slope = 0.154 pC/s). ***E,*** Endocytosis half-time plotted against ΔC_m responses. Data comprises 100 responses to varying pulse durations (0.5 to 300 ms), were ordered by ΔC_m

size, and plotted as bins of 20 values. Solid line represents linear fit to data (R^2 = 0.9279; slope = 0.0076 s/fF). ***F,*** Summary plot of endocytosis half-times for each pulse duration. Notice how endocytosis is faster with longer pulse durations. Closed circles represent values from individual cells and open circles with error bars denote mean ± SEM. Statistical significance in panel was determined with a one-way ANOVA test and *post hoc* Tukey's test.

We measured ΔC_m responses using different pulse durations ranging from 0.5 ms to 100 ms (Fig. 3.2A). Estimations of the vesicle pool size were made by plotting the ΔC_m response against pulse duration (Fig 3.2B). The ΔC_m responses saturate around 10 to 20 ms, which indicates that the fast readily releasable pool (RRP) of vesicles is depleting. A secondary vesicle pool is uncovered with longer pulse durations of 50-100 ms as ΔC_m continues to increase. Initial and secondary RRP have been observed in mouse AII-ACs (Balakrishnan et al., 2015; Meadows et al., 2021). Our estimates in adult rats showed a larger initial RRP (57.6 fF), estimated by averaging the values from 5-20 ms. The initial release rate was (35.6 fF/s), determined by dividing the pool size by the fast time constant (τ_1 = 1.62 ms), which accounted for 52% of the total amplitude of the RRP. The secondary pool size was 76.8 fF with a release rate of 2.36 fF/s, which had a much slower time constant (32.5 ms). Notice that this estimation only includes responses up to 100 ms, and longer pulse durations may be needed for more accurate estimations.

3.3.2 Endocytosis Increases with larger capacitance jumps

Comparisons for the endocytosis rate were made by normalizing C_m responses for each pulse duration. We chose the endocytosis half-time as a measure of endocytosis because the decay of the C_m responses had both linear and/or exponential components. The endocytosis half-time was simply the duration for the C_m response to decay by 50%. Comparisons of the 1 ms and 50 ms responses shows that longer pulse durations had slower endocytosis (Fig. 3.2C). L-type Ca^{2+} currents are shown, along with plots of the Q_{Ca} (Fig. 3.2D) that was corrected by subtracting the unblocked $K_{Ca}1.1$ (BK) current (see materials and methods; Fig. S3.3). We plotted the endocytosis half-time against the ΔC_m response to demonstrate that the endocytosis rate was affected by the exocytosis load (Fig. 3.2E). We found a positive correlation between the two variables (R^2 = 0.9279; p =.008; Pearson), suggesting that endocytosis is slowed down by large levels of exocytosis. We also showed this by comparing the endocytosis half-time for different pulse durations (Fig. 3.2F). Graded levels of release are regulated by L-type Ca^{2+} currents that are non-

inactivating (Fig. 3.2D). Therefore, it is difficult to discern if increasing the pulse duration causes the endocytotic machinery to be slowed down by the mass action vesicle fusion, inhibition by Ca^{2+}, or both (Cork and Thoreson, 2014).

We recorded L-type Ca^{2+} currents ($I_{Ca,}$ for each pulse duration (Fig. 3.1D). We found a notch in the I_{Ca} responses (I_{notch}), which was not previously observed in mouse AII-ACs (Balakrishnan et al., 2015; Meadows et al., 2021). This would be the first evidence that AII-ACS have BK channels, although reports show that BK channels regulate reciprocal feedback from A17 amacrine cells to RBCs regulating low mesopic vision (Grimes et al., 2009; Tanimoto et al., 2012). We found that I_{notch} was eliminated with 100 nM Iberiotoxin (Fig. S3.3), indicating that I_{notch} is produced by a $K_{Ca1.1}$ (BK) current. The total charge transfer composed currents from L-type Ca^{2+} and BK channels; therefore we corrected Q_{ca} for the contaminating BK current charge ($Q_{Ca} = |Q_{total}| - |Q_{notch}|$). The mean corrected Q_{Ca} was plotted against pulse duration (Fig. 3.1D). It had a linear relationship with pulse duration ($R^2 = 0.8907$; slope = 0.154 pC/s).

3.3.3 Developmental changes in endocytosis at AII-AC synapses

We performed whole-cell voltage-clamp recordings in young (p21-25; n = 12) and adult (5-13 mo; n = 27) brown Norway rats using our control internal solution with 2 mM EGTA. To demonstrate how robust whole-cell C_m recordings are in adult rats we recorded C_m responses to a 20 ms depolarizing pulse each minute after break-in for up to 30 min (Fig. 3.3A). resulting in a 2-fold higher synaptic exocytosis efficiency (young: 11.32 ± 1.256 fF/pC, and mature: 21.59 ± 2.308 fF/pC; $p < 0.0001$; Mann-Whitney; Fig. 3.3E). Unlike young rats, the endocytosis in adult rats did not rundown. We observed some variability in endocytosis from trace to trace with some traces exhibiting an overshoot in adult rats, especially right after break-in. Prominent rundown was observed in young rats and endocytosis was absent after 25 minutes from break-in. Grand average traces of C_m responses show that exocytosis was smaller in younger rats with reduced endocytosis (Fig. 3.3B), while I_{Ca} responses still had BK currents. Summary plots show that ΔC_m was 2-fold larger in adult AII-ACs (young: 29.06 ± 3.13 fF, and mature: 62.0 ± 5.33 fF; $p < 0.0001$; Mann-Whitney; Fig. 3.3C). There was no significant difference in the Q_{Ca} (young: 2.65 ± 0.20 pC and mature: 2.99 ± 0.13 pC; Student's t-test).

Figure[3.3]

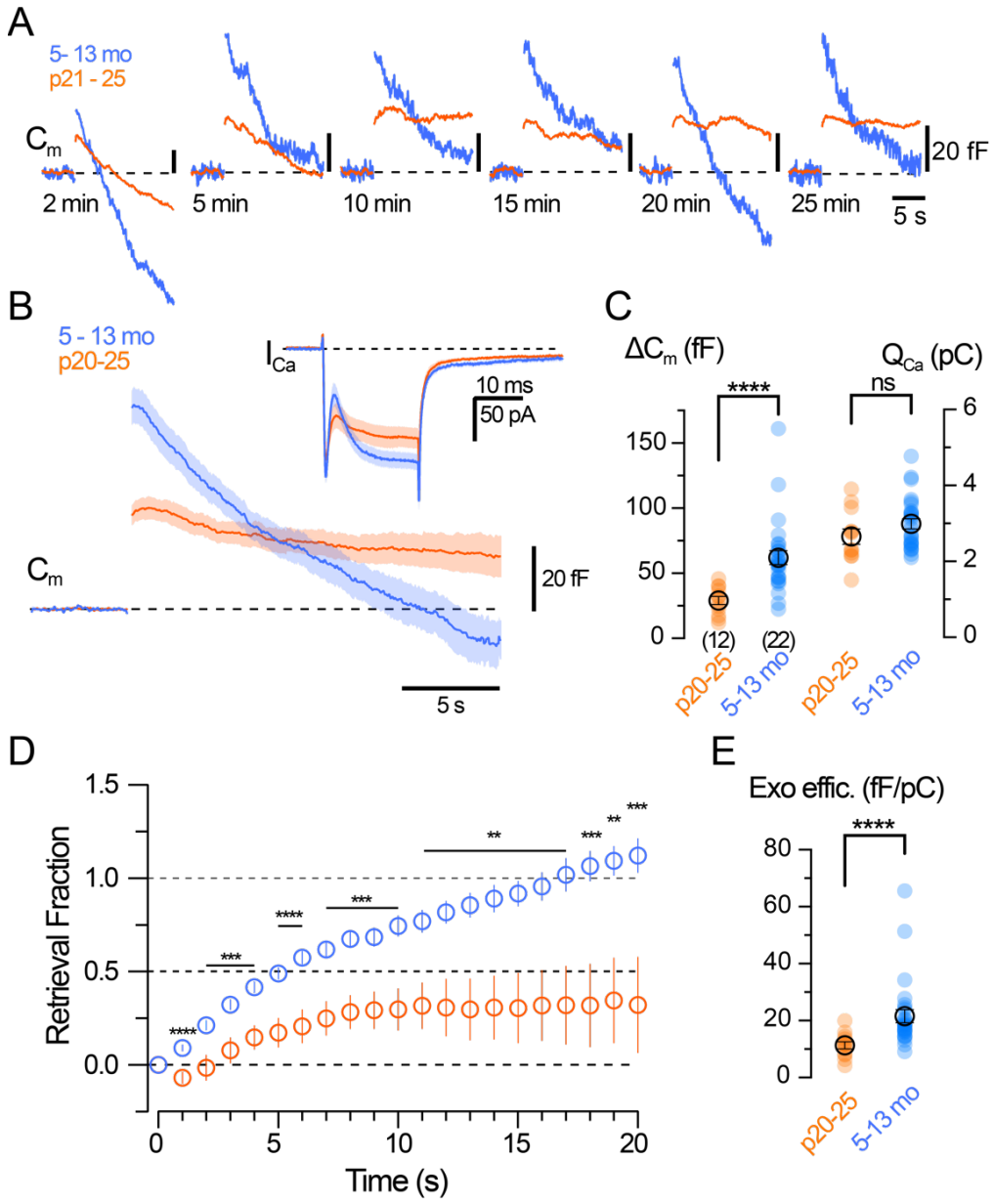

[3.3] Maturation of AII-AC synapses increases exocytosis and stabilizes endocytosis.

A, Example C_m responses from young (orange) and old (blue) AII-ACs. C_m was recorded for 5 s before giving a 20 ms depolarizing pulse, and C_m responses were recorded for 20 s following jump (ΔC_m). ***B,*** Grand average C_m responses to a 20 ms depolarizing pulse for young and old AII-ACs and corresponding Ca^{2+} current (I_{Ca}; inset). Grand averages were made from individual cell averages comprising C_m responses between 4 and 30 mins. ***C,*** Summary plots for ΔC_m (left) and corrected I_{Ca} charge transfer (Q_{Ca}; right). Closed circles represent values from individual AII-ACs for young (orange; n=12) and old (blue; n=22) datasets. ***D,*** Retrieval fraction against time after the initial ΔC_m response (t = 0) for each dataset. Notice how the RF for younger animals only partially recovers. ***E,*** Histogram comparing synaptic efficiency (ΔC_m / Q_{Ca}). Notice how adult animals have higher synaptic efficiency. Open circles with error bars depict mean ± SEM. Statistical comparisons were made using a student's t test.

Endocytosis was also analyzed by measuring the retrieval fraction (RF) for each dataset (Fig. 3.3D), which measures the proportion of membrane recovery after the initial ΔC_m response, determined by the following equation:

$$RF = 1 - \frac{C_x}{\Delta C_m}$$

Where C_x represents the C_m measurements after ΔC_m (initial ΔC_m response). Endocytosis was faster for the mature dataset ($t_{1/2} \approx 5$ s) compared to the young dataset ($RF_{t = 5\ s}$; young: 0.17 ± 0.08, and mature: 0.50 ± 0.03; $p < 0.0001$; Student's t-test), whereas the RF in young rats plateaued at only 25% recovery by 8 seconds. It appears that endocytosis is faster in older animals. This could be due to an increase in endocytotic machinery or a resistance to rundown during whole-cell dialysis. Several developmental changes in neonatal AII-ACs occur after eye-opening, where L-type Ca^{2+} channels sequester in lobules as synapses mature (Balakrishnan et al., 2015). Our results suggest further late refinement occurs after P21-25 into adulthood causing synaptic vesicle pools to increase and to become more tightly coupled with L-type Ca^{2+} channels

3.3.4 Ca^{2+} buffers can strongly influence AII-AC endocytosis

3.3.4a EGTA [10 mM] does not affect exo- and endocytosis

The Ca^{2+} dependency for endocytosis has been studied in several excitatory synapses, although mechanisms differ and remain controversial. We next tested how changing Ca^{2+} buffer strength, concentration, and type (EGTA vs. BAPTA) affected endocytosis for inhibitory AII-AC synapses. We first tested different concentrations of EGTA ranging from 0.2 mM to 10 mM (Fig. 3.1,S3.4). Average C_m responses to different depolarizing pulse durations from 0.5 ms to 20 ms are shown from recordings with a 10 mM EGTA solution (Fig. 3.4A). We still observed graded levels of release and even short depolarizations (0.5 ms and 1 ms) still produced a clear C_m jump with the higher 10 mM EGTA internal. The ΔC_m response was plotted against pulse duration for 10 mM and 2 mM EGTA datasets, which were not significantly different (Fig. 3.4B). There were no differences in the initial RRP size (2 mM: 60.50 ± 4.82 fF, and 10 mM: 62.82 ± 8.79 fF; $p = 0.8014$; Student's t-test) and single exponential function fits had similar time constants (2 mM: $\tau = 3.51$ s, and 10 mM: $\tau = 3.34$ s). Example traces for C_m responses to a 20 ms depolarizing pulse are

Figure[3.4]

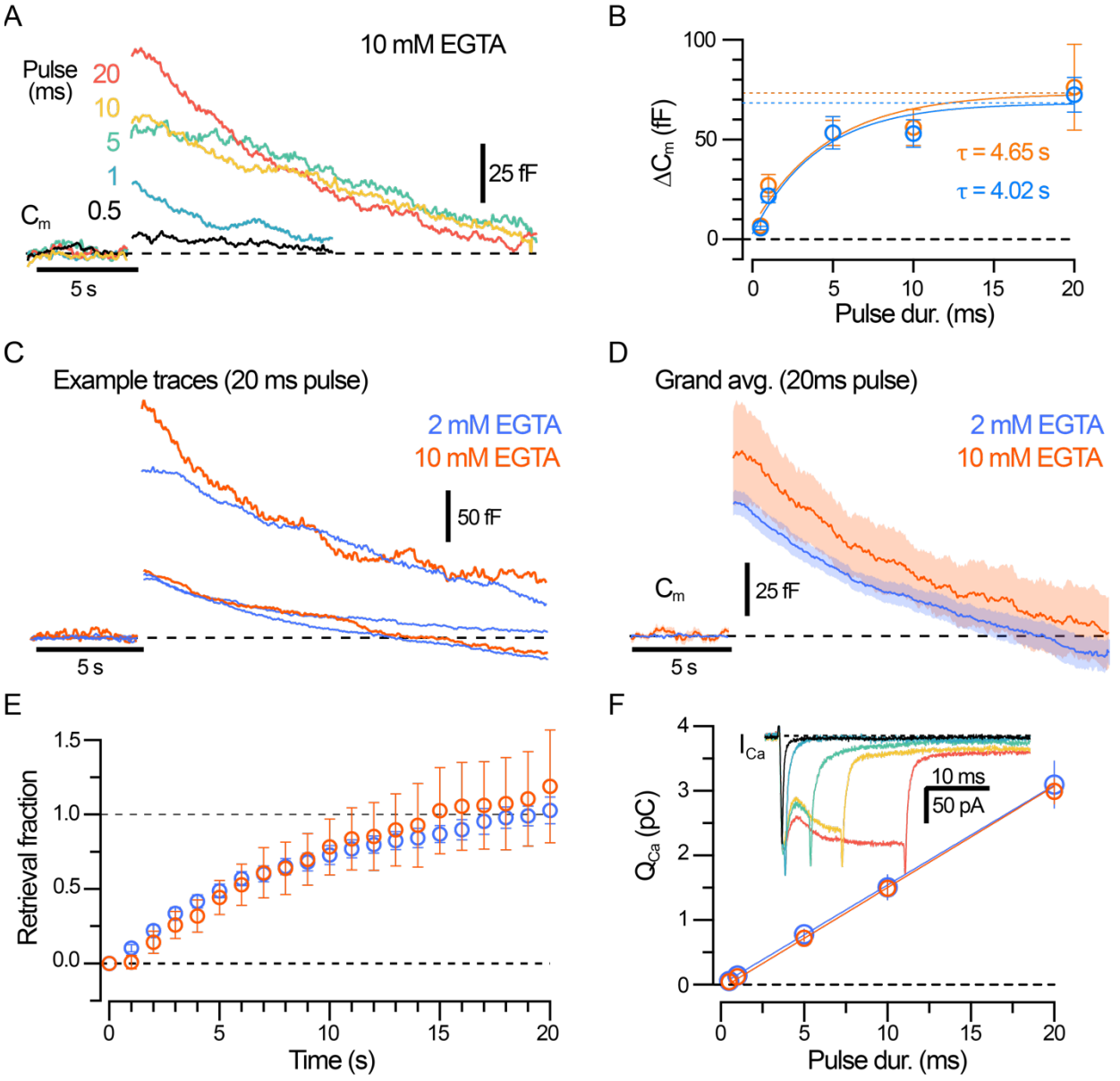

[3.4] Endocytosis in AII-ACs is independent of microdomain Ca^{2+}.

A, Grand average C_m responses to incremental square pulse durations (labeled on graph in ms). Recordings performed in AII-ACs from mature BN rats with a 10 mM EGTA internal solution @ 33 °C. ***B,*** ΔC_m plotted against pulse duration for recordings using 2 mM (blue; n = 13) and 10 mM (orange; n = 6) EGTA. Solid lines represent single exponential functions fitted for 2 mM (τ = 3.51 s; R^2 = 0.5230) and 10 mM (τ = 3.34 s; R^2 = 0.3904). ***C,*** Example traces of C_m responses to a 20 ms depolarizing pulse for recordings with 2 mM (blue) and 10 mM (orange) EGTA. Shown are examples with a small (top) and large (bottom) ΔC_m responses (top) and notice that some responses have an overshoot. ***D,*** Grand average C_m responses to a 20 ms depolarizing pulse. Solid line with shaded region denotes mean ± SEM. Grand averages were made from individual cell averages comprising C_m responses from individual AII-ACs recordings from 4 and 30 min after break-in, performed at 33 °C. ***E,*** Membrane retrieval

fraction plotted for C_m response to a 20 ms pulse as a function of time, starting at the initial ΔC_m response (t = 0). Notice how both datasets fully retrieve membrane (RF = 1: dashed line) at the same rate. ***F,*** Corrected charge transfer ($Q_{Ca,}$ for Ca^{2+} current (I_{Ca}: inset) plotted against pulse duration. Continuous line represents linear fits for 2 mM (slope =0.154; R^2 = 0.9030) and 10 mM (slope = 0.155; R^2 = 0.8496) datasets. Open circles and error bars represent mean ± SEM. Statistical comparisons were made using Student's t-tests and were not significant.

shown for recordings with 2 mM and 10 mM EGTA to illustrate the heterogeneity among AII-ACs (Fig. 3.4C). While a majority of the C_m responses produce jump sizes of ~50 to 60 fF, some responses were much larger ~100 to 200 fF. An endocytosis overshoot was also observed in some AII-ACs. Similarities between 2 mM and 10 mM EGTA can also be seen in the grand average traces (Fig. 3.4D). We observed no changes in the retrieval fraction in relation to EGTA concentration (Fig. 3.4E). We further tested a range of EGTA concentrations from 0.2 mM to 10 mM and found no changes to the RRP or endocytosis in normalized traces (Fig. S3.4). Furthermore, I_{Ca} and Q_{Ca} were not impacted by the change in EGTA concentration (Fig. 3.4F). Importantly, C_m recordings measure the net changes in cellular surface area and membrane dynamics, including putative asynchronous release caused by residual Ca^{2+} after a depolarizing pulse. A higher concentration of EGTA (10 mM vs 2 mM) should buffer asynchronous release, yet we observed no differences between the two. This would suggest that asynchronous release is not contaminating our measurements of endocytosis to a large extent. Accordingly, paired recordings from AII-AC to OFF-CBC reveal little asynchronous release (Graydon et al., 2018; Hartveit et al., 2020; Grimes et al., 2021).

3.3.4b Nanodomain Ca^{2+} and endocytosis rate at AII-AC synapses

We next performed experiments using an internal solution with 1 mM BAPTA, a Ca^{2+} buffer that is 140-fold faster than EGTA (Naraghi & Neher, 1997). We observed the effects of 1 mM BAPTA by 4 min after break-in, which reduced the ΔC_m response and the BK current (Fig. 3.5A). ΔC_m responses for pulse durations ranging from 0.5 to 20 ms were smaller than EGTA responses (Fig. 3.5B), resulting in a smaller RRP (Fig. 3.5C). Meanwhile, the corrected Q_{Ca} did not change (Fig. 3.5D). Although exocytosis was reduced was blocked by only ~30%. We compared normalized C_m responses to a 20 ms depolarization for recordings with 1 mM BAPTA to those made with 2 mM EGTA as a control. The block of endocytosis by 1 mM BAPTA can be clearly seen from the grand

Figure[3.5]

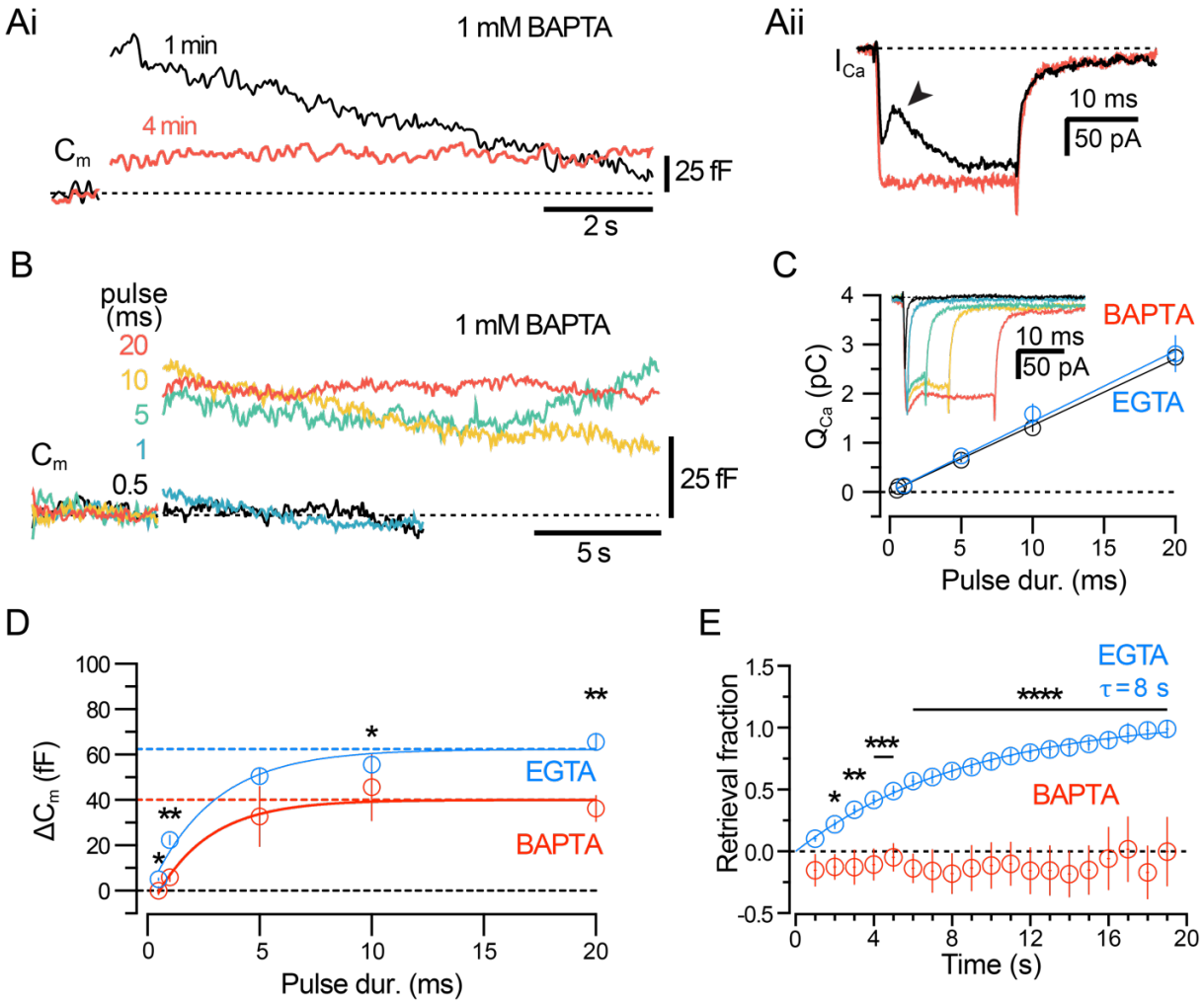

[3.5] Effects of 1 mM BAPTA show that nanodomain Ca^{2+} is required for exo- and endocytosis in AII-ACs.

A, Example traces for C_m (***Ai***) and I_{Ca} (***Aii***) responses to 20 ms depolarizing pulses using an internal solution containing 1 mM BAPTA. Shown are recordings performed at 1 min (black) and 4 min (red), after break-in. Notice how the ΔC_m response reduces after 1 mM BAPTA dialyzed for 4 min, and the reduction of I_{notch} (arrowhead) indicates the suppression of an unblocked Ca^{2+} dependent potassium current (see also Fig. S3.3). ***B,*** Grand average C_m responses to a range of depolarizing pulse durations (0.5 to 20 ms) using an internal solution containing 1 mM BAPTA. Grand averages were made from individual cell averages comprising C_m responses from individual AII-ACs performed between 4 and 30 mins. Notice how with 1 mM BAPTA, the ΔC_m response and endocytosis are different than with EGTA internals (see Fig. 3.2,3.4,S3.4). ***C,*** Plots of corrected Q_{Ca} for BAPTA and 2 mM EGTA datasets. Average I_{Ca} traces for the BAPTA dataset are shown (inset). Continuous lines represent linear fits for EGTA (slope =0.154; R^2 = 0.9030) and BAPTA (slope = 0.1134; R^2 = 0.8592). Notice how Q_{Ca} follows a positive linear trend for both datasets, and were similar after subtracting the charge transfer of the BK current (I_{notch}; see Fig. S3.3). ***D,*** Plots for ΔC_m responses against pulse duration for recordings performed with 2 mM EGTA (blue; same as Fig. 3.2; n = 13) and 1 mM BAPTA (red; n =7). Continuous lines represent single exponential fits for 2 mM EGTA (τ = 3.51

s; R^2 = 0.5230) and 1 mM BAPTA (τ = 3.482 s; R^2 = 0.4666) datasets. Notice how the RRP was significantly reduced with 1 mM BAPTA. **E,** Membrane RF plotted against time after the initial ΔC_m (t = 0) for each dataset. Continuous line represents a single exponential fit to 2 mM EGTA dataset (τ = 8.17 s; R^2 = 0.4144). Notice how the retrieval fraction for the BAPTA dataset is significantly less than EGTA starting at (t = 2 s). Open circles with error bars denote mean ± SEM. Statistical comparisons between datasets were made between all buffer datasets using an ANOVA and *post hoc* Tukey's test.

average trace when compared to 2 mM EGTA (Fig. 3.5E). We also compared the RF for BAPTA and EGTA datasets for the 20 ms pulse responses (Fig. 3.5F). The RF for the EGTA dataset could be fit with a single exponential function (τ = 8.17 s; R^2 = 0.4144) and fully recovered by 20 s. However, we observed little membrane retrieval for the BAPTA dataset. These results indicate that blocking local nanodomain Ca^{2+} with 1 mM BAPTA is sufficient to block fast endocytosis, whereas 10 mM EGTA was not enough to block fast endocytosis.

3.3.5 Effects of GTP hydrolysis on exo- and endocytosis at inhibitory AII-ACs

Our control solution contained 0.4 mM GTP. This was sufficient for producing ΔC_m jumps followed by endocytosis. Because GTP is a critical component for dynamin-dependent endocytosis, we performed experiments using an internal solution with 0 mM GTP (GTP-free) and with GTP substituted for the non-hydrolyzable GTPγS (Fig. 3.6). The grand average C_m (Fig. 3.6A) and I_{Ca} (Fig. 3.6B) responses to a 20 ms depolarizing pulse are shown for each internal solution to illustrate the critical importance of GTP on exo- and endocytosis in AII-ACs. Summary plots showing ΔC_m and Q_{Ca} for each dataset (Fig. 3.6D). The mean ΔC_m and Q_{Ca} for 0.4 mM GTP were (ΔC_m = 62.2 ± 5.54 fF; Q_{Ca} = 3.06 ± 0.132 pC; n = 26). We did not observe any change in ΔCm response with GTP-free internal solution (ΔC_m = 67.74 ± 4.84 fF; Q_{Ca} = 3.30 ± 0.315 pC; n = 6). The ΔC_m was reduced with 0.2 mM GTPγS (38.07 ± 5.00 fF; Q_{Ca} = 3.43 ± 0.17; n = 5).

In these experiments we reduced the ATP concentration from 5 mM to 3 mM, but found no effect on exocytosis or the rate of endocytosis from AII-ACs for 3 mM or 5 mM ATP (Fig. S3.5). However, we cannot rule out the role of ATP on exo- and endocytosis in the AII-AC. A study in goldfish bipolar cells showed that ATPγS can inhibit fast compensatory endocytosis at synaptic terminals, while simply reducing ATP had no effect (Heidelberger, 2001).

Figure 3.6

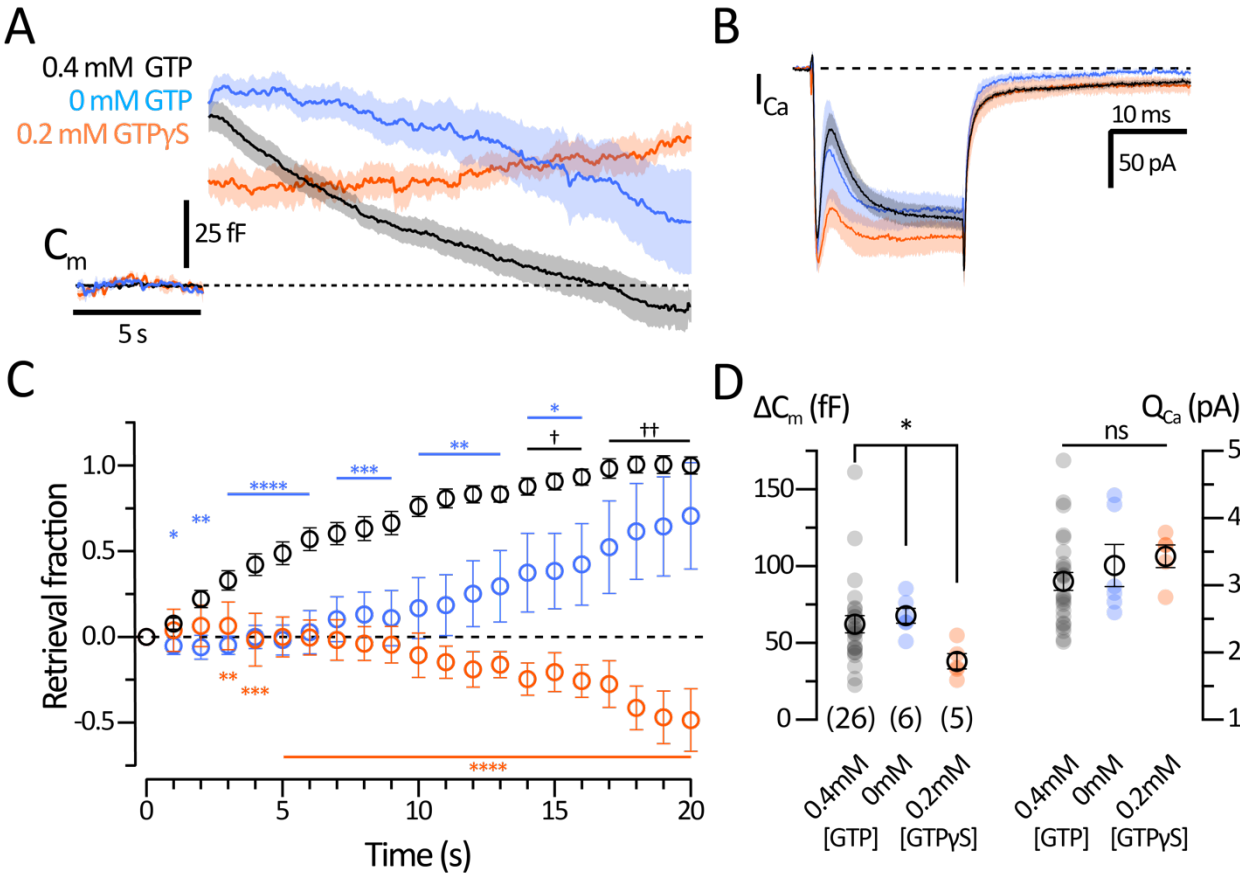

3.6 GTP dependent processes regulate endocytosis in inhibitory AII-ACs.

A, Grand average C_m responses to a 20 ms depolarizing pulse for recordings with internal solutions containing 0.4 mM GTP (black; same dataset as Fig. 3.2), 0 mM GTP (blue) and 0.2 mM GTPγS (orange). Shown are solid lines with shaded regions depicting mean ± SEM for each dataset. Notice that endocytosis was reduced using a GTP-free internal solution (0 mM GTP) and blocked with 0.2 GTPγS. ***B,*** Grand average I_{Ca} responses to a 20 ms depolarizing pulse for recordings corresponding to C_m responses (***A***). Notice how I_{Ca} amplitudes are similar among datasets, yet the I_{notch} is reduced with 0.2 mM GTPγS. ***C,*** Membrane retrieval fraction plotted against time after ΔC_m (t = 0) for each dataset. Notice how the membrane retrieval for the 0 mM GTP has a half-time (RF = 0.5) of 17 s, compared to 6 s for the 0.4 mM GTP dataset, and the 0.2 mM GTPγS dataset does not recover. ***D,*** Summary plots for ΔC_m (left) and Q_{Ca} (right) sowing comparisons for each dataset. Notice how GTPγS significantly reduced the ΔC_m (Kruskal-Wallis and Dunn's test; p = 0.0125), while no significant changes were detected for Q_{Ca} (ANOVA test and Tukey's test; p = 0.4379). Closed circles represent values from individual AII-ACs, and open circles with error bars denote mean ± SEM.

comparisons of non-parametric data (DF = 37; p = 0.0125), detecting a significant change. We found that ΔC_m of the GTPγS dataset was significantly smaller than control (p = 0.049) and GTP free (p = 0.0112) datasets with a *post-hoc* Dunn's test. No significant was found for Q_{Ca} using a

One-way ANOVA test (F = 0.8462; p = 0.4379; DF = 37). Plots of the retrieval fraction for each dataset (Fig. 3.6C) shows that recordings with 0.4 mM GTP have a faster endocytosis half-time than recordings with a GTP-free internal solution; 6 and 17 seconds, respectively. Furthermore, endocytosis was not observed with a GTPɣS internal solution. We also performed experiments with 1 mM GTP, to see if endocytosis rates were accelerated, but no added effect on exo- or endocytosis was observed (Fig. S3.6A-D). We also compared 0.2 and 2 mM GTPɣS, which both had a similar effect in blocking endocytosis (Fig. S3.6E,F). We conclude that endocytosis is critically dependent on GTP.

Although GTP concentration and GTPɣS did not significantly change the Q_{Ca}, we did observe a reduced I_{notch} for the GTPɣS datasets (Fig. 3.6B). We also saw the I_{notch} become larger with the higher 1 mM GTP internal solution (Fig. S3.6A). This finding suggests some modifications to $K_{Ca}1.1$ (BK) channels by GTP may occur. This was not further investigated.

3.3.6 Major molecular regulators of endocytosis in AII-ACs

3.3.6a Dyngo-4a blocks dynamin dependent endocytosis in AII-ACs

We next studied how endocytosis in AII-ACs depends on Dynamin, a GTPase protein that is involved in a late step of the endocytosis process: the final constriction and scission of the endosomal neck (De Camilli et al., 1995). Dynamin inhibitors like Dyngo-4a (dynasore derivative) have been used to study endocytosis at multiple synapses and secretory cells (. The retrieval and scission of plasma membranes during endocytosis at synaptic active zones is blocked by Dyngo-4a. We pre-incubated retina slices for 8-10 min with 30 µM Dyngo-4a in the bath solution before patching AII-ACs and continued perfusion for the duration of recording. C_m responses to a 20 ms depolarizing pulse were recorded. Example traces show that C_m responses with 30 µM Dyngo-4a lose endocytosis at ~8 min after break-in (Fig. 3.7A). In contrast, our example traces for the vehicle control (Ames with 0.1% DMSO) taken in the same retina slice shows endocytosis occurring for up to 20 min after recording. The grand average C_m and I_{Ca} traces are composed of individual cell averages made between 4 and 30 min after break-in (Fig. 3.7B). We observed similar size ΔC_m responses for Dyngo-4a and control datasets, but the traces with Dyngo-4a did not have endocytosis. Furthermore, the I_{Ca} responses were slightly smaller with Dyngo-4a.

Figure[3.7]

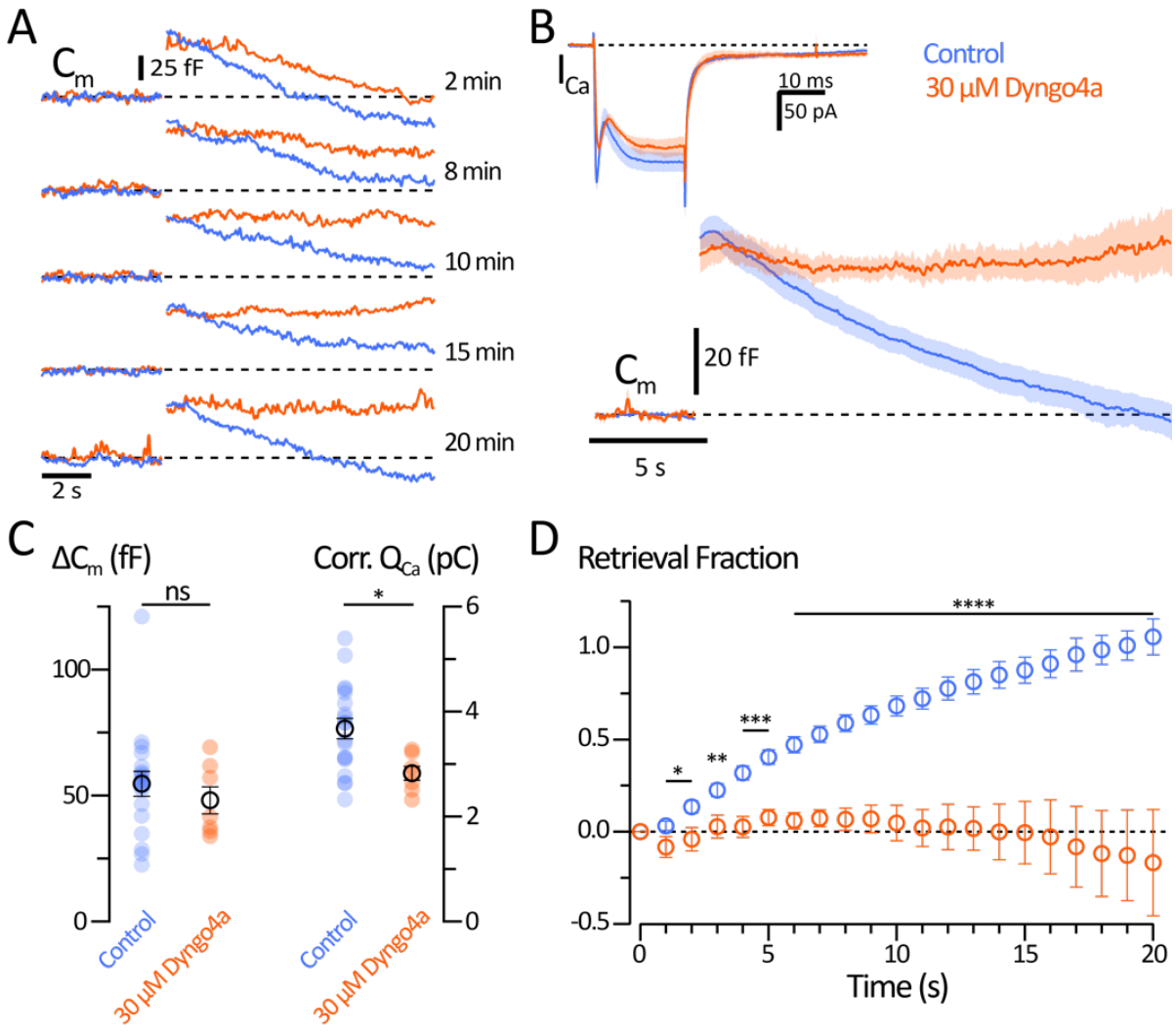

[3.7] Dyngo-4a blocks dynamin dependent endocytosis in AII-ACs.

A, Example traces of C_m responses to a 20 ms pulse for recording performed with a bath solution containing 30 µM Dyngo-4a (orange), and a control solution containing 0.1% DMSO (blue). Internal solution contained 2 mM EGTA and recordings were made from 2 min to 20 min after break-in. Notice how control C_m responses have lasting endocytosis, while responses with 30 µM Dyngo-4a show a reduction in endocytosis over time. ***B,*** Grand average C_m and I_{Ca} (inset) responses to a 20 ms depolarizing pulse. Shown are solid lines with shaded areas depicting mean ± SEM for control (n = 19) and 30 µM Dyngo (n = 7) datasets. Grand averages comprise individual cell averages of traces obtained between 4 and 30 mins after break-in. Notice how the C_m response with 30 µM Dyngo-4a does not return back to baseline, suggesting an inhibition of endocytosis. ***C,*** Summary plots of ΔC_m (left) and corrected Q_{Ca} (right) showing comparisons for each dataset. Notice how ΔC_m responses were not different despite the Q_{Ca} for the Dyngo-4a dataset being significantly smaller. ***D,*** Plot of the membrane retrieval fraction against time after the initial ΔC_m response (t = 0). Notice how the membrane completely recovers (RF = 1; dashed line, for the control dataset unlike the Dyngo-4a dataset, which does not show any membrane retrieval. Closed circles represent data from individual AII-ACs, and open circles with error bars denote mean ± SEM. Statistical comparisons between datasets were made using Student's t-tests.

Summary plots for ΔC_m and Q_{Ca} show the comparisons between Dyngo-4a and control datasets (Fig. 3.7C). The mean Q_{Ca} for the Dingo-4a was significantly smaller (control: 3.68 ± 0.19 pC; n =19, and Dyngo-4a: 2.83 ± 0.13 pC; n = 7; p = 0.0172; Student's t-test). However, Dyngo-4a did not significantly change the ΔC_m response (control: 54.7 + 4.92 fF; n =19, and Dyngo-4a: 48.1 + 5.49 fF; n = 7; p = 0.4624; Student's t-test). The plots of the retrieval fraction show that Dyngo-4a significantly blocks membrane retrieval (Fig. 3.7D). With Dyngo-4a, we observed a small increase in C_m trace that trails after the initial ΔC_m response, about 10-15 s after the depolarizing pulse. Similar drifts in C_m traces were also seen with GTPɣS (Fig. 3.6A,C). We do not know what is causing this upward drift in C_m recordings; however, it is possible that Dyngo-4a is compromising the integrity of the cellular membrane.

3.3.6b Actin polymerization regulates endocytosis kinetics for inhibitory AII-ACs

Endocytosis may require actin polymerization. We thus used latrunculin-A (LatA) to block actin polymerization to test if this process is required for endocytosis in AII-ACs. Here we pre-incubated retinal slices with 25 µM LatA in the recording bath solution for 8-10 min before whole-cell break-in and also for the duration of recording. C_m responses to a 20 ms pulse were recorded for cells treated with LatA and in-slice controls (0.1% DMSO in Ames medium). Example C_m responses are shown for a recording with LatA and control to illustrate that endocytosis failures occurred with LatA throughout the recording duration (Fig. 3.8A). The grand average traces show how LatA affects the C_m and I_{Ca} responses (Fig. 3.8B). We noticed that there was still some endocytosis, although it was slower for the LatA dataset. Summary plots for ΔC_m and Q_{Ca} show comparisons between the LatA and control datasets (Fig. 3.8C). Though the I_{Ca} was slightly smaller with LatA compared to controls, there was no significant difference in Q_{Ca} (control: 3.68 ± 0.19 pC, and LatA: 3.25 ± 0.24 pC; n =19; p = 0.194; Student's t test). Statistical comparisons of ΔC_m for each dataset (control: 54.7 ± 4.92 fF; n = 19, and LatA: 70.0 ± 6.00 fF; p = 0.07; Student's t test), indicate that change in exocytosis statistically significant. Comparisons of the RF show that membrane retrieval for the LatA dataset was significantly reduced from controls (Fig. 3.8D). We saw significant reduction in the RF by 5 s after the initial ΔC_m response (control: 0.41 ± 0.04, and LatA: 0.22 ± 0.06; p = 0.016; Student's t test). Furthermore, the endocytosis half-time was much longer

Figure[3.8]

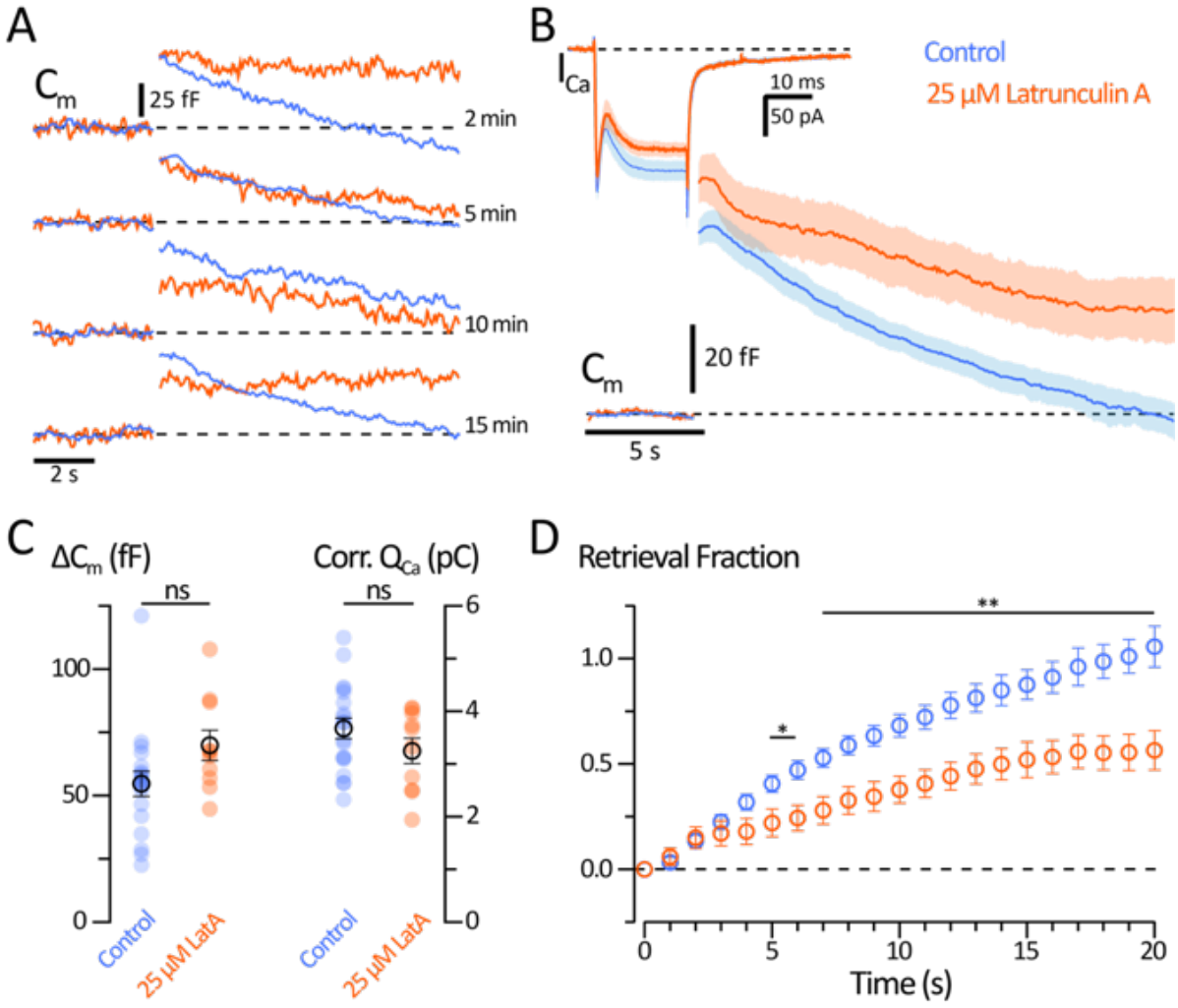

[3.8] Latrunculin-A reduces endocytosis by blocking actin polymerization.

A, Example traces of C_m responses to a 20 ms pulse from recordings using a bath solution containing 25 µM LatA (orange), and a control solution containing 0.1% DMSO (blue; same as Fig. 3.7). Shown are traces from recordings with a 2 mM EGTA internal solution performed at 2 min to 15 min after break-in. Notice how responses with 25 µM LatA do not consistently show endocytosis. ***B,*** Grand average C_m and I_{Ca} (inset) responses for LatA (n = 10) and control (n = 19; same as Fig. 3.7) datasets. Solid traces with shaded areas depicting mean ± SEM. Grand averages comprise individual cell averages of traces obtained between 4 and 30 mins after break-in. Notice how the C_m response the LatA dataset has reduced endocytosis. ***C,*** Summary plot for ΔC_m (left) and Q_{Ca} (right) responses showing comparisons for each dataset. Notice how there was no significant difference between each dataset. ***D,*** Plot for membrane retrieval fraction against time after the initial ΔC_m response (t = 0) for each dataset. Notice how by t = 5 s the RF for the LatA dataset is significantly less than control, and has a slower half-time (RF = 0.5). Closed circles represent data from individual AII-ACs, and open circles depict mean ± SEM. Statistic comparisons were made using Student's t-tests.

with LatA (17 s) versus control (6 s). These results show that blocking the polymerization of actin filaments causes disruptions to endocytosis, though it does not completely block the membrane retrieval process.

3.3.6c Clathrin is perhaps essential for endocytosis in AII-ACs

Figure[3.9]

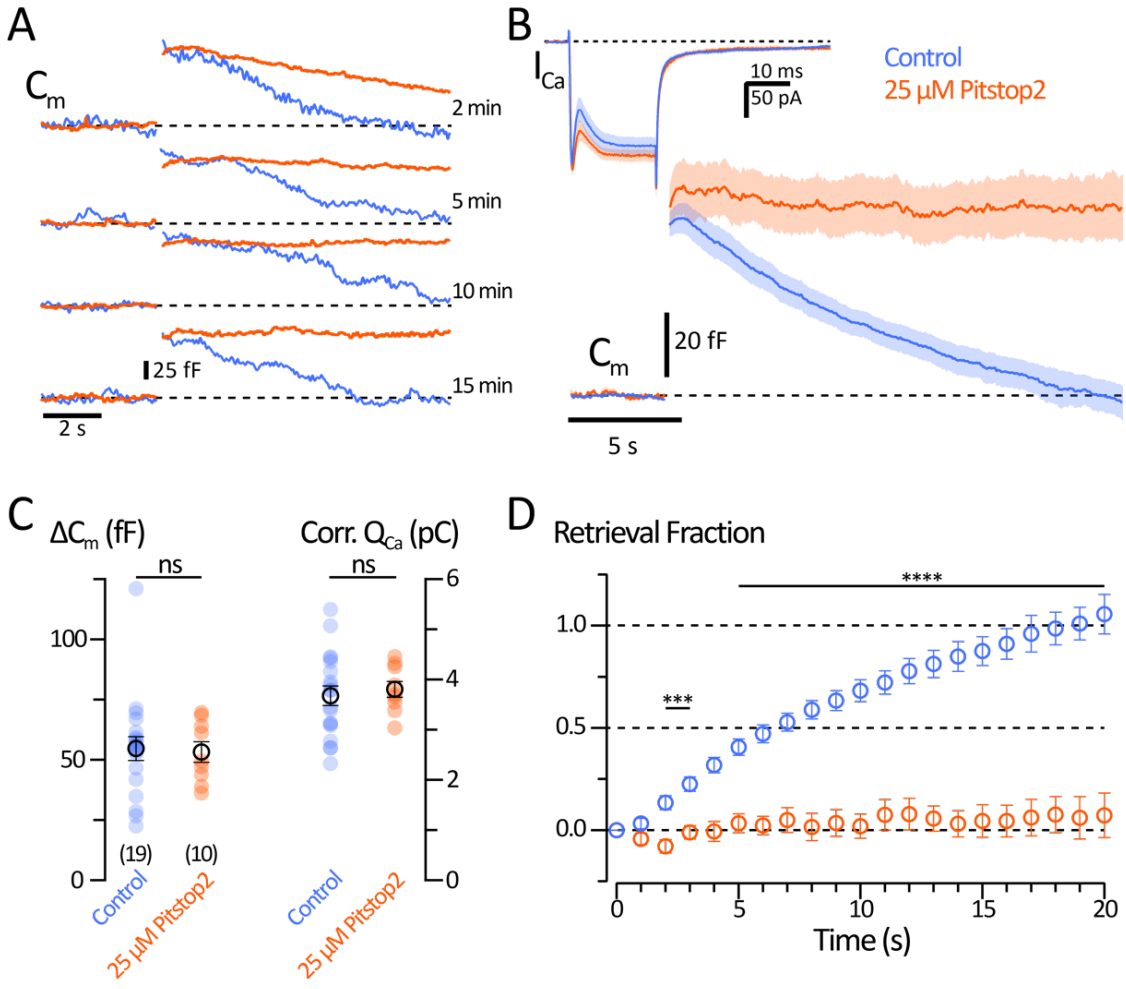

[3.9] Pitstop-2 blocks clathrin dependent endocytosis in AII-ACs.

A, Example traces of C_m responses to a 20 ms pulses from recordings using a bath solution containing 25 µM Pitstop-2 (orange), and a control solution containing 0.1% DMSO (blue; same as Figure 3.6). Recordings were performed in AII-ACs with an internal solution containing 2 mM EGTA made at 2 min to 20 min after whole-cell break-in. Notice how responses for the Pitstop-2 dataset no longer show endocytosis 5 min after break-in. ***B,*** Grand average C_m and I_{Ca} (inset) responses to a 20 ms pulse for Pitstop-2 (n = 10) and control (n = 19) datasets. Shown are solid traces with shaded areas denoting mean ± SEM. Grand averages comprise individual cell averages of traces obtained between 4 and 30 mins after break-in. Notice how the similarities in the ΔC_m and I_{Ca} responses, but the trace for the Pitstop-2 dataset does not return back to baseline (dashed line). ***C,*** Summary plots for ΔC_m

corrected Q_{Ca} (right) responses showing comparisons between each dataset. Note that there were no significant differences. ***D,*** Plot of the membrane retrieval fraction against time after the initial ΔC_m response (t = 0). Notice that by 2 s the membrane retrieval for the Pitstop-2 dataset was significantly less than control and did not have an endocytosis half-time (RF = 0.5). Closed circles represent data from individual AII-ACs, and open circles with error bars denote mean ± SEM. Statistical comparisons were made using Student's t-tests.

Clathrin-mediated endocytosis can be seen at several synapses and is often associated with kinetically slow membrane retrieval. We used 25 µM Pitstop-2 to block clathrin-mediated endocytosis by pre-incubating slices for 8-10 min before whole-cell break-in (von Kleist et al., 2011). Example C_m responses compare recordings with Pitstop-2 and controls within the same retina section (Fig. 3.9A). These example recordings from 2 to 20 min after break-in show that pitstop-2 inhibits completely endocytosis without interfering with exocytosis or causing a late upward drift in C_m traces. Grand average responses showed that Pitstop-2 had a minimal effect on I_{Ca}, and blocked endocytosis without affecting the C_m jump (Fig. 3.9B). This trend is also demonstrated by the summary plots for ΔC_m and Q_{Ca} (Fig. 3.9C). Pitstop-2 did not significantly change ΔC_m (control: 54.7 ± 4.92 fF; n = 19, and Pitstop-2: 59.3 ± 7.19 fF; n = 10; p = 0.592; Student's t test), or the mean Q_{Ca} (control: 3.68 ± 0.19 pC; n =19, and Pitstop-2: 3.81 ± 0.14 pC; n = 10; p = 0.651; Student's t test). The membrane retrieval plots indicate that endocytosis was completely blocked by Pitstop-2 (Fig. 3.9D). This suggests clathrin formation mediates endocytosis at AII-AC synapses. We are hesitant to make a strong conclusion about clathrin's role in AII-AC endocytosis because Pitstop-2 has been suggested to also strongly block clathrin-independent endocytosis (Dutta et al., 2012; Willox et al., 2014). However, in reviewing electron micrographs from Strettoi et al. (1992) of adult rabbit AII-ACs, we can see apparent clathrin-cages and coated-vesicles near the periphery of the presynaptic active zones (Fig. 3.10). We think that these images are showing evidence of clathrin-coated vesicles that have formed on newly retrieved vesicle membranes. We thus propose that clathrin could be involved in endocytosis in AII-ACs. The presence of several putative endocytotic pits in electron micrographs (EM) with clear clathrin-coated membranes and clathrin "cages" near the plasma membrane provide EM evidence of membrane retrieval on the periphery of the active zone of adult rabbit AII-ACs (Strettoi et al., 1992). However, this clathrin-mediated endocytosis may be promoted if lower temperatures are present during tissue fixation (Watanabe et al., 2013).

Figure[3.10]

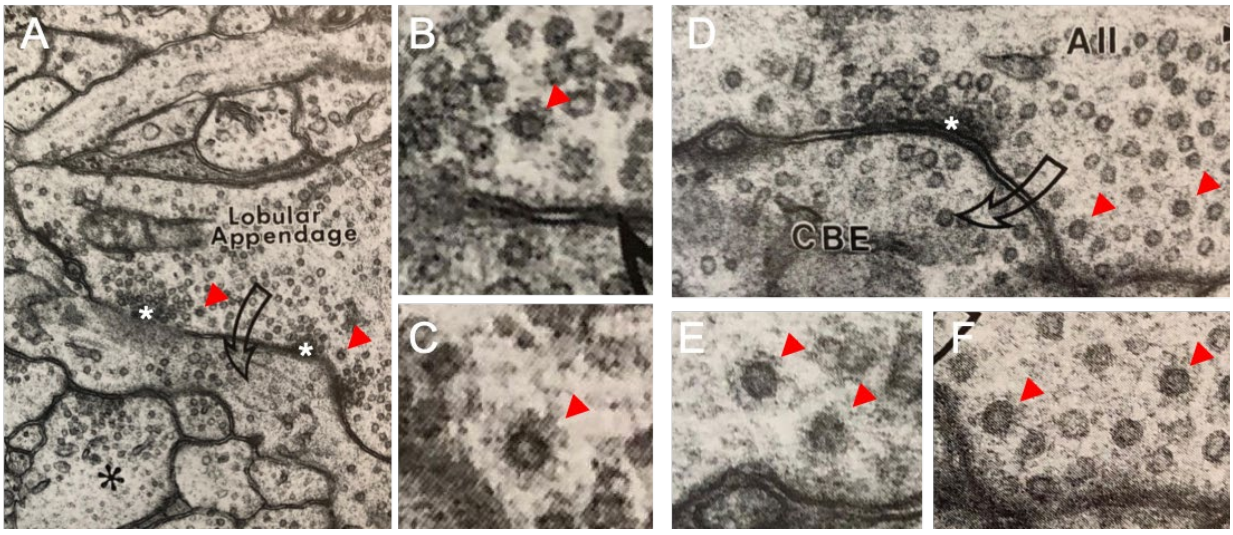

[3.10] Clathrin-coated vesicles in AII-AC lobules.

A-F, Electron micrographs of AII-AC lobular ultrastructure. Shown are micrographs adapted from Strettoi et al. (1992), depicting AII-AC presynaptic active zones (white asterisks). ***A,*** Micrograph showing a lobule with at least two active zones surrounded by vesicles. Red arrows mark clathrin-coated vesicles that are also shown in ***B & C***. ***D,*** Micrograph showing a lobule with one active zone. Red arrows point out regions of clathrin-coated vesicles that are expanded in ***E & F***. Notice how the clathrin- coated vesicles are located peripheral to the active zones.

Section 3.4: Discussion

3.4.1 Ca^{2+}-dependent endocytosis at CNS nerve terminals

The effects that internal Ca^{2+} has on compensatory endocytosis vary among cell types, nerve terminals and experimental preparations. While Ca^{2+} was first proposed to inhibit endocytosis in goldfish bipolar cells (von Gersdorff and Matthews, 1994), other studies have proposed that Ca^{2+} elevations trigger endocytosis (Hull and von Gersdorff, 2004; Yamashita et al., 2010). One method to study Ca^{2+} effects on endocytosis is by changing the stimulation intensity or duration. Increasing the stimulation strength in goldfish BC terminals and the calyx of Held nerve terminal causes endocytosis to slow. However, the interpretation remains problematic because exo- and endocytosis are inextricably coupled and increasing the stimulation duration increases the membrane load which could strain the endocytotic process through mass action depletion of endocytotic proteins (Cork and Thoreson, 2014). Conversely, at calyx of Held synapses increasing the stimulation intensity to high levels reveals two modes of endocytosis (a fast and slow mode)

which may result from two kinetically distinct retrievable pools of vesicles. There is also ample evidence that endocytosis is sensitive to strong internal Ca^{2+} buffers, however the effects of these buffers may change during postnatal development (Yamashita et al., 2010).

3.4.2 C_m measurements from AII-AC and estimation of synaptic vesicle pools

C_m measurements were originally developed for measuring exocytosis in voltage-clamped "spherical" cells with no space-clamp issues (e.g. chromaffin cells; Lindau and Neher 1988; Gillis 1995). This technique has since been used to measure exocytosis, endocytosis, and estimate vesicle pool size in cells with simple morphology (i.e. chromaffin cells or pancreatic beta-cells that secrete insulin). Auditory hair cells from mouse (Neef et al., 2014) and bullfrog (Cho and von Gersdorff, 2012; Chen and von Gersdorff, 2019) are also ideal for C_m measurements. This technique can also be performed with large synaptic terminals; specifically, retinal bipolar cell terminals, calyx of Held (Sun and Wu, 2001; Renden and von Gersdorff, 2007), mossy fiber terminals (Delvendahl et al., 2016), and cone photoreceptor terminals (Van Hook and Thoreson, 2012). Computational models from mossy fiber boutons found that C_m measurements can be used to study more complicated synaptic terminals with two axonal processes (Hallermann et al., 2003; Kushmerick and von Gersdorff, 2003). Fluorescent imaging has also been used to temporally track the fusion and retrieval of individual vesicles (Lagnado and Schmitz, 2015; Smith et al., 2008). Although imaging techniques have relatively low temporal resolution they can be used to monitor single vesicle trafficking.

Increasingly more complex cells are being used now for C_m measurements (Kim and von Gersdorff, 2010), although C_m measurements require fast voltage clamp and good space clamp to faithfully assay exocytosis (Hartveit et al., 2019). Compartmental modeling of hippocampal CA1 mossy fiber boutons showed it is possible to perform C_m measurements from bouton terminals with attached axons and to estimate the overall readily releasable pool (RRP; Hallermann et al., 2003). Models of rat rod bipolar cells found that their long axons impede high frequency sinusoidal waves when C_m is measured using a patch pipette on the cell soma, leading to underestimates of the RRP size (Oltedal and Hartveit, 2010). However, C_m measurements done

with lower sinewave frequency could report the total RRP size of the rod bipolar cells (Oltedal and Hartveit, 2010).

Here we used direct presynaptic C_m recordings in live AII-ACs embedded in retinal slices to study the endocytosis kinetics with high temporal resolution. AII-ACs are narrow-field compact interneurons with bistratified dendrites that receive glutamatergic and electrically coupled (gap junction) inputs in the S3-4 layer and presynaptic glycine release from AII-AC lobular appendages in the S1-2 layer near the soma (Fig. 3.1; Strettoi et al., 1992). Early modeling studies of mouse AII-ACs suggested that their compact size makes their dendritic arbors electronically isopotential with the cell soma (Vardi and Smith, 1996). However, recent models suggest that a high frequency sine wave (2 kHz) might be significantly attenuated by the thin necks connecting lobules, especially those located further away from the soma (Hartveit et al., 2020). Somatic whole-cell capacitance recordings have found evidence of two distinct vesicle pools in mouse AII-ACs: a fast releasing pool, activated by short depolarizing pulses, and a slow pool activated by more prolonged pulses (Balakrishnan et al., 2015). Both the fast and slow pool are potentiated by cAMP via Ca^{2+} release from Ca^{2+} stores (Meadows et al., 2021). Importantly, C_m measurements done with lower sinewave frequencies report the same ΔC_m jump in both young mouse (Balakrishnan et al., 2015) and adult rat AII-ACs (Figure S3.2).

3.4.3 Developmental changes to AII-AC synaptic active zones

We noticed that C_m measurements post-eye-opening juvenile rats (p21-25) had initially had endocytosis shortly after break-in, but endocytosis begins to rundown after several minutes. Similar observations were also found in young mouse AII-ACs in our previous studies (Balakrishnan et al., 2015; Meadows et al., 2021). C_m recordings at bipolar cell terminals also found that whole-cell dialysis disrupts exo-endocytosis, perhaps due to a “washout” of synaptic proteins or disruption of the cytoskeleton. However, perforated-patch experiments that allow the cytosolic constituents of the cell to remain intact prevented this rundown (Hull and von Gersdorff, 2004). Unlike recordings in mouse (Fig. S3.1), Ca^{2+} currents and exocytosis did not rundown even several minutes after whole-cell break-in for recordings in juvenile rats. Remarkably, we found that whole-cell C_m recordings of exocytosis and endocytosis did not

rundown in mature rats (5-13 mo). This suggests that the mature synapses within AII-AC lobules do not rundown or suffer from major washout of vital synaptic proteins. We speculate that mature synapses have more diffusional barriers that prevent the dialysis of the lobules, although our observed effects of BAPTA on exo- and endocytosis suggests that small molecules in our internal solution still effectively penetrate these barriers. Alternatively, the resistance to washout could also develop as lobular cytoskeleton and scaffolding protein complexes become more abundant and mature in adult synapses.

Actin dynamics plays important roles in nerve terminals, spine formation and stability, and in long-term memory (Cingolani and Goda, 2008; Basu and Lamprecht, 2018). Disruption of actin polymerization causes perturbation of spines and can have detrimental effects on long-term memory. The AII-AC lobules differ from dendritic spines in that they have synaptic vesicles and active zones (Fig 3.10). They are thus presynaptic. Here we have shown actin stability is also important for presynaptic integrity and function because after disrupting actin polymerization with LatA the rate of endocytosis is significantly reduced.

3.4.4 Hydrolysis of GTP regulates endocytosis

The importance of GTP- hydrolysis has on exo- and endocytosis has been observed in retina bipolar cells (Jockusch et al., 2005), auditory hair cells (Neef et al., 2014), and the calyx of Held (Yamashita et al., 2005). We found significant reduction in endocytosis using a GTP-free solution, indicating that depletion of endogenous GTP can disrupt endocytotic processes within minutes after break-in. Our results with GTPγS together with results with Dyngo-4a suggest that the GTPase, dynamin regulates fast endocytosis in the AII-AC. Dynamin inhibitors like dynasore and Dyngo-4a, work by blocking the GTP-dependent assembly around the endosomal necks (Mohanakrishnan et al., 2017). Other studies have used these inhibitors to demonstrate dynamin's role in fast endocytosis (Delvendahl et al., 2016); however, there are potential off-target effects of dynasore derivatives (Park et al 2013).

3.4.5 Mechanisms of ultrafast, fast and slow endocytosis

We found that treatment with the dynamin inhibitor, Dyngo-4a, and clathrin inhibitor, Pitstop-2, fully blocked endocytosis responses to a 20 ms stimulation, in which control responses had an exponential time constant of about 8 s (Fig. 3.7, 3.8, 3.9). Results from inner hair cells found two modes of endocytosis (fast exponential and slow linear) could be separated using 20 and 200 ms pulse stimulations; apparently, dynamin and clathrin-mediated only the slow linear mode of endocytosis (Neef et al., 2014). The fast mode is exponential at inner hair cell synapses and occurs after a strong (200 ms) depolarization, or via flash-photolysis of caged-Ca^{2+}, compared to near-linear decay responses to 20 ms depolarizing pulses (Neef et al., 2014). Endocytosis in rod and cone photoreceptors in salamanders can be fitted with fast single exponentials (τ ~450 ms and 250 ms), although only rods showed evidence of a dynamin-dependent mechanism (Van Hook and Thoreson, 2012). Evidence of dynamin and clathrin distribution in photoreceptors indicate that this form of endocytosis may come from a separate retrievable pool of vesicles (Zampighi et al., 2011). Clathrin-mediated endocytosis is reportedly associated with slower kinetics for sensory and central synapses (see review: Royle and Lagnado, 2010). C_m recordings in cerebellar and hippocampal mossy fiber synapses found distinct fast and slow membrane retrieval modes that are clathrin-independent and dependent respectively (Delvendahl, et al., 2016). These results support earlier flash and freeze EM data showing that actin and dynamin are involved in the invagination and fission of vesicle membranes without clathrin associated proteins in the peri-active zone (Watanabe et al., 2013). Our results with 20 ms pulse stimulations produced a ΔC_m jump followed by an exponential endocytosis time course comparable to that observed for 1 - 30 ms responses in mossy fiber terminals (Delvendahl et al., 2016), where clathrin-mediated mechanisms contribute to retrieval rates of ~1 - 3 s, which are faster than previous observations of ~10 - 20 seconds in goldfish bipolar cell terminals (von Gersdorff and Matthews, 1994).

Ultrafast endocytic events with an exponential time-constant τ = 300 ms have been observed using C_m measurements at inner hair cells (Beutner et al., 2001) and cone photoreceptors (Van Hook et al 2012). Ultrafast endocytosis (τ = 470 ms) was also observed at cerebellar and hippocampal mossy fiber synapses in response to a single action potential (Delvendahl et al.,

2016). Fast endocytosis also occurs within 1 to 4 s for a short AP train, but slows down after more prolonged stimulation that leads to multivesicular release.

Clathrin-coated vesicles are observed at both ribbon and conventional synapses (reviewed in LoGiudice and Mathews, 2007). Early capacitance experiments in goldfish rod bipolar cells report a slow mode of endocytosis (von Gersdorff and Matthews, 1994; Neves and Lagnado, 1999; Heidelberger, 2002). Later studies demonstrated that endocytosis can be mediated by separate clathrin and clathrin-independent mechanisms (Jockusch et al., 2005; Llobet et al., 2011), where clathrin-coated vesicles are located peripheral to the active-zone (Pelassa et al., 2014). Photoreceptors pedicles have retrieval pools that use clathrin-mediated and clathrin independent mechanisms for endocytosis (Fuchs et al., 2014). The distinction between clathrin-mediated and clathrin-independent endocytosis is not limited to ribbon synapses (Granseth et al., 2006; Wu, et al., 2009). We were initially reluctant to state that AII-ACs exhibit clathrin-mediated endocytosis because our only evidence uses pitstop-2, an inhibitor of clathrin-mediated endocytosis (von Kleist et al., 2011). However, this compound can also block clathrin-independent endocytosis in some cells (Dutta et al., 2012; Willox et al., 2014). However, EM published data from Strettoi et al. (1992) of AII-AC lobular ultrastructure shows coated vesicles on the periphery of the active zone (Fig. 3.10). We think this represents evidence for clathrin-coated vesicles in AII-ACs, supporting our finding with Pitstop-2, which blocks clathrin-mediated endocytosis as proposed by Delvendahl et al. (2016) for mossy fiber terminals.

3.4.6 Ca^{2+} nanodomain coupling of synaptic vesicle exocytosis

We found that exocytosis in mature AII-ACs was dependent on nanodomain Ca^{2+} and reduced with 1 mM BAPTA, while changing EGTA concentration from 2 to 10 mM had no effect. L-type Ca^{2+} channels cluster in AII-AC lobules (Habermann et al., 2003; Borghuis et al., 2011; Balakrishnan et al., 2015), which is also the location of active zones (Strettoi et al., 1992). C_m recordings in mouse AII-ACs found that EGTA sensitivity changed from pre-eye-opening (p9) to young adult (p25), suggesting that there are developmental changes in the microdomain structure of the active zone (Balakrishnan et al., 2015). However, our finding in mature rat AII-ACs agrees with tighter, nanodomain Ca^{2+} channel coupling observed at other inhibitory synapses

(Williams et al., 2012; for a review on nanodomains see: Eggermann et al., 2011). In addition, the change in synaptic efficiency would suggest further remodeling of the AII-AC active zones. Two mechanisms could explain this: (1) There are extra-synaptic L-type channels that move closer to the active zone, or (2) Changes in sensitivity of the Ca^{2+} binding sensor.

3.4.7 Ca^{2+}-dependent regulation of endocytosis

The influence of Ca^{2+} on endocytosis has been heavily studied and debated since it was first observed in goldfish bipolar cells (von Gersdorff and Matthews, 1994). Some studies suggest an inhibitory effect of Ca^{2+} and a slowing of endocytosis as more exocytosis occurs with stronger stimulation (von Gersdorff and Matthews, 1994; Leitz and Kavalali, 2011). This agrees with what we observed in the AII-AC, where longer pulses had longer half-times. Slowing down of endocytosis could be dependent on a depletion of readily available endocytic proteins, Ca^{2+} influx activating an upstream protein like calmodulin (Yao and Sakaba, 2012), or a kinase like calcineurin (Yamashita et al., 2010; Cork and Thoreson, 2014). High levels of Ca^{2+} influx can even trigger release locally at the ribbon or from non-ribbon sites with different retrieval mechanisms (Chen et al., 2012, 2014).

At the calyx of Held nerve terminal robust Ca^{2+} influx can accelerate endocytosis after strong stimulations that trigger copious exocytosis (Wu et al., 2009; Yamashita, 2012). The use of internal solutions with different buffer strength suggested that endocytosis is Ca^{2+}-dependent, although these manipulations were most effective in younger animals. In our study, we found that 1 mM BAPTA eliminated endocytosis similarly to results found in juvenile calyx of Held (Hosoi et al., 2009), and contrary to findings at the hippocampal mossy fiber synapses (Miyano et al., 2019). At the more mature, but still young postnatal P14-15 calyx of Held synapse, 10 mM BAPTA was necessary to completely block endocytosis, suggesting that it was triggered by local Ca^{2+} nanodomains (Yamashita et al, 2010). We also found that AII-ACs were insensitive to changes to EGTA concentrations, indicating that exo- and endocytosis are dependent on nanodomain Ca^{2+}. Fast and slow modes of endocytosis are regulated by different Ca^{2+} channel subtypes in the calyx of Held (Midorikawa et al., 2014), yet the AII-AC only expresses L-type Ca^{2+} channels (Habermann et al., 2003; Balakrishnan et al., 2015). Therefore, we propose that there are perhaps different

clusters of Ca^{2+} channels some specific for exocytosis at active zones and some specific for endocytosis at the peri-active zone (or hot spot of endocytosis). Rapid endocytosis may also become more robust in adult synapses via a clustering of endocytotic proteins near the plasma membrane at hot spots of endocytosis in the peri-active zone (Watanabe et al., 2013).

Section 3.5: Materials & Methods

Animals

Procedures were approved by the Institutional Animal Care and Use Committee of OHSU, and were in accordance with National Institutes of Health guidelines. Brown Norway (BN) rats (Charles River) and C57bl/6j mice (Jackson Laboratory). Unless indicated, BN rats were 5-13 months old. Animals were anesthetized with isoflurane (Novaplus) and then after euthanasia, the eyes were removed and dissected to extract the retina in carbogenated Ames medium (USBiologicals) at room temperature.

Retina slices

Retinas were embedded in low melting temperature agarose (sigma type VIIA, 3% in Ames medium) and 250 µm slices were prepared using a vibratome (Leica VT1200S) in carbogenated low-Na^+ sucrose-based cutting solution containing (in mM): 2.5 KCL, 35 NaHCO3, 1.25 NaH2PO4, 0.5 $CaCl_2$, 6 $MgCl_2$, 10 glucose, 3 Na-pyruvate, 210 sucrose, and 20 HEPES. Retinal slices were stored at room temperature in carbogenated Ames solution before being transferred to the recording chamber.

External and Internal Solutions

Ames medium (containing 1.15 mM free Ca^{2+}; Ames and Nesbett, 1981) was used for our external recording solution, which was continuously perfused and heated to near physiological temperature (33 - 34°C). Ames was supplemented with (in µM): 10 6-cyano-7-nitroquinoxaline-2,3-dione (CNQX), 50 DL-2-Amino-5-phosphonopentanoic acid (DL-AP5), 2 strychnine, 3 SR95531, 5 (-)-bicuculline methiodide, and 1 tetrodotoxin (TTX). These drugs blocked AMPA, NMDA, glycine and GABA receptors, as well as Na^+ channels.

Internal solutions were Cesium-based to block potassium currents. Our control solution with ethylene glycol-bis(β-aminoethyl ether)-N,N,N',N'-tetraacetic acid (EGTA) was prepared as

followed (in mM): 50 CsCl, 66 Cs gluconate, 10 tetraethyl ammonium chloride (TEA-Cl), 10 HEPES, 5 adenosine 5'-triphosphate magnesium salt (ATP-Mg), 0.4 guanosine 5'-triphosphate disodium salt (GTP-Na2), and 2 EGTA. We used solutions with different EGTA concentrations (0.2, 5, and 10 mM) when indicated, prepared by substituting Cs gluconate. We used a solution containing 1,2-bis(o-aminophenoxy)ethane-N,N,N',N'-tetraacetic acid (BAPTA; 1 mM) when indicated, prepared by substituting EGTA and Cs gluconate. We used solutions containing low ATP-Mg (3 mM) with different GTP concentrations (0, 0.4, and 2 mM) or with GTPγS (0.2, and 2 mM) prepared by substituting Cs-gluconate. Stock internal solutions were made at 1.25x concentration, adjusted pH to 7.4 with CsOH, adjusted osmolarity with D-glucose, and kept frozen for up to 3 months. Internal solutions were diluted to 1x concentration (275 mOSM) before use and 10 µM Alexa 594 hydrazine (Invitrogen) was added. Pipette filling syringes containing internal solutions were kept on ice to avoid thermal degradation of GTP and ATP.

Stock concentrations of drugs and salts were prepared using purified water (Milli-Q; Millipore). Stocks of latrunculin-A, Pitstop-2, and Dyngo-4a were made with DMSO and added to external solution when indicated (final DMSO concentration was 0.1% v/v). Ultrapure salts for internal were purchased from Sigma-Aldrich (St. Louis, MO). CNQX, SR95531, DL-AP5, bicuculline, and latrunculin-A were purchased from Tocris Bioscience (R&D Systems, Minnesota). Tetrodotoxin (TTX) and strychnine were purchased from Sigma (St. Louis, MO). Pitstop-2 and Dyngo-4a were purchased from abcam (Waltham, MA).

Patch clamp electrophysiology

Electrophysiological recordings using a double EPC-9 or EPC-10 patch clamp amplifier and Patchmaster software (HEKA Elektronik, Lambrecht/Pfalz, Germany). Data acquisition performed with a sampling rate of 100 kHz, filtered with 2 kHz low-pass filter. Thick walled borosilicate glass pipettes were used for whole-cell patch-clamp experiments (8-10 MΩ; 1B150F-4, World Precision Instruments, Sarasota, FL). Pipettes were pulled with a Narishige puller-PP830 (Tokyo, Japan), and wrapped with parafilm to reduce stray capacitance and electrical noise. Whole-cell voltage-clamp recordings of membrane capacitance (C_m) and Ca^{2+} currents (I_{Ca}) in AII-ACs from BN rat retina slices; retina slices from C57 BL6J mice were used when indicated (Fig. S3.1). Retinal slices were kept in low-light (photopic) conditions.

Time-resolved C_m measurements were made using the "sine+DC" method (Gillis, 2000; Balakrishnan et al., 2015; Hartveit et al., 2019; Meadows et al., 2021). A pair of sinusoidal waves (2 kHz; 30 mV peak-to-peak) superimposed on membrane holding potential (-80 mV) were given before and after a square depolarizing pulse from -80 mV to -10 mV for maximal I_{Ca} activation (Balakrishnan et al., 2015), which triggered Ca^{2+}-dependent vesicle fusion (exocytosis). Leak voltage-clamp pulses (to -73 mV) were given after each C_m recording and used for offline leak-subtraction. Additionally, some slices were treated with 100 nM iberiotoxin to inhibit K_{Ca} 1.1 channels not completely blocked by our Cs-based internal solution. Experiments were not corrected for liquid junction potential, which was measured (-10 mV) post-hoc using methods described by Neher (1992). Online calculations of passive membrane properties (C_m, G_s, G_m) were done by the HEKA software.

Data processing

Traces were imported to IgorPro software (Wavemetrics, Lake Oswego, OR) for offline analysis. The inverse was calculated for G_s and G_m traces for measuring series resistance (R_s), membrane resistance (R_m). Traces were processed using a lowpass Hanning filter with a cutoff at 40 kHz. The baseline R_s, R_m, and C_m was measured 100 ms before the stimulus. Linear fits were made to C_m response 5 s before the stimulus and extended to the duration of the entire trace. Subtraction of the C_m traces and the linear fits were made to offset persistent changes to the baseline C_m response.

Cm measurements and vesicle pool estimates

C_m measurements were made 100 ms before the stimulus (baseline; C_b) and 100 ms after (jump; C_j). Each measurement is the mean of data points over a sample duration of 100 ms. The following formula was used to calculate the changes in C_m response (ΔC_m):

$$\Delta C_m = C_j - C_b$$

An estimate of the total number of vesicle fusions (v) that produce the net ΔC_m change is obtained from the following formula:

$$v = \frac{\Delta C_m}{c_V}$$

Given the average vesicle diameter (d) is 37 nm and specific capacitance (c_s) is 10 fF/μm^2, the capacitance of a single spherical vesicle ($c_V \approx 40$ attoF) was estimated from:

$$c_V = \pi d^2 c_s$$

Ca^{2+} currents and estimates of charge transfer

L-type Ca^{2+} current (I_{Ca}) were made using offline leak subtraction (P/10) taking the difference of the current response and the summed leak responses. The notch in the I_{Ca} was determined to be an unblocked BK (big potassium) current using iberiotoxin (S, a potent KCa1.1 inhibitor. The charge transfer (Q) was measured by integrating I_{Ca} under the region of the pulse duration. The Q_{total} consists the total Q for the Ca^{2+} charge transfer (Q_{Ca}) flux and is corrected for the contaminating BK charge transfer (Q_{notch}).

Experimental design and statistical analysis

Datasets for all experiments were tested for normal distribution using a Shapiro-Wilk test. For most experiments pairwise comparisons were made between recordings taken within 1 min (30 s to 1 min) and at 4 min after break-in using a two-tailed paired t-test or Wilcoxon test; respectively for datasets with normal and non-normal distribution with an α level of 0.05. For comparisons of independent groups we performed either a Student's t-test or Mann-Whitney test; respectively for normal and non-normal distribution. For comparisons between multiple groups, we indicate where we use one-way and two-way ANOVA tests followed by *post hoc* tests. All statistical tests were performed in Prism 9 software (GraphPad, San Diego, CA). Grouped data are written as mean ± SEM. Statistical significance is noted by asterisks (* $p < 0.05$, ** $p < 0.01$, *** $p < 0.001$, and **** $p < 0.0001$), while not significant ($p > 0.05$) is either labeled (ns) or not indicated.

Section 3.6: Supplemental Figures

Figure[S3.1]

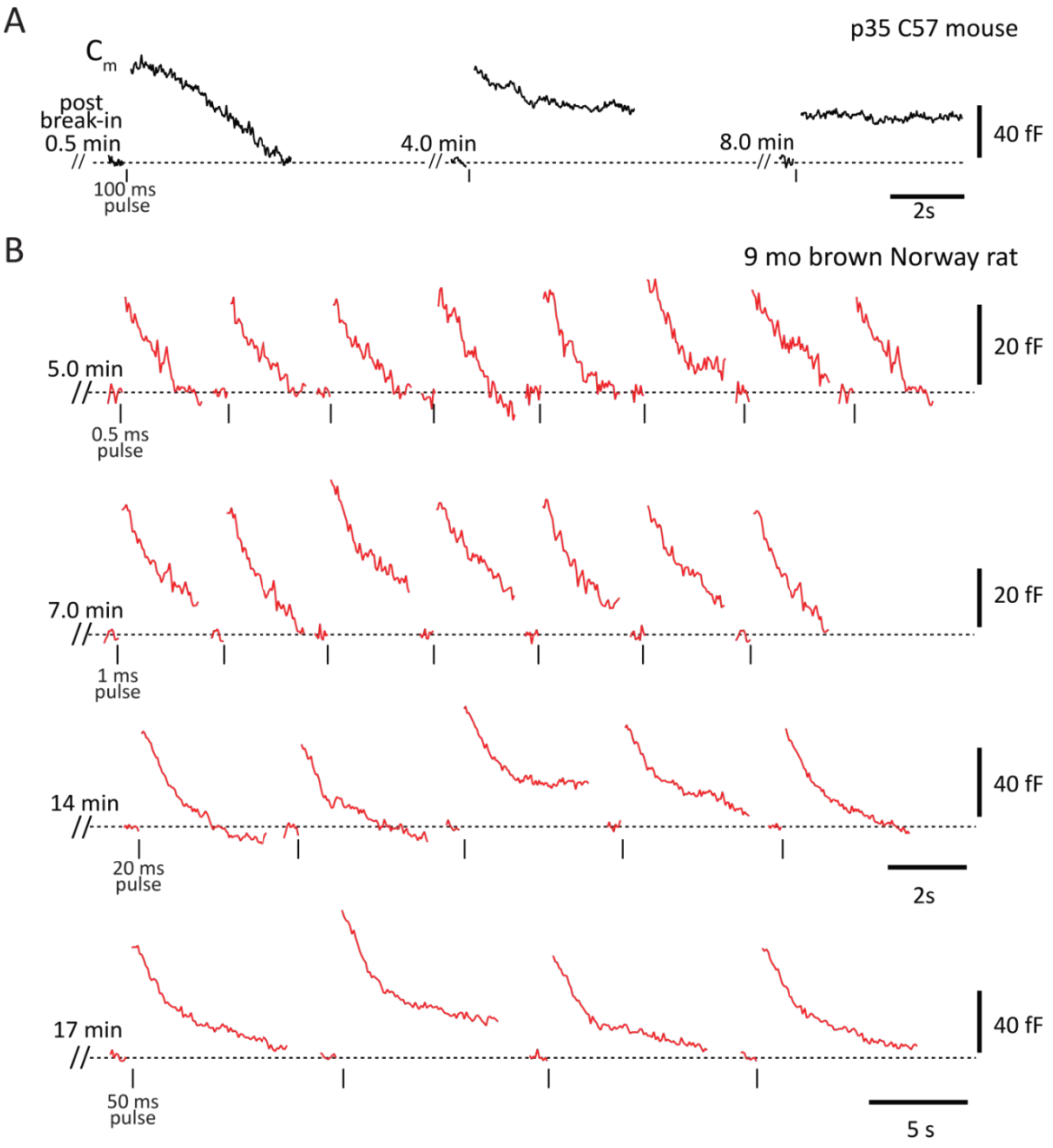

[S3.1] Whole-cell C_m recordings of endocytosis in mature brown Norway rats.

A, Example traces for C_m responses to a 100 ms depolarizing pulse for an AII-AC from a p35 C57 mouse. Shown are traces recorded at 0.5, 4, and 8 mins after break-in. Notice how at 4 min the C_m trace does not return to baseline (dashed line) and by 8 min the ΔC_m begins to rundown. **B,** Example traces for C_m responses for an AII-AC from a mature (5 mo) brown Norway rat. Shown (top row) are multiple C_m responses to 0.5 ms depolarizing pulses, starting 5 min after break-in, responses to 1 ms pulses occurring 7 min after break-in (second row), responses to 20 ms pulses occurring 14 min after break-in (third row; note the change in y-axis scale bar), and responses to 50 ms pulses occurring 17 min after break-in (bottom; note the change in time scale bar). Notice how whole-cell recordings in rat AII-ACs can produce reliable ΔC_m responses which return back to baseline, a feature persisting for long recording sessions.

Figure[S3.2]

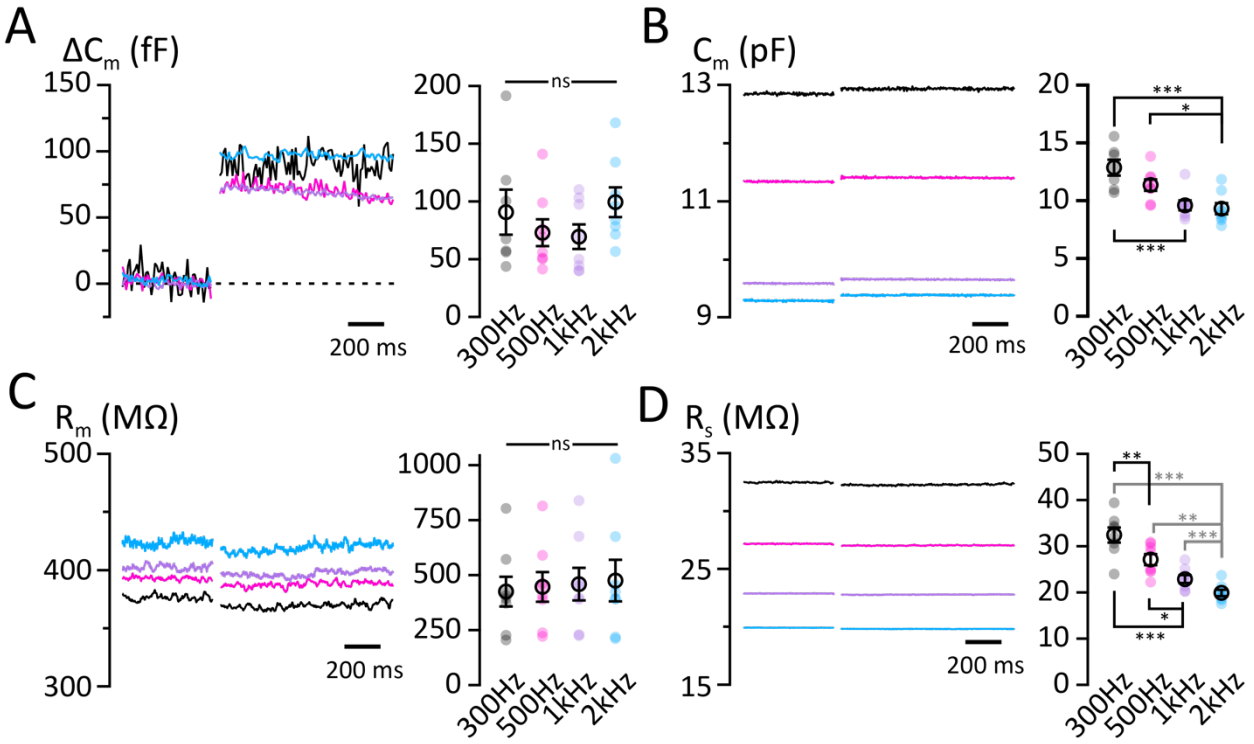

[S3.2] Effects of sinusoidal frequency on estimates of C_m recordings and exocytosis.

A-D, whole-cell voltage-clamp recordings showing responses to different sinusoidal frequencies (in Hertz: 300, 500, 1000, and 2000) respectively colored (black, magenta, mauve, and blue). Shown are grand average traces (right) and summary plots (left) for responses to a 20 ms depolarizing pulse recorded from AII-ACs using an internal solution containing 2 mM EGTA. ***A,*** C_m responses (left) were baseline subtracted to compare C_m jumps (ΔC_m). Notice how in the summary plots comparing ΔC_m responses there was no significant changes between sinusoidal frequencies. ***B,*** Traces and summary plots for basal C_m responses show significant reductions in basal C_m as sinusoidal frequency increases. **C,** Traces and summary plots for membrane resistance (R_m) did not significantly change. **D,** Traces and summary plots for series resistance did significantly reduce as sinusoidal frequency increased. Closed circles represent data from individual AII-ACs (n = 7), and closed circles with error bars denote mean ± SEM. Statistical comparisons were made using one-way ANOVA and *post hoc* Tukey's tests.

Figure[S3.3]

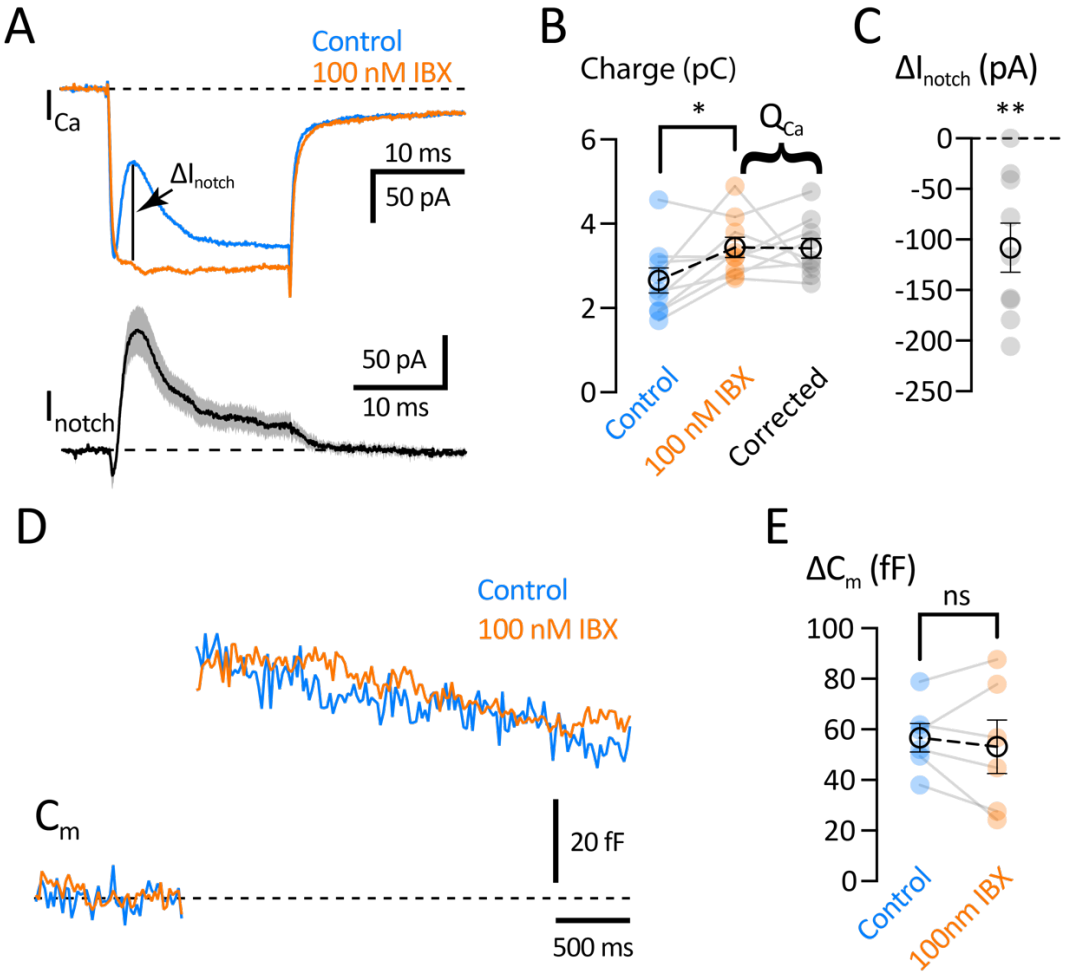

[S3.3] K_{Ca} 1.1 (BK) current contributes to notch in I_{Ca}.

A, Grand average traces for I_{Ca} responses (top panel) to a 20 ms pulse for recordings with 100 nM iberiotoxin (orange; n = 9) and control bath solution before drug wash (blue; n = 9). Recordings were performed at 33 °C using a Cs-based internal solution with 2 mM EGTA (see materials and methods). Trace for I_{notch} (bottom panel) was made by subtracting control and iberiotoxin traces, shaded region indicates SEM. Arrow pointing to a vertical bar indicates change in I_{notch} (ΔI_{notch}). ***B,*** Summary plot of the charge transfer (Q) for current responses to a 20 ms depolarizing pulse for each dataset and the corrected Q_{Ca} (grey), which is $Q_{Ca} = |Q_{control}| + |Q_{notch}|$. Notice how iberiotoxin dataset is larger than control, due to the contaminating I_{notch} (control: 2.65 ± 0.30 pC and ibx: 3.44 ± 1.24 pC; n = 9; p = 0.021). When the control dataset is corrected by artificially subtracting I_{notch}, the Q_{Ca} is now the same as the iberiotoxin dataset (corrected: 3.42 ± 0.24 pC; n = 9; p = 0.946). Therefore the true Q_{Ca} (indicated on histogram) can be obtained by blocking BK currents with iberiotoxin or similarly by adding Q_{notch} arithmetically. ***C,*** Histogram showing the notch reduction ΔI_{notch} after iberiotoxin, measured at the peak I_{notch} observed in control datasets (-108.1 ± 24.2 pA; p = .0021). ***D,*** Grand average C_m responses for control, and 100nM iberiotoxin datasets. Notice how blocking BK currents does not affect C_m responses (control: 56.7 ± 5.64 fF, and ibx: 53.1 ± 10.6 fF; n = 6; p = 0.594). ***E,*** Summary plots of ΔC_m responses for control and iberiotoxin datasets, show no significant difference between datasets. Closed circles represent data from individual AII-ACs, and open circles with error bars denote mean ± SEM. Statistical comparison was made using a paired t-test.

Figure[S3.4]

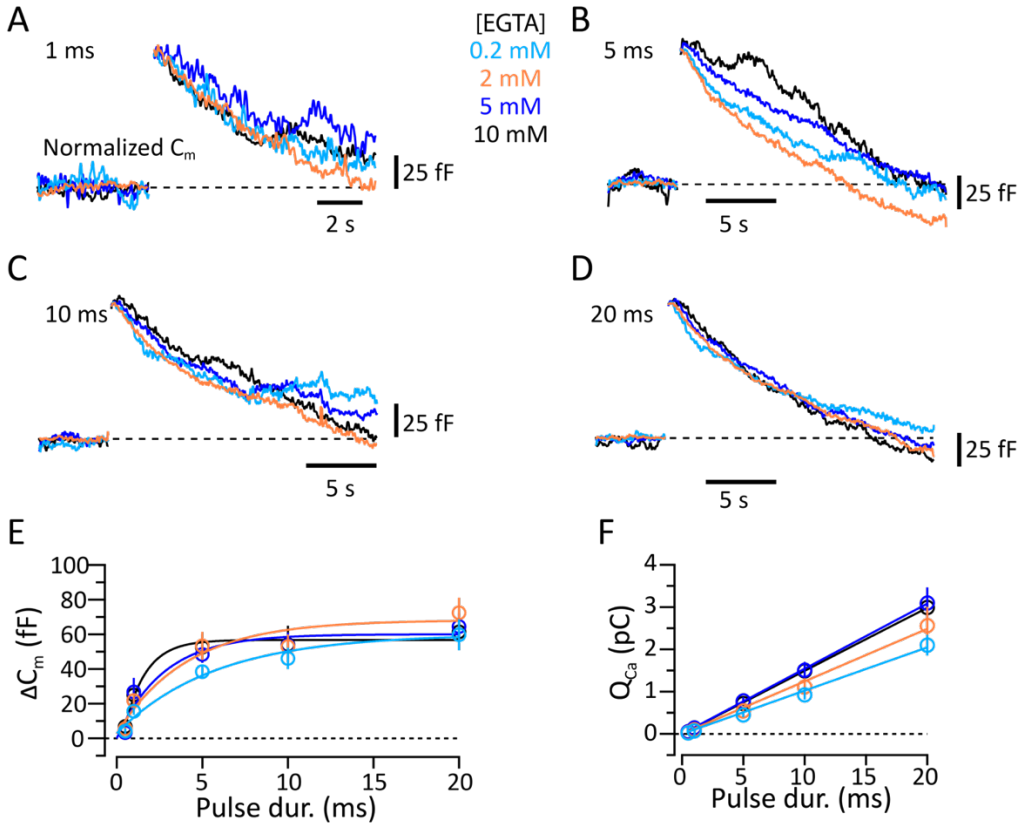

[S3.4] [EGTA] does not affect exo- and endocytosis in AII-ACs.

A-D, Normalized trace averages of C_m responses from AII-ACs. Recordings were performed with different internal EGTA concentrations (0.2, 2, 5, and 10 mM). Traces are shown for responses depolarization durations of 1 ms (***A***), 5 ms (***B***), 10 ms (***C***), and 20 ms (***D***). ***E,*** ΔC_m responses plotted against pulse duration for each [EGTA] dataset. ***F,*** Q_{Ca} plotted against pulse duration for each [EGTA] dataset.

Figure[S3.5]

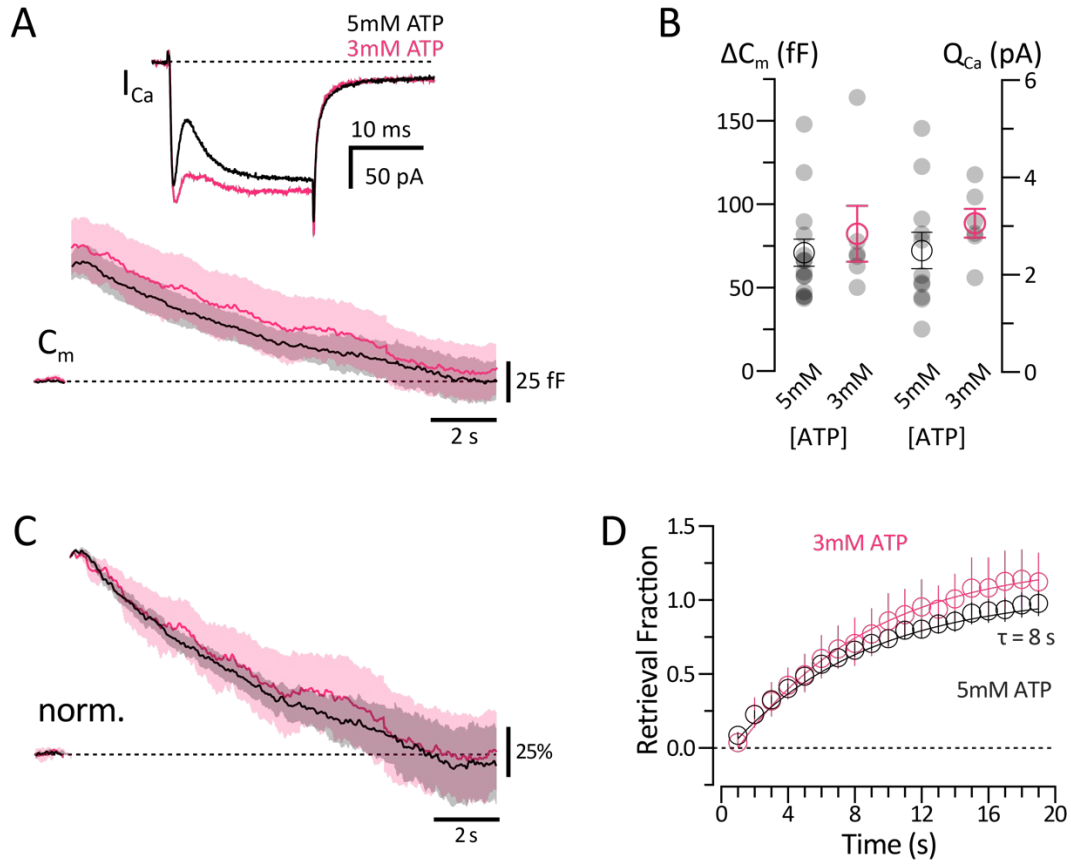

[S3.5] [ATP] reduction does not affect exo- and endocytosis in AII-ACs.

A, Average C_m and I_{Ca} responses to a 20 ms depolarizing pulse for recordings using internal solutions containing 5 mM ATP (black) and 3 mM ATP (magenta). Solid traces and shaded region represent mean ± SEM for datasets, although shaded region was removed for I_{Ca} for visual clarity. Notice that C_m responses for both datasets are similar, yet I_{Ca} responses differ in the I_{notch} is smaller for 3 mM ATP. ***B,*** Summary plots for ΔC_m (left) and corrected Q_{Ca} (right) showing comparisons between values from each dataset (closed circles). Statistical comparisons were made using student's t-tests and were not significantly different. ***C,*** Normalized grand average C_m responses for 5 mM and 3 mM ATP datasets. Notice how traces for both ATP concentrations return back to baseline (dashed line) at the same rate. ***D,*** Membrane retrieval fraction plotted against time after the initial ΔC_m response (t = 0) for each dataset. Continuous lines represent single exponential fits to each dataset, showing that both have the same rate of membrane retrieval (τ = 8 s). Open circles represent mean ± SEM. Statistical comparisons were made using student's t-tests resulting in no significant changes in retrieval fraction.

Figure[S3.6]

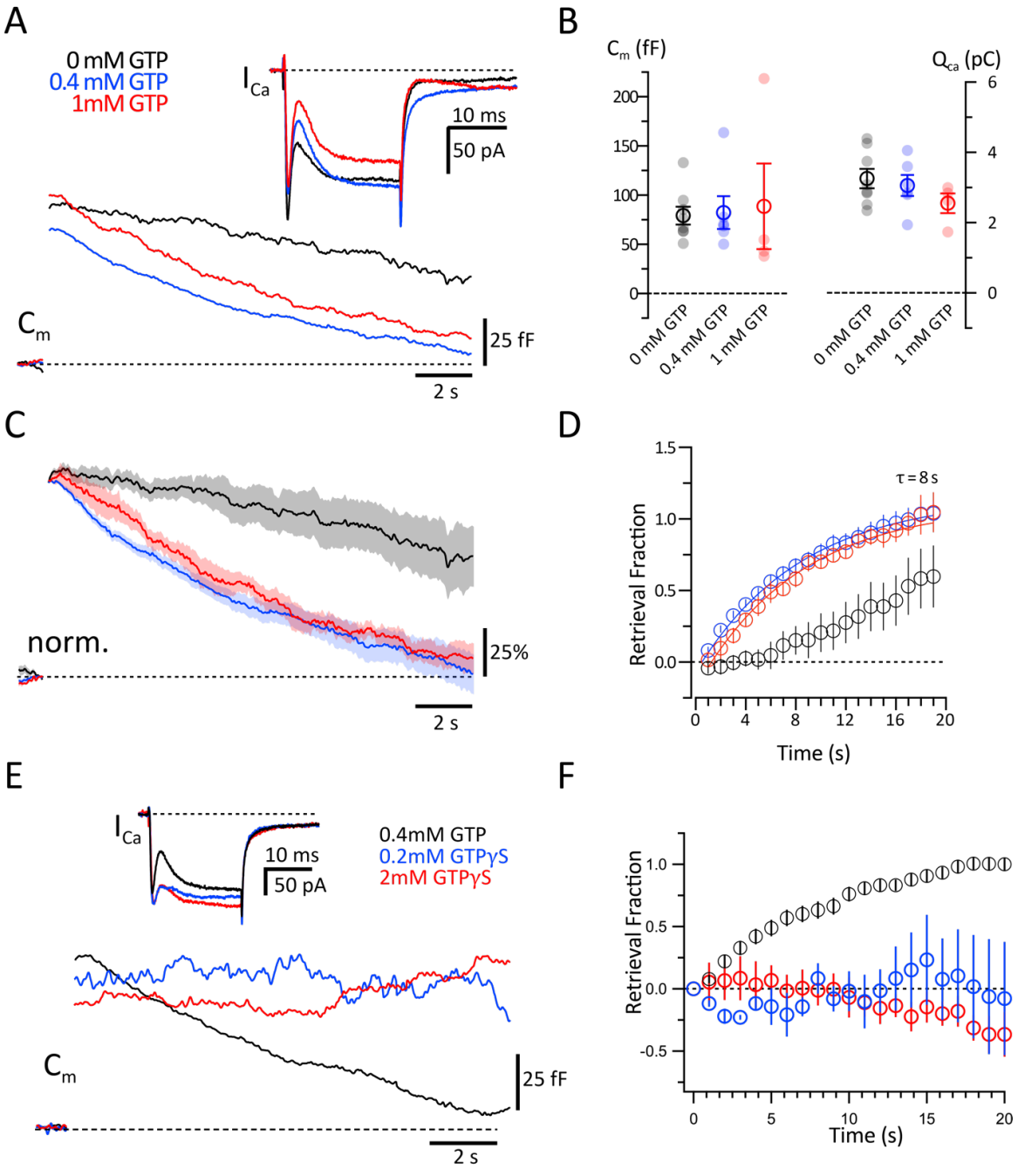

[S3.6] GTPγS [0.2-2 mM] blocks endocytosis in AII-ACs.

A, Average C_m and I_{ca} responses to a 20 ms depolarizing pulse for recordings performed using an internal solution containing 0 mM GTP (black; same as Fig. 3.6), 0.4 mM GTP (blue; same as Fig. 3.6), and 1 mM GTPS (red). Internal solution was Cs-based with 3 mM ATP and 2 mM EGTA. ***B,*** Summary plots for ΔC_m (left) and corrected Q_{Ca} (right) comparing each dataset. ***C,*** Normalized C_m responses to a 20 ms depolarizing pulse for 0 (black), 1 (blue) and 0.4 (red), mM GTP. Traces are displayed with shaded regions depicting mean ± SEM, comprising an average of several C_m responses for each individual cell ranging from 4 to 30 min after break-in. Note how the C_m response with a GTP free (0 mM GTP) solution has slower endocytosis, which does not return to baseline with 20s, and an increase

to 1 mM GTP did not change the endocytosis. ***D,*** Membrane retrieval fraction plotted against time after the initial C_m response (t = 0) for each dataset in panel A. Shown are open circles with error bars representing mean ± SEM and plotted as 1s bins. Continuous lines represent single exponential fits to 0.4 and 1 mM GTP datasets. Notice how the membrane does not fully recover (RF = 1) for the 0 mM GTP dataset, while both 0.4 and 1 mM GTP datasets fully recover at the same rate. ***E,*** Grand average C_m and I_{Ca} responses to a 20 ms depolarizing pulse for recordings with internal solutions containing (in mM) 0.4 GTP (black), 0.2 GTPɣS (blue) and 2 GTPɣS (red). Notice how the C_m responses for both 0.2 and 2 mM GTPɣs do not return back to baseline (dashed line). ***F,*** Membrane retrieval fraction plotted against time after initial ΔC_m response (t = 0) for 0.4 mM GTP, 0.2 mM GTPɣs, and 2 mM GTPɣS datasets. Notice that both 0.2 mM and 2 mM GTPɣS sufficiently block endocytosis. Open circles with error bars depicting mean ± SEM. Statistical comparisons were made using an ANOVA test and *post hoc* Tukey's test.

Section 3.7: Acknowledgements

This work was supported by National Institutes of Health Grants EY014043 and DC12938 to H.v.G.; and Casey Eye Institute P30 Grant EY010572. This work was union-made and upheld fair labor practices approved by AFSCME Local 402 OHSUGRU. Special thanks to my laboratory members Andre Dagostin, Benjamin Zemel, and Paulo Strazza. I am truly grateful for my thesis committee members Catherine Morgans, Stephen Smith, Benjamin Sivyer, Anusha Mishra, and Stefan Hallermann for their guidance and support. Special thanks to Tobias Moser and Jakob Neef for their perspectives and numerous discussions.

Section 3.8: References

Balakrishnan V, Puthussery T, Kim MH, Taylor WR, von Gersdorff H (2015) Synaptic vesicle exocytosis at the dendritic lobules of an inhibitory interneuron in the mammalian retina. Neuron 87:563-575.

Basu S, Lamprecht R (2018) The Role of Actin Cytoskeleton in Dendritic Spines in the Maintenance of Long-Term Memory. Front Mol Neurosci 11:143.

Borghuis BG, Tian L, Xu Y, Nikonov SS, Vardi N, Zemelman BV, Looger LL (2011) Imaging light responses of targeted neuron populations in the rodent retina. J Neurosci 31(8):2855-67.

Beutner D, Voets T, Neher E, Moser T (2001) Calcium dependence of exocytosis and endocytosis at the cochlear inner hair cell afferent synapse. Neuron 29(3):681-90.

Chen M, von Gersdorff H (2019) How to build a fast and highly sensitive sound detector that remains robust to temperature shifts. J Neurosci 39:7260-7276.

Cingolani LA, Goda Y. Actin in action: the interplay between the actin cytoskeleton and synaptic efficacy. Nat Rev Neurosci. 2008 May;9(5):344-56. doi: 10.1038/nrn2373. Erratum in: Nat Rev Neurosci. 2008 Jun;9(6):494.

Cho S, von Gersdorff H (2012) Ca(2+) influx and neurotransmitter release at ribbon synapses. Cell Calcium 52(3-4):208-16.

Cork KM, Thoreson WB (2014) Rapid kinetics of endocytosis at rod photoreceptor synapses depends upon endocytic load and calcium. Vis Neurosci 31(3):227-35.

Delvendahl, I., Vyleta, N.P., von Gersdorff, H, Hallermann, S (2016) Fast, Temperature-Sensitive and Clathrin-Independent Endocytosis at Central Synapses. Neuron. May 4;90(3):492-8.

De Camilli P, Takei K, McPherson PS (1995) The function of dynamin in endocytosis. Curr Opin Neurobiol. 5(5):559-65.

Dutta D, Williamson CD, Cole NB, Donaldson JG. Pitstop 2 is a potent inhibitor of clathrin-independent endocytosis. PLoS One. 2012;7(9):e45799.

Eggermann E, Bucurenciu I, Goswami SP, Jonas P (2011) Nanodomain coupling between Ca^{2+} channels and sensors of exocytosis at fast mammalian synapses. Nat Rev Neurosci 13(1):7-21.

Gillis KD (2000) Admittance-based measurement of membrane capacitance using the EPC-9 patch-clamp amplifier. Pflugers Arch 439:655-664.

Gillis KD, Mossner R, Neher E (1996) Protein kinase C enhances exocytosis from chromaffin cells by increasing the size of the readily releasable pool of secretory granules. Neuron 16(6):1209-20.

Granseth B, Odermatt B, Royle SJ, Lagnado L (2006) Clathrin-mediated endocytosis is the dominant mechanism of vesicle retrieval at hippocampal synapses. Neuron 51, 773–786.

Graydon CW, Lieberman EE, Rho N, Briggman KL, Singer JH, Diamond JS (2018) Synaptic transfer between rod and cone pathways mediated by AII amacrine cells in the mouse retina. Curr Biol 28:2739-2751.

Grimes WN, Li W, Chávez AE, Diamond JS. BK channels modulate pre- and postsynaptic signaling at reciprocal synapses in retina. Nat Neurosci. 2009 May;12(5):585-92.

Grimes WN, Sedlacek M, Musgrove M, Nath A, Tian H, Hoon M, Rieke F, Singer JH, Diamond JS (2021) Dendro-somatic synaptic inputs to ganglion cells contradict receptive field and connectivity conventions in the mammalian retina. Curr Biol S0960-9822(21)01528-1.

Habermann CJ, O'Brien BJ, Wässle H, Protti DA (2003) AII amacrine cells express L-type calcium channels at their output synapses. J. Neurosci 23(17):6904-13.

Hallermann S, Pawlu C, Jonas P, Heckmann M (2003) A large pool of releasable vesicles in a cortical glutamatergic synapse. Proc Natl Acad Sci USA 100(15):8975-80.

Hallermann S, Silver RA. Sustaining rapid vesicular release at active zones: potential roles for vesicle tethering. Trends Neurosci. 2013 Mar;36(3):185-94.

Hartveit, E., M.L. Veruki, and B.J. Zandt (2019) Capacitance measurement of dendritic exocytosis in an electrically coupled inhibitory retinal interneuron: an experimental and computational study. Physiol Rep 7(15): p. e14186.

Heidelberger R (2001) ATP is required at an early step in compensatory endocytosis in synaptic terminals. J Neurosci 21(17):6467-74.

Heidelberger R, Sterling P, Matthews G (2002) Roles of ATP in depletion and replenishment of the releasable pool of synaptic vesicles. J. Neurophysiol 88, 98–106.

Hosoi N, Holt M, Sakaba T (2009) Calcium dependence of exo- and endocytotic coupling at a glutamatergic synapse. Neuron 63(2):216-29.

Hull C, von Gersdorff H (2004) Fast endocytosis is inhibited by GABA-mediated chloride influx at a presynaptic terminal. Neuron 44(3):469-82.

Jackman SL, Choi SY, Thoreson WB, Rabl K, Bartoletti TM, Kramer RH. Role of the synaptic ribbon in transmitting the cone light response. Nat Neurosci. 2009 Mar;12(3):303-10.

Jockusch WJ, Praefcke GJ, McMahon HT, Lagnado L (2005) Clathrin-dependent and clathrin-independent retrieval of synaptic vesicles in retinal bipolar cells. Neuron 46(6):869-78.

Krinner S, Butola T, Jung S, Wichmann C, Moser T (2017) RIM-Binding Protein 2 promotes a large number of Cav1.3 Ca2+ channels and contributes to fast synaptic vesicle replenishment at hair cell active zones. Front Cell Neurosci 11:334.

Lagnado L, Schmitz F (2015) Ribbon Synapses and Visual Processing in the Retina. Annu Rev Vis Sci 1:235-262.

Leitz J, Kavalali ET (2011) Ca^{2+} influx slows single synaptic vesicle endocytosis. J Neurosci 31(45):16318-26.

Lindau M, Neher E. Patch-clamp techniques for time-resolved capacitance measurements in single cells. Pflugers Arch. 1988 Feb;411(2):137-46.

LoGiudice L, Matthews G (2007) Endocytosis at ribbon synapses. Traffic 8(9):1123-8.

Llobet A, Gallop JL, Burden JJE, Çamdere G, Chandra P, Vallis Y, Hopkins CR, Lagnado L, McMahon HT. Endophilin drives the fast mode of vesicle retrieval in a ribbon synapse. J Neurosci. 2011 Jun 8;31(23):8512-8519.

Meadows MA, Balakrishnan V, Wang X, von Gersdorff H (2021) Glycine Release Is Potentiated by cAMP via EPAC2 and Ca2+ Stores in a Retinal Interneuron. J Neurosci 41(46):9503-9520.

Miyano R, Miki T, Sakaba T (2019) Ca-dependence of synaptic vesicle exocytosis and endocytosis at the hippocampal mossy fibre terminal. J Physiol 597(16):4373-4386.

Mohanakrishnan A, Tran TVM, Kumar M, Chen H, Posner BA, Schmid SL. A highly-sensitive high throughput assay for dynamin's basal GTPase activity. PLoS One. 2017 Sep 28;12(9):e0185639.

Moser T, Grabner CP, Schmitz F. Sensory Processing at Ribbon Synapses in the Retina and the Cochlea. Physiol Rev. 2020 Jan 1;100(1):103-144.

Naraghi M, Neher E. Linearized buffered Ca2+ diffusion in microdomains and its implications for calculation of [Ca2+] at the mouth of a calcium channel. J Neurosci. 1997 Sep 15;17(18):6961-73.

Neef J, Jung S, Wong AB, Reuter K, Pangrsic T, Chakrabarti R, Kügler S, Lenz C, Nouvian R, Boumil RM, Frankel WN, Wichmann C, Moser T (2014) Modes and regulation of endocytic membrane retrieval in mouse auditory hair cells. J Neurosci. 34(3):705-16.

Neher, E (1992) Correction for liquid junction potential in patch clamp experiments. Enzymol. 207:123.

Neves G, Lagnado L (1999) The kinetics of exocytosis and endocytosis in the synaptic terminal of goldfish retinal bipolar cells. J Physiol 515 (Pt 1)(Pt 1):181-202.

Oltedal L, Mørkve SH, Veruki ML, Hartveit E (2007) Patch-clamp investigations and compartmental modeling of rod bipolar axon terminals in an in vitro thin-slice preparation of the mammalian retina. J Neurophysiol 97(2):1171-87.

Oltedal L, Hartveit E (2010) Transient release kinetics of rod bipolar cells revealed by capacitance measurement of exocytosis from axon terminals in rat retinal slices. J Physiol 588(Pt 9):1469-87.

Park RJ, Shen H, Liu L, Liu X, Ferguson SM, De Camilli P. Dynamin triple knockout cells reveal off target effects of commonly used dynamin inhibitors. J Cell Sci. 2013 Nov 15;126(Pt 22):5305-12.

Pyle JL, Kavalali ET, Piedras-Rentería ES, Tsien RW. Rapid reuse of readily releasable pool vesicles at hippocampal synapses. Neuron. 2000 Oct;28(1):221-31.

Pelassa I, Zhao C, Pasche M, Odermatt B, Lagnado L (2014) Synaptic vesicles are "primed" for fast clathrin-mediated endocytosis at the ribbon synapse. Front Mol Neurosci 7:91.

Renden R, von Gersdorff H. Synaptic vesicle endocytosis at a CNS nerve terminal: faster kinetics at physiological temperatures and increased endocytotic capacity during maturation. J Neurophysiol. 2007 Dec;98(6):3349-59.

Royle SJ, Lagnado L (2010) Clathrin-mediated endocytosis at the synaptic terminal: bridging the gap between physiology and molecules. Traffic 11:1489–1497.

Strettoi E, Raviola E, Dacheux RF (1992) Synaptic connections of the narrow-field, bistratified rod amacrine cell (AII) in the rabbit retina. J Comp Neurol 325:152-168.

Tanimoto N, Sothilingam V, Euler T, Ruth P, Seeliger MW, Schubert T. BK channels mediate pathway-specific modulation of visual signals in the in vivo mouse retina. J Neurosci. 2012 Apr 4;32(14):4861-6.

Van Hook MJ, Thoreson WB (2012) Rapid synaptic vesicle endocytosis in cone photoreceptors of salamander retina. J Neurosci. 32(50):18112-23.

Vardi N, Smith RG. The AII amacrine network: coupling can increase correlated activity. Vision Res. 1996 Dec;36(23):3743-57.

von Gersdorff H, Matthews G (1994a) Dynamics of synaptic vesicle fusion and membrane retrieval in synaptic terminals. Nature. 367(6465):735-9.

von Gersdorff H, Matthews G (1994b) Inhibition of endocytosis by elevated internal calcium in a synaptic terminal. Nature 370(6491):652-5.

Watanabe S, Liu Q, Davis MW, Hollopeter G, Thomas N, Jorgensen NB, Jorgensen EM (2013) Ultrafast endocytosis at Caenorhabditis elegans neuromuscular junctions. Elife 2:e00723.

Watanabe S, Rost BR, Camacho-Pérez M, Davis MW, Söhl-Kielczynski B, Rosenmund C, Jorgensen EM (2013b) Ultrafast endocytosis at mouse hippocampal synapses. Nature. 504(7479):242-247.

Williams C, Chen W, Lee CH, Yaeger D, Vyleta NP, Smith SM. Coactivation of multiple tightly coupled calcium channels triggers spontaneous release of GABA. Nat Neurosci. 2012 Sep;15(9):1195-7.

Willox AK, Sahraoui YM, Royle SJ. Non-specificity of Pitstop 2 in clathrin-mediated endocytosis. Biol Open. 2014 Apr 4;3(5):326-31.

Yamashita T, Hige T, Takahashi T. Vesicle endocytosis requires dynamin-dependent GTP hydrolysis at a fast CNS synapse. Science. 2005 Jan 7;307(5706):124-7.

Yamashita T, Eguchi K, Saitoh N, von Gersdorff H, Takahashi T (2010) Developmental shift to a mechanism of synaptic vesicle endocytosis requiring nanodomain Ca2+. Nat Neurosci 13(7):838-44.

Yamashita, T. (2012) Ca2+-dependent regulation of synaptic vesicle endocytosis. Neurosci Res. 73(1):1-7.

Yao L, Sakaba T (2012) Activity-dependent modulation of endocytosis by calmodulin at a large central synapse. Proc Natl Acad Sci USA 109(1):291-6.

Zandt BJ, Veruki ML, Hartveit E (2018) Electrotonic signal processing in AII amacrine cells: compartmental models and passive membrane properties for a gap junction-coupled retinal neuron. Brain Struct Funct 223:3383-3410.

Zampighi GA, Schietroma C, Zampighi LM, Woodruff M, Wright EM, Brecha NC (2011) Conical tomography of a ribbon synapse: structural evidence for vesicle fusion. PLoS One 6(3):e16944.

Chapter 4: Ca^{2+} imaging in AII-ACs and crossover inhibition network modulation by dopamine

Marc A. Meadows,[1] Xiaohan Wang[1] and Henrique von Gersdorff[1,2,3]

[1]The Vollum Institute, Oregon Health & Science University, Portland, Oregon 97239

[2]Casey Eye Institute, Department of Ophthalmology, Oregon Health & Science University, Portland, Oregon 97239

[3]Department of Chemical Physiology and Biochemistry, Oregon Health & Science University, Portland, Oregon 97239

Author Contributions: M.A.M. and H.v.G. designed the studies; XW collected data for figure 4.8; M.A.M performed experiments; M.A.M. and H.v.G. wrote the paper.

Unpublished works

Section 4.1: Summary

The published findings that cAMP and EPAC2 potentiates AII-AC glycine release is overviewed in chapter 2 of this thesis. Those findings demonstrate that Ca^{2+} induced Ca^{2+} release (CICR) from internal stores plays a pivotal role in potentiating AII-ACs. This chapter presents preliminary results building on the published findings in chapter 2 by exploring how CICR is modulated in AII-ACs. We used calcium imaging to explore the kinetics of CICR using a genetically encoded calcium sensor in addition to pre- and postsynaptic recordings. We found picospritzer injections of the EPAC2 activator (8-pCPT) triggered CICR in AII-ACs. However, we also found that dopamine reduced glycine release, and the mechanism initiating cAMP-dependent potentiation is still elusive and warrants further study.

Section 4.2: Introduction

Crossover inhibition refers to when excitatory input from rod or ON bipolar cells is converted by AII-ACs into inhibition of the OFF-CBC. There are both GABA and glycinergic inputs to OFF-CBCs and AII-ACs release glycine, providing crosstalk from the parallel ON pathways. The rod BC makes chemical glutamatergic synapses with AII-ACs. This synapse is unidirectional aside from GABAergic feedback from A17 ACs. Electrical synapses between AII-ACs and ON-CBCs via gap junctions, however, are presumably bidirectional. Furthermore, homomeric gap junction coupling allows signals to spread throughout a network of junction coupled AII-ACs (Reviewed in Demb and Singer, 2012).

Glycine release by the AII-AC increases the signal-to-noise ratio of ON light responses by suppressing the OFF-CBC activity within the same receptive field. Potentiation induced by cAMP is observed in AII-ACs, allowing them to adapt to changing luminance providing increased inhibition to OFF-CBCs. We showed cAMP induced potentiation is dependent on an EPAC2 pathway (Meadows et al., 2021). This process also relies on Ca^{2+} induced Ca^{2+} release (CICR) from internal Ca^{2+} stores in the endoplasmic reticulum (ER). CICR is enhanced by EPAC2 at central synapses. This has been shown directly measuring BK currents or with Ca^{2+} imaging at these central circuits (Ster et al., 2007), however this has not been demonstrated in the AII-AC. Ca^{2+} imaging is a useful tool for studying stimulation dependent activity in cellular compartments. Ca^{2+} indicator dyes were used in AII-ACs, to show that L-type $Ca_V1.3$ channels localize to the lobular compartments (Balakrishnan et al., 2015). GCaMP6F is the genetically encoded Ca^{2+} indicator with fast kinetics, strong fluorescence signal, and is widely used to study single or populations of neurons (Chen et al., 2013). We targeted expression of GcAMP6f to inhibitory retinal neurons using a GlyT2-cre mouse line, which labeled narrow field amacrine cells including the AII-ACs. This allowed us to develop methods for live Ca^{2+} imaging to study AII-AC networks.

The initial mechanism upregulating cAMP in the AII-AC lobules is still unknown and therefore the mechanism for long-term potentiation induction is unknown for these cells. We showed that adenylyl cyclase activation induces potentiation, which validates the presence of local cAMP upregulation in the lobules (Meadows et al., 2021). Adenylyl cyclases are activated by either Ca^{2+}

or by G-proteins activated by G-protein coupled receptors (GPCRs), depending on subtype (Sadana and Dessauer, 2009; Halls and Cooper, 2011). Dopamine, among other neuromodulators, released throughout the retina alters visual process across transitions from daytime to nighttime conditions (Roy and Field, 2019). We tested the effects of dopamine on the sIPSC in type 2 OFF-CBCs and found a reduction in frequency, which may arise from the uncoupling of the AII-AC network and from ON-CBCs (Hampson et al., 1992; Mills and Massey, 1995 ; Xia and Mills, 2004). It is currently unknown if dopamine signaling initiates the signaling cascade, involving cAMP, that induces potentiation in AII-ACs; however, dopamine is one likely candidate due to the known role that D1-like receptors have in AII-AC coupling.

Section 4.3: Results

There are still many unanswered questions following up our published manuscript on cAMP potentiation in AII-ACs (Meadows et al., 2021). Can EPAC2 trigger CICR? How far are Ca^{2+} stores from the active zones? Does dopamine induce potentiation? We attempt to address these questions in this chapter.

4.3.1 GCaMP6F imaging to study single and population AII-AC activity

The expression patterns of the Glyt2-Cre mouse line have never been reported in the mouse retina. The expression of glycine transporters in the inner retina (Peña-Rangel et al., 2008) indicate that this could be a useful tool for studying amacrine cells. We performed crosses to generate the Glyt2-Cre;TdTomato and Glyt2-Cre;GCaMP6F mouse lines (see Section 4.5: Materials & Methods).

4.3.1a Targeted expression of tdTomato in the retina using the Glyt2-Cre mouse line

GlyT2-Cre expression in the retina was first assessed by using the Glyt2-Cre;TdTomato mouse line (confocal images were provided by Benjamin; Fig. 4.1). Broad TdTomato expression was observed in post-fixed whole-mount preparations using low magnification (10x) confocal imaging (Fig. 4.1A). At higher magnification, we were able to image cell bodies in the INL and projections into the IPL (Fig. 4.1 B, C). We observed TdTomato expression in a subset of ganglion cells (data not shown). Further analysis determined that a majority of TdTomato labeling in the INL were from

glycinergic amacrine cells (poster abstract: Sivyer et al., 2019). We also imaged live retinal slices from the Glyt2-Cre;TdTomato mouse. We were able to see TdTomato expression in a morphologically distinct AII-AC (Fig. 4.1D).

Figure[4.1]

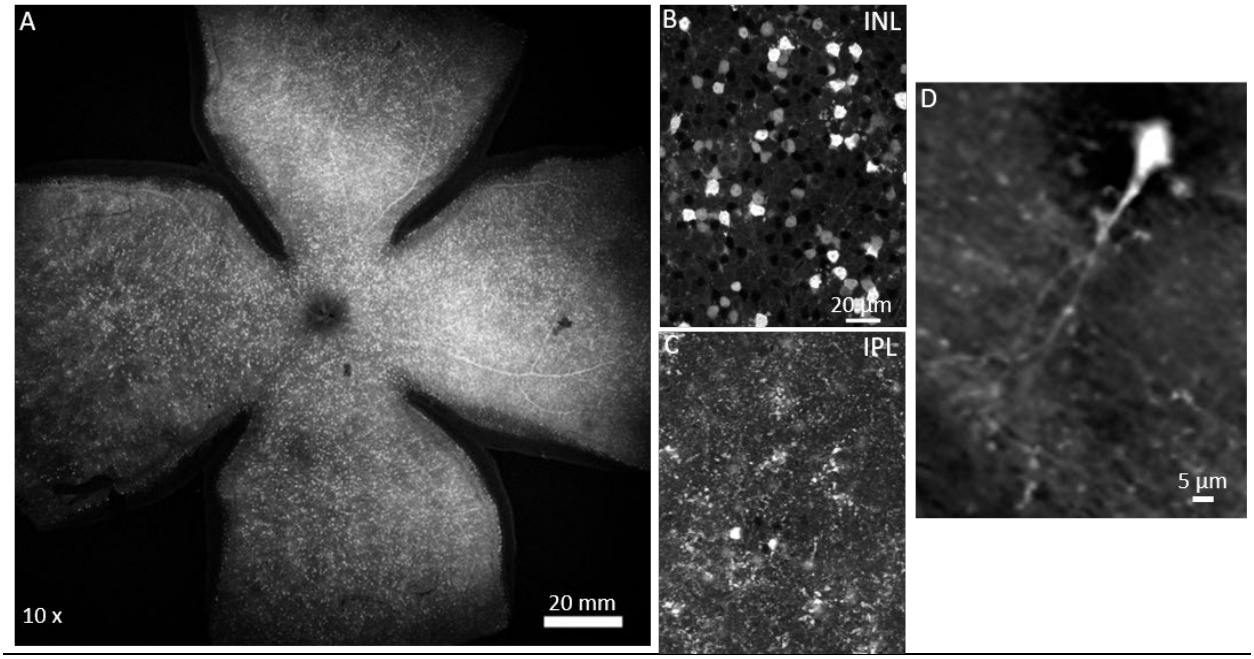

[4.1] TdTomato expression driven by Glyt2-Cre.

Glyt2-Cre;TdTomato mouse retinae were imaged to validate GlyT2-Cre expression. Post-fixed whole-mount retina was imaged (***A*** **-** ***C***). ***A,*** Confocal (Leica) micrograph of whole-mount tile-scan image at 10x magnification; scale bare is 20 mm. ***B & C***, Confocal micrograph focused on the INL (***B***) and IPL (***C***) imaged using a 40 x objective; scale bar is 20 µm. ***D,*** Slice projection (Olympus) of an AII-AC expressing TdTomato. Images (***A*** **-** ***D***) were provided by Benjamin Sivyer.

4.3.1b Compartmental localization of GCaMP6F signaling and Ca^{2+} handling in AII-AC dendrites

AII-ACs have a single class of L-type calcium channels ($Ca_v1.3$) that localize to the dendritic lobules after eye-opening (Balakrishnan et al 2015). There are narrow caliber processes, called necks, connecting the lobules to the root dendrite. The thin necks may make lobules isolated compartments that confines Ca^{2+} into areas suitable for calcium extrusion, (i.e. Na-Ca exchange proteins). We predict that lobules have faster calcium extrusion than larger cellular compartments like the AII-AC soma. We used the *Glyt2-Cre;GCaMP6f* mouse line to test if lobule have faster extrusion than the larger soma compartment by performing whole-cell voltage-clamp

recordings on AII-ACs using a Cs-based, EGTA-free solution (Fig. 4.2). We used a 2 mM EGTA solution, which yielded no Ca^{2+} fluorescence response (data not shown). We observed characteristic C_m responses and I_{Ca} for AII-ACs as well as passive R_m and R_s responses (Fig. 4.2A).

Figure[4.2]

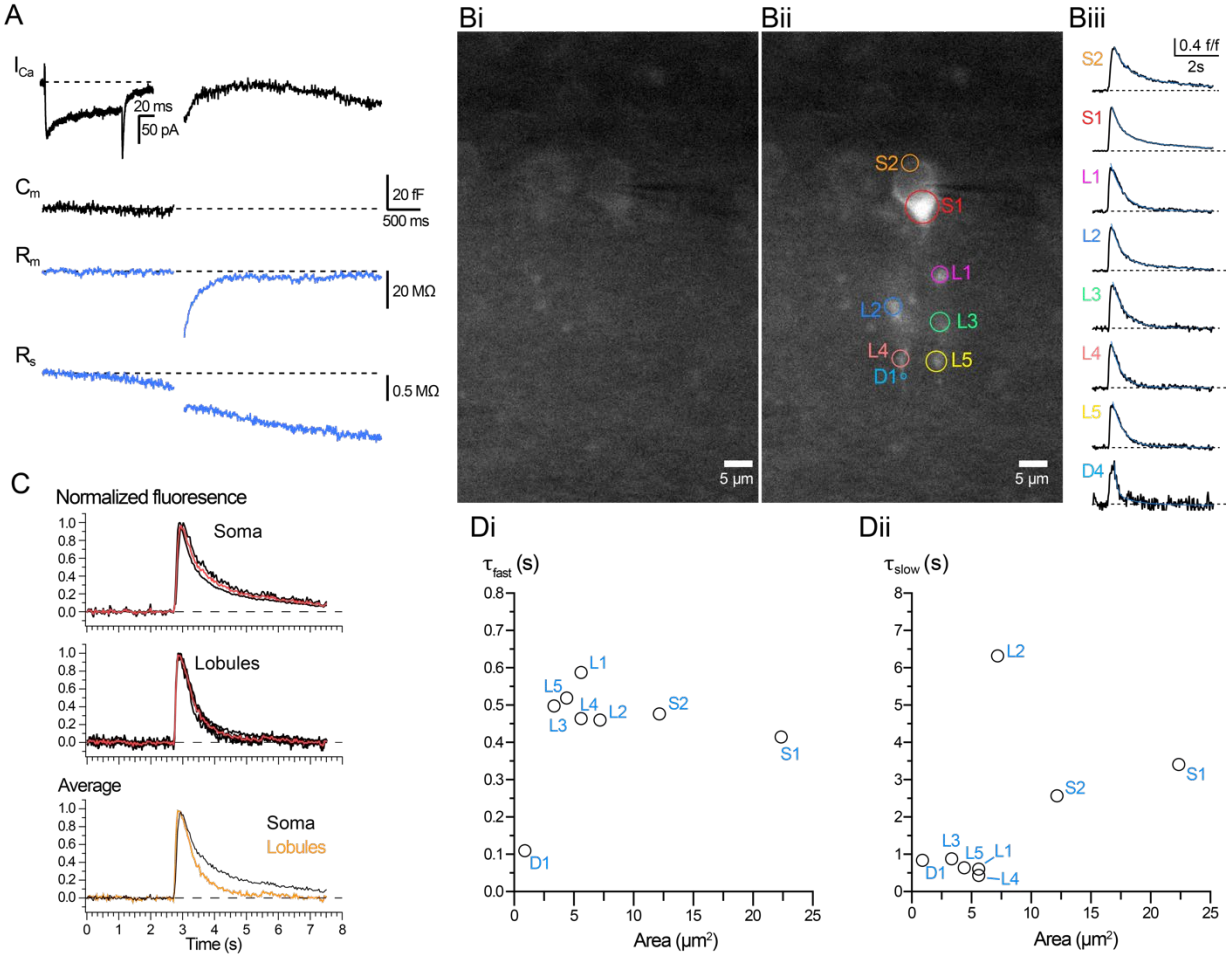

[4.2] Calcium imaging in AII-ACs.

Whole-cell voltage-clamp recordings performed on a single AII-AC from a *Glyt2-Cre;GCaMP6F* mouse***. A,*** Voltage-clamp responses to a 100 ms depolarizing pulse (from -80 to -10 mV), showing I_{Ca} and C_m responses (black traces). Also shown are R_m and R_s traces. Notice that the ΔC_m response is about 50 fF, which is comparable to our other recordings in wild-type C57 mice***. B,*** Epifluorescence imaging before stimulation ***(Bi)*** and during stimulation **(*Bii*)**, image shown is at peak GCaMP6F response. Labeled on the graph are ROIs that correspond to fluorescence traces in ***Biii*** and blue lines represent double exponential fits***. C,*** Normalized fluorescence traces for the soma (top) and lobules (bottom). Black traces represent individual ROIs and red trace depicts the mean. Notice that the decay is slower for soma ROIs***. D,*** Plot of time constants against ROI area from double exponential fits. Shown are plots for τ_{fast} **(*Di*)** and τ_{slow} **(*Dii*)**, and each ROI is labeled on the graph. Notice that τ_{fast} values are similar, while the τ_{slow} values for lobules and soma are different.

We observed a continual increase in the C_m response after depolarization that could indicate to asynchronous release. The reduction of the Ca^{2+} buffer concentration could contribute to asynchronous release due to residual free-Ca^{2+} at the active zone. However, we also saw a similar trend in the R_m response indicating that cross-talk between the R_m and C_m calculation could be responsible, rather than asynchronous release. Epifluorescence imaging captured GCaMP signals during the depolarizing pulse (Fig. 4.2B). We marked Ca^{2+} hotspots in Figure 4.2Bii for the soma, lobules and dendritic branch as regions of interest (ROI) and included fluorescence traces that that were baseline corrected using the background fluorescence before the stimuli, shown in figure 4.2Bi. Fluorescence traces were scaled between 0 and 1 using the formula:

$$Normalized\ Fluorescence = \frac{F - F_{min}}{F_{max} - F_{min}}$$

Where F, F_{min}, and F_{max} were the instantaneous, minimum, and maximum fluorescence intensity. The normalized fluorescence traces were used to compare decay kinetics (Fig. 4.1C), which were fitted with a double exponential function. The fast time constant (τ_{fast}) for lobules and soma ROIs were similar (~ 0.5 s), which may correspond to the off rate of Ca^{2+} binding to the GCaMP6F sensor. We did find that the slow time constant (τ_{slow}) was faster in lobules (~ 1 s) than in the soma (~ 3 s); however, more work needs to be done to determine if there is a correlation between the compartment area and the decay (Fig. 4.2D). Although this work is preliminary, it is promising evidence that Ca^{2+} clearance is faster in lobular compartments when compared to the soma. Furthermore, the dim signals in the dendritic branch ROI did not fit well possibly due to low signal to noise.

4.3.1c ON-CBCs signals propagate to AII-ACs through gap junction coupling.

Gap junctions in the distal dendrites of AII-ACs allow these cells to form homocellular electrically coupled networks. Gap junctions also form between AII-ACs and ON-CBCs (Hampson et al., 1992; Mills and Massey, 1995). These function as electrical synapses allowing signals to pass from AII-AC to ON-CBC and vice versa (Fournel et al., 2021). AII-ACs can also use these electrical synapses to relay excitatory synaptic signals from single RBCs to ON-CBCs (Graydon et al., 2018). We used the Glyt2-Cre;GCaMP6F mouse to demonstrate that electrical signals from ON-CBCs can activate

Figure[4.3]

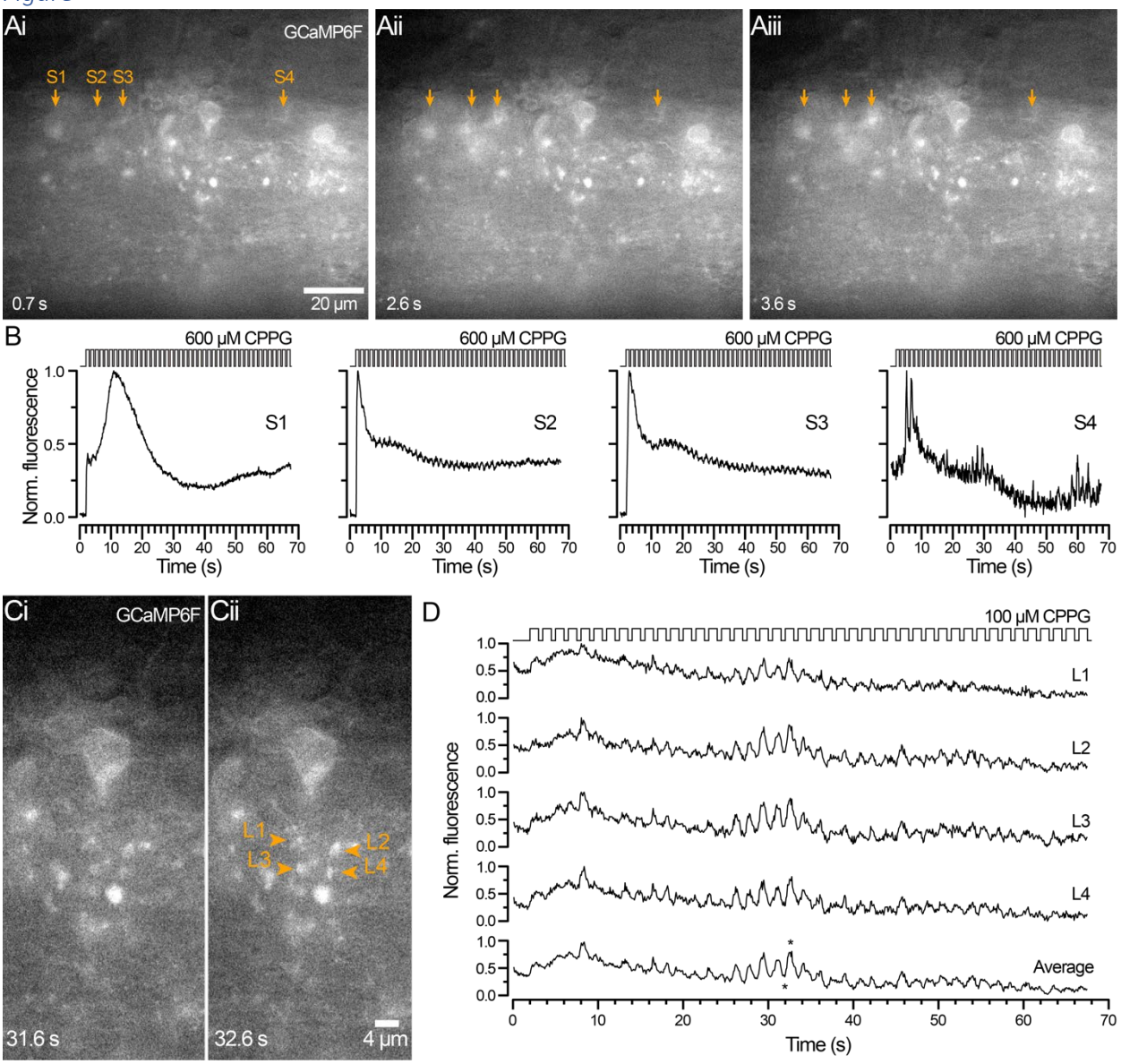

[4.3] CPPG puffs demonstrate transmission from ON-CBCs to AII-AC networks.

Retina slices prepared from *Glyt2-Cre;GCaMP6F* mice were perfused with an external solution containing Ames medium with 10 µM L-AP4, CNQX, and DL-AP5. A pipette containing 600 µM CPPG in solution in Ames medium was lowered near the OPL before image capture. Picospritzer injection pulses (1 s duration; 0.5 s intervals) given 2 s into time-lapse imaging (10 ms exposures)***. A,*** Micrographs showing epifluorescence signals from AII-ACs expressing GCaMP6F after background subtraction. Shown are images taken before injection (***Ai***) and during injections (***Aii***-***Aiii***) at fluorescence signal. Arrows indicate location of AII-ACs that exhibited fluorescent signals. Scale bar is labeled on ***Ai***, and labeled on each micrograph is a time stamp displaying seconds***. B,*** Histograms of normalized fluorescence intensity over time for each ROI, labeled above each trace. Above each graph is the CPPG injection pattern***. C,*** Micrographs showing GCaMP6F fluorescence in lobules during the same time-lapse sequence

as ***A***. Shown are images during a flicker response to CPPG injection pulses when fluorescence was low (***Ci***) and peaked (***Cii***). Labeled on ***Cii*** are arrowheads that indicate ROIs marking lobules with entrained flicker responses. ***D,*** Histograms of normalized fluorescence intensity over time for each ROI from panel ***Cii*** and average response (bottom trace). The CPPG injection pattern is labeled at the top of graphs, and ROIs are labeled above each trace. Asterisks represent timepoints for each image in ***C***. Notice how the baseline fluorescence before injections in this region was higher than in AII-AC somas from panels **A-B**, and strong flicker events occurred 26 seconds after the start of injections.

AII-ACs (Fig. 4.3). We used CNQX and DL-AP5 to block glutamatergic excitation of the AII-ACs by RBCs. Group III mGluR mediated depolarization of rod and ON-CBCs was blocked using mGluR activator L-2-amino-4-phosphonobutyrate (L-AP4; 10 µM). L-AP4 mediated block can be reversed by 200 µM mGluR antagonist (RS)-α-cyclopropyl-4-phosphonophenylglycine (CPPG; Awatramani and Slaughter, 2001). We used a picospritzer to puff 600 µM CPPG prepared in Ames medium. We observed a chain reaction of GCaMP signaling within the INL (Fig. 4.3A, B). Furthermore, in focus AII-AC lobules exhibited fluorescent GCaMP signals in response to the CPPG puff (Fig. 4.3C, D). Therefore, we demonstrate that signals from the ON-CBC are propagating to the AII-ACs through heterocellular gap junctions.

4.3.1d Fluorescent GCaMP6F imaging of EPAC2-dependent Ca^{2+} release from internal stores

Our previous study indicates cAMP potentiates AII-ACs by enhancing Ca^{2+} release from internal stores. We also proposed that an EPAC-mediated pathway is involved in regulating CICR in the AII-ACs. However, we did not directly show that EPAC2-activation enhances or triggers CICR in AII-ACs. Here we used the *Glyt2-Cre;GCaMP6F* mouse to demonstrate that the membrane permeable EPAC-activator, 8-pCPT, evokes fluorescent GCaMP signals (Fig. 4.4). We pre-incubated slices in 10 µM L-AP4 to prevent light dependent responses. L-AP4 was continuously perfused during imaging. We lowered a pipette containing 100 µM 8-pCPT in Ames medium near the INL for local application with a picospritzer. Before 8-pCPT injection, we observed spontaneous fluorescence signals, though these cells were not included in our region of interest. During the puff administration of 8-pCPT we observed GCaMP responses in AII-ACs (Fig. 4.4A). Some signals were monophasic responses immediately following the puff, and others occurred sporadically over the duration of the 8-pCPT injection (Fig. 4.4B).

Figure[4.4]

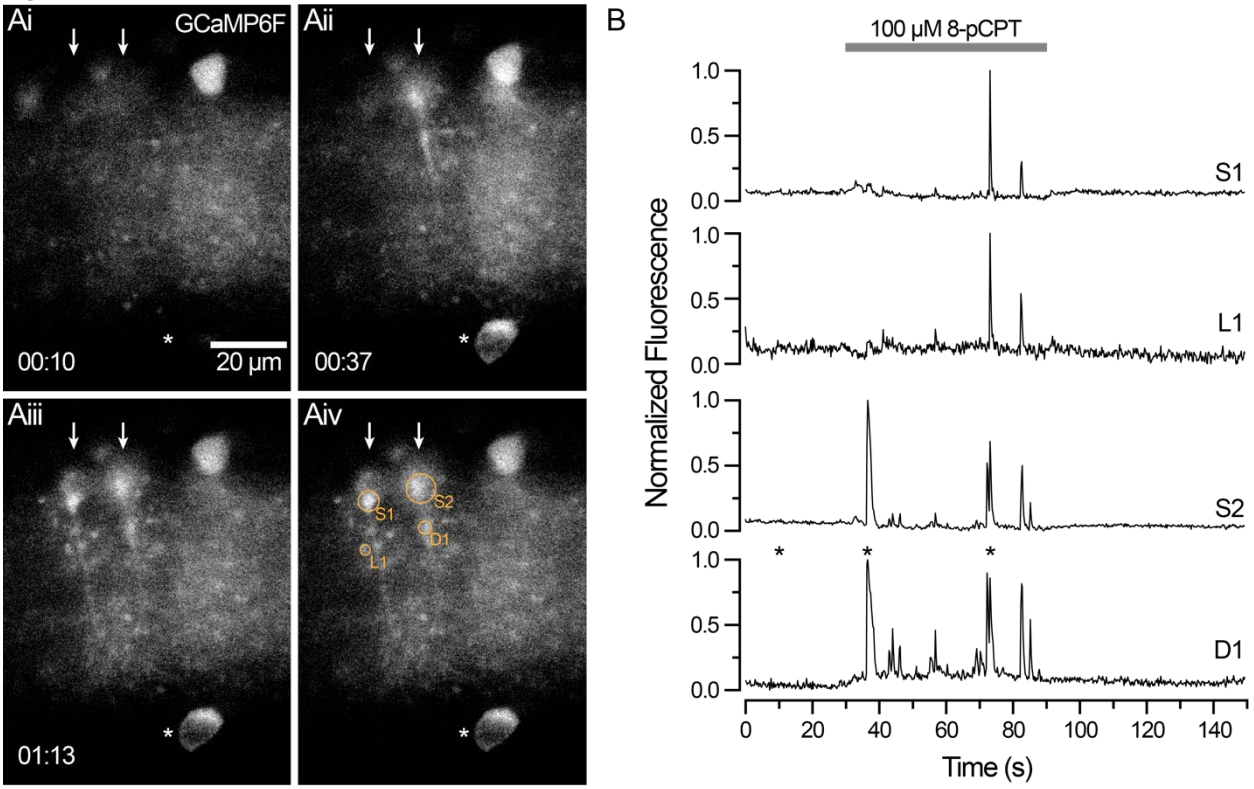

[4.4] EPAC induces fluorescent signals in AII-ACs from *Glyt2-Cre;GCaMP6F* mice.

Retina slices prepared from *Glyt2-cre;GCaMP6F* mice were perfused with an external solution containing Ames medium with 10 µM L-AP4. A pipette containing 100 µM 8-pCPT in solution same as the external solution was lowered near the retina slice. Time-lapse images were captured using 200 ms exposures***. A,*** Micrographs showing epifluorescence signals from AII-ACs expressing GCaMP6F after background subtraction. Shown are images taken before (***Ai***) and during (***Aii*** - ***Aiii***) injection of 100 µM 8-pCPT. Arrows indicate location of AII-ACs and asterisks label a ganglion cell that exhibit fluorescent signals. Scale bar is labeled on ***Ai***. Time stamp displays mm:ss and labeled on each micrograph. ***Aiv*** shows the location of ROIs for each AII-AC soma (S1-2), a lobule (L1), and dendrite (D1)***. B,*** Histograms of normalized fluorescence intensity over time for each ROI, labeled above each trace. Grey bar indicates region of 8-pCPT injection. Asterisks above the bottom panel indicate time points shown in ***A***. Notice how rises in fluorescence signal only occurs during 8-pCPT injection.

These preliminary results suggest that EPAC2 activation can either trigger CICR or increase the release probability of ryanodine receptors. We also found that Ca^{2+} release from internal stores can be triggered within the same AII-ACs by either 8-pCPT or 10 mM caffeine (Fig. 4.5). We observed three amacrine cells within a field of view that responded to injections of 100 µM 8-pCPT, and at least two exhibited lobules indicating they are AII-ACs (Fig. 4.4Ai - Aii).

Figure[4.5]

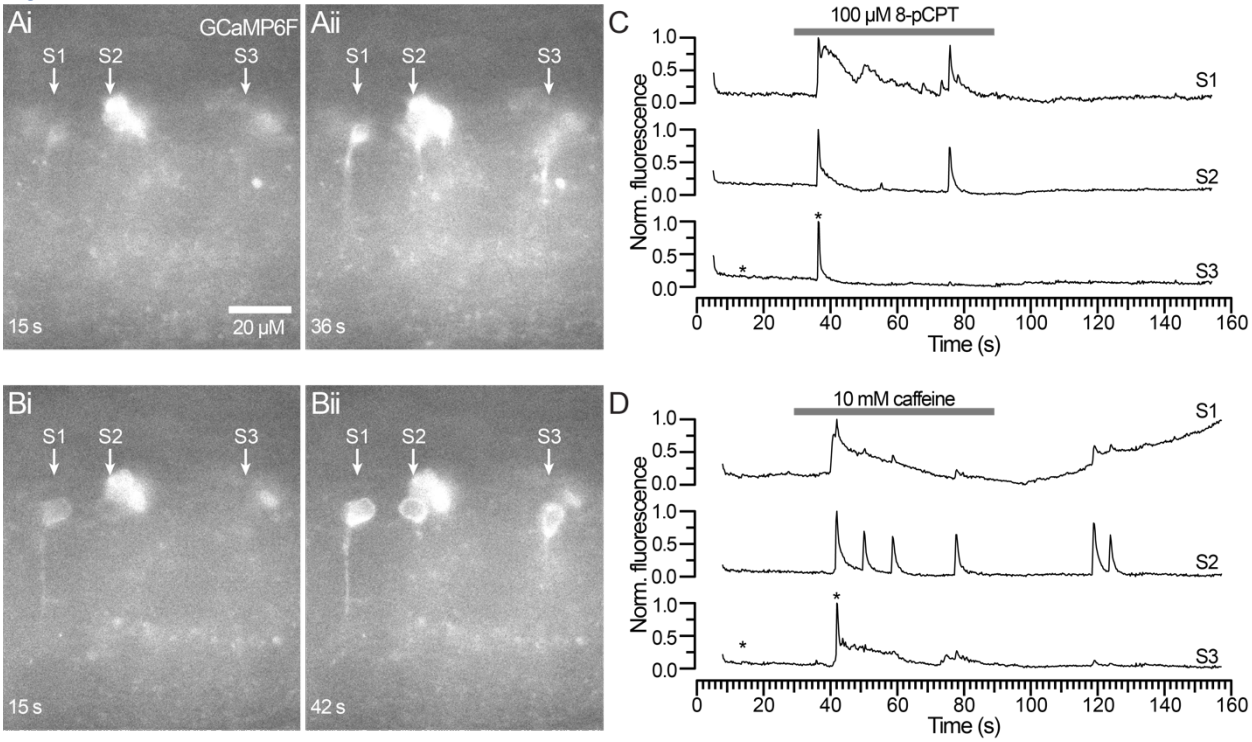

[4.5] Ca^{2+}stores produce GCaMP6F signals in response to 8-pCPT and caffeine.

Retina slices prepared from *Glyt2-Cre;GCaMP6F* mice were perfused with an external solution containing Ames medium with 10 µM L-AP4. Injections of 100 µM 8-pCPT were performed first and followed by injections with 10 mM Caffeine; both were prepared in the external solution. Time-lapse images were captured using 200 ms exposures. ***A-B,*** Micrographs showing epifluorescence GCaMP6F signals without background subtraction. Shown in ***Ai*** & ***Bi*** are images of the same region before picospritzer injection. Scale bar is labeled on each micrograph. Also shown are images during injection of 8-pCPT (***Aii***) and caffeine (***Bii***). Arrows label AII-ACs used for analysis. Notice how each indicated AII-AC respond to both 8-pCPT and caffeine. Although the focal plane did change between experiments, fluorescence responses can be seen in dendrites and somas. ***C - D,*** Histograms of normalized fluorescence intensity over time for each AII-AC. Shown are traces from experiments with 8-pCPT ***(C)*** and caffeine (***D***). Grey bar above intensity histograms indicates the time of injection. Labeled above each trace is the AII-AC marked on micrographs. Asterisks on bottom panel (**C & *D***) indicate the timepoints shown in micrographs (***A*** & ***B***).

We changed out the injection pipette with a solution containing 10 mM caffeine which is within the adequate concentration range to stimulate CICR (5- 20 mM; Ehrlich et al., 1994; Vyleta and Smith, 2008) and observed calcium responses from the same amacrine cells (Fig. 4.5Bi-ii). The intensity profiles from each experiment show that a maximal fluorescent GCaMP6F signal occurred within 10-15 seconds after the start of the injection. We observed a second smaller,

smaller GCaMP6F signal in some AII-ACs that occurred during the 8-pCPT injection (Fig. 4.5C). Subsequent GCaMP6F signals occurred during caffeine injections, which continued after the injection (Fig. 4.5D). These preliminary results provide qualitative data that EPAC2 can trigger calcium release from internal ER stores; however, more data will be required for statistical analysis. Furthermore, we must determine that injections of drug-free solution do not trigger GCaMP6f responses as a proper negative control.

4.3.2 Ca^{2+} release from ER stores is peripheral to the AII-AC active zones

Figure[4.6]

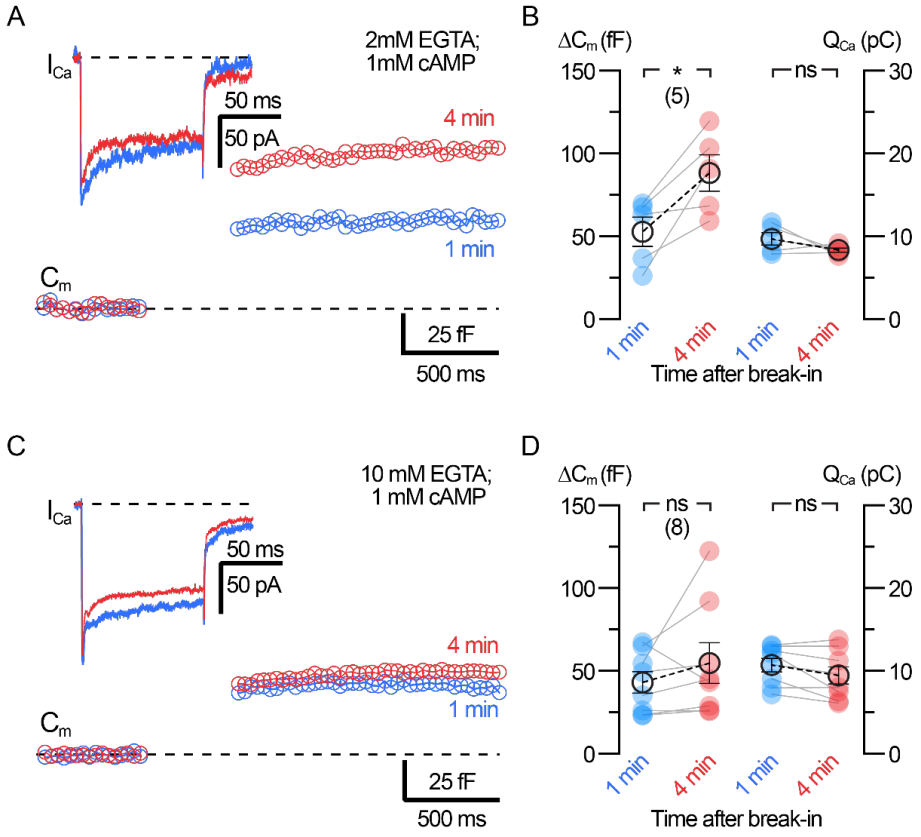

[4.6] cAMP-induced potentiation via Ca^{2+} release from stores is blocked by high [EGTA].

A & ***C,*** Average traces of I_{Ca} (inset) and C_m responses from AII-ACs. Shown are traces recorded within 1 min (blue) and at 4 min (red) after whole-cell break-in. Each panel shows recordings performed with 1 mM cAMP and either 2 mM ***(A)*** or 10 mM ***(C)*** EGTA in the patch pipette. ***B*** & ***D,*** Summary plots for ΔC_m and Q_{Ca} showing pairwise comparisons between each time after break-in. Panels display results for 2 mM ***(B)*** and 10 mM (***D***) datasets. Closed circles represent data from individual AII-ACs and open circles with error bars depict mean ± SEM. Notice how the ΔC_m responses in the 2 mM EGTA dataset significantly increase after 4 min and do not increase with the 10 mM EGTA dataset. Also, the slight reduction in Q_{Ca} was not significant for either dataset. Statistical significance was determined using a Paired t-test. (ns; $p > 0.05$, *; $p < 0.05$).

We provide clear evidence that cAMP, EPAC2, and CICR are involved with potentiating synaptic release in AII-ACs. Electron micrographs indicate that AII-AC lobules are densely packed with synaptic vesicles (Marc et al., 2014). The surplus of vesicles gives rise to a 2-pool release model of closely primed vesicles and a secondary reserve vesicle pool (Balakrishnan et al., 2015; Meadows et al., 2021). The spatial organization of calcium stores and internal calcium channels relative to vesicle trafficking and fusion machinery is not known for AII-ACs, so we turned back to C_m recordings to test how calcium buffer concentration affects cAMP-induced potentiation (Fig. 4.6). In this experiment we prepared two internal solutions; one with 2 mM and with 10 mM EGTA. Both solutions also contained 1 mM cAMP. We observed increased ΔC_m responses 4 min after break-in when using a 2 mM EGTA internal solution containing 1 mM cAMP (Fig. 4.5A-B). This result was consistent with our published findings (Meadows et al., 2021). In the same set of slices, we did not observe cAMP-induced potentiation when using the 10 mM EGTA internal solution with 1 mM cAMP (Fig. 4.6C-D). Since 10 mM EGTA can block the cAMP-induced potentiation without inhibiting exocytosis, we conclude that the effect of CICR occurs further from the vesicle release machinery (i.e. synaptotagmin). Therefore, CICR may induce potentiation by enhancing vesicle trafficking to the active zone.

4.3.3 Modulation of glycine release

4.3.3a Dopamine reduces glycine release to OFF-CBCs

To follow up on our conclusion that cAMP increases synaptic transmission to the OFF-CBC, we are interested in how cAMP is upregulated in the presynaptic AII-ACs. Regulation of adenylyl cyclase by G-protein coupled receptors is a ubiquitous mechanism among cells to convert ATP to cAMP. Among the neuromodulators found in the retina, we chose to test dopamine because D1-like receptor signaling has been characterized in AII-ACs. We performed whole-cell voltage-clamp recordings in OFF-CBCs of sIPSCs. We targeted type 2 OFF-CBCs using the *Syt2*-EGFP, which receive 82% AII-AC outputs (Graydon et al., 2018). Glycinergic currents were isolated using iGluR and GABAR blockers (CNQX, DL-AP5, bicuculline, and gabazine). The bath application of 10 µM dopamine caused a reduction of the sIPSC frequency by 30 seconds after drug application, as seen in the raw traces and diary plot (Fig. 4.7A-B). We observed a 50% decrease in the normalized sIPSC frequency (Fig. 4.7F; $p = 0.0031$) and raw values (pre-treatment: 87.3 ± 32.8 Hz, and

Figure[4.7]

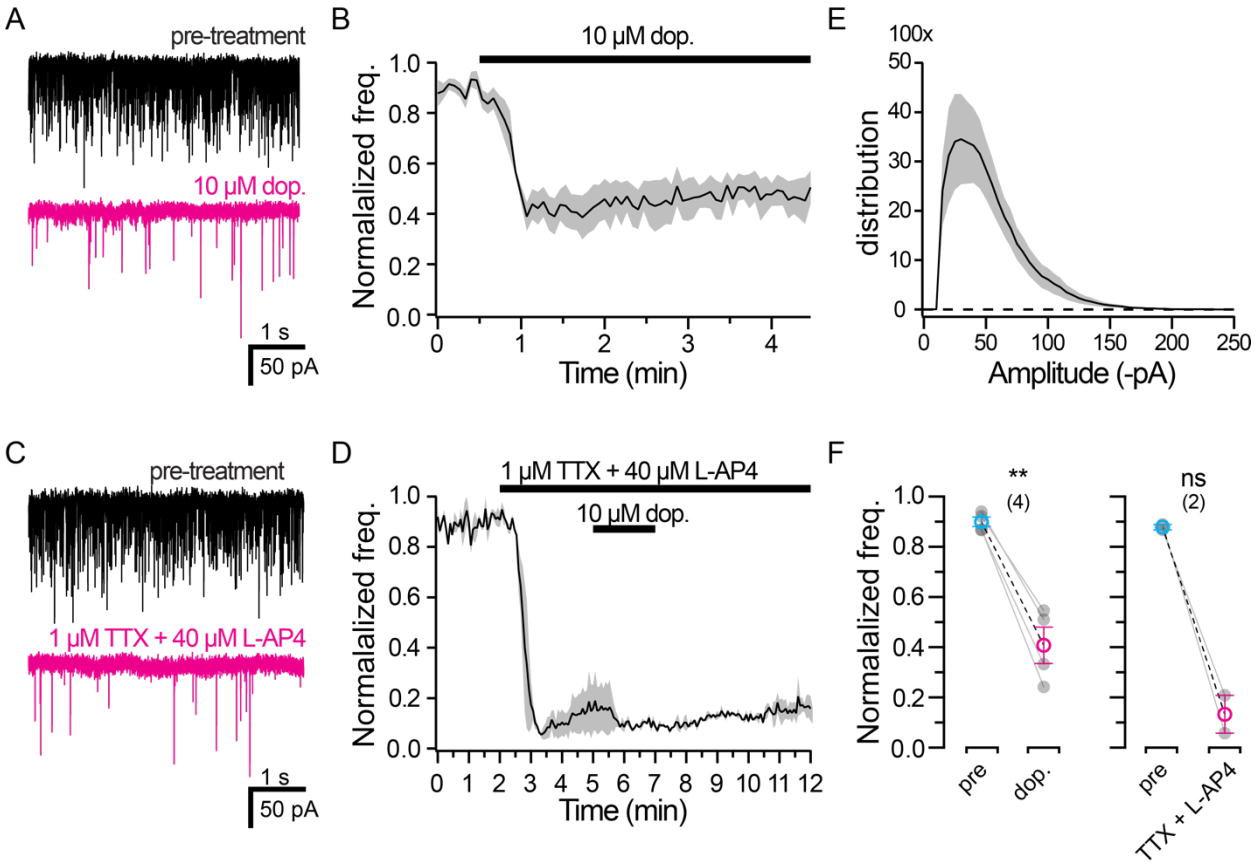

[4.7] Dopamine reduces glycinergic sIPSC frequency in OFF-CBCs from *Syt2*-EGFP mice.

Whole-cell voltage-clamp recordings performed at 33-34 °C using a high chloride internal and Ames medium external. Recordings were performed in low photopic conditions using type 3 OFF-CBCs from *Syt2*-EGFP mice (p25-35). Drugs were bath applied to block glutamatergic and GABAergic currents held at -70 mV. ***A* & *C,*** Example recordings of sIPSCs before drug application (pre-treatment; black) and shown in magenta are traces during the treatment of 10 µM dopamine ***(A)*** or 1 µM TTX and 40 µM L-AP4 ***(B)***. Notice how both drug applications reduce the number of events. ***B* & *D,*** Diary plots of the normalized sIPSC frequency for each drug application, indicated by black bar and label above each graph. Black line with grey region depicts mean ± SEM. Notice how the sIPSC frequency drops after each drug application***. E,*** Histogram showing the frequency distribution of sIPSC amplitudes. Black line with grey region depicts mean ± SEM for all OFF-CBCs (n = 6)**.** measured before drug application, although amplitudes did not change (data not shown)**. *F,*** Summary plot of the normalized sIPSC frequency for each dataset. Frequency was measure during the 30s before drug application (pre) and after 2 mins of drug wash. Grey circles represent values from individual OFF-CBCs and open circles with error bars depict mean ± SEM. Notice how the sIPSC frequency is significantly reduced with dopamine (~50%; n = 4) or with TTX and L-AP4 (~80%; n = 2). Statistical comparisons were made using parametric paired t tests and statistical significance is denoted using asterisks (ns, $p > 0.05$; **, $p < 0.01$).

dopamine: 46.1 ± 20.4 Hz; n = 4, p = 0.046). In our experiments we did not block activation of ON-CBCs, where TRPM1 channels are opened when mGluR6 activity is reduced by the light-mediated reduction of glutamate. Therefore, the high basal sIPSC frequency might be caused by light-dependent signals transmitted through gap junctions between ON-CBCs and AII-ACs. Our preliminary experiments aim to chemically mimic scotopic conditions by washing 40 µM L-AP4 (mGluR6 agonist) and 1 µM TTX (to block Na currents in AII-ACs), which reduced the sIPSC frequency (Fig. 4.7C). We then washed 10 µM dopamine to detect any changes to the sIPSC frequency, yet it is difficult to determine any effect of dopamine in this condition because of an unstable rate of sIPSCs (Fig. 4.7D). Our preliminary results suggest that the sIPSC frequency was reduced by 80% with TTX and L-AP4 (n = 2), but more experiments must be done to verify any statistical significance (Fig. 4.7F). Furthermore, we did not compare changes in sIPSC amplitude but the average amplitude for all treatments was about -40 pA, similar to our previous recordings of glycinergic sIPSCs (Fig. 4.7E).

4.3.3b Na^+ and L-type Ca^{2+} channels regulate sIPSC frequency in OFF-CBCs

We also tested how Na^+ and L-type Ca^{2+} currents regulate spontaneous release from AII-ACs in from Sprague-Dawley rat retinas by measuring sIPSCs from OFF-CBCs (Fig. 4.8). Key differences in this experiment from figure 4.6*C* is that these recordings were performed at room temperature, and in an ACSF solution instead of Ames medium. The ASCF solution contained (in mM): 110 NaCl, 2.5 KCl, 35 NaHCO3, 1.25 NaH2PO4, 2 CaCl2, 1 MgCl2, 10 glucose, and 20 HEPES. Example traces from these experiments show that the number of sIPSCs reduces after treatment with 1 µM TTX or 2 µM isradipine (L-type channel blocker) in our bath solution (Fig. 4.8A, B). Average sIPSC traces had smaller amplitudes with each treatment, but exponential fits to the decay were similar (Fig. 4.8C, D). Analysis sIPSC frequency was performed by plotting the cumulative frequency of the interevent interval times (Fig. 4.8 E, F). Plots for TTX and isradipine datasets shifted to the right of the pre-treatment groups indicative of a reduction in the event frequency. The shift in the interevent interval was not significant for the TTX dataset ($p = 0.93$) but was for the isradipine dataset ($p < 0.001$) using a Kolmogorov-Smirnov test. Plotting the absolute frequency before and after drug wash also illustrates that TTX and Isradipine reduce the sIPSC frequency (Fig. 4.8G). The slight reduction is sIPSC frequency was significant for the

Figure[4.8]

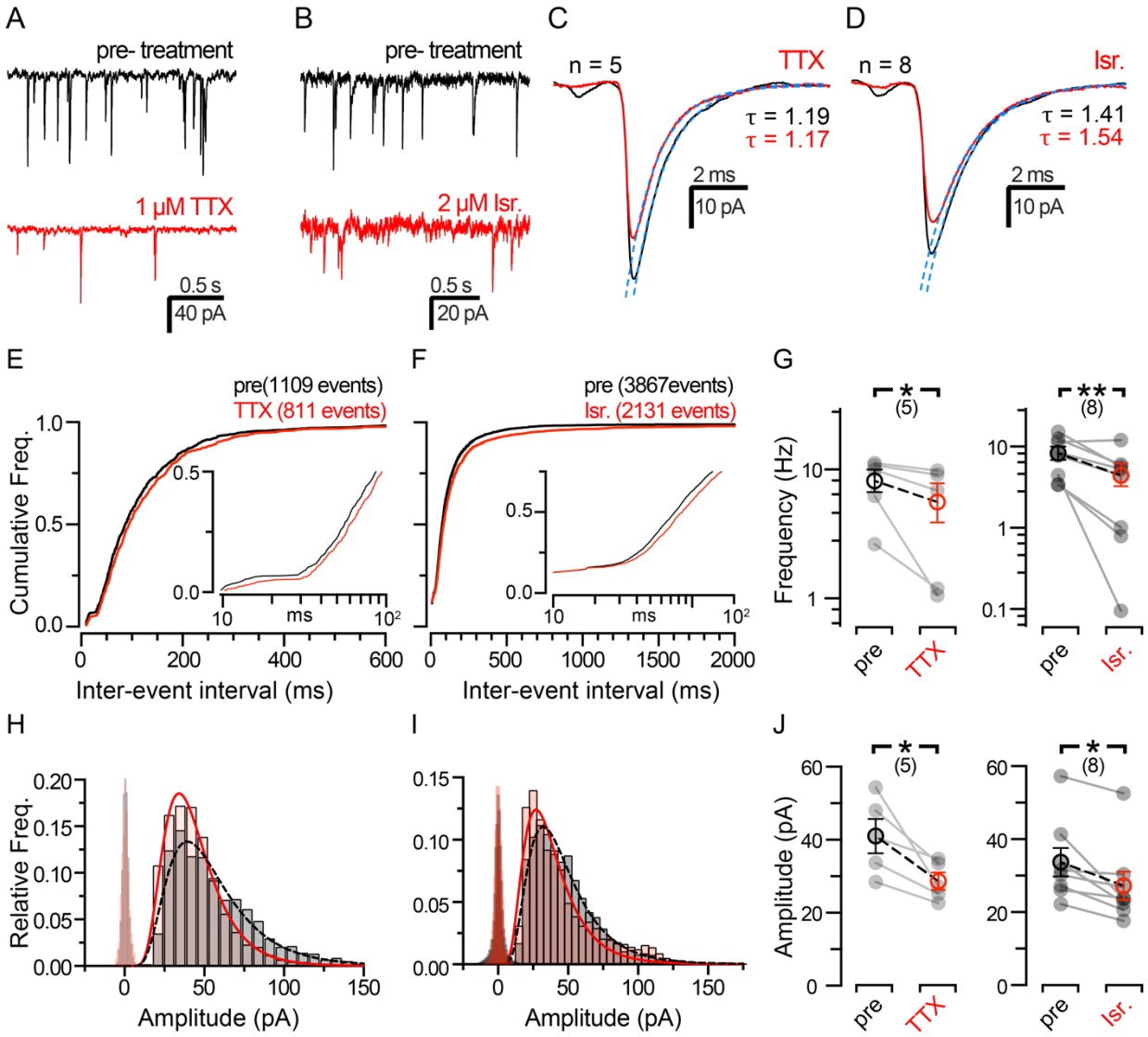

[4.8] Glycinergic sIPSC frequency and amplitude in rat OFF-CBCs are reduced by TTX and isradipine.

Whole-cell voltage clamp recordings were performed in OFF-CBCs from Sprague-Dawley rats (P25-35). Recordings were performed at 32 °C using a high chloride internal and ACSF external solution; OFF-CBCs were held at -70 mV. ***A-B,*** Recordings of sIPSCs from OFF-CBCs showing inward currents before drug wash (pre-treatment; black) and red traces represent sIPSC recordings during external drug perfusion of ***(A)*** 1 µM TTX and ***(B)*** 2 µM isradipine. ***C-D,*** Grand average sIPSCs for each dataset. Dashed lines represent single exponential fit for the current decay, and labeled on the graph are the time constants for each dataset. Notice that the amplitude slightly decreases with each treatment group, while the decay does not change. ***E-F,*** Cumulative frequency histograms of the inter-event interval with an inset showing the fast events (< 100 ms) on a log timescale (x-axis). Labeled on graphs are the number of events used in this analysis. Notice that the plot slightly shifts to the right with each treatment, indicating that the inter-event interval is longer. ***G,*** Summary plot of the sIPSC frequency measured over a 10 second window for each dataset. Notice how that the frequency was significantly reduced for the TTX dataset

(left panel) and for the isradipine dataset (right panel). ***H-I,*** Relative frequency histogram of the sIPSC amplitude for each dataset. Open columns represent the noise analysis, and closed bars represent binned proportion of events. Lines represent log Gaussian fits to each dataset. Notice how the peak shifts to the left for each treatment. ***J,*** Summary plots of the median amplitudes acquired from log Gaussian fits. Comparisons of the mean were made for each dataset using paired t-tests. Notice how the amplitude significantly decreases for the TTX dataset (left panel) and isradipine dataset (right panel). Grey circles in ***G & J*** values from individual cells and open circles with error bars depict mean ± SEM. Statistical comparisons were made using parametric paired t tests and statistical significance is denoted using asterisks (*, $p < 0.05$; **, $p < 0.01$). Data was collected by Dr. Xiaohan Wang and analysis was done by Marc Meadows.

TTX dataset (control: 8.16 ± 1.64 Hz, and TTX: 5.60 ± 1.89 Hz; n = 5; p = 0.024; Student's t-test). The reduction in sIPSC frequency indicates that voltage gated sodium channels (VGSCs) and calcium channels (VGCCs) regulate spontaneous vesicle fusion. However, it is possible that light-dependent activation of VGSCs is occurring, where signals from ON-CBCs could depolarize AII-ACs near the threshold of the VGSCs. We also observed a decrease in the sIPSC frequency for the isradipine dataset (control: 8.29 ± 1.56 Hz, and isradipine: 4.40 ± 1.37 Hz; n = 8; p = 0.008; Student's t test). The result with isradipine would indicate that L-type $Ca_v1.3$ regulated spontaneous vesicle release in AII-ACs. We plotted the relative distribution of mini amplitudes for all OFF-CBCs recordings to analyze the effects of TTX or isradipine on the sIPSC amplitude (Fig. 4.8H, I). The sIPSC amplitude distribution was above the noise analysis for each dataset and were fitted with log-Gaussian functions. The peak of the fitting shifted slightly for the TTX dataset (control: $R^2 = 0.96$, and TTX: $R^2 = 0.99$; DF = 20) and for the isradipine dataset (control: $R^2 = 0.99$, and Isr: $R^2 = 0.97$; DF = 51). Comparisons of the median amplitudes from individual cells also showed that sIPSC amplitude decreased significantly for TTX dataset (control: 41.0 ± 4.69 pA, and TTX: 28.65 ± 2.37 pA; p = 0.037; Student's t test) and isradipine dataset (control: 33.6 ± 3.91 pA, and Isr: 27.2 ± 3.85 pA; p = 0.12; Student's test).

4.3.3c Dopamine alters the spike properties in AII-ACs

The dopamine dependent changes observed in the sIPSC frequency (Fig. 4.7) could be due to alterations in coupling between AII-ACs and ON-CBCs. Changes to the coupling state can change the spike properties of AII-ACs (Choi et al., 2014). We tested if dopamine affects AII-AC spiking with current-clamp recordings from AII-ACs (Fig. 4.9).

Figure[4.9]

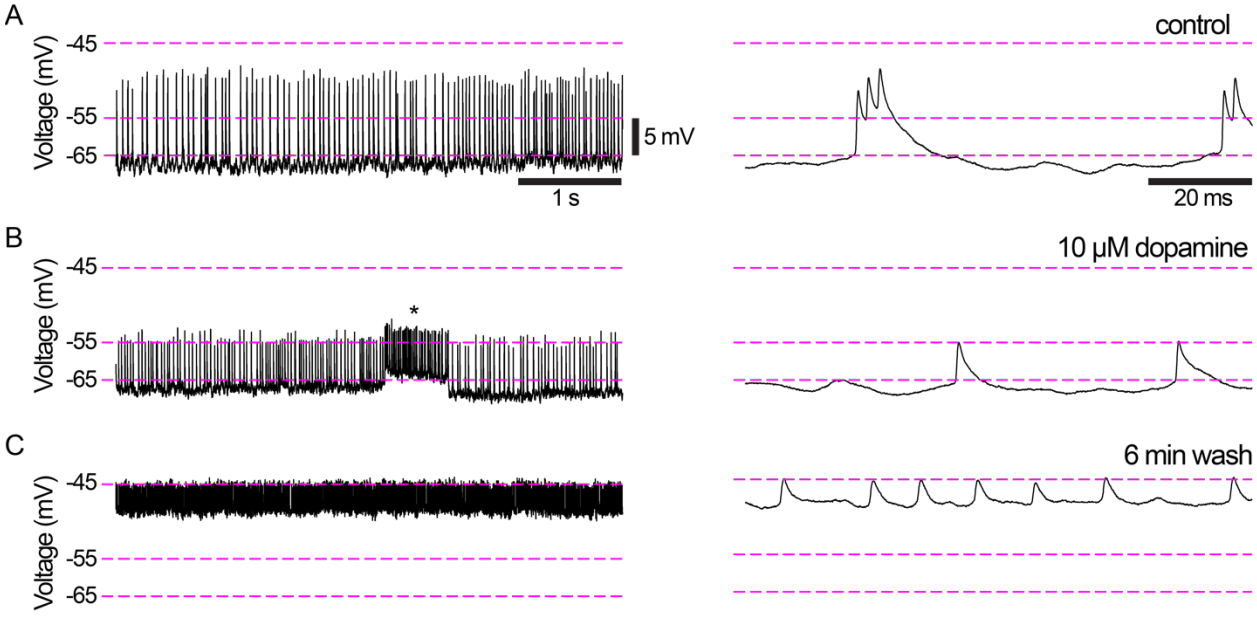

[4.9] Dopamine alters the spike pattern of AII-ACs.

Whole-cell current-clamp recordings performed in AII-ACs from C57 mice (p27). A current injection of -69 pA was given to hold the AII-AC at spiking threshold***. A,*** Examples V_m responses from an AII-ACs in normal Ames medium (control) using a K-based internal solution. Notice the resting potential is below -65 mV with periodic bursts above -55 mV. The burst waveform can be seen with an expanded x-axis (right) with burst spikes***. B,*** Example V_m responses during 10 µM dopamine wash. Notice that the RMP did not change, while periodic single spikes are smaller than bursts seen during pre-treatment. Marked with asterisk is a sporadic depolarization event***. C,*** Example V_m responses to the same current injection during attempt to wash out dopamine. Notice how the cell hyperpolarizes and spikelet amplitude decreases. Also, the single spikes qualitatively increased in frequency.

A current injection was given (-44 pA and -69 pA for either cell; n = 2) to hold AII-ACs at spiking threshold (-65 mV; Tian et al., 2010). Example AII-AC recording with a -69 pA current injection, which held the cell just below -65 mV (Fig. 4.9A). In control conditions, with the synaptic blockers, we observed many subthreshold spikes in the membrane voltage, or burst spiking, with multiple peaks. With 10 µM dopamine we observed the spike pattern changed from bursting to single events (Fig. 4.9B). We also observed sporadic depolarization events when dopamine was present. The cell depolarized and the spikelet frequency increased when we attempted to wash out dopamine (Fig. 4.9C); however, more experiments are required to conclude if this is physiologically relevant.

Section 4.4: Discussion

4.4.1 Ca^{2+} imaging in AII-ACs using GCaMP6F

We were able to target expression of GCaMP6F into amacrine cells using the GlyT2-cre mouse line. The most recent in-situ hybridization studies of glycine transporter expression in the retina show that both GlyT1 and GlyT2 is expressed in the inner nuclear layer (Peña-Rangel et al., 2008); in addition to mRNA expression found in photoreceptors and in the ganglion cell layers. Our use of the GlyT2-cre mouse line to drive either tdTomato or GCaMP6F resulted in similar expression patterns, allowing us to identify AII-ACs by their morphology. GCaMP6F is a widely used genetically encoded calcium indicator that is both fast and has a high fluorescence signal (Chen et al., 2013). Using GCaMP6F we were able to detect fluorescence signals in the AII-AC lobules, similar to previous findings with Ca^{2+} indicator dyes (Balakrishnan et al., 2015). Although we will need to perform more experiments, our preliminary results indicate that we will be able to determine the kinetics of Ca^{2+} clearing in AII-AC lobules. Just as in dendritic spines, the thin necks of AII-ACs may restrict the diffusion of calcium from the lobular compartment with a higher concentration of extrusion mechanisms (i.e. SERCA pumps, and Ca-Na exchangers). Observation of calcium extrusion in CA1 pyramidal neurons shows that it is faster in spines than in adjacent dendritic branches (Majewska et al., 2000).

4.4.2 Signal transmission from ON-CBCs to AII-ACs through electrical synapses

GcAMP6F is a genetically encoded Ca^{2+} sensor that is useful for studying signal propagation throughout populations of neurons (Chen et al 2013; Li et al., 2019). We were able to stimulate populations of ON-CBCs pharmacologically. Synaptic transmission from photoreceptors to OFF-CBCs is mediated by AMPA/Kainate receptors (Gilbertson et al., 1991; DeVries and Schwartz, 1999; DeVries, 2000). Transmission to ON-BCs, like rod and ON-CBCs, causes hyperpolarization and is mediated by mGluR6-dependent closure of TRPM1 channels (Morgans et al., 2010). Experiments using CPPG to activate TRPM1 by reducing mGluR6 activity simulating light responses in ON-BCs (Snellman et al., 2008). The canonical pathways involving the AII-ACs involve chemical inputs from rod BCs, and these signals are transmitted to ON-CBC terminals through gap junctions or converted to glycine release to OFF-CBCs (reviewed in Demb and Singer, 2012).

We presume that we are blocking synaptic transmission from Rod BCs or OFF-CBCs because we used CNQX to block AMPA/Kainate receptors— isolating signals from ON-CBCs through gap junctions. Paired recordings between ON-CBCs and AII-ACs demonstrate that these gap junctions are bi-directional (Graydon et al., 2018). Our results confirm that signals from ON-CBCs can propagate to AII-ACs. Two caveats to this experiment include: (1) CPPG stimulates multiple ON-CBCs, and (2) the efficacy diminished over a short period. Therefore, it is difficult to determine how many ON-CBCs are activated at a given time. It will be interesting to use whole-cell or sharp electrodes to stimulate either individual or populations of ON-CBCs, to determine how signals propagate through the AII-AC network. It is an open question: how important sodium channels are in AII-ACs for this signal propagation?

4.4.3 EPAC2 triggers CICR in AII-ACs

CICR is a common signaling mechanism in amacrine cells and is shown to enhance GABA release in cultured amacrine cells (Warrier et al., 2005), and A17 amacrine cells (Egger and Diamond, 2020). EPAC-mediated CICR has been observed in cerebellar granular cells also using calcium imaging through the activation of p38 MAPK (Ster et al., 2006). Although we previously showed that CICR can enhance glycine release from the AII-AC (Meadows et al., 2021), this is the first direct evidence that CICR in AII-ACs can be triggered by EPAC activation. Future experiments will also focus on different CICR mechanisms, using ryanodine or 2-APB (IP3 receptor antagonist) during 8-pCPT puffs. We expect that these inhibitors will prevent or reduce GCaMP6F signals in response to 8-pCPT, and show that an EPAC2-mediated pathway enhances CICR. Warrier et al. (2005) showed that ryanodine receptor and IP3 receptor mediated CICR have different kinetics in widefield amacrines. We will consider reducing the exposure times during imaging so that we can track GCaMP6f signals with better temporal resolution, which might help distinguish different CICR pathways. The results from these future experiments may verify our previous findings, and uncover which signaling pathways are present in AII-ACs for CICR.

4.4.4 Dopamine reduces glycinergic sIPSC frequency in type 2 OFF-CBCs

Our finding that dopamine reduced glycinergic sIPSC frequency in OFF-CBCs was contrary to our initial expectation that the activation of D1-like receptors would increase cAMP in AII-ACs and

we would see an increase in the sIPSC frequency as we did in our experiments with forskolin (Meadows et al., 2021). Results from Mazade et al. (2019), published shortly after we performed experiments with dopamine (Fig. 4.7, 4.9), show that glycinergic inhibition to OFF-CBCs is reduced by D1 receptor activation and light adaptation. There is a broad expression of D1 receptors in the retina including amacrine cells, horizontal cells, and bipolar cells (Farshi et al., 2016; Nguyen-Legros et al., 1997; Veruki and Wässle 1996), while D2 receptors appear on dopaminergic amacrine cells (Nguyen-Legros et al., 1999). Furthermore, there is some evidence that D1 receptors are found in type 5-2, XBC, 6, and 7 ON-CBCs in addition to a subset of AII-ACs (Farshi et al., 2016). Dopamine has been shown to alter the homologous gap junction coupling between AII-ACs (Hampson et al., 1992; Mills and Massey, 1995). These tracer-dye experiments measuring relative brightness did not detect changes in AII-AC to ON-CBC coupling, yet dopamine reduces the diffusion coefficient of tracer dyes (Xia and Mills, 2004). Therefore, dopamine causes long-term network changes that could affect AII-AC responses to ON-CBC inputs.

Tamalu and Watanabe (2007) show that glutamatergic inputs from rods can induce spiking in AII-ACs, which can be blocked by L-AP4. Since we are using blockers of synaptic glutamate receptors, our results show electrical inputs from the ON-CBCs can generate spikes in AII-ACs. Previous studies have only determined how dopamine effects the diffusion of tracer-dyes through gap junctions, but it is still not clear how dye-diffusion influences conductance. The spike bursts we observed are similar in nature to the intrinsic bursting patterns of AII-ACs when given a hyperpolarizing current injection in wildtype mice or seen at rest in rd1 mice (Choi et al., 2014). In this study, Choi et al. found that spike oscillations were blocked with MFA, a gap-junction blocker, but could be restored with a current injection. These spike bursts are thought be regulated by a slow M-type K^+ current active near the AII-AC spike threshold (Cembrowski et al., 2010). Modeling suggests that changes in M-current conductance changes the oscillation pattern (ranging from 0.036 to 0.02 S/cm^2), and reducing the M-current conductance below 0.1 S/cm^2 resulted in a membrane depolarization and tonic spiking. As a possible mechanism, dopamine might be modulating the gap junction or ion channel conductance of the AII-AC and altering the excitatory input from the ON-CBCs.

Our results in Figure 4.7D & 4.8 shows a reduction in the sIPSCs frequency when blocking sodium channels alone or with the addition of L-AP4 to block light-mediated ON-CBC depolarization. The spontaneous release of vesicles independent of sodium channel activation is well known from its discovery by Fatt and Katz (1952). Our observations indicate that the AII-ACs are being depolarized near the threshold of their sodium channel activation (Tian et al., 2010). We noticed that the basal sIPSC rate in Figure 4.7 was much higher than for Figure 4.8— sometimes approaching 100 Hz. Two key differences in the experimental design were the use of Ames' medium and higher recording temperature in Figure 4.6. These conditions could be more favorable for light-dependent activation of retinal circuits.

4.4.5 Ca^{2+} dependence of spontaneous vesicle release

We also found that blocking L-type Ca^{2+} channels significantly reduced the sIPSC frequency. L-type $Ca_v1.3$ are a non-inactivating voltage gated calcium channel (VGCC) known for their role in controlling synchronized and graded vesicle release in sensory ribbon type synapses. They are also the sole VACC in AII-ACs (Balakrishnan et al., 2015). Findings from cortical neurons suggest that VGCCs control spontaneous release at inhibitory synapses, and not in excitatory synapses of the cortex and brainstem (Vyleta and Smith, 2011; Williams et al., 2012; Tsintsadze et al., 2017). Although this study is still in development, the findings in Figure 4.8 suggest that the AII-ACs are another inhibitory type synapse where VGCCs regulate spontaneous or asynchronous vesicle fusion. It is important to note that excitatory synapses in the retina as well as auditory hair cell synapses exhibit VGCC control of the mEPSC frequency (Graydon et al., 2011; Kim et al., 2013; Cork et al., 2016). Like the cortical neurons the display VGCC-dependent spontaneous release, the AII-AC has conventional synapses. A common feature among AII-ACs and the ribbon type synapses of the retina is the presence of L-type Ca^{2+} channels, which are non-inactivating. Activation of L-type $Ca_v1.4$ channels can trigger multi-quantal vesicle release in hair cells in response to long lasting, low-level depolarization (Graydon et al., 2011). Our data suggests that L-type Ca^{2+} AII-ACs could translate low threshold, graded signals into tonic inhibition of OFF-CBCs.

Section 4.5: Materials & Methods

Animals

The *GlyT2-Cre;GCAMP6F* mouse line was generated by crossing *GlyT2-Cre* mice [Tg(Slc6a5-cre)KF109Gsat/Mmucd, RRID:MMRRC_030730-UCD] with the floxed RCL-GCaMP6f Cre Ai95 reporter line [Gt(ROSA)26Sor$^{tm95.1(CAG-GCaMP6f)Hze}$, RRID:IMSR_JAX:028865]. Male and female mice were used in experiments ages p25-35.

The GlyT2-Cre;TdTomato mouse line was generated by crossing GlyT2-Cre mice [Tg(Slc6a5-cre)KF109Gsat/Mmucd, RRID:MMRRC_030730-UCD] with the floxed Ai9 tdTomato Cre reporter line [B6.Cg-Gt(ROSA)26Sortm9(CAG-tdTomato)Hze/J, RRID:IMSR_JAX:007909].

Calcium Imaging

Retinal slices were observed using a water immersion objective lens (60×, Olympus) on a fixed stage, upright microscope (BX51WI, Olympus). Single plane, time-series image acquisition was performed using an Orca Flash 4.0LT CMOS camera (Hamamatsu Photonics) controlled with CellSens image software (Olympus). Regions of interest were selected by eye. Background subtraction and fluorescence intensity profiles were generated in CellSens (Olympus) and exported to IgorPro software (Wavemetrics) for analysis.

Local drug application

Drugs were mixed to final concentration using external recording solution just before application. 8-pCPT and CPPG were purchased from Tocris; caffeine was generously donated by Catherine Morgans (purchased from Sigma). Local injections of drugs were administered using a picospritzer (Parker Instruments) using 4 psi to 'puff' solutions thick-walled borosilicate glass pipettes (1-2 MΩ; 1B150F-4, World Precision Instruments). Injections and camera were triggered using an EPC10 double patch clamp amplifier (HEKA) and Real Time Controller (U-RTC; Olympus). External bath solutions were continuously perfused during injections. The bath solution contained CNQX, bicuculline, gabazine, DL-AP5, and L-AP4 (Tocris); solutions also contained TTX when indicated (Sigma).

Whole-cell current-clamp recording in AII-ACs

AII-ACs were targeted and patched with thick-walled borosilicate glass pipettes (8-10 MΩ; 1B150F-4, World Precision Instruments). Pipettes were filled with a K-based internal solution containing (in mM): 135 mM potassium gluconate, 7 NaCl, 10 HEPES, 10 phosphocreatine, 2 Na_2-ATP, 0.3 mM Na-GTP, and 2 $MgCl_2$ (pH 7.3-7.4 KOH). Synaptic blockers were added to the external solution, including: CNQX, bicuculline, gabazine, and DL-AP5. Once in whole-cell configuration, AII-ACs were held at -65 mV before switching to current-clamp configuration. Recordings were performed with an EPC10 double patch clamp amplifier (HEKA). Data were acquired at 10 or 20 kHz sampling rate and filtered with 2 kHz low-pass filter.

Section 4.6: Acknowledgements

This work was supported by National Institutes of Health Grants EY014043 and DC12938 to H.v.G.; and Casey Eye Institute P30 Grant EY010572. This work was union-made and upheld fair labor practices approved by AFSCME Local 402 OHSUGRU. Holger Taschenberger provided mini-IPSC software analysis procedures. Thanks to laboratory members Andre Dagostin, Benjamin Zemel, and Paulo Strazza; committee members Catherine Morgans, Benjamin Sivyer, Stephen Smith, and Anusha Mishra. Special thanks to Joseph Leffler for discussions, and manuscript revisions.

Section 4.7: References

Awatramani GB, Slaughter MM (2001) Intensity-dependent, rapid activation of presynaptic metabotropic glutamate receptors at a central synapse. J Neurosci 21(2):741-9.

Balakrishnan V, Puthussery T, Kim MH, Taylor WR, von Gersdorff H (2015) Synaptic vesicle exocytosis at the dendritic lobules of an inhibitory interneuron in the mammalian retina. Neuron 87:563-575.

Cembrowski MS, Logan SM, Tian M, Jia L, Li W, Kath WL, Riecke H, Singer JH (2012) The mechanisms of repetitive spike generation in an axonless retinal interneuron. Cell Rep 1(2):155-66.

Chen TW, Wardill TJ, Sun Y, Pulver SR, Renninger SL, Baohan A, Schreiter ER, Kerr RA, Orger MB, Jayaraman V, Looger LL, Svoboda K, Kim DS (2013) Ultrasensitive fluorescent proteins for imaging neuronal activity. Nature 499(7458):295-300.

Choi H, Zhang L, Cembrowski MS, Sabottke CF, Markowitz AL, Butts DA, Kath WL, Singer JH, Riecke H (2014) Intrinsic bursting of AII amacrine cells underlies oscillations in the rd1 mouse retina. J Neurophysiol 112(6):1491-504.

Cork KM, Van Hook MJ, Thoreson WB (2016) Mechanisms, pools, and sites of spontaneous vesicle release at synapses of rod and cone photoreceptors. Eur J Neurosci 44(3):2015-27.

Demb JB, Singer JH. Intrinsic properties and functional circuitry of the AII amacrine cell (2012) Vis Neurosci 29(1):51-60.

Egger V, Diamond JS (2020) A17 amacrine cells and olfactory granule cells: parallel processors of early sensory information. Front Cell Neurosci 14:600537.

Ehrlich BE, Kaftan E, Bezprozvannaya S, Bezprozvanny I (1994) The pharmacology of intracellular Ca(2+)-release channels. Trends Pharmacol Sci 15(5):145-9.

Farshi P, Fyk-Kolodziej B, Krolewski DM, Walker PD, Ichinose T. Dopamine D1 receptor expression is bipolar cell type-specific in the mouse retina. J Comp Neurol. 2016 Jul 1;524(10):2059-79.

Fatt P, Katz B (1952) Spontaneous subthreshold activity at motor nerve endings. J Physiol 117, 109–128.

Fournel R, Hartveit E, Veruki ML (2021) Differential Contribution of Gap Junctions to the Membrane Properties of ON- and OFF-Bipolar Cells of the Rat Retina. Cell Mol Neurobiol 41(2):229-245.

Graydon CW, Cho S, Li GL, Kachar B, von Gersdorff H (2011) Sharp Ca^{2+} nanodomains beneath the ribbon promote highly synchronous multivesicular release at hair cell synapses. J Neurosci 31(46):16637-50.

Graydon CW, Lieberman EE, Rho N, Briggman KL, Singer JH, Diamond JS (2018) Synaptic transfer between rod and cone pathways mediated by AII amacrine cells in the mouse retina. Curr Biol 28(17):2739-2751.e3.

Halls ML, Cooper DMF (2011) Regulation of Ca^{2+}-signaling pathways of adenylyl cyclases. Cold Spring Harb Perspect Biol 3:a004143.

Hampson EC, Vaney DI, Weiler R (1992) Dopaminergic modulation of gap junction permeability between amacrine cells in mammalian retina. J Neurosci 12:4911–4922.

Kim MH, Li GL, von Gersdorff H (2013) Single Ca2+ channels and exocytosis at sensory synapses. J Physiol 591(13):3167-78.

Li P, Geng X, Jiang H, Caccavano A, Vicini S, Wu JY (2019) Measuring sharp waves and oscillatory population activity with the genetically encoded calcium indicator GCaMP6f. Front Cell Neurosci 19;13:274.

Majewska A, Brown E, Ross J, Yuste R (2000) Mechanisms of calcium decay kinetics in hippocampal spines: role of spine calcium pumps and calcium diffusion through the spine neck in biochemical compartmentalization. J Neurosci 20(5):1722-34.

Marc RE, Anderson JR, Jones BW, Sigulinsky CL, Lauritzen JS (2014) The AII amacrine cell connectome: a dense network hub. Front Neural Circuits 8:104.

Mazade RE, Flood MD, Eggers ED (2019) Dopamine D1 receptor activation reduces local inner retinal inhibition to light-adapted levels. J Neurophysiol 121(4):1232-1243.

Meadows MA, Balakrishnan V, Wang X, von Gersdorff H (2021) Glycine release is potentiated by cAMP via EPAC2 and Ca2+ stores in a retinal interneuron. J Neurosci 41(46):9503-9520.

Mills SL, Massey SC (1995) Differential properties of two gap junctional pathways made by AII amacrine cells. Nature 377(6551):734-7.

Morgans CW, Brown RL, Duvoisin RM (2010) TRPM1: the endpoint of the mGluR6 signal transduction cascade in retinal ON-bipolar cells. Bioessays 32(7):609-14.

Nguyen-Legros J, Simon A, Caillé I, Bloch B (1997) Immunocytochemical localization of dopamine D1 receptors in the retina of mammals. Vis Neurosci 14(3):545-51.

Nguyen-Legros J, Versaux-Botteri C, Vernier P (1999) Dopamine receptor localization in the mammalian retina. Mol Neurobiol 19(3):181-204.

Peña-Rangel MT, Riesgo-Escovar JR, Sánchez-Chávez G, Salceda R (2008) Glycine transporters (glycine transporter 1 and glycine transporter 2) are expressed in retina. Neuroreport 19(13):1295-9.

Roy S, Field GD (2019) Dopaminergic modulation of retinal processing from starlight to sunlight. J Pharmacol 140(1):86-93.

Ster J, De Bock F, Guérineau NC, Janossy A, Barrère-Lemaire S, Bos JL, Bockaert J, Fagni L (2007) Exchange protein activated by cAMP (Epac) mediates cAMP activation of p38 MAPK and modulation of Ca2+-dependent K+ channels in cerebellar neurons. Proc Natl Acad Sci USA 104(7):2519-24.

Sadana R, Dessauer CW (2007) Physiological roles for G protein-regulated adenylyl cyclase isoforms: insights from knockout and overexpression studies. Neurosignals 17 (1):5-22.

Snellman J, Zenisek D, Nawy S. Switching between transient and sustained signaling at the rod bipolar-AII amacrine cell synapse of the mouse retina. J Physiol. 2009 Jun 1;587(Pt 11):2443-55.

Sivyer B, Williams SR (2013) Direction selectivity is computed by active dendritic integration in retinal ganglion cells. Nat Neurosci. 16(12):1848-56.

Sivyer B, Meadows MA, Kerstein PC, Wright KM, Gersdorff H (2019) Axon-bearing amacrine cells labelled in transgenic GlyT2 mice. iOVS Vol.60, 542.

Tamalu F, and Watanabe S. (2007). Glutamatergic input is coded by spike frequency at the soma and proximal dendrite of AII amacrine cells in the mouse retina. Eur. J. Neurosci. 25, 3243–3252.

Tian M, Jarsky T, Murphy GJ, Rieke F, Singer JH (2010) Voltage-gated Na channels in AII amacrine cells accelerate scotopic light responses mediated by the rod bipolar cell pathway. J Neurosci 30(13):4650-9.

Tsintsadze T, Williams CL, Weingarten DJ, von Gersdorff H, Smith SM (2017) Distinct Actions of Voltage-Activated Ca2+ Channel Block on Spontaneous Release at Excitatory and Inhibitory Central Synapses. J Neurosci 37(16):4301-4310.

Vyleta NP, Smith SM (2011) Spontaneous glutamate release is independent of calcium influx and tonically activated by the calcium-sensing receptor. J Neurosci 31:4593–4606.

Vyleta NP, Smith SM (2008) Fast inhibition of glutamate-activated currents by caffeine. PLoS One 3(9):e3155.

Veruki ML, Wässle H (1996) Immunohistochemical localization of dopamine D1 receptors in rat retina. Eur J Neurosci 8: 2286–2297.

Warrier A, Borges S, Dalcino D, Walters C, Wilson M (2005) Calcium from internal stores triggers GABA release from retinal amacrine cells. J Neurophysiol 94(6):4196-208.

Williams C, Chen W, Lee CH, Yaeger D, Vyleta NP, Smith SM (2012) Coactivation of multiple tightly coupled calcium channels triggers spontaneous release of GABA. Nat Neurosci 15:1195–1197.

Xia XB, Mills SL (2004) Gap junctional regulatory mechanisms in the AII amacrine cell of the rabbit retina. Vis Neurosci. 2004 Sep-Oct;21(5):791-805

Chapter 5: Thesis Summary

Section 5.1: Highlights

5.1.1 Chapter 2 highlights: Molecular mechanisms for cAMP-induced potentiation in AII-ACs

1. cAMP potentiates exocytosis by increasing the vesicle pool size without changing P_r. (Fig. 2.1 - 2.7)
2. cAMP-induced potentiation is through an EPAC2 dependent pathway. (Fig. 2.8, 2.9)
3. Ca^{2+} release from stores mediates cAMP-induced potentiation. (Fig. 2.10)

5.1.2 Chapter 4 highlights: Ca^{2+} imaging in AII amacrine cells and synaptic modulation

1. EPAC-induced Ca^{2+} release from stores: Ca2+ imaging with GlyT2-Cre;GCaMP6f mice. (Fig. 4.4, 4.5)
2. [EGTA] blocks potentiation that operates via microdomain Ca^{2+} binding proteins. (Fig. 4.6)
3. Dopamine alters AII-AC spike properties and reduces glycine release to OFF-CBCs. (Fig. 4.7, 4.9)

5.1.2 Chapter 3 highlights: Synaptic vesicle endocytosis mechanisms in the AII amacrine cell

1. Measurements of endocytosis kinetics at an inhibitory glycinergic synapse. (Fig. 3.1 – 3.2)
2. Clathrin, dynamin, and actin are required constituents for fast endocytosis in AII-ACs. (Fig. 3.6 - 3.9)
3. Endocytosis in AII-ACs is dependent on nanodomain Ca^{2+}: EGTA and BAPTA (Fig. 3.2 - 3.5)

Section 5.2: Summary of the cAMP signaling cascade for potentiation in AII-ACs

Previous studies have uncovered the cAMP signaling cascade involved in the regulation of gap junction coupling of AII amacrine cell networks, involving the PKA-mediated dephosphorylation of Cx36 (see Urschel et al., 2009). The induction of a cAMP signaling pathway via the activation D1-like receptors has been proposed for the light dependent adaptation of retinal circuits. Our recently published work outlined in chapter 2, provides the first evidence that cAMP can also modulate crossover inhibition in the AII. Figure 5.1 provides a summary illustration of the cAMP signaling pathway in AII-AC lobules that is responsible for the potentiation of glycine release to

the OFF-CBC. Here I will outline the published findings of chapter 2 and the unpublished results in chapter 4. This summary reviews the important known (blue) and unknown (orange) steps in the cAMP signal cascade responsible for the exocytosis potentiation in the AII-AC:

i. The initiation of the cAMP signaling pathway begins with the activation of adenylyl cyclase, which catalyzes the conversion of ATP to cAMP. We showed evidence for adenylyl cyclase activity in AII-ACs by inducing potentiation with forskolin (Fig. 2.6, 2.7). It is still unclear how adenylyl cyclases are regulated in AII-AC lobules. Dopamine signaling is one possibility and D1-like receptor activation is known to regulate AII coupled networks. It is still unclear

Figure[5.1]

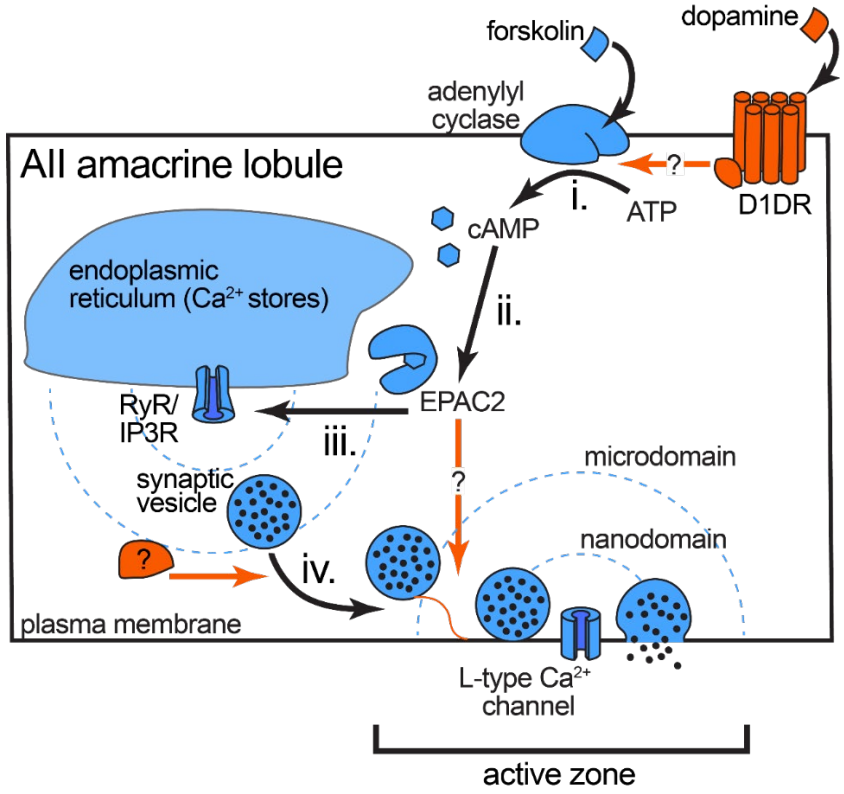

[5.1] Molecular mechanisms involved in the cAMP-induction pathway that potentiates AII-ACs.
Summary diagram of results from Chapters 2 and 4. Shown are synaptic vesicles tethered and primed to the plasma membrane at the active zone of the AII-AC lobule. The primed synaptic vesicle is nanodomain coupled to L-type Ca^{2+} channels, and stimulus-dependent fusion of the synaptic vesicle to the plasma membrane (exocytosis) releases glycine into the synaptic cleft. Also shown, is the signaling pathway for cAMP-dependent potentiation through an EPAC2-dependent pathway that involves Ca^{2+} release from internal Ca^{2+} stores in the endoplasmic reticulum (ER). A detailed description of the steps (i to iv) in the pathway is provided in the text of section 5.2, which covers the known (blue) and unknown (orange) components of the cAMP signal cascade in the AII-AC lobules.

if dopamine regulates cAMP levels in the lobules, since we found that dopamine reduced glycine release to OFF-CBCs (Fig. 4.7). D1-like receptors are Gα coupled receptors, so it is not likely that dopamine is inhibiting cAMP production. Our results that show dopamine changes the AII-AC spiking could account for this reduction in glycine release. Other avenues worth exploring are other GPCRs in the retina (i.e., mGluR or melatonin and CB1 receptors). Ca^{2+}/calmodulin activated adenylyl cyclases, which function as coincidence detectors linked to LTP in the hippocampus, is also a possible mechanism for local cAMP control near the AII-AC synapse. Now that cAMP-induced potentiation has been discovered and established in the AII-AC by the work of thesis, we can also test if phosphodiesterase regulates potentiation by degrading cAMP and restricting diffusion from local hotspots near the synapse.

ii. We show that potentiation requires cAMP signaling via an EPAC2 dependent pathway using a specific EPAC1/2 activator and a specific antagonist EPAC2 (Fig. 2.8, 2.9). A PKA-dependent mechanism was ruled out because H89 (PKA inhibitor) did not block potentiation (Fig. 2.8). A similar cAMP/EPAC dependent signaling pathways was also observed in the calyx of Held (Gekel and Neher, 2008), while hMFBs exhibit a PKA-dependent pathway (Midorikawa and Sakaba, 2017).

iii. We also confirmed that EPAC increases Ca^{2+} release from Ca^{2+} stores by using Ca^{2+} imaging paired with local micro injections of external 8-pCPT puffed onto the retinal slice (Fig. 4.4, 4.5). However, we have not uncovered the EPAC pathways that modulates Ca^{2+} induced Ca^{2+} release (CICR) in the AII-AC. Extensive studies in cardiac myocytes have linked EPAC pathways to excitation contraction by increasing CICR from the sarcoplasmic reticulum. EPAC can also activate phospholipase C epsilon (PLCε), which splits CICR signaling into two pathways by producing (a) inositide 1,4,5 trisphosphate (IP3) and (b) diacyl glycerol (DAG):

    a. Some Ca^{2+} release can be attributed to IP3 binding to IP3 receptors. The Ca^{2+} binds to calmodulin, which activates the Ca^{2+}/calmodulin activated kinase II (CaMKII).
    b. The alternative DAG signaling activates phosphokinase C (PKC) that activates CaMKII.

In both pathways, the activation of CaMKII will phosphorylate the ryanodine receptor and increase the receptors open probability (see review Ruiz-Hurtado et al., 2013). Are these

pathways also found in the AII-AC? We can test components of these pathways using similar pharmacological tools (e.g., Phorbol 12,13-dibutyrate; PKC activator) or inhibitors of calmodulin/CaMKII interaction (Gekel and Neher, 2008; Sakaba and Neher, 2001; Yao and Sakaba, 2010). We can also use Ca^{2+} imaging to test the EPAC analog in combination with ryanodine, and 2-APB to differentiate between DAG and IP3 dependent effects on CICR. These experiments will be performed during a short post-doctoral position with Henrique von Gersdorff. We thus intend to perform further experiments from Chapter 4 for publication.

iv. Ca^{2+} release from stores is required for cAMP-induced potentiation by trafficking vesicles to the active zone. We were able to determine that Ca^{2+} release from stores is responsible for cAMP-induced potentiation by blocking RyR and IP3R (Fig. 2.10). Additionally, we found that potentiation was blocked by a high internal [EGTA] (Fig. 4.6), which does not reduce the standard exocytosis seen with 2 mM internal EGTA. This result indicates that normal exocytosis is nanodomain coupled to L-type Ca^{2+} channels, while the potentiation mechanism is microdomain coupled to internal Ca^{2+} release. We currently do not know the exact mechanism for vesicle trafficking in AII-ACs. However, Sakaba and Neher have proposed that calmodulin can accelerate vesicle recruitment in the calyx of Held (2001). It is possible that calmodulin also plays a role in the AII-AC by either activating CaMKII, promoting CICR, or by modulating synaptic vesicle binding scaffold proteins (e.g, piccolo and bassoon) that form vesicle mobilization complexes. Piccolo, for example, is responsible for vesicle trafficking in the calyx of Held. Piccolo also has Ca^{2+} binding domains where changes in $[Ca^{2+}]$ cause conformational changes (Parthier et al 2018). However, nothing is known about the role of piccolo and bassoon in the AII-AC exocytosis, which could be a potential model synapse for studying these proteins at an inhibitory synapse.

Section 5.3: Summary of endocytosis in the AII amacrine cell

The work in chapter 3 of this thesis presents the first study of fast ($\tau_{1/2}$ = 5 - 6 s) endocytosis at an inhibitory synapse using C_m measurements. Before this study, our understanding about endocytosis kinetics and the molecular processes in neurons came from excitatory synapses. We found that endocytosis can be reliably measured from mature rat AII-ACs using different stimulus

strengths (Fig. 3.1, 3.2, S3.1). Illustrated in this section is a review of the fundamental mechanisms for endocytosis in the AII-AC (Fig. 5.2), which highlights key known (blue) and unknown (orange) steps:

Figure[5.2]

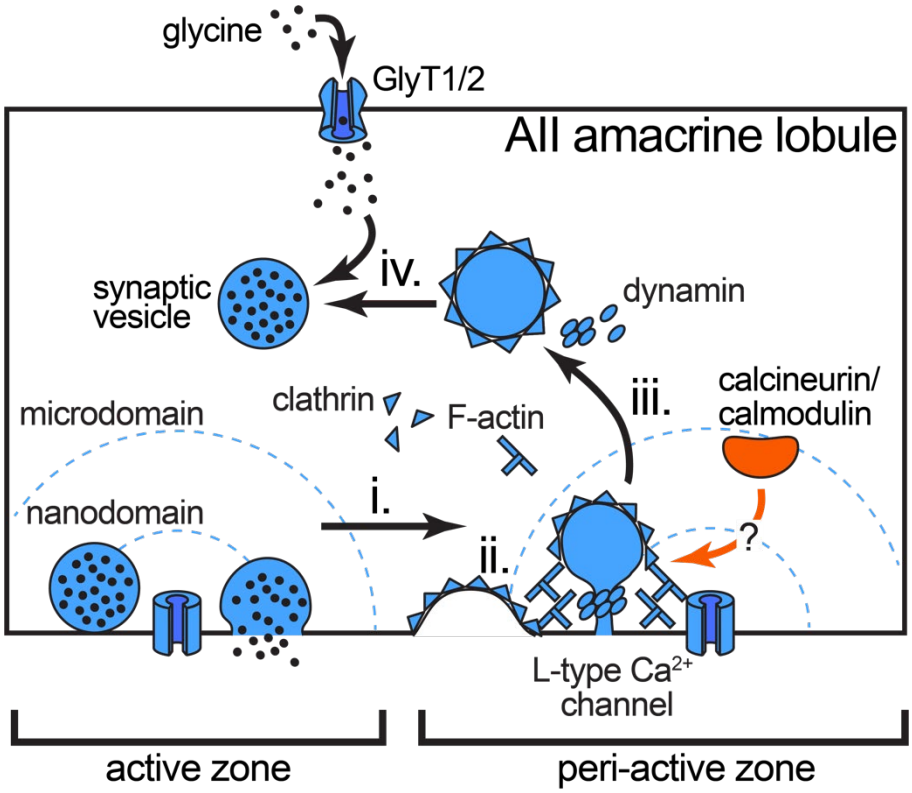

[5.2]Molecular mechanisms for synaptic vesicle endocytosis in AII amacrine cell lobules.
Summary diagram of the results from chapter 3. Shown are the mechanisms for membrane retrieval (endocytosis) that occurs after exocytosis. Synaptic vesicle exocytosis occurs at the active zone where vesicle fusion is nanodomain coupled to L-type Ca^{2+} channels, while endocytosis in the peri-active zone is loosely nanodomain coupled to Ca^{2+} channels. Endocytosis is sensitive to low [BAPTA]; however, the mechanism for Ca^{2+} dependence is unknown. A detailed description (i to iv) is provided in section 5.3, reviewing the known (blue) and unknown (orange) components of endocytosis in the AII-AC lobules.

i. The synaptic vesicle membrane collapses during full-fusion exocytosis, perhaps modulated by turgor pressure and membrane tension. Endocytosis has a time course described by a half-time of 5 - 6 s for a 20 ms depolarizing pulse (Fig. 3.3 - 3.9). The initiation of endocytosis is regulated by a Ca^{2+} dependent process that is loosely nanodomain coupled to L-type Ca^{2+} channels. In AII-ACs we found that exo/endocytosis is unaffected by high [EGTA], but low

[BAPTA] fully blocks endocytosis while exocytosis is only partially blocked (Fig. 3.2, 3.4, 3.5). This was different from findings in the calyx of Held where both high [EGTA] and low [BAPTA] reduced exocytosis with no effect on endocytosis, while endocytosis was only blocked by high [BAPTA] when a majority of exocytosis was blocked (Yamashita et al., 2010). Endocytosis presumably occurs in the peri-active zone, where we propose that endocytosis hotspots are loosely nanodomain coupled, yet the exact mechanism is unknown. It was proposed that calmodulin initiates endocytosis in the calyx of Held (Wu et al., 2009), yet CaMKII/calmodulin do not seem to affect endocytosis after hearing development (Yamashita et al., 2010). There is also evidence that endophilin can form complexes between the synaptic vesicle and Ca^{2+} channels, and these interactions are Ca^{2+} dependent (recently reviewed in Gandini and Zamponi, 2021). Uncovering the mechanism that triggers Ca^{2+}-dependent endocytosis in the AII-AC is one of our next goals moving forward with this study.

ii. Clathrin-coated pits form in the peri-active zone following exocytosis and this generates curvature and subsequent invagination of the plasma membrane (see review, Lacy et al., 2018). This process is fully blocked by Pitstop-2 (Fig. 3.9). This evidence for clathrin-mediated endocytosis is supported by EM ultrastructure micrographs of AII-AC lobules showing evidence for coated vesicles (Fig. 3.10, adapted from Strettoi et al. 1992) with striking resemblance to early endosomes during clathrin-mediated endocytosis (CME) found using flash-and-freeze techniques in hippocampal neurons (Watanabe et al., 2013). In panel B of Figure 3.10, the coated pits can be seen lining the plasma membrane. Our data is similar to findings in cMFB, where Delvendahl et al. (2016) found that slow endocytosis can be blocked with Pitstop-2 for long pulses; however they found that the CME inhibitor did not block fast endocytosis for short pulses. Therefore, we will also test the effects of Pitstop-2 using short depolarizations in the AII-AC to see if fast endocytosis is clathrin-independent.

iii. Elongation of the endocytic invagination is regulated by the polymerization of F-actin. We found that blocking actin polymerization with latrunculin-A reduced endocytosis in AII-ACs (Fig. 3.8). Dynamin helices form around the endosomal neck during elongation, and GTP-dependent constriction causes scission of the endocytic invagination. We were able to block

dynamin-dependent scission with the non-hydrolyzable GTPγS in our recording pipette and with Dyngo-4a, indicating that dynamin is required for endocytosis in AII-ACs.

iv. Disassembly of the endocytotic machinery occurs after the synaptic vesicle is retrieved and fully formed, at which point the synaptic vesicle is recycled back to the vesicle pool and loaded with neurotransmitter. The vesicular glycine reloading requires vATPase-mediated vesicle acidification and vGAT for proton mediated glycine transport into the synaptic vesicle (Abery, 2016). Glycine transporters can move glycine from the synaptic cleft to the cytoplasm, and both isoforms (GLyT1 and GlyT2) are expressed in the inner nuclear layer (Peña-Rangel et al., 2008). Results from our GlyT2-Cre expression strongly suggest that AIIs have GlyT2. However, a recent study shows that loss of GlyT1 in AII-ACs impairs both glycine transmission and reuptake (Eulenburg et al., 2018). Thus, AII-ACs probably express both GLyT1 and GlyT2 in their plasma membranes.

Section 5.4: Future Directions

1. Ca^{2+} imaging to test EPAC-dependent CICR pathways.
    a. Further test Ca^{2+} imaging with the EPAC analog (8-pCPT). We have nice preliminary data showing that 8-pCPT induces Ca^{2+} release from stores, we will now perform more experiments for statistical analysis. We will also perform control where we puff normal Ames (vehicle control) where we expect to see no GCaMP6F responses. We will also do more experiments puffing caffeine (positive control) to reproduce results in chapter 4.
    b. Test ryanodine and 2-APB together with 8-pCPT. Here, we can bath apply each CICR inhibitor during Ca^{2+} imaging with the GCaMP6F expressing retina slices. We expect that either of these drugs or both will reduce GCaMP6F signals during local puffs of 8-pCPT. This will tell us which CICR pathways in the AII-AC involve EPAC-dependent signaling.
    c. Test effects dopamine and other GPCR agonists with Ca^{2+}-imaging. We can theoretically observe GCaMP6F signals in AII-AC lobules with local or bath applications of dopamine, if this induction pathway is responsible for CICR in AIIs.
    d. Test if dopamine-cAMP hyperpolarization activates Ca^{2+}-dependent BK channels. We have shown that AII-ACs express BK currents which can be activated by CICR and in turn

hyperpolarize the cell. This could contribute to the changes we see in AII-AC spike properties and sIPSC frequency. We can bath apply dopamine during whole-cell patch-clamp experiments, where we expect to see an increase in BK currents (isolating CICR activated events by blocking VGCCs with isradipine or cadmium).

e. Test in current clamp whether 8-pCPT depolarizes the AII-AC membrane potential. This experiment was inspired by a comment from Tom Baden, where the GCaMP6F signals looked like they were voltage gated responses because they occurred globally across the whole cell. Therefore, we can see if 8-pCPT is causing a voltage gated response by blocking different ion channels (e.g. Na_v, or Ca_v).

2. Fast clathrin-mediated endocytosis.

a. Test Pitstop-2 with short pulse durations. As described above, Delvendahl et al. (2016) showed that Pitstop-2 blocked "slower" high temperature (5-6 s) endocytosis responses with Pitstop-2, which had similar kinetics to our responses in the AII-AC. They also found no effect on fast responses to short depolarizations, indicating that fast endocytosis was clathrin-independent. We have to test this in the AII-AC to determine if clathrin-mediated endocytosis is the sole mechanism in AII-ACs.

b. Test endocytosis at higher temperature (37 ^{o}C). Endocytosis is highly temperature dependent, which drastically accelerates when changing bath temperatures from 30-37^{o}C (Delvendahl et al., 2016), which uncovered an ultrafast (100 – 300 ms) mode of endocytosis. We expect that high temperature with short pulses, will uncover a similar mode of endocytosis in AII-ACs.

c. Test if Ca^{2+} mediated endocytosis is blocked by calmodulin and calcineurin inhibitors. myosin light-chain kinase (MLCK) peptide and CaM-binding domain (CBD) peptide are two examples of calmodulin inhibitors. We include either of these peptides in our internal solution recording solution with the expectation that they will block Ca^{2+} endocytosis. Likewise, two examples of calcineurin inhibitors are CaN inhibitors FK-506 and CysA, which we will use accordingly (Yao and Sakaba, 2012).

Section 5.5: Acknowledgements

This work was supported by National Institutes of Health Grants EY014043 and DC12938 to H.v.G.; and Casey Eye Institute P30 Grant EY010572. This work was union-made and upheld fair labor practices approved by AFSCME Local 402 OHSUGRU. Thanks to my thesis committee members Catherine Morgans, Stephen Smith, Benjamin Sivyer, Anusha Mishra, and Stefan Hallermann for their valuable input and support.

Section 5.6: References

Aubrey KR (2016) Presynaptic control of inhibitory neurotransmitter content in VIAAT containing synaptic vesicles. Neurochem Int 98:94-102.

Eulenburg V, Knop G, Sedmak T, Schuster S, Hauf K, Schneider J, Feigenspan A, Joachimsthaler A, Brandstätter JH (2018) GlyT1 determines the glycinergic phenotype of amacrine cells in the mouse retina. Brain Struct Funct 223(7):3251-3266.

Gandini MA, Zamponi GW (2021) Voltage-gated calcium channel nanodomains: molecular composition and function. FEBS J. doi: 10.1111/febs.15759. Epub ahead of print.

Gekel I , Neher E (2008) Application of an Epac activator enhances neurotransmitter release at excitatory central synapses. J Neurosci 28: 7991–8002.

Lacy MM, Ma R, Ravindra NG, Berro (2018) Molecular mechanisms of force production in clathrin-mediated endocytosis. FEBS Lett 592(21):3586-3605.

Midorikawa M, Sakaba T (2017) Kinetics of Releasable Synaptic Vesicles and Their Plastic Changes at Hippocampal Mossy Fiber Synapses. Neuron 96(5):1033-1040.e3.

Parthier D, Kuner T, Körber C (2018) The presynaptic scaffolding protein Piccolo organizes the readily releasable pool at the calyx of Held. J Physiol 596, 1485–1499.

Peña-Rangel MT, Riesgo-Escovar JR, Sánchez-Chávez G, Salceda R (2008) Glycine transporters (glycine transporter 1 and glycine transporter 2) are expressed in retina. Neuroreport 19(13):1295-9.

Sakaba T, Neher E (2001) Calmodulin mediates rapid recruitment of fast-releasing synaptic vesicles at a calyx-type synapse. Neuron 32(6):1119-31.

Watanabe S, Rost BR, Camacho-Pérez M, Davis MW, Söhl-Kielczynski B, Rosenmund C, Jorgensen EM (2013) Ultrafast endocytosis at mouse hippocampal synapses. Nature 504(7479):242-247.

Wu XS, McNeil BD, Xu J, Fan J, Xue L, Melicoff E, Adachi R, Bai L, Wu LG (2009) Ca^{2+} and calmodulin initiate all forms of endocytosis during depolarization at a nerve terminal. Nat Neurosci 12(8):1003-1010.

Yao L, Sakaba T (2012) Activity-dependent modulation of endocytosis by calmodulin at a large central synapse. Proc Natl Acad Sci USA 109(1):291-6.